On the controllability of saturating crossflow vortices

Tobias Backer Dirks

School of Mathematics, Computer Science & Engineering

City, University of London

Submitted in part fulfilment of the degree of

Doctor of Philosophy

7th December 2018

Contents

List of Figures

List of Tables

Acknowledgements

First and foremost I would like to thank my supervisor Prof. Chris Atkin for all of his support, guidance and patience throughout, and for proof-reading my thesis and making me remove all the fancy words. I would also like to acknowledge the financial support of Airbus Group Innovations, in particular Dr. Stephen Rolston, with whom I very much enjoyed working for during my time in Filton. I would also like to thank Mr. Mike Smith for helping me iron the kinks out of the design for the rotating disk and annulus experiment, may he rest in peace.

This journey would have been a lot lonelier if not for my colleagues, especially the cast of Star-Wars; Chetan, Marco, Nick and Ed, who made the last few years far more enjoyable. Thank you for listening to me complain, helping out where possible, teaching me how to handle my drink and making lunch time an event.

I would also like to thank my parents and siblings for their unwavering support and optimism, without whom I would never have finished. Avgi for keeping me well fed and Gauss for all of the love and giving me an excuse to go walkies. Finally, I would like to thank my loving girlfriend Nicky for always being there for me and not being as much of a pain as I was to her when she was writing up.

Declaration

I, Tobias Backer Dirks, declare that this thesis entitled *On the controllability of saturating crossflow vortices* and the work presented in the thesis are both my own, and have been generated by me as the result of my own original research. I grant powers of discretion to the University Librarian to allow the thesis to be copied in whole or in part without further reference to the author. This permission covers only single copies made for study purposes, subject to normal conditions of acknowledgements. I confirm that:

- this work was done wholly or mainly while in candidature for a research degree at this University;
- where I have consulted the published work of others, this is always clearly attributed;
- where I have quoted from the work of others, the source is always given. With the exception of such quotations, this thesis is entirely my own work;
- I have acknowledged all main sources of help;
- parts of this work have been published as Backer Dirks and Atkin (2018).

Signed:.....

Date:.....

Summary

This thesis examines the suitability of the crossflow generated by rotating boundary layers for investigating crossflow amplification control thresholds at scales suitable for university wind tunnels. Using rotating disk flow as a starting point, it was postulated that the addition of a concentric annulus, rotating at a different angular velocity to the inner disk, would allow controlled changes in crossflow growth just prior to non-linear saturation. A novel formulation for the boundary layer a rotating disk with radially variable angular velocity was derived for application on the disk-annulus system, though ultimately it was determined that the resultant equations were elliptical in character and therefore no longer representative of the physics of the swept-wing boundary layer.

In order to ensure parabolicity, a configuration involving a rotating body in an axial flow was proposed. It was speculated that local variations in edge velocity, induced by the body geometry, would provide an appropriate analogue to the variable pressure gradients found in the vicinity of swept-wing leading edge. A novel formulation for the boundary layer equations for a generalised rotating body of revolution, both with and without an incompressible axial flow, was subsequently derived, implemented within the QinetiQ `BL2D` boundary layer method and validated against other shape-specific formulations. The formulation employs a velocity switch, u^*, which allows for a seamless transition between quiescent and axial flow investigations and provides a valuable alternative to other shape and flow specific formulations.

The perturbation and stability equations in a general orthogonal curvilinear co-ordinate system were derived to include Coriolis accelerations terms, as well as retaining viscous curvature. The existing QinetiQ e^N method, `CoDS`, was modified and extended to enable the analysis of rotating boundary layers and provided qualitatively good agreement with results published by Garrett (2002), with quantitative differences attributed mainly to scaling.

The methods were combined in order to answer the original research question, whether the boundary layer due to a rotating body could be used as a viable analogue for swept-wing flow in the context of crossflow growth control. Velocity profiles for rotating axi-symmetric bodies were shown to provide a good match to those of swept-wing flow, with differences only in the second wall-normal derivatives. Results showed that geometries could be selected which demonstrated non-monotonic N-factor growth, of the type encountered during HYLTEC and AFLoNext. An axi-symmetric body derived from the upper surface of the RAE2822 demonstrated N-factor amplification followed by sudden stabilisation.

Nomenclature

Greek symbols

α_r, α_i . . . . . Complex wavenumber in streamline direction.

α_t . . . . . Local surface tangent angle w.r.t. axis of revolution.

α_H . . . . . Hartree parameter describing radial evolution.

β_H . . . . . Hartree parameter describing meridional edge velocity evolution.

β_r, β_i . . . . . Complex wavenumber in crossflow direction.

$\gamma(s)$ . . . . . Strength of ring vortex.

γ . . . . . Equal to β_H in an axial flow, α_H without.

δ^* . . . . . Local boundary layer displacement thickness.

ζ_r . . . . . Square of the ratio of rotational velocity to meridional velocity.

ζ . . . . . General function representing a system of ODEs.

η . . . . . Overall efficiency of aircraft propulsion system.

η . . . . . Transformed wall-normal co-ordinate.

$\Delta\eta$ . . . . . Wall-normal mesh increment.

θ_l . . . . . Angle of latitude.

κ_1, κ_2 . . . . . Principal curvatures.

κ_{xy}, κ_{zy} . . . . . Local geodesic curvature.

κ_{xz}, κ_{zx} . . . . . Local streamline curvature.

ν . . . . . Kinematic viscosity.

ξ_s . . . . . Derivative of ξ w.r.t. s.

ξ . . . . . Transformed meridional co-ordinate.

ρ . . . . . Density of fluid.

τ_u, τ_w . . . . . Disturbance derivative substitutions.

ϕ_c . . . . . Cone half-angle.

ϕ_w . . . . . Disturbance wave angle.

ϕ, ψ . . . . . Functions of dimensionless stream functions.

ψ_s . . . . . External streamline angle.

ω_r, ω_i . . . . . Complex frequency of disturbance.

$\Omega_s, \Omega_y, \Omega_\theta$ . . . Components of angular velocity in meridional, wall-normal and azimuthal directions.

$\Omega_x, \Omega_y, \Omega_z$ . . . Components of angular velocity in streamline, wall-normal and crossflow directions.

Ω . . . . . Angular velocity.

$\vec{\Omega}$ . . . . . Angular velocity vector.

Latin symbols

A_0 . . . . . Initial amplitude of crossflow mode.

$A_{tr,cf}$ . . . . . Amplitude of most amplified crossflow mode at transition.

A . . . . . Compact-difference matrix.

B . . . . . Compact-difference residuals matrix.

C_D . . . . . Drag coefficient.

C_{D0} . . . . . Zero-lift drag coefficient.

C_{Df} . . . . . Form drag coefficient.

C_f . . . . . Skin friction drag coefficient.

C_L . . . . . Lift coefficient.

C_p . . . . . Pressure coefficient.

D . . . . . Aircraft drag force.

dS . . . . . Incremental arc length in curvilinear co-ordinate system.

$E(k)$ . . . . . Complete elliptic integral of the second kind.

e . . . . . Eccentricity of ellipsoid.

f, g, p . . . . . Dimensionless stream functions.

f_n, u_n, τ_n . . . . Non-dimensional iterative solution at nth iteration.

$\Delta f, \Delta u, \Delta \tau$ . . . Non-dimensional iteration increments.

g_n, w_n, σ_n . . . . Non-dimensional iterative solution at nth iteration.

$\Delta g, \Delta w, \Delta \sigma$ . . . Non-dimensional iteration increments.

H . . . . . Fuel energy per unit weight.

h_x, h_y, h_z	Co-ordinate metrics in streamline, wall-normal and crossflow directions.
$K(k)$	Complete elliptic integral of the first kind.
K	Lift induced drag factor.
$\bar{K}$	Vortex sheet coupling coefficient.
k_c	Flow scaling constant for self-similar solutions.
k_ξ	Local flow factor for ξ derivatives.
$k_{u/s}$	Function of known upstream flow.
k_w	Wavenumber magnitude.
k	Elliptic modulus.
L_ξ	Viscous length scale.
L	Aircraft lift force.
m	Exponent characterising inviscid flow.
N_{CF}	Crossflow N-factor.
N_{CTRL}	Control N-factor.
N_{TS}	Tollmien-Schlichting N-factor.
$N_{tr,cf}$	Crossflow transition critical N-factor.
$N_{tr,cf}$	Crossflow transition critical N-factor.
N	Number of ring vortex elements.
P	Dimensional pressure.
p_0	Non-dimensional pressure at the wall.
Q_e	Local boundary layer edge velocity.
R_1, R_2	Principal radii of curvature.
Re_d	Reynolds number.
Re_∞	Freestream Reynolds number.
Re	Local displacement thickness Reynolds number.
R	Aircraft range.
r, θ, y	Radial, azimuthal and wall-normal co-ordinates.
r_0	Disk length scale, e.g. outer radius.
$\vec{r}$	Perpendicular distance to axis of rotation.
s, θ, y	Meridional, azimuthal and wall-normal co-ordinates.

T_s . . . . . Ratio of freestream to maximum rotational velocity.

U, V, W . . . . . Velocity components in streamline, wall-normal and crossflow directions.

U_d . . . . . Velocity scale for disk.

$\tilde{u}, \tilde{v}, \tilde{w}, \tilde{p}$ . . . . Fluctuating velocity components in streamline, wall-normal and crossflow directions.

$\hat{u}, \hat{v}, \hat{w}, \hat{p}$ . . . . Perturbation velocity components in streamline, wall-normal and crossflow directions.

$\vec{u}_{\text{in}}$ . . . . . Velocity vector in inertial frame of reference.

$\vec{u}_{\text{rot}}$ . . . . . Velocity vector in rotating frame of reference.

u, τ, w, σ . . . . Linearised derivatives of dimensionless stream functions.

u, v, w, p . . . . Time-averaged velocity components in streamline, wall-normal and crossflow directions.

u, v, w . . . . . Velocity components in meridional, wall-normal and azimuthal directions.

u^* . . . . . Switchable velocity scale for rotating body formulation.

u_e . . . . . Local boundary layer edge velocity.

u_r, v, w . . . . . Velocity components in radial, wall-normal and azimuthal directions.

u_∞ . . . . . Freestream velocity.

$u_{ij}, w_{i,j}$ . . . . . Induced velocity components for a unit ring vortex.

W_1 . . . . . Aircraft start weight.

W_2 . . . . . Aircraft end weight.

x, y, z . . . . . Re-scaled co-ordinates in streamline, wall-normal and crossflow directions.

x_0 . . . . . Location of neutral point.

$\hat{x}, \hat{y}, \hat{z}$ . . . . . Co-ordinates in streamline, wall-normal and crossflow directions.

Acronyms

2-D . . . . . Two-dimensional.

3-D . . . . . Three-dimensional.

AFLoNext . . . Active flow, loads & noise control on next generation wing.

CF . . . . . Crossflow.

CNC . . . . . Computer numerical control.

CPI . . . . . Consumer price index.

DC . . . . . Direct current.

HLFC . . . . . Hybrid laminar flow control.

LDA . . . . . Laser Doppler anemometry.

LFC . . . . . Laminar flow control.

N-S . . . . . Navier-Stokes.

ODE . . . . . Ordinary differential equation.

PDE . . . . . Partial differential equation.

PSE . . . . . Parabolised stability equations.

RPM . . . . . Revolutions per minute.

T-S . . . . . Tollmien-Schlichting.

WIPS . . . . . Wing ice protection systems.

1 Background

Contents

1.1 Introduction

The aircraft industry is continually searching for ways in which it can reduce drag at aircraft level, in turn reducing fuel costs for a given flight envelope. In addition to this, the environmental impact of aircraft travel has been heavily scrutinised, as the effects of climate change continue to worsen, and global warming becomes an ever more real threat. This has led to an increased push by aircraft manufacturers to produce 'cleaner' aircraft to reduce CO_2 and NO_x emissions. This encompasses everything from more ecologically friendly material sourcing to higher fuel economy. From an economical perspective, the price of Brent crude oil has risen from \$35 to \$80 a barrel since the beginning of the 21st century (figure 1.1), having reached \$145 before crashing again

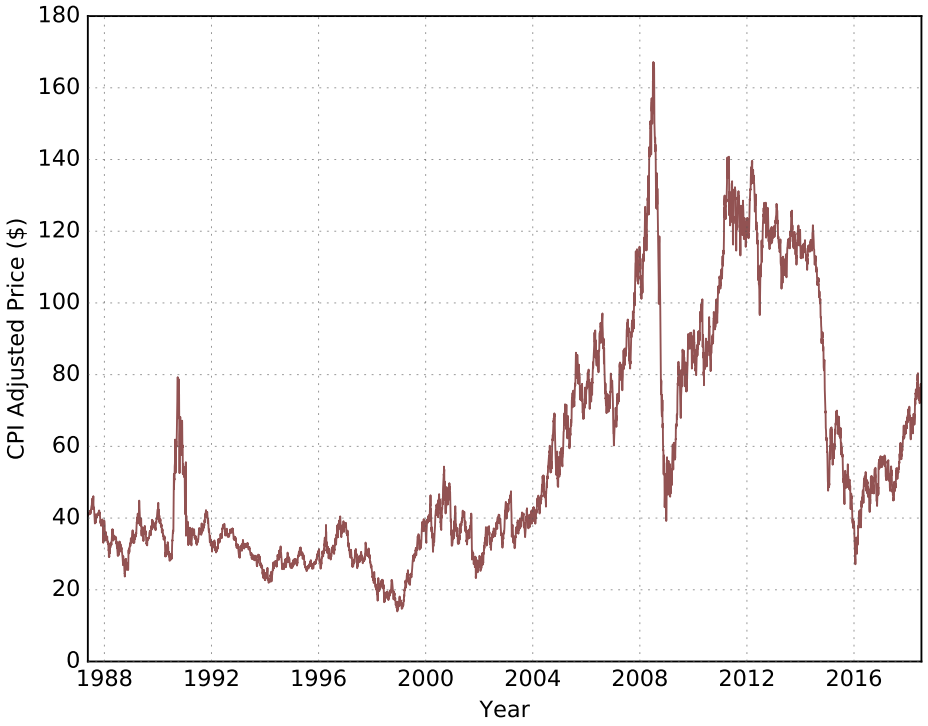

Figure 1.1: Global average price in U.S. Dollars for a barrel of Europe Brent Crude oil from 1987 to the present, data from the U.S. Energy Information Administration (2018) and adjusted using Consumer Price Index (CPI) data from the U.S. Bureau of Labor Statistics (2018).

during the 2008 global recession. Subsequently the general trend has indicated sustained rise, as demand for fossil fuels increases in the developing world while stockpiles begin to diminish as conventional extraction methods become less cost effective.

Recent advances in alternate power sources and battery technology have caused a surge of enthusiasm for electric vehicles, and aircraft are no different. Companies such as Wright Electric (2018), a start-up supported by Y-Combinator (2018) which aims to develop a 150 passenger fully electric, zero emission passenger jet in the future, have been working on making electric flight a reality. The main hurdle to overcome is the energy density of current battery technology. While this has improved in recent years to the extent that electric cars, with a higher tolerance for heavy components, have become a possibility, the energy density of current batteries is still only a maximum of 260 kWh/kg, 45 times lower than that of kerosene. Start-up Eviation Aircraft (2018) are in the process

of completing an electric powered prototype, the Eviation Alice. This 6- to 9-seater aircraft will have over 3500 kg of batteries and a range of just 1000 km. Extrapolating the battery mass per passenger to a 150 seat jet yields a mass between 58 and 87 tonnes for a range of 1000km. Expanding the range to inter-continental levels reveals masses exceeding the maximum take-off weight of even an Airbus A380 - just in batteries.

$$R = H \times \eta \times \frac{L}{D} \times \ln\left(\frac{W_1}{W_2}\right) \tag{1.1}$$

The reasons for this gulf in performance can be found by inspecting the Bréguet Range Equation, 1.1. In it, R is the range of the aircraft, W_1 and W_2 are the aircraft start and end weights, L/D is the lift-to-drag ratio of the aircraft, η is the overall efficiency of the propulsion system and H is the energy of the fuel per unit weight. For a jet like the Airbus A380 the efficiency of the propulsion system is circa 0.37, while the energy per unit weight for kerosene, when expressed as a distance, is 4350 km (kJ/N). For electric aircraft the efficiency of propulsion systems, for example the SP260D by Siemens (2018), can be as high as 0.95. On the other hand the energy per unit weight of the most modern batteries is only 95 km. Assuming equal lift-to-drag ratios and start-end weights (in reality electric aircraft won't lose any mass during the flight), it is clear that a jet consuming fossil fuels will still yield a range nearly 18 times greater than its electric counterpart. Due to this aircraft travel still relies heavily on the use of fossil fuel and will remain to do so for the foreseeable future, which comes with its own set of considerations.

One of the ways in which we can help lower fuel consumption, and therefore CO_2 and NO_x emissions, is by reducing aircraft drag. Aircraft drag arises from two main sources (equation 1.2), which are known as lift induced drag, KC_L^2, and zero-lift drag, C_{D_0}. The former is a function of lift and aspect ratio. Lift induced drag accounts for around 40% of the drag experienced by aircraft and is the result of the formation of a horse-shoe vortex system on the wing.

$$C_D = C_{D_0} + KC_L^2 \tag{1.2}$$

Zero-lift drag, also known as viscous drag, accounts for nearly 50% of the drag. It can be broken down into two further categories, skin friction drag, C_f, and form drag, C_{D_f}.

Friction drag relates to velocity gradients at the surface, and is greater for a turbulent boundary layer than a laminar one. Alternatively, form drag, also known as pressure drag, arises due to the effective changes in aerofoil shape due to the presence of a boundary layer. For an aerofoil this again is greater for a turbulent boundary layer than a laminar one as the former is thicker.

$$C_{D_0} = C_f + C_{D_f} \tag{1.3}$$

Friction drag accounts for the majority of viscous drag and is commonly the main target for designers searching for ways to reduce aircraft drag. Laminar Flow Control (LFC) technology holds great promise in this respect. LFC methods either actively or passively control (extend) the region of laminar flow within the boundary-layer, delaying transition to turbulence and ultimately reducing both friction and form drag. For the primary transition mechanisms (section 1.2) this is done by altering the velocity profile over the aerofoil, usually either by applying small amounts of suction within the early stages of the boundary-layer or with changes in shape to alter the pressure gradient within the boundary-layer. Atkin (2004), Atkin (2008) and Green (2008) discuss the current state of LFC technologies and their readiness for implementation on commercial aircraft. Both authors allude to the disparity between potential drag reduction and actual drag reduction at aircraft level. Claims of theoretical fuel savings of up to 25% in some cases are quickly lowered to low single digits once weight penalties and efficiencies are accounted for. Add to this the complexity in getting these systems properly certified and altering manufacturing processes and the savings have rarely added up on paper. This has led to scepticism amongst research budget holders and, up to recently, an unwillingness to commit to extensive research on LFC as it was deemed well understood and too marginal. One of the biggest reasons for the disparity between theoretical and perceived savings is due to the criteria on which we base transition prediction, namely instability amplification rates, known as N-factors (section 1.3). Transition N-factors can vary substantially depending on the type of instability, speed (compressible vs. incompressible) or the initial flow conditions. These variations can have a large impact on design, affecting systems weight and effectiveness at aircraft level.

1.2 Transition and crossflow instability

Boundary-layer transition can occur through many different ways, or paths, as described by Morkovin, Reshotko and Herbert (1994), and as shown in figure 1.2. Disturbances from the freestream enter the boundary-layer through sound waves, vortical structures or even as particles and introduce perturbations to the idealised steady-state flow. This process is known as receptivity (Morkovin, 1969) and is responsible for providing the initial disturbance amplitudes and frequencies. In flight, where freestream disturbances are small, these initial disturbances can result in the growth of primary instability modes. For swept wings the four main types of instability that lead to transition are the leading-edge instability and contamination, streamwise, centrifugal and crossflow instabilities.

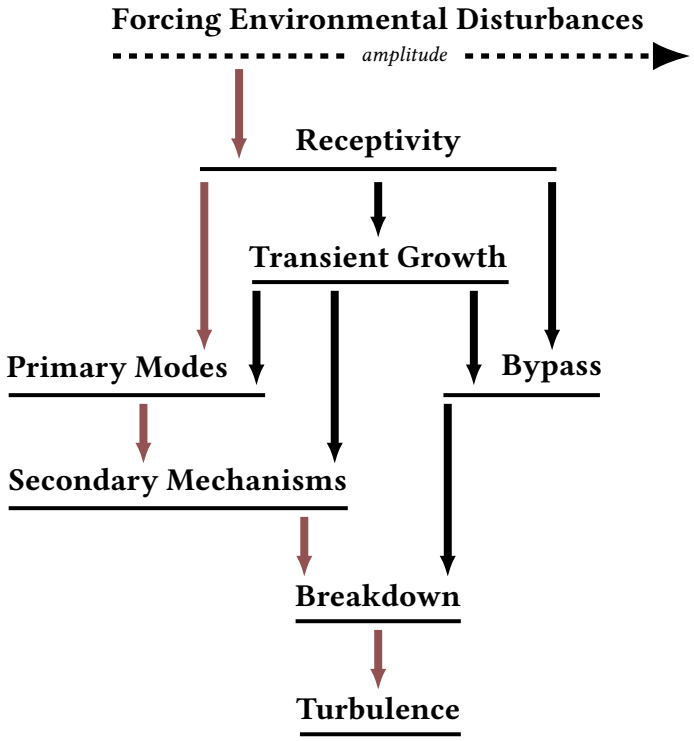

Figure 1.2: A road map to transition, adapted from Morkovin, Reshotko and Herbert (1994).

The type of instability which occurs depends on a number of factors, ranging from geometry (surface curvature and therefore pressure gradient) to Reynolds number, sweep angle and surface roughness. Whether or not externally-forced disturbances grow can be explored, for small amplitudes, using linear theory, summarised by Mack (1984). Leading-edge instabilities occur along the attachment-line of a wing, where the

leading edge flow splits between the upper and lower surfaces and are attributed to a basic instability of the attachment-line flow. Attachment line contamination on the other hand is the result of turbulence structures which arise on the fuselage of the aircraft and propagate along the wing leading edge (Poll, 1979). The streamwise instability is associated with chordwise component of the flow and follows the streamlines. This results in the generation of Tollmien-Schlichting (T-S) waves (Schubauer and Skramstad, 1948) and occurs in areas on a wing of little to adverse pressure gradients. T-S waves are usually countered in transonic wing design by the use of a prolonged favourable pressure gradient on the upper surface. Centrifugal instabilities, due to concave curvature, can produce Görtler vortices (Floryan and Saric, 1982; Hall, 1983) - though Hall (1985) showed these have little effect on wings with greater-than-moderate sweep angles and T-S instabilities are expected to grow in their stead.

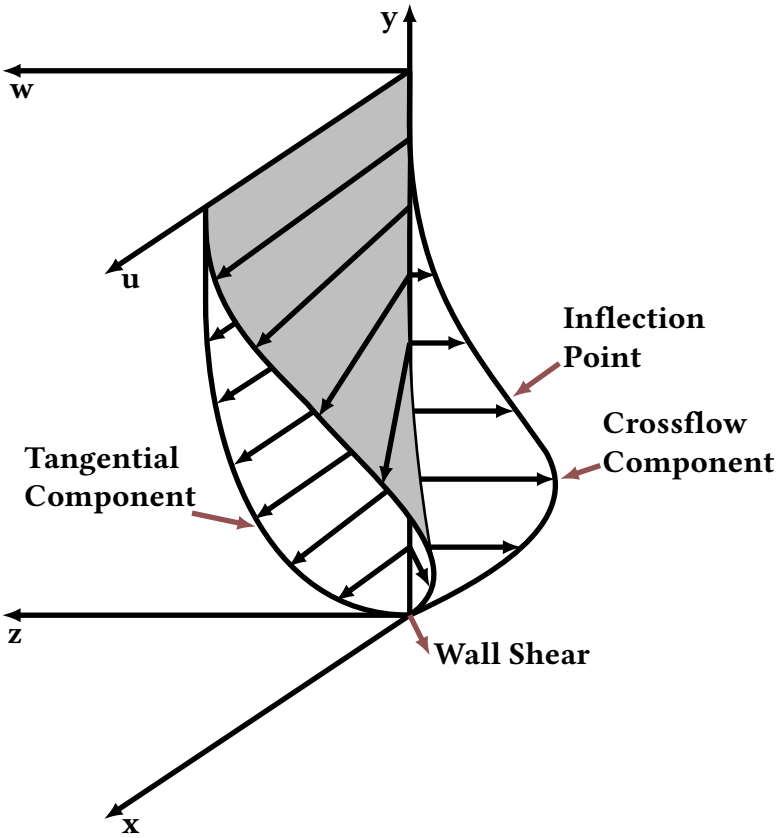

Figure 1.3: A typical crossflow profile for a swept-wing boundary-layer, adapted from Reed and Saric (1989).

The primary instability of the crossflow boundary-layer arises due to a combination

of sweep and high curvature. In-plane curvature of streamlines causes centrifugal forces, which outside the boundary-layer are balanced by pressure forces. However, within the boundary-layer the centrifugal forces decrease towards the wall proportionally to velocity, figure 1.3, whereas pressure remains largely constant. The resultant pressure force creates a crossflow and a 3-D velocity profile. This inflectional profile, which is unstable according to Rayleigh (1880) and Fjørtoft (1950), produces an inflectional instability which takes the form of a set of co-rotating vortices in the streamwise direction (Gregory, Stuart and Walker, 1955). Crossflow is the main cause of transition on swept-wing flows and both stationary and travelling vortices can arise from crossflow instabilities, which one dominates is determined by the receptivity process, though in low turbulence environments such as flight, transition is usually attributed to stationary vortices. In wind tunnels and other high turbulence environments travelling crossflow vortices are thought to be the main cause due to their larger amplification rates and the receptivity conditions (Deyhle and Bippes, 1996). Conversely, stationary crossflow

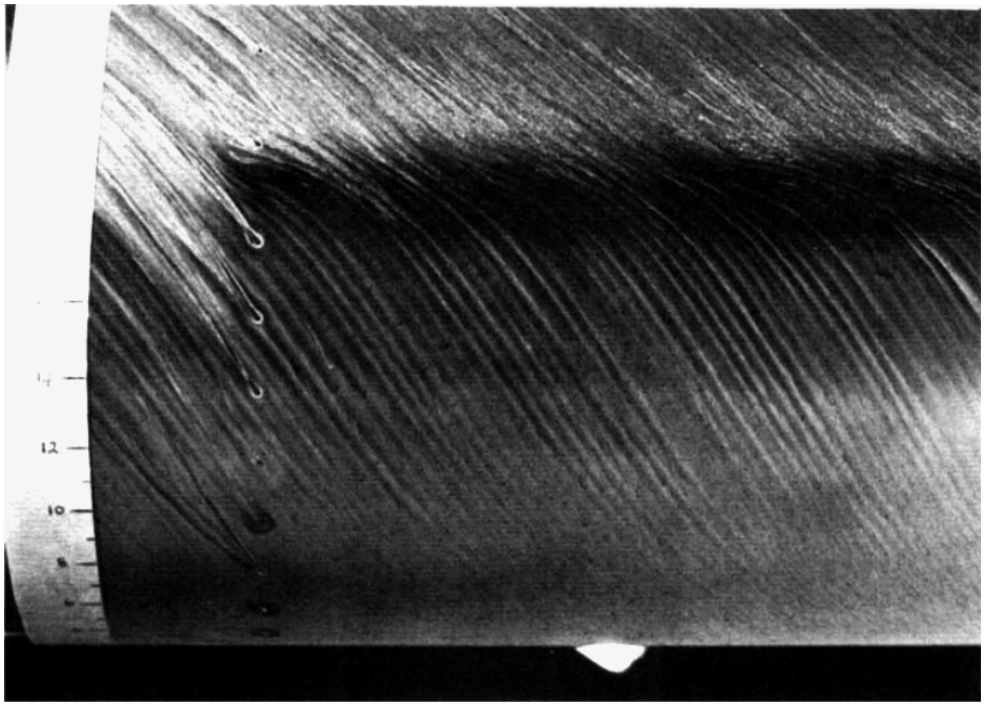

Figure 1.4: Stationary crossflow vortices leading to transition on a 55° swept cylinder (flow direction from bottom to top). Surface oil-flow visualisation by Poll (1985).

vortices (parallel streaks in figure 1.4) have larger initial amplitudes and consequently

their integrated effect generates a significant distortion of the mean-flow in low turbulence environments. This produces a saturation of the streamwise crossflow modes between 10% and 30% amplitude (Saric, Reed and White, 2003). Downstream of this amplitude saturation, inflectional shear layers caused by a distorted mean-flow produce a secondary instability resulting in rapid breakdown to turbulence, typically seen as a jagged transition front (White and Saric, 2005).

1.3 Analysis tools

Transition tools using linear stability theory (Mack, 1984) are based on an e^N criterion, where N is the log of amplification ratio, A/A_0, of the most amplified mode at breakdown and the initial amplitude of the disturbance (Van Ingen, 1956; Smith and Gamberoni, 1956; Van Ingen, 2008). Linear theory can predict the growth of instabilities accurately, at least initially, yielding the most unstable mode. However, the accuracy of transition prediction relies on correct initial, or receptivity, amplitudes. Figure 1.5 provides a schematic of crossflow instability growth for the idealised version of the primary instability growth process assumed by e^N theory. During the receptivity phase disturbances are introduced into the boundary layer and, following the neutral point, these grow according to linear theory from an initial amplitude A_0. A region wherein non-linear effects govern growth follows, and eventually secondary instabilities lead to rapid breakdown to turbulence. By integrating the gradient of the line given by linear theory, typical amplitudes for receptivity and breakdown can be estimated. The logarithmic ratio between the two is known as the critical N-factor. According to Obremski et al. (1969) the region governed by linear theory can be as high as 75–85% of the total transition process. Owing to this, and because the interval between the onset of non-linear growth and breakdown is finite, the approach is deemed to contain enough physics so that a semi-empirical extension can be used to predict transition location. The accuracy of this approach will rely on a representative experiment to accurately measure the location of breakdown, which can then be used to inform future linear stability calculations in similar conditions.

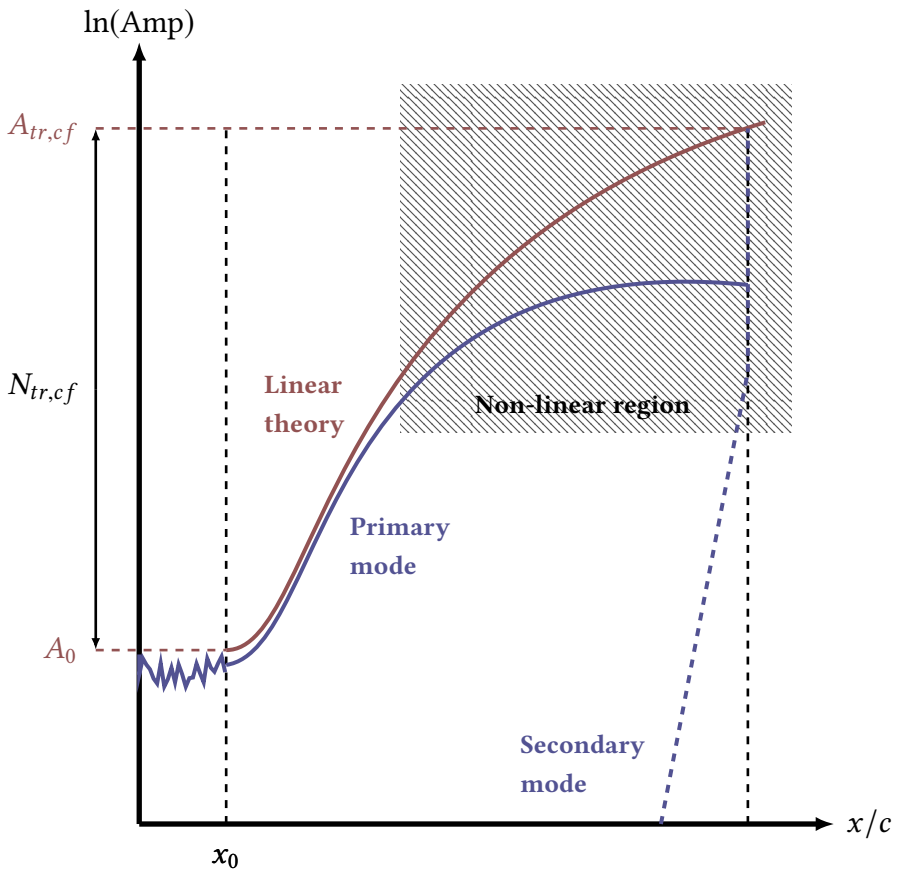

Figure 1.5: Sketch of crossflow instability growth, adapted from Atkin (2009). The blue line represents the unknown real growth while the red line is the prediction from linear theory.

1.4 Effects on design

As there is still some uncertainty in the exact critical N-factor when following linear theory, large safety margins are employed when designing flow control systems. Further uncertainty arises from the choice of stability method employed. Using a method which includes non-parallel effects, such as linear Parabolised Stability Equations (PSE) instead can reduce the estimated net drag by 9% (Atkin, 2004). This is due to the inclusion of convex streamwise curvature and the stabilisation of crossflow modes which that brings near the leading edge. Backer Dirks and Atkin (2015) further reinforced these findings while working on the "Active Flow, Loads & Noise control on next generation wing", AFLoNext, project, in which the choice of 'control' N-factors played a significant role in affecting the design constraints for a Hybrid Laminar Flow Control (HLFC) suction system.

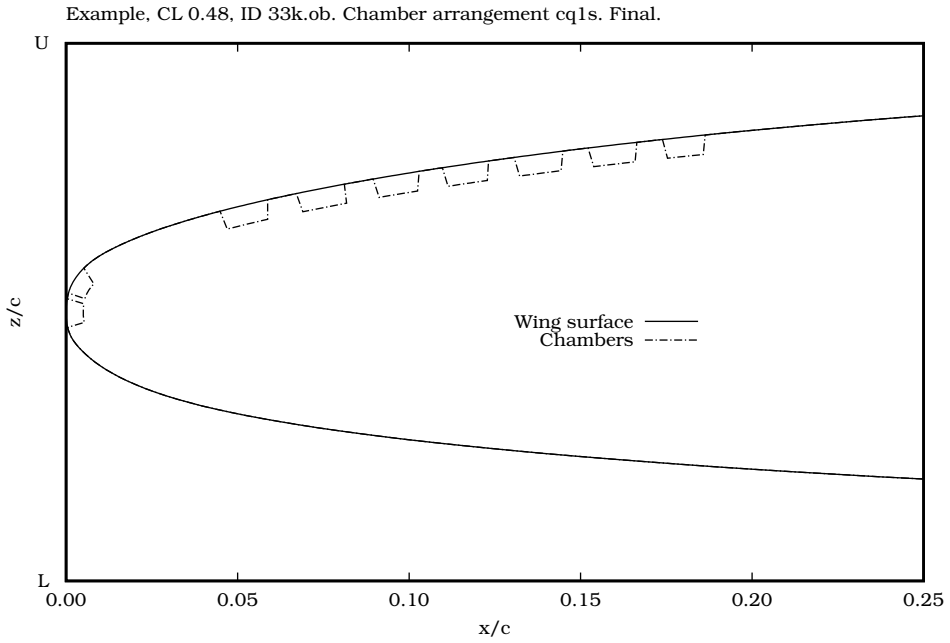

Figure 1.6: Example suction plenum chamber layout on a representative AFLoNext HLFC wing.

An HLFC suction system applies small amounts of suction within the initial boundary layer over a wing using a series of plenum chambers. This has a stabilising effect on instability growth. An example of such a suction system is shown in figure 1.6. The control N-factor of a suction system is an arbitrary N-factor which the designer does not wish to exceed within a specified chordwise distance. This ultimately delays further growth, and therefore also determines where transition will occur further downstream. Figure 1.7 shows two N-factor distributions for the suction system detailed in figure 1.6. The first, controlling crossflow N-factor growth until 0.25 s/c using a control N-factor (a) 4, the second using a control N-factor of (b) 5. Focusing our attention on the red lines (the envelope of maximum crossflow N-factors) and assuming a crossflow transition N-factor of 7, we note that transition location is only slightly affected by relaxing the crossflow control N-factor, with estimates of 0.58 s/c and 0.54 s/c using control N-factors of 4 and 5 respectively.

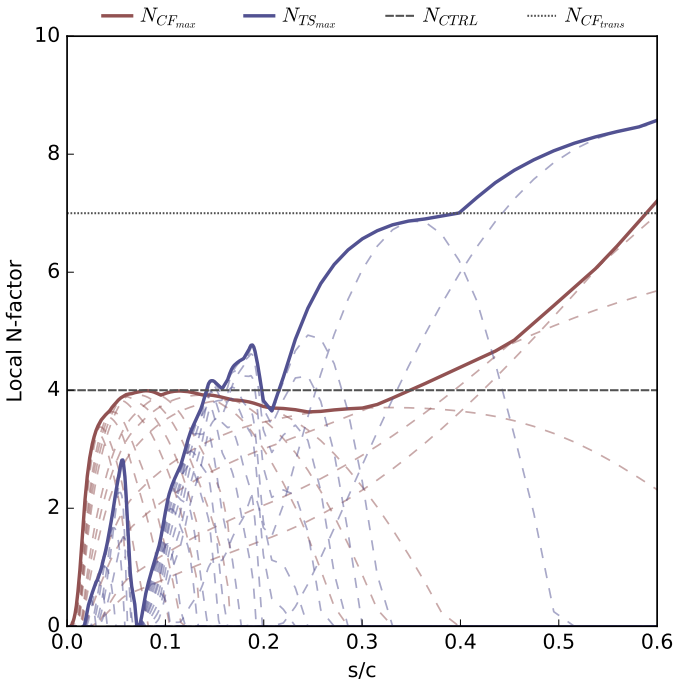

(a) *Crossflow control N-factor of 4.*

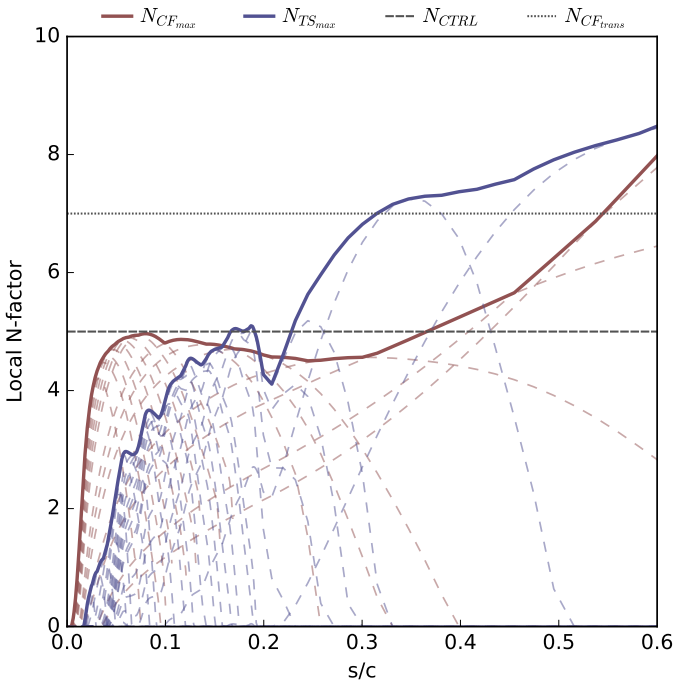

(b) *Crossflow control N-factor of 5.*

Figure 1.7: Maximum N-factor distributions for a representative AFLoNext HLFC wing using crossflow control N-factors of (*a*) 4 and (*b*) 5. Crossflow N-factors are only controlled until 0.25 s/c and allowed to grow thereafter.

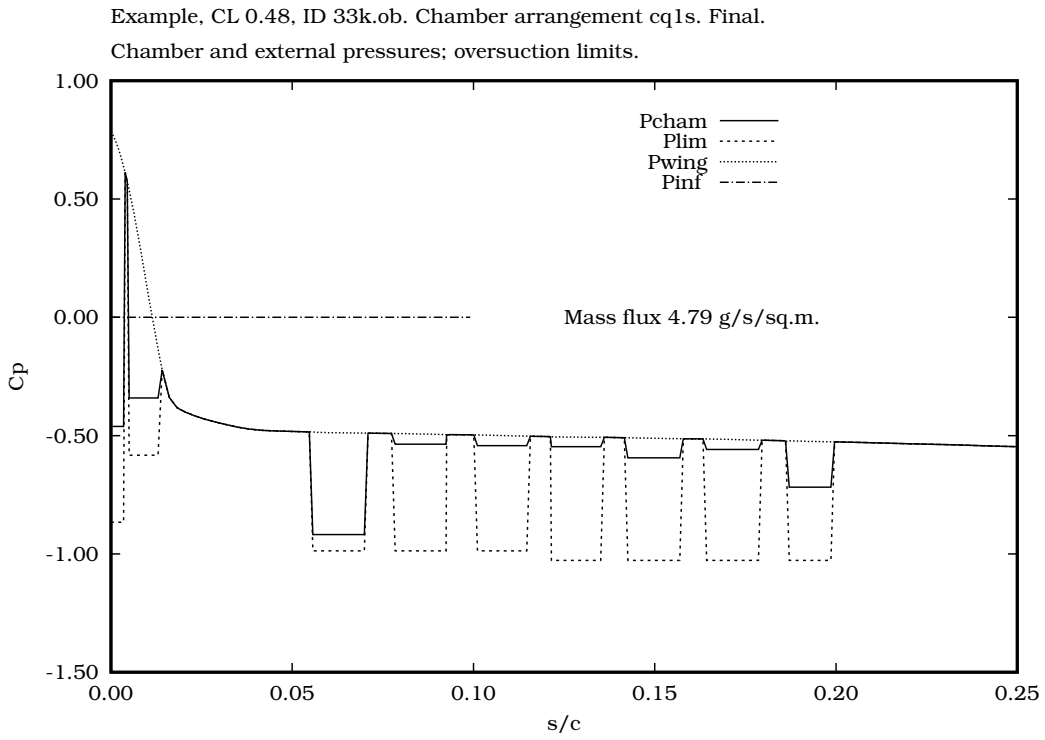

(a) *Crossflow control N-factor of 4.*

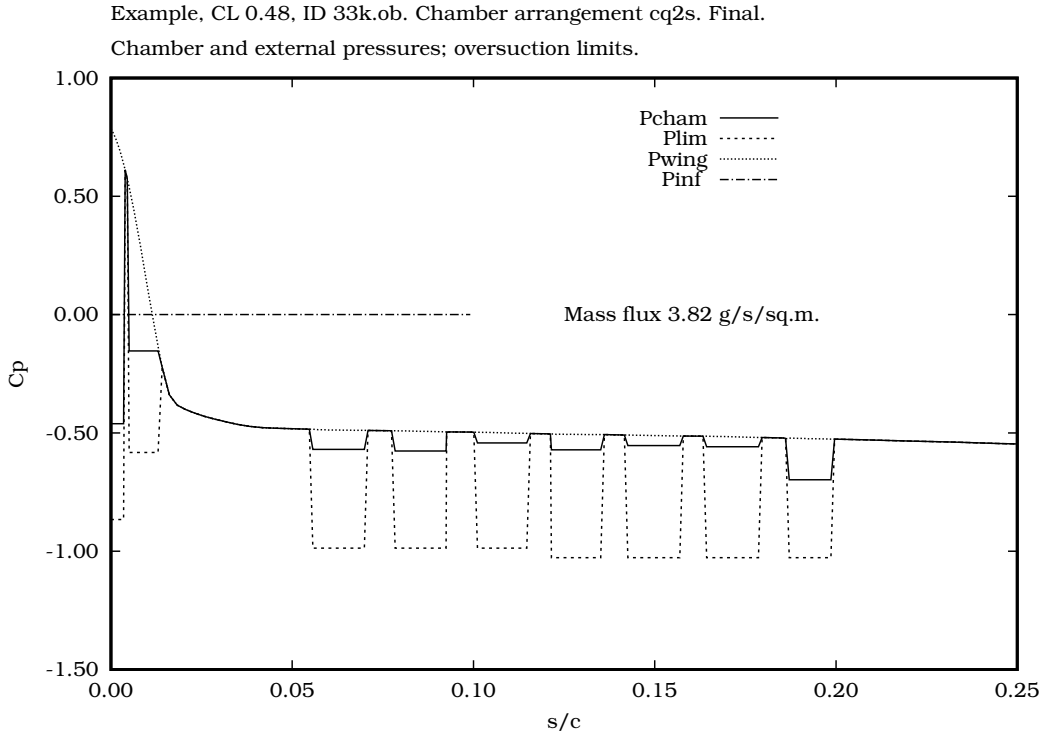

(b) *Crossflow control N-factor of 5.*

Figure 1.8: Suction chamber layout and plenum pressures for a representative AFLoNext HLFC system using crossflow control N-factors of (*a*) 4 and (*b*) 5. Note the 20.2% reduction in mass flow rate when the crossflow control N-factor is relaxed from 4 to 5.

On the other hand, the effect of this change in control N-factor on the required chamber pressures for the suction system, shown in figure 1.8, shows a 20.2% reduction in mass flux. This reduction in mass flux would lower the pump requirements, and in turn lower the weight of the system and/or the chamber sizes. During the AFLoNext project it was noted that the systems team was constrained for leading edge cavity space. This was due both to the size of suction chambers and the pressures required - which increased pump sizes and weight. Add to this the requirement for Wing Ice Protection Systems (WIPS) and high lift systems to be incorporated into the same leading edge cavity the result was a very tight fit and balance between each system. Any benefit from reducing the size or power of the suction system would be amplified due to the added benefit to the other systems.

The control of the growth of crossflow modes by pressure gradient, or as here with suction, is predicated by the fact that linear theory assumes infinitesimally small disturbance amplitudes. How accurate an assumption this is, and whether this is an accurate representation of the physical process, is not fully understood. The motivation (section 1.6) for the present work stems from this uncertainty. An investigation into the limits of control of crossflow modes using changes in pressure gradient, as well as a subsequent experiment, are required. Crossflow investigations are usually carried out in large industrial wind tunnels to increase the region of spanwise invariance, present due to wall-effects. In a university setting, where large tunnels with low freestream-turbulence levels are not the norm, it is possible to shape the walls of the wind tunnel in order to mitigate this. Alternatively, such modifications could be avoided by generating the required crossflow by another means.

1.5 Swept-wing flow analogues

There are a number of flows which produce crossflow profiles similar to those generated by swept-wing flow. Employing one of these rather than making use of a swept-wing could provide an easier route to experimental investigations. A swept wing model would either require a suction system or multiple models/leading edges to be manufactured for this investigation. In order to select an appropriate alternative, we first need to explore

the body of work already available for each of these flows in order to better establish their suitability for the application of variable pressure gradients.

The flow due to a rotating disk in still air is often used as a canonical example of crossflow and the crossflow instability and as such has attracted much attention and research. As in swept-wing flow, rotating disk flow exhibits a three dimensional, inflectional boundary-layer velocity profile. Therefore, it is also susceptible to the crossflow instability. The advantages of using a rotating disk flow over that of a swept wing are the availability of an exact solution and radius-independent velocity profiles and boundary layer thickness. Due to the axi-symmetric nature of a rotating disk Von Kármán (1921) was able to employ similarity methods in order to produce an exact solution for the Navier-Stokes equations. Cochran (1934) was able to verify and improve on Von Kármán's solution numerically, tabulating boundary-layer profiles and their derivatives. Later, Benton (1966) further increased the accuracy of the steady state solution using asymptotic methods, before investigating the evolution of an impulsively started non-steady velocity field. He concluded that the asymptotic steady state solution is converged upon and reached after a rotation of circa 2 radians.

Experimentally, Gregory, Stuart and Walker (1955) were able to show the existence of stationary, outwardly spiralling co-rotating vortices, figure 1.9, characteristic of the crossflow instability. These occur due to the inflection point in the crossflow profile and are aligned with the streamwise direction. In the same paper, Stuart presented the full 3-D incompressible disturbance equations, including streamwise and spanwise derivatives of the mean flow. Much of the work on stability and crossflow transition has been carried out on the rotating disk problem because of this available solution and the fact the laminar boundary-layer thickness is independent of radius. Malik (1981) used linear stability analysis on the rotating disk flow and observed transition at an N-factor of 11 and the presence of stationary vortices at a critical Reynolds number of 287 ($Re_d = r\sqrt{\Omega/\nu}$, where r is the radius of the disk, Ω the angular frequency and ν the kinematic viscosity). Hall (1986) then extended the work of Gregory *et al* to include viscous effects, while Malik (1986) calculated neutral curves using 6^{th} order linear stability equations with the inclusion of streamline curvature terms, and found

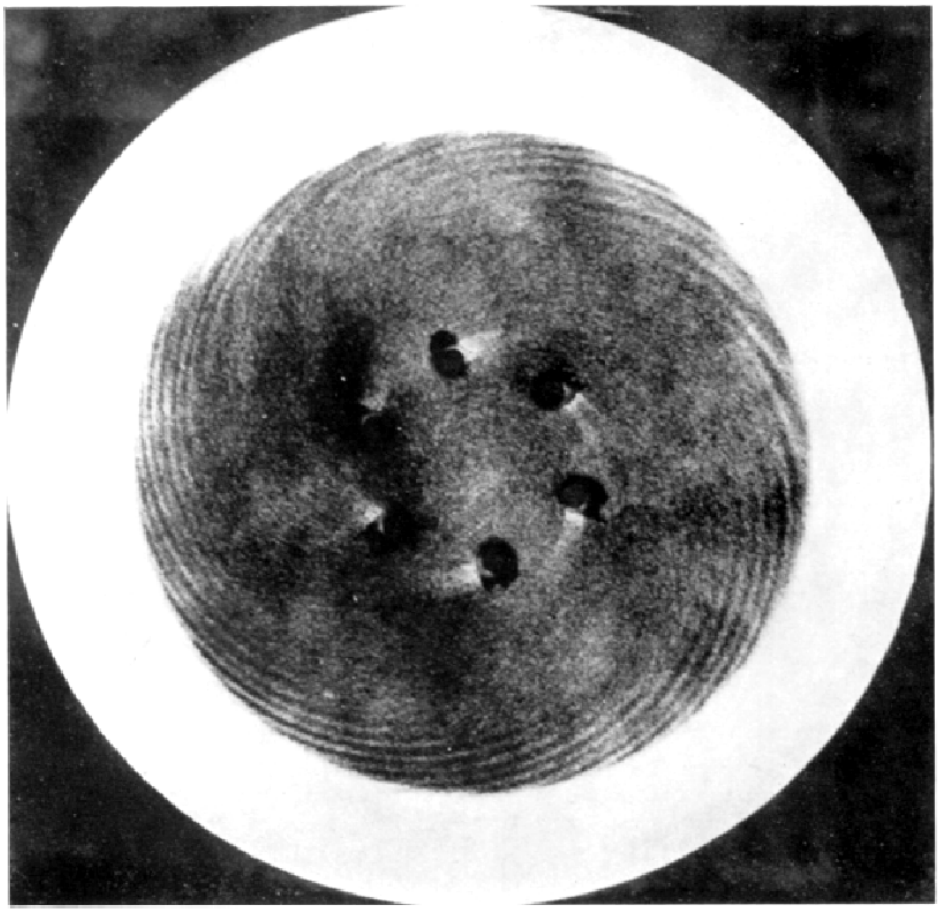

Figure 1.9: Rotating disk flow china clay visualisation by Gregory, Stuart and Walker (1955) showing outwardly spiralling vortices and the laminar-to-turbulent transition front.

two critical Reynolds number minima corresponding to the upper and lower branches of the neutral curve, at critical Reynolds numbers of 285 and 440 respectively.

One of the most significant findings in recent history concerning the rotating disk flow was that of Lingwood (1995), who following a suggestion by Gaster (1992) that the rotating disk flow may contain an absolute instability, was indeed able to observe this at a Reynolds number of 510. Lingwood employed Briggs' method using a parallel flow approximation, which provides a method of solving the Fourier-Laplace integral that arises from the solution of the initial boundary value problem for an impulsively forced flow. Huerre and Monkewitz (1990) state that if the group velocity of a disturbance wave packet diminishes to zero while the temporal growth rate remains positive, the flow is absolutely unstable, otherwise it may simply be convectively unstable. The

implication of this absolute instability is that a laminar boundary-layer cannot exist beyond a certain Reynolds number. Lingwood concluded that the absolute instability had its origins in an inviscid mechanism after observing a pinch-point between two branches of the dispersion relation at Reynolds numbers over 510. This point is a singularity in the dispersion relation which is associated with when two or more modes of waves propagating in opposite directions coalesce. If this point occurs at positive temporal growth rates then the flow is absolutely unstable, otherwise it is convectively unstable. Lingwood was subsequently able to verify her findings experimentally (Lingwood, 1996).

Building upon the work of von Kármán and Cochran, Wu (1959) and Tien (1960) derived the boundary layer equations for a rotating cone, for which the rotating disk flow is a solution at cone half-angle of $\psi_c = 90°$. Koh and Price (1967) subsequently provided an alternate formulation using exponent values for semi-infinite cones as given in Hess and Faulkner (1965) and produced updated velocity profiles as well as torque, drag and heat transfer characteristics. Temporal linear stability analysis (Kobayashi, 1981) and the first transition experiments on the rotating cone were carried out by Kobayashi and Izumi (1983) for a series of cones of varying half-angle in still air, and Kobayashi, Kohama and Kurosawa (1983) for a cone in an axial flow. They were able to predict critical and transition Reynolds numbers as well as the number of spiral vortices generated and their direction. His naphthalene flow visualisation, figure 1.10, corroborated his numerical predictions.

Gasperas (1987) and Malik and Spall (1991) derived the compressible perturbation equations for axi-symmetric bodies and applied them to supersonic non-rotating cones at Mach numbers between 3 and 8. Their findings showed that azimuthal curvature (section 4.2.3) has a stabilising effect on both axi-symmetric first and second mode disturbances and a destabilising effect on oblique asymmetric first modes. Streamwise curvature was found to be stabilising to both instability modes. More recently Garrett (2002), Garrett and Peake (2007), Garrett, Hussain and Stephen (2009) and subsequently Garrett, Hussain and Stephen (2010) and Hussain (2010) with an improved steady-flow formulation based on the work of Koh, extended Lingwood's work to the rotating cone, investigating the possibility of an absolute instability. They concluded that, for rotating

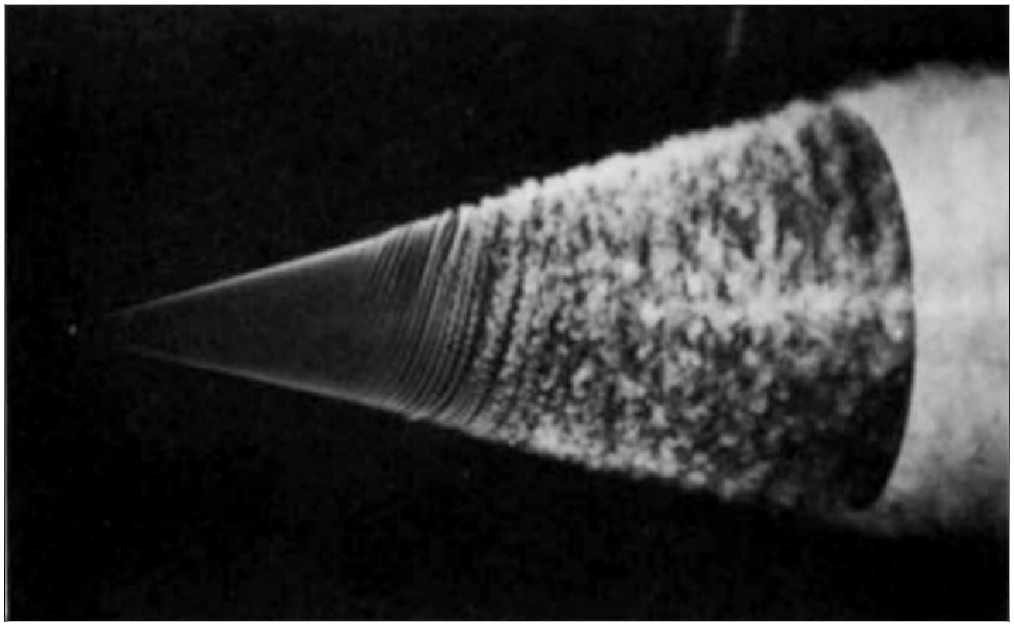

Figure 1.10: Naphthalene flow visualisation of a rotating cone in an axial flow showing spiral vortices and transition to turbulence, Kobayashi, Kohama and Kurosawa (1983).

cones with half-angles greater than 40°, the flow was both convectively and absolutely unstable, though below 40° the transition mechanism was believed to have different origins, namely of a centrifugal Görtler type. Axial flow was found to be stabilising to both convective and absolute instabilities.

Bluff body formulations of the boundary layer equations began in earnest in the early 1930s, during which time air ships were garnering a lot of attention. Fage (1936) obtained a more accurate expansion for the mean-flow than inviscid theory provided, and was able to verify his findings experimentally by taking surface pressure and skin friction measurements on a sphere. Later, Merksyn (1947) derived the laminar boundary layer equations for a body of revolution and was able to partially solve them, favourably comparing results with Fage. Howarth (1951) then produced a sphere-specific formulation of the boundary layer equations for a rotating sphere in a quiescent flow, in a similar manner to von Kármán, and generated some approximate solutions. Banks (1965) calculated more complete solutions for the rotating sphere boundary layer using the expansion suggested by Howarth, while Benton (1965) studied the evolution of an impulsively started rotating sphere boundary layer in time. Manohar (1967) and

then Banks (1976) used finite difference techniques to obtain increasingly accurate results. Finally, El-Shaarawi, El-Refaie and El-Bedeawi (1985) calculated a solution for the rotating sphere boundary layer in an axial flow.

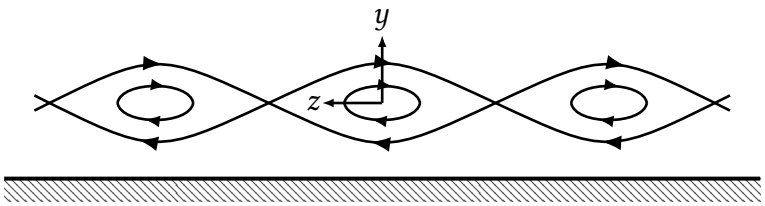

Figure 1.11: Sketch of "cat's eye" crossflow vortices, adapted from Reed and Saric (1989).

Experiments by Sawatzki (1970) used hot-wire anemometry and optical methods to investigate the evolution of the boundary layer due to a rotating sphere, confirming the presence of "cat's eye" crossflow vortices (Gregory, Stuart and Walker, 1955). Further investigations into the transition mechanisms of the laminar flow on a rotating sphere were carried out by Kohama and Kobayashi (1983), in which they measured critical and transition Reynolds numbers as well as the number and direction of stationary vortices. Numerical investigations into the stability of the rotating sphere boundary layer were carried out by Taniguchi, Kobayashi and Fukunishi (1998). Linear stability analysis showed that crossflow and streamline-curvature instabilities are present in boundary-layer of the rotating sphere in still fluid and yielded neutral curves of spiral vortices with varying Reynolds number. Subsequently, Garrett (2002), Garrett and Peake (2002) and Garrett and Peake (2004) also extended Lingwood's work to include the rotating sphere, both with and without an axial flow. They concluded that the flow was susceptible to both convective and absolute instabilities and axial flow was found to have a stabilising effect on both. They proposed an investigation into more general rotating axi-symmetric bodies, which thus far have only included ellipsoids due to the increasing complexity of the governing boundary layer equations. More recently, Barrow, Garrett and Peake (2015) performed an initial global linear stability analysis on the rotating sphere and ultimately proposed that while the rotating sphere boundary layer shares many similarities with the rotating disk, the transition mechanism may be fundamentally different due to the presence of a linear unstable global mode. Segalini and Garrett (2017)

have since investigated the non-parallel stability of the rotating sphere boundary layer, applying corrections to local type I and type II (arising from inviscid and viscous effects, respectively) convective instability modes. They have shown very good agreement between the number of spiral vortices found and with those observed in experiments.

Further shape-specific formulations of the boundary layer equations for rotating axi-symmetric bodies include those of prolate and oblate spheroids, initially derived by Fadnis (1954), using an approach similar to that of Howarth for the sphere. More recently, Samad and Garrett (2010) develop alternative boundary layer equations for prolate and oblate spheroids, using distinct co-ordinate systems for each, and produced velocity profiles for a selection of eccentricities using both numerical methods and series solutions. Unfortunately Samad was not able to compare his velocity profiles with other numerical or experimental sources and eludes to larger errors in his wall-normal velocity distributions, raising concerns over their accuracy. Samad and Garrett (2014) subsequently investigated convective instabilities using linear stability on rotating prolate and oblate spheroids as a generalisation of previous work on the rotating sphere by Garrett *et al.* Their findings indicated that eccentricity has a stabilising effect on instabilities at latitudes (the angle the surface tangent makes with the axis of revolution) below 50°, which follows from Malik and Poll (1985), who found that curvature has a stabilising effect on crossflow instabilities. Above this latitude, increased eccentricity was found to destabilise the flow for the prolate spheroid while continuing to stabilise it for the oblate spheroid. This is presumably due to a viscous instability dominating at higher latitudes.

A more generalised formulation of the boundary layer equations for a rotating body of revolution in an axial flow were derived by Schlichting (1953). In these Schlichting used a shape parameter K, analogous to the λ of the Pohlhausen method of boundary layer approximation, to attempt to generate solutions for a general axi-symmetric body. His equations provided initial velocity, drag, torque and skin friction results for a variety of streamlined bodies of revolution but struggled to compute accurate results for bluff bodies, a sphere in this case, due to inadequate slip velocity distributions from potential flow. His formulation was also unable to generate results for quiescent cases. Sheridan

(1968) later derived the axi-symmetric boundary layer equations for a non-rotating body of revolution, presenting a FORTRAN IV computer code and velocity profiles for a sphere and an ellipsoid. Malik and Spall (1991) later present the compressible boundary layer equations for an axi-symmetric body in an imposed axial flow making use of the Mangler-Levy-Lees transformation, in a similar fashion to the present work. However, their formulation is also limited to cases with an axial flow, and rotation is not considered.

Experimental investigations into more complex axi-symmetric bodies include the works of Mueller, Nelson, Kegelman and Zehentner (1981), Mueller, Nelson, Kegelman and Morkovin (1981) and Kegelman, Nelson and Mueller (1983), who performed smoke visualisations on a fixed and spinning secant-ogive nose cone in an axial. For the non-spinning case, transition was attributed to T-S instabilities, while for the spinning case it was attributed to crossflow (inflectional instability). They were able to observe both T-S and crossflow vortices concurrently and noted that higher angular velocities increased crossflow dominance. Kohama (1985) subsequently experimented on an ogival body of revolution but was unable to detect concurrent crossflow and T-S instabilities, unlike Mueller *et al*. He postulated that this was due to two discontinuities in curvature in the secant-ogive body, which were not present in his ogive, creating an inflection point in the streamwise velocity profile. Kohama also noted that the spiral vortices detected by Mueller *et al* were later discovered to be counter-rotating, and therefore not crossflow. He suggested that they originated from a centrifugal instability.

1.6 Motivation and objectives

The origins for the motivation of the present work lie in the uncertainties in crossflow transition N-factors, described in section 1.4, and the safety factors used by aircraft manufacturers as a result. An investigation is proposed into their sensitivity by altering the boundary layer velocity profile, using changes in pressure gradient or local surface curvature near the point of primary crossflow mode saturation. In order to accomplish this a swept-wing flow analogue is to be employed in the form of a rotating boundary layer.

It it proposed that a rotating disk with a concentric annulus spinning at a different, usually lower, angular velocity could potentially be used to apply a step change in pressure gradient. This approach would have the benefits of only having to design a single model and experiment, and also having a relatively simply and well-understood base-flow. Furthermore, a rotating disk and annulus would increase the speed at which various changes in pressure gradient could be analysed while also avoiding wind tunnel turbulence and blockage effects. The downsides of this approach would include an increased complexity of the experiment, and likely the numerical formulation. The objectives of the project can be summarised as

- Designing an appropriate experimental model with the view of conducting the above investigation within the constraints of a small scale university wind tunnel.
- Producing the necessary numerical tool set for a) predicting the required boundary layers and b) analysing their linear stability characteristics.
- Determining whether a crossflow generated by a rotating body can be used as a substitute for a swept wing flow in the context of controlling transition.

1.7 Thesis outline

Chapter 2 will discuss the rotating disk boundary-layer, and investigate how a co-axially spinning annulus could be used to apply a step change in pressure gradient, as well as the complications which may arise by using this approach. In Chapter 3 the boundary-layer equations for a generalised axi-symmetric rotating body of revolution are derived, and the formulation and numerical scheme are validated for a variety of shapes. Subsequently, Chapter 4 sets out the full perturbation and stability equations for a three dimensional (3-D), generalised, orthogonal co-ordinate system and provides a comparison of convective instability neutral curves for a rotating sphere in an axial flow. Chapter 5 will then employ the boundary-layer equations and stability formulation to investigate and discuss the effects of shape change on the controllability of the crossflow instability. Finally, Chapter 6 will summarise the findings of the work and suggest possible avenues for further investigation.

2

The boundary layer on a rotating disk with a concentric annulus

Contents

This chapter explores the mathematical formulation of the boundary layer equations, and proposes a possible experiment, for a rotating disk with a concentric rotating annulus. The annulus will be rotated at a different, usually lower, angular velocity providing a step change in pressure gradient, resulting in a stabilising effect on the crossflow velocity profile. Using a variation of a rotating disk flow has the advantage of having a well defined exact solution as well as the knowledge of the absolute instability and its position.

2.1 Proposed experiment

In order to design an experiment for a rotating disk with a concentric annulus we first look to the apparatus of previous experiments carried out on the rotating disk for inspiration. Eaton (1989) carried out experiments on a heated rotating disk spinning at 1000 rpm. He employed a composite disk comprised of an aluminium top plate and base, sandwiching a phenolic sheet layer which included embedded copper heating strips. The disk was driven using a variable speed motor connected via pulleys to a two-bearing spindle and mounted to a heavy steel base. A fixed concentric annulus was used to ensure the isolation of upper and lower flows, and the experiment was carried out in a sufficiently large room filled with quiescent air. Measurements were taken by Laser Doppler Anemometry (LDA) using a single argon-ion laser. The air in the test chamber was filtered and seeded with titanium-dioxide particles prior to experimentation.

Later, Lingwood (1996) performed an investigation in order to confirm the findings of her theoretical study predicting the presence of an absolute instability. The experimental apparatus consisted of a diamond-cut aluminium disk mounted on an air-bearing spindle and driven by a DC servo-motor, mounted on a heavy concrete base to reduce vibrations. A slotted smoothing screen above the disk was used to reduce the freestream-turbulence level of the incoming axial flow. Measurements were taking using a hot-wire anemometer mounted on a two component traverse which allowed for radial and axial freedom.

Most recently, Imayama (2012) used a modified version of the apparatus used in Lingwood's experiments (figure 2.1). In his experiments he employed a float glass disk, which provides a much flatter surface to aluminium diamond-cut disks as these tend to exhibit grooving left over from the cutting process. The glass disk was mounted to aluminium base disk and connected on an air-bearing spindle, driven by a d.c. servo-motor. A fixed concentric annulus, similar to that employed by Eaton, was used to isolate the upper and lower flows. Measurements were taken with a radially-fixed hot-wire anemometer, connected to an axial traverse. Local Reynolds number was varied by altering both the rotational speed and the radial position of the hot-wire.

The proposed experiment would use a combination of the above designs and extend them to a rotating disk and rotating concentric annulus combination. A sketch of this

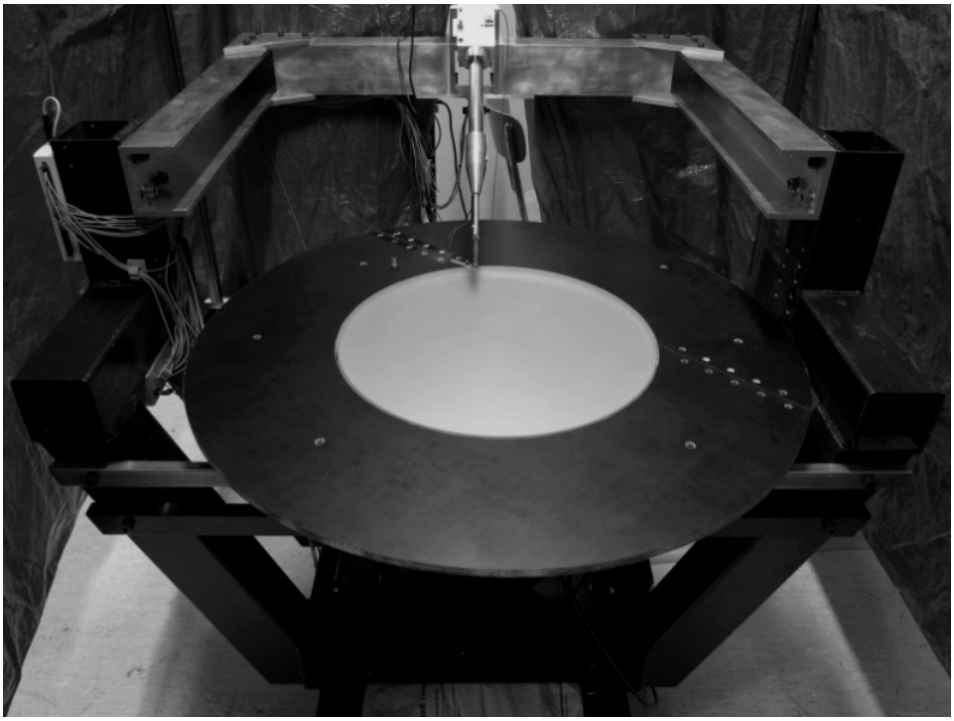

Figure 2.1: Rotating disk experimental arrangement by Imayama (2012), showing float glass disk and concentric annulus.

proposed assembly is presented in figure 2.2. An aluminium annulus, with a central machined recess for the disk, will be mounted on a thick hollow rod and connected to a base using thrust bearings to restrict movement. Aluminium is chosen as opposed to float glass as a recess is more easily machined into metal, enabling this design. The disk is then to be mounted on a concentric rod, using thrust bearings within the annulus recess and hollow rod, to fix it in place. Both the annulus and the disk can then be separately belt driven using direct current (DC) motors. A further fixed concentric annulus would also be employed in order to mitigate up-wash from the lower side of the system. In order to size the rotating disk and annulus combination, table 2.1, compares rotating disk Reynolds numbers,

$$Re_d = r\sqrt{\frac{\Omega}{\nu}}, \tag{2.1}$$

at different radii and angular velocities. Reynolds number values greater than 510, determined by Lingwood, 1995 to be the onset of the absolute instability, are highlighted and excluded from the design space as the present work aims to focus on convective

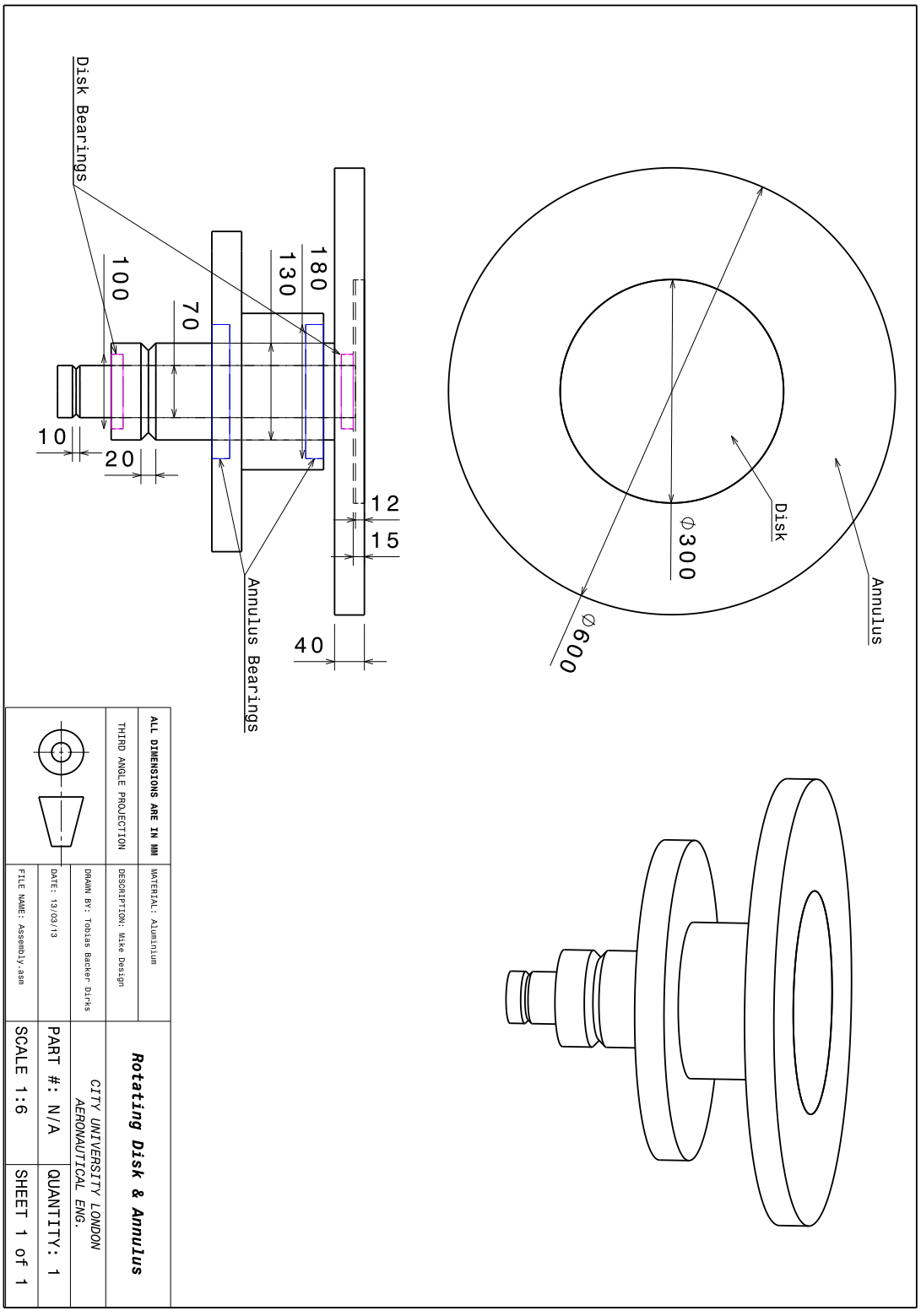

Figure 2.2: Proposed experimental assembly for a rotating disk with a concentric annulus.

instabilities, whose onset emerges at lower Reynolds numbers. From this we can deduce that an appropriate maximum radius should lie within 150 to 250 mm, as this would provide us with the largest experimental domain. The boundary layer thickness,

Angular Velocity (rad s^{-1}) \ Outer Radius (mm)	100	150	200	250	300	350	400	Boundary Layer Thickness (mm)
10	83	124	165	207	248	289	331	7.26
20	117	175	234	292	351	409	468	5.13
30	143	215	286	358	429	501	573	4.19
40	165	248	331	413	496	579	661	3.63
50	185	277	370	462	554	647	739	3.25
60	202	304	405	506	607	709	810	2.96
70	219	328	437	547	656	765	875	2.74
80	234	351	468	584	701	818	935	2.57
90	248	372	496	620	744	868	992	2.42
100	261	392	523	653	784	915	1046	2.30
110	274	411	548	685	822	959	1097	2.19
120	286	429	573	716	859	1002	1145	2.10
130	298	447	596	745	894	1043	1192	2.01
140	309	464	619	773	928	1082	1237	1.94
150	320	480	640	800	960	1120	1281	1.87
160	331	496	661	827	992	1157	1323	1.81
170	341	511	682	852	1022	1196	1363	1.76
180	351	526	701	877	1052	1227	1403	1.71
190	360	540	721	901	1081	1261	1441	1.67
200	370	554	739	924	1109	1294	1479	1.62

Reynolds Number

Table 2.1: Rotating disk Reynolds numbers at different radii for varying angular velocities. Boundary layer thickness calculated at $\eta = 6$.

calculated at $\eta = 6$ and assumed to be radially constant, is used to determine available measurement techniques. For the proposed radii the boundary layer thickness will lie between circa 2 and 3mm, therefore measurements can feasibly be taken using either LDA or hot-wire anemometry, though the former is preferred as it offers greater resolution for thin boundary layers. With this in mind, it is desirable to perform the experiment in a confined environment, preferably with an air filtration system, to simplify ambient seeding.

The main concerns with the proposed design revolve around manufacturing tolerances and concerns for the survival of the boundary layer when transitioning from the disk to the annulus. Variations in surface height due to finish and the vertical alignment between the disk and annulus can be reduced by performing the final machining on the combined assembly. The size of the gap between the disk and annulus must be kept to a minimum, of the order of μ-metres, as otherwise boundary layer contamination could lead to laminar-to-turbulent transition. This could possibly be mitigated by using a seal under the disk (the dashed region in figure 2.2). Finally, noise and vibrations due to an imbalance of either the disk or the annulus can introduce additional unwanted instabilities. These will need to be countered by using a heavy base for the assembly and ensuring the system is perfectly balanced.

2.2 Mathematical formulation

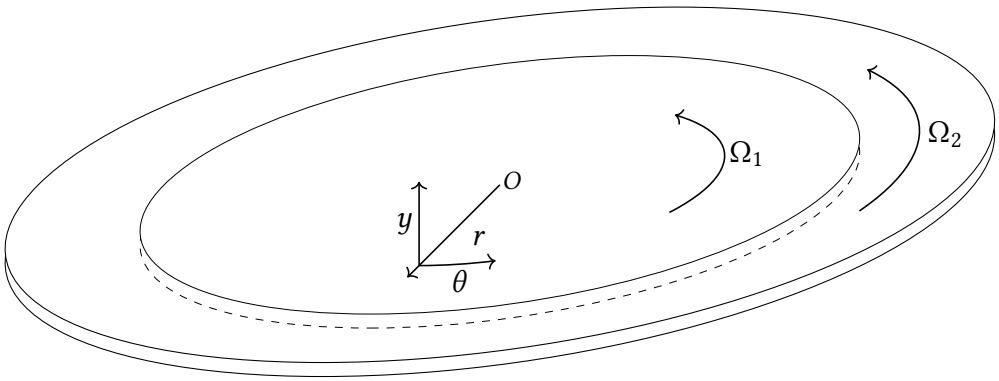

Figure 2.3: A sketch of the co-ordinate system for a rotating disk with a concentric annulus.

The continuity and momentum equations for a steady, axially-symmetric, incompressible flow in a cylindrical co-ordinate system are

$$\frac{\partial}{\partial r}(ru_r) + \frac{\partial}{\partial y}(rv) = 0 \tag{2.2}$$

$$u_r\frac{\partial u_r}{\partial r}+v\frac{\partial u_r}{\partial y}-\frac{w^2}{r} = -\frac{1}{\rho}\frac{\partial p}{\partial r}+\nu\left[\frac{\partial^2 u_r}{\partial r^2}+\frac{\partial}{\partial r}\left(\frac{u_r}{r}\right)+\frac{\partial^2 u_r}{\partial y^2}\right] \tag{2.3a}$$

$$u_r\frac{\partial v}{\partial r}+v\frac{\partial v}{\partial y} = -\frac{1}{\rho}\frac{\partial p}{\partial y}+\nu\left[\frac{\partial^2 v}{\partial r^2}+\frac{\partial}{\partial r}\left(\frac{v}{r}\right)+\frac{\partial^2 v}{\partial y^2}\right] \tag{2.3b}$$

$$u_r\frac{\partial w}{\partial r}+\frac{u_r w}{r}+v\frac{\partial w}{\partial y} = \nu\left[\frac{\partial^2 w}{\partial r^2}+\frac{\partial}{\partial r}\left(\frac{w}{r}\right)+\frac{\partial^2 w}{\partial y^2}\right] \tag{2.3c}$$

where u_r, v, w are velocity components in the directions of increasing r, y and θ, as shown in figure 2.3. In a fixed frame of reference these are subject to the boundary conditions

$$u_r = v = w - r\Omega = 0 \qquad \text{at} \quad y = 0 \tag{2.4a}$$

$$u_r = w = 0 \qquad \text{as} \quad y \to \infty. \tag{2.4b}$$

where Ω is the local angular velocity about the origin (O). A two-component stream function is defined

$$u_r = \frac{r_0}{r}\frac{\partial \psi}{\partial y}, \quad v = -\frac{r_0}{r}\frac{\partial \psi}{\partial r}, \quad w = \frac{r_0}{r}\frac{\partial \phi}{\partial y}. \tag{2.5a–c}$$

which satisfies the continuity equation (2.2) and which allows for consistent treatment of the azimuthal velocity component w. r_0 is an arbitrary reference length, while ψ and ϕ are defined as functions of dimensionless stream functions f and g,

$$\psi = U_d L_\xi\, f(\xi,\eta), \qquad \phi = U_d L_\xi\, g(\xi,\eta), \tag{2.6a,b}$$

wherein L_ξ and U_d are a length and velocity scale, respectively. In order to match Benton (1966) the length and velocity scales are chosen as

$$L_\xi = \frac{r^2}{r_0}, \qquad U_d = \sqrt{\Omega\nu}, \tag{2.7a,b}$$

and a right-handed co-ordinate system is defined in which

$$\eta = y\sqrt{\frac{\Omega}{\nu}}, \qquad \xi = r. \tag{2.8a,b}$$

Substituting these transformations into equations 2.5a–c results in a form of the von Kármán similarity transforms for both the velocity field and pressure for a rotating disk where angular velocity, Ω, varies with radial position,

$$u_r = \xi\Omega f', \qquad w = \xi\Omega g', \qquad P = -\rho\nu\Omega p, \tag{2.9a–c}$$

$$v = -2\sqrt{\Omega\nu}f - \xi\sqrt{\Omega\nu}\left[\frac{\partial f}{\partial\xi} - \frac{1}{2\Omega}\frac{\partial\Omega}{\partial\xi}(\eta f' + f)\right] \tag{2.9d}$$

where a prime denotes differentiation with respect to η. Inserting equations 2.9a–d into the governing equations (2.3a–c) ultimately yields

$$\begin{aligned}
&f''' + 2ff'' - f'^2 + g'^2 - \frac{\xi}{\Omega}\frac{\partial\Omega}{\partial\xi}f'^2 - \xi\frac{\partial f'}{\partial\xi}f' + \xi f''\frac{\partial f}{\partial\xi} + \frac{\xi}{2\Omega}\frac{\partial\Omega}{\partial\xi}ff'' \\
&\quad + \nu\left[\frac{1}{\xi\Omega^2}\frac{\partial\Omega}{\partial\xi}p + \frac{1}{\xi\Omega}\frac{\partial p}{\partial\xi} + \eta\frac{1}{2\xi\Omega^2}\frac{\partial\Omega}{\partial\xi}p' + \frac{3}{\xi\Omega^2}\frac{\partial\Omega}{\partial\xi}f' + \frac{3}{\xi\Omega}\frac{\partial f'}{\partial\xi} + \frac{1}{\Omega^2}\frac{\partial^2\Omega}{\partial\xi^2}f'\right. \\
&\quad + \frac{2}{\Omega^2}\frac{\partial\Omega}{\partial\xi}\frac{\partial f'}{\partial\xi} + \frac{1}{\Omega}\frac{\partial^2 f'}{\partial\xi^2} + \eta\frac{3}{2\xi\Omega^2}\frac{\partial\Omega}{\partial\xi}f'' + \eta\frac{3}{4\Omega^3}\left(\frac{\partial\Omega}{\partial\xi}\right)^2 f'' + \eta\frac{1}{\Omega^2}\frac{\partial\Omega}{\partial\xi}\frac{\partial f''}{\partial\xi} \\
&\quad \left. + \eta\frac{1}{2\Omega^2}\frac{\partial^2\Omega}{\partial\xi^2}f'' + \eta^2\frac{1}{4\Omega^3}\left(\frac{\partial\Omega}{\partial\xi}\right)^2 f'''\right] = 0
\end{aligned} \tag{2.10a}$$

$$\begin{aligned}
&g''' + 2fg'' - 2f'g' - \frac{\xi}{\Omega}\frac{\partial\Omega}{\partial\xi}f'g' - \xi\frac{\partial g'}{\partial\xi}f' + \xi\frac{\partial f}{\partial\xi}g'' + \frac{\xi}{2\Omega}\frac{\partial\Omega}{\partial\xi}fg'' \\
&\quad + \nu\left[\frac{3}{\xi\Omega^2}\frac{\partial\Omega}{\partial\xi}g' + \frac{3}{\xi\Omega}\frac{\partial g'}{\partial\xi} + \frac{1}{\Omega^2}\frac{\partial^2\Omega}{\partial\xi^2}g' + \frac{2}{\Omega^2}\frac{\partial\Omega}{\partial\xi}\frac{\partial g'}{\partial\xi} + \frac{1}{\Omega}\frac{\partial^2 g'}{\partial\xi^2} + \eta\frac{3}{2\xi\Omega^2}\frac{\partial\Omega}{\partial\xi}g''\right. \\
&\quad \left. + \eta\frac{3}{4\Omega^3}\left(\frac{\partial\Omega}{\partial\xi}\right)^2 g'' + \eta\frac{1}{\Omega^2}\frac{\partial\Omega}{\partial\xi}\frac{\partial g''}{\partial\xi} + \eta\frac{1}{2\Omega^2}\frac{\partial^2\Omega}{\partial\xi^2}g'' + \eta^2\frac{1}{4\Omega^3}\left(\frac{\partial\Omega}{\partial\xi}\right)^2 g'''\right] = 0.
\end{aligned} \tag{2.10b}$$

$$
\begin{aligned}
&p' - 4ff' - 2f'' + \frac{\xi^2}{2\Omega}\frac{\partial f}{\partial \xi}\frac{\partial \Omega}{\partial \xi}f' + \xi\frac{\partial f}{\partial \xi}f' + \xi^2\frac{\partial^2 f}{\partial \xi^2}f' + \eta\frac{\xi}{2\Omega}\frac{\partial \Omega}{\partial \xi}f'f' \\
&+ \eta\frac{\xi^2}{2\Omega}\frac{\partial^2 \Omega}{\partial \xi^2}f'f' + \eta\frac{\xi^3}{2}\frac{\partial \Omega}{\partial \xi}\frac{\partial f'}{\partial \xi}f'f' - \frac{\xi^2}{2\Omega^2}\left(\frac{\partial \Omega}{\partial \xi}\right)^2 ff' - \frac{\xi}{2\Omega}\frac{\partial \Omega}{\partial \xi}ff' \\
&+ \frac{\xi^2}{2\Omega}\frac{\partial^2 \Omega}{\partial \xi^2}ff' - \xi^2\frac{\partial f}{\partial \xi}\frac{\partial f'}{\partial \xi} - \eta\frac{\xi^2}{2\Omega}\frac{\partial \Omega}{\partial \xi}\frac{\partial f}{\partial \xi}f'' - \eta\frac{\xi^2}{4\Omega^2}\left(\frac{\partial \Omega}{\partial \xi}\right)^2 f'f' \\
&- \frac{\xi^2}{2\Omega}\frac{\partial \Omega}{\partial \xi}\frac{\partial f'}{\partial \xi}f - \eta\frac{\xi^2}{4\Omega^2}\left(\frac{\partial \Omega}{\partial \xi}\right)^2 ff'' - 2\xi\frac{\partial f'}{\partial \xi}f - \eta\frac{\xi}{\Omega}\frac{\partial \Omega}{\partial \xi}ff'' \\
&+ \nu\Bigg[\frac{3\xi}{4\Omega^3}\left(\frac{\partial \Omega}{\partial \xi}\right)^2\frac{\partial f}{\partial \xi} - \frac{5}{\Omega^2}\frac{\partial \Omega}{\partial \xi}\frac{\partial f}{\partial \xi} - \frac{3\xi}{2\Omega^2}\frac{\partial \Omega}{\partial \xi}\frac{\partial^2 f}{\partial \xi^2} - \frac{3\xi}{2\Omega^2}\frac{\partial^2 \Omega}{\partial \xi^2}\frac{\partial f}{\partial \xi} \\
&- \frac{5}{\Omega}\frac{\partial^2 f}{\partial \xi^2} - \frac{\xi}{\Omega}\frac{\partial^3 f}{\partial \xi^3} + \eta\frac{1}{2\Omega^3}\left(\frac{\partial \Omega}{\partial \xi}\right)^2 f' - \eta\frac{5}{2\Omega^2}\frac{\partial^2 \Omega}{\partial \xi^2}f' - \eta\frac{9}{2\Omega^2}\frac{\partial \Omega}{\partial \xi}\frac{\partial f'}{\partial \xi} \\
&- \eta\frac{\xi}{2\Omega^2}\frac{\partial^3 \Omega}{\partial \xi^3}f' - \eta\frac{3\xi}{2\Omega^2}\frac{\partial^2 \Omega}{\partial \xi^2}\frac{\partial f'}{\partial \xi} - \eta\frac{3\xi}{2\Omega^2}\frac{\partial \Omega}{\partial \xi}\frac{\partial^2 f'}{\partial \xi^2} - \frac{3\xi}{8\Omega^4}\left(\frac{\partial \Omega}{\partial \xi}\right)^3 f \\
&+ \frac{5}{4\Omega^3}\left(\frac{\partial \Omega}{\partial \xi}\right)^2 f - \frac{1}{2\Omega^2}\frac{\partial^2 \Omega}{\partial \xi^2}f + \frac{3\xi}{4\Omega^3}\frac{\partial \Omega}{\partial \xi}\frac{\partial^2 \Omega}{\partial \xi^2}f - \frac{2}{\Omega^2}\frac{\partial^2 \Omega}{\partial \xi^2}f - \frac{\xi}{2\Omega^2}\frac{\partial^3 \Omega}{\partial \xi^3}f \\
&- \eta^2\frac{3}{2\Omega^3}\left(\frac{\partial \Omega}{\partial \xi}\right)^2 f'' - \eta^2\frac{3\xi}{4\Omega^3}\frac{\partial \Omega}{\partial \xi}\frac{\partial^2 \Omega}{\partial \xi^2}f'' - \eta^2\frac{3\xi}{4\Omega^3}\left(\frac{\partial \Omega}{\partial \xi}\right)^2\frac{\partial f''}{\partial \xi} \\
&- \eta^3\frac{\xi}{8\Omega^4}\left(\frac{\partial \Omega}{\partial \xi}\right)^3 f''' - \eta^2\frac{\xi}{2\Omega^4}\left(\frac{\partial \Omega}{\partial \xi}\right)^3 f'' - \eta\frac{\xi}{4\Omega^3}\left(\frac{\partial \Omega}{\partial \xi}\right)^2\frac{\partial f'}{\partial \xi} - \frac{3}{\xi\Omega}\frac{\partial f}{\partial \xi} \\
&- \eta\frac{5}{2\xi\Omega^2}\frac{\partial \Omega}{\partial \xi}f' - \frac{3}{2\xi\Omega^2}\frac{\partial \Omega}{\partial \xi}f - \frac{\xi}{\nu}\frac{\partial f''}{\partial \xi} - \eta\frac{\xi}{2\Omega\nu}\frac{\partial \Omega}{\partial \xi}f''' - \frac{\xi}{2\Omega\nu}\frac{\partial \Omega}{\partial \xi}f''\Bigg] = 0
\end{aligned}
\tag{2.10c}
$$

Equations 2.10a,b are subject to the following non-dimensional boundary conditions

$$f = f' = g = g' - 1 = 0 \qquad \text{at} \quad \eta = 0 \tag{2.11a}$$

$$f' = g' = 0 \qquad \text{as} \quad \eta \to \infty, \tag{2.11b}$$

while equation 2.10c is also subject to

$$p = p_0 \qquad \text{at} \quad \eta = 0 \tag{2.11c}$$

The velocity field for a rotating disk where angular velocity varies with radius can be obtained by solving equations 2.10a,b alone, as the solution of the pressure field (obtained from equation 2.10c) can be de-coupled. The presence of a variable angular velocity ($\frac{\partial \Omega}{\partial \xi} \neq 0$) will enable the solution of a number of interesting cases, for example

- The simple case of constant Ω will yield the classic rotating disk system.

- A single step change in Ω represents a disk and single annulus combination (as shown in figure 2.3), while additional step changes in Ω represent additional annuli.

- Smoothly varying Ω with radius represents an un-physical, albeit interesting, case wherein we can explore the effect of different rates of change for Ω on the stability of the boundary layer.

A more complete derivation of equations 2.10a–c can be found in appendix A.1.

2.3 Constant angular velocity

In order to verify the proposed formulation and validate the solution strategy it is useful to first compute the basic case of a rigid rotating disk. This formulation can be obtained by assuming that $\frac{\partial \Omega}{\partial \xi} = 0$, after which equations 2.10a–c reduce to a more familiar form

$$\begin{aligned} f''' + 2ff'' - f'^2 + g'^2 &= \xi\left[\frac{\partial f'}{\partial \xi}f' - \frac{\partial f}{\partial \xi}f''\right] \\ &\quad - \nu\left[\frac{1}{\xi\Omega}\frac{\partial p}{\partial \xi} + 3\frac{1}{\xi\Omega}\frac{\partial f'}{\partial \xi} + \frac{1}{\Omega}\frac{\partial^2 f'}{\partial \xi^2}\right] \end{aligned} \tag{2.12a}$$

$$g''' + 2fg'' - 2f'g' = \xi\left[\frac{\partial g'}{\partial \xi}f' - \frac{\partial f}{\partial \xi}g''\right] - \nu\left[\frac{3}{\xi\Omega}\frac{\partial g'}{\partial \xi} + \frac{1}{\Omega}\frac{\partial^2 g'}{\partial \xi^2}\right] \tag{2.12b}$$

$$\begin{aligned} p' - 4ff' - 2f'' &= \xi\left[2\frac{\partial f'}{\partial \xi}f + \xi\frac{\partial f}{\partial \xi}\frac{\partial f'}{\partial \xi} - \frac{\partial f}{\partial \xi}f' - \xi\frac{\partial^2 f}{\partial \xi^2}f'\right] \\ &\quad + \nu\left[\frac{5}{\Omega}\frac{\partial^2 f}{\partial \xi^2} + \frac{\xi}{\Omega}\frac{\partial^3 f}{\partial \xi^3} + \frac{3}{\xi\Omega}\frac{\partial f}{\partial \xi} + \frac{\xi}{\nu}\frac{\partial f''}{\partial \xi}\right]. \end{aligned} \tag{2.12c}$$

The flow due to a rotating disk famously provides an exact solution to the Navier-Stokes equations due to the problem being self-similar, as suggested by von Kármán and proven rigorously by McLeod (1969). Owing to this we can neglect all ξ derivatives, leaving

us with the well known equations for a rotating disk

$$f''' + 2ff'' - f'^2 + g'^2 = 0 \tag{2.13a}$$

$$g''' + 2fg'' - 2f'g' = 0 \tag{2.13b}$$

$$p' - 4ff' - 2f'' = 0 \tag{2.13c}$$

where the boundary conditions are as detailed in equations 2.10a,b.

2.3.1 Solution strategy

The PDE for the pressure field, equation 2.13c, is de-coupled from the other two equations, 2.13a,b which define the velocity field, and as such can be solved separately. Equations 2.13a,b can be converted into a system of coupled first-order ODEs by introducing the following variables

$$f' = u, \qquad u' = \tau \qquad \text{and} \qquad g' = w, \qquad w' = \sigma. \tag{2.14a–d}$$

The system is solved iteratively using the following expansions in f, u, τ, g, w and σ, where the subscript n refers to the solution at the n-th iteration,

$$f = f_n + \Delta f, \quad u = u_n + \Delta u, \quad \tau = \tau_n + \Delta\tau, \tag{2.15a–c}$$

$$g = g_n + \Delta g, \quad w = w_n + \Delta w, \quad \sigma = \sigma_n + \Delta\sigma. \tag{2.15d–f}$$

The resultant linear equations governing the system at step $n + 1$ can be written in matrix form as

$$\begin{bmatrix} \Delta\tau \\ \Delta u \\ \Delta f \\ \Delta\sigma \\ \Delta v \\ \Delta g \end{bmatrix}' = \begin{bmatrix} -2f_n & 2u_n & -2\tau_n & 0 & -2v_n & 0 \\ 1 & 0 & 0 & 0 & 0 & 0 \\ 0 & 1 & 0 & 0 & 0 & 0 \\ 0 & 2v_n & -2\sigma_n & -2f_n & 2u_n & 0 \\ 0 & 0 & 0 & 1 & 0 & 0 \\ 0 & 0 & 0 & 0 & 1 & 0 \end{bmatrix} \begin{bmatrix} \Delta\tau \\ \Delta u \\ \Delta f \\ \Delta\sigma \\ \Delta v \\ \Delta g \end{bmatrix} + \begin{bmatrix} B_\tau \\ B_u \\ B_f \\ B_\sigma \\ B_v \\ B_g \end{bmatrix} \tag{2.16}$$

where the constants are given by

$$
\begin{aligned}
B_\tau &= -\tau_n' - 2f_n\tau_n + u_n^2 - w_n^2 \\
B_u &= \tau_n - u_n' \\
B_f &= u_n - f_n' \\
B_\sigma &= -\sigma_n' - 2f_n\sigma_n + 2u_n w_n \\
B_w &= \sigma_n - w_n' \\
B_u &= w_n - g_n'.
\end{aligned}
\tag{2.17a–f}
$$

The matrix 2.16 can be solved using a 4^{th}-order accurate, two-point compact-difference scheme (Malik, 1990), detailed in section 3.3.3. The pressure field can then be obtained by taking p_0 as the dimensionless pressure at $y = 0$, and then integrating equation 2.13c, which results in the non-dimensional pressure difference

$$p - p_0 = 2f' + 2f^2. \tag{2.18}$$

2.3.2 Comparison with Benton

Figure 2.4 presents a comparison of the dimensionless stream functions and pressure difference obtained using the present approach with those published by Benton, 1966. Benton also published tabulated values for derivatives of the dimensionless stream functions and these compare favourably and are presented in appendix A.2.

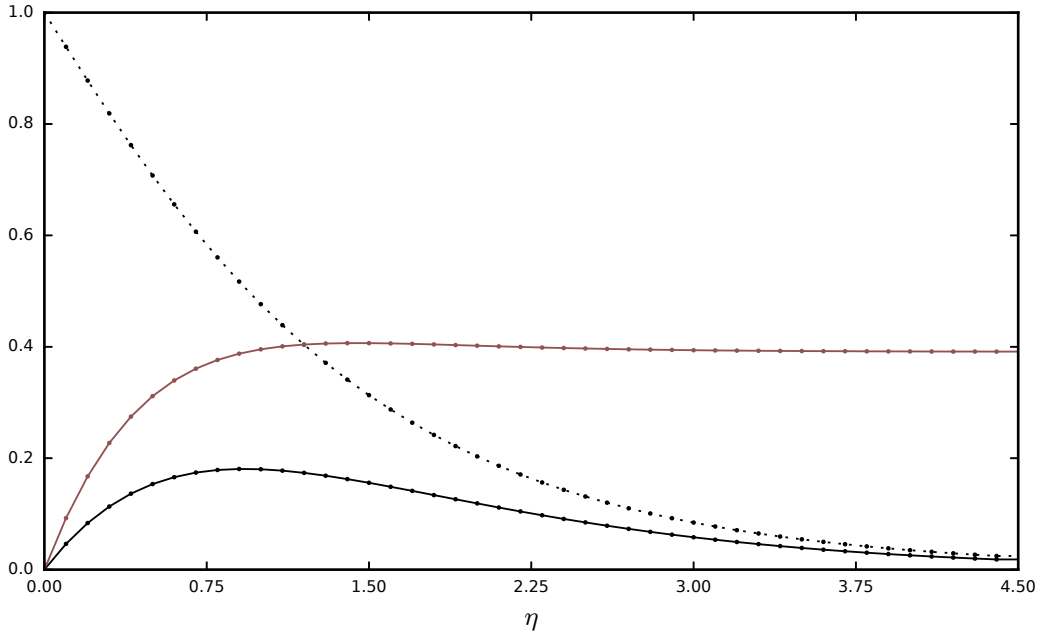

Figure 2.4: Comparison of the dimensionless stream functions f' (——), g' (·····) and dimensionless pressure difference (——), obtained using the present approach, with those reported by Benton (1966) (·); η as defined in equation 2.8a.

2.4 Evaluation of the disk and annulus concept

Equations 2.10a,b represent a system of partial differential equations (PDEs) that are no longer self-similar, are elliptic in character, and whose solution is non trivial. The problem therefore no longer provides a clear analogue to swept-wing boundary-layer flow, the governing equations of which are parabolic. Furthermore, the devised experimental setup detailed in section 2.1 comes with many inherent risks. The design requires very fine tolerances which would increase the manufacturing costs. Assuming that the design tolerances were met, the survival of the laminar boundary layer is not guaranteed due to contamination at the disk-annulus interface. Given this, the rotating disk and concentric rotating annulus investigation was deemed too risky to continue pursuing.

Returning to the motivations from section 1.6, the focused control of instability growth rates could be achieved in one of two ways:

1. using radially variable angular velocity, as was explored in this chapter,

2. using variable body shape at a constant angular velocity.

The latter could be performed by using a rotating axi-symmetric body. The shape and curvature near the leading edge of this body could then be modified to induce changes in pressure gradient at specific locations, requiring the manufacture of various leading edges. This would however increase the cost, both financially and in time, of any experiment. Also, the presence of an axial flow is required to ensure parabolicity, therefore requiring the use of a wind tunnel. The following chapter conceptualises a possible experiment and derives a generalised formulation for the boundary layer on rotating axi-symmetric bodies.

3

The boundary layer on rotating axi-symmetric bodies

Contents

Section 1.5 previously provided an overview of the different approaches used for solving and experimenting on axi-symmetric and rotating boundary layers. Much of this previous work on the stability of rotating axi-symmetric boundary layers has been carried out on disks, cones and spheres, each necessitating a re-formulation of the base equations. Attempts to analyse more complex shapes, such as ellipsoids or a rotating disk with a concentric annulus, as derived in the previous chapter, rapidly result in increasingly complicated equations. More general formulations, such as those

of Schlichting (1953) or Malik and Spall (1991) do not encompass quiescent or rotating cases, respectively. Accurate boundary layer profiles are a prerequisite for such stability analyses. Given the variety of manipulations to be found in the literature, this chapter looks to formulate a consolidated set of transformations for the boundary layer equations on a general rotating body of revolution applicable to bodies both in still air and in an axial flow, and to validate numerical solutions of these equations for a range of shapes and flow conditions. The work presented in this chapter is contained in part within Backer Dirks and Atkin (2018), published in the European Journal of Mechanics - B/Fluids.

3.1 Proposed experiment

Before proceeding with the mathematical formulation of the problem it is perhaps useful to provide context to the motivation of the present work by first conceptualising an experiment. Using a rotating body in an axial flow in order to modify local pressure gradients could be simplified by making use of replaceable nose sections, thereby only requiring a single experimental assembly. The replaceable nose sections could be manufactured from aluminium using a computer numerical control (CNC) lathe, or 3-D printed for rapid prototyping. Figure 3.1 shows a sketch of such an experimental assembly, with further engineering drawings found in appendix B.4. In it, two thrust

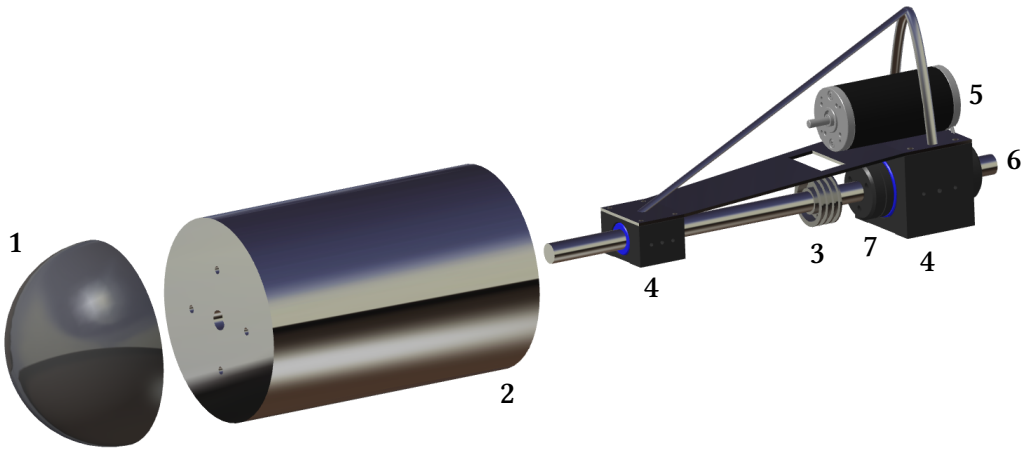

Figure 3.1: Expanded view of the proposed experimental assembly for a rotating body using replaceable nose-cones; 1) Replaceable nose section, 2) Aerodynamic fairing, 3) Belt driven pulley, 4) Thrust air bushings, 5) D/C motor, 6) Steel shaft, 7) Face collar.

air bushings, operated between 40 and 100 psi, would be mounted on a support frame. A steel shaft, secured axially using face collars, would be mounted on an aerodynamic fairing to which the replaceable nose sections can be secured using a reversed (to the direction of rotation) thread. Care would need to be taken to ensure the nose-fairing interface is smooth, though the analysis would primarily focus on the flow over the nose itself, relaxing the required tolerances. The system could be belt driven using a DC motor and a pulley fixed to the shaft.

In contrast to the proposed rotating disk experiment, where the experiment was to take place in a closed environment, this experiment would necessitate the use of a wind tunnel. Hot-wire anemometry measurements could be taken using the 3-component traverse in the UK National Low Turbulence wind tunnel, located at City, University of London. The wind tunnel is of a closed loop design and has low freestream turbulence levels, making it well suited to the study of laminar-turbulent transition. The turbulence intensity levels are of the order of <0.01% for flow speeds up to 20 m/s, while the tunnel is capable of a maximum flow speed of 45 m/s. The tunnel has a Reynolds number range between 0.34×10^6 and 3.1×10^6 and a 6.75:1 contraction ratio.

3.2 Mathematical formulation

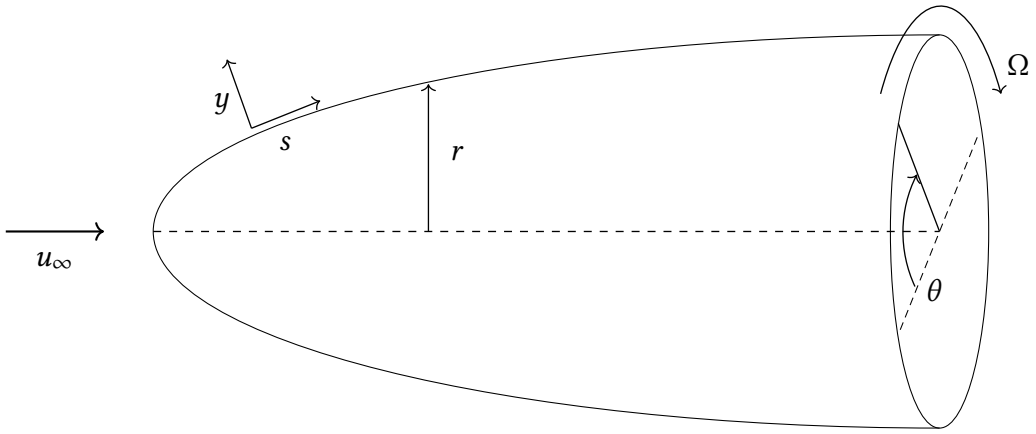

Figure 3.2: A sketch of the co-ordinate system for a generalised body of revolution.

The governing equations (3.1a–c) below were derived by Mangler (1945) for a rotationally symmetric flow past a rotating body of revolution. u, v, w are velocity components in

the directions of increasing s, y and θ as shown in figure 3.2.

$$\frac{\partial}{\partial s}(ru) + \frac{\partial}{\partial y}(rv) = 0, \tag{3.1a}$$

$$u\frac{\partial u}{\partial s} + v\frac{\partial u}{\partial y} - \frac{w^2}{r}\frac{\partial r}{\partial s} = u_e\frac{\partial u_e}{\partial s} + \nu\frac{\partial^2 u}{\partial y^2}, \tag{3.1b}$$

$$u\frac{\partial w}{\partial s} + v\frac{\partial w}{\partial y} + \frac{uw}{r}\frac{\partial r}{\partial s} = \nu\frac{\partial^2 w}{\partial y^2} \tag{3.1c}$$

In a fixed frame of reference these are subject to the boundary conditions

$$u = v = w - r\Omega = 0 \qquad \text{at} \quad y = 0 \tag{3.2a}$$

$$\begin{cases} u - u_e = w = 0, & u_\infty \neq 0 \\ u = w = 0, & u_\infty = 0 \end{cases} \qquad \text{as} \quad y \to \infty \tag{3.2b}$$

where Ω is the angular velocity about the axis of symmetry and u_e is the boundary-layer edge velocity. A two-component stream function is defined

$$u = \frac{1}{r}\frac{\partial \psi}{\partial y}, \quad v = -\frac{1}{r}\frac{\partial \psi}{\partial s}, \quad w = \frac{1}{r}\frac{\partial \phi}{\partial y}, \tag{3.3a–c}$$

which satisfies the continuity equation (3.1a) and which allows a consistent treatment of the azimuthal velocity component w. Subsequently ψ and ϕ are defined as functions of dimensionless stream functions f and g,

$$\psi = ru^* L_\xi f(\xi, \eta), \qquad \phi = r^2 \Omega L_\xi g(\xi, \eta), \tag{3.4a,b}$$

where L_ξ is a viscous length scale and u^* is a switchable velocity scale of the form

$$u^* = \begin{cases} u_e, & u_\infty \neq 0 \\ r\Omega, & u_\infty = 0. \end{cases} \tag{3.5}$$

A switchable velocity scale for u was chosen so as to encompass both quiescent and axial-flow domains, enabling the use of a single formulation. Using a variation of the Mangler-Levy-Lees transformation as presented by Horton and Stock (1995), a right-handed co-ordinate system is defined, in which

$$\eta = \frac{y}{L_\xi}, \qquad L_\xi = \frac{\sqrt{2\xi}}{u^*}, \qquad \xi = \int \xi_s ds, \qquad \xi_s = \nu u^*. \tag{3.6a–d}$$

Substituting these transformations into equations 3.3a–c yields

$$u = u^* f', \qquad w = r\Omega g', \tag{3.7a, b}$$

$$v = -\frac{u^* \nu}{\sqrt{2\xi}} \left[(\alpha_H + 1) f + \eta(\gamma - 1) f' + 2\xi \frac{\partial f}{\partial \xi} \right], \tag{3.7c}$$

where a prime denotes differentiation with respect to η. Inserting 3.7a–c in to the governing equations (3.1a–c) ultimately yields

$$f''' + (\alpha_H + 1) f f'' + \alpha_H \zeta_r g'^2 - \gamma f'^2 + \beta_H = 2\xi \left[\frac{\partial f'}{\partial \xi} f' - \frac{\partial f}{\partial \xi} f'' \right], \tag{3.8a}$$

$$g''' + (\alpha_H + 1) f g'' - 2\alpha_H f' g' = 2\xi \left[\frac{\partial g'}{\partial \xi} f' - \frac{\partial f}{\partial \xi} g'' \right], \tag{3.8b}$$

where the coefficients are

$$\alpha_H = \frac{2\xi}{r} \frac{\partial r}{\partial \xi}, \qquad \beta_H = \frac{2\xi u_e}{u^{*2}} \frac{\partial u_e}{\partial \xi}, \qquad \gamma = \frac{2\xi}{u^*} \frac{\partial u^*}{\partial \xi}, \qquad \zeta_r = \left(\frac{r\Omega}{u^*} \right)^2. \tag{3.9a–d}$$

The coefficient α_H relates to the shape of the body, β_H encompasses the meridional edge velocity distribution ($\beta_H = 0$ in still air), while ζ_r is the square of the ratio of rotational velocity to meridional velocity ($\zeta_r = 1$ in still air). Finally, depending on the form of u^*, γ follows as

$$\gamma = \begin{cases} \beta_H, & u_\infty \neq 0 \\ \alpha_H, & u_\infty = 0. \end{cases} \tag{3.10}$$

Equations 3.8a,b are subject to the following non-dimensional boundary conditions

$$f = f' = g = g' - 1 = 0 \qquad \text{at} \quad \eta = 0 \tag{3.11a}$$

$$\begin{cases} f' - 1 = g' = 0, & u_\infty \neq 0 \\ f' = g' = 0, & u_\infty = 0 \end{cases} \qquad \text{as} \quad \eta \to \infty \tag{3.11b}$$

The complete derivation of equations 3.8a,b can be found in appendix B.1.

3.3 Solution strategy

Equations 3.8a,b are parabolic in character and can be reduced to a system of partially-coupled 1D equations by employing a finite difference expression for the ξ-derivatives (section 3.3.2). Because this system is parabolic, and also self-similar at the nose of the

body, it allows us to march downstream on an initial-boundary-value problem. The coefficients defined by equations 3.9a,b are then obtained by numerical differentiation of the relevant geometry and the associated inviscid solution, here obtained using an axi-symmetric vortex sheet method, described in section 3.3.4, except for self-similar cases.

3.3.1 Marching scheme and leading edge treatment

Equations 3.8a,b are parabolic in nature and can be solved by marching in the ξ direction from some initial condition, with the solution at a given location only being dependant on the local conditions and the upstream solution. The ξ derivatives are expressed as the sum of a local flow factor k_ξ and a function of the known upstream flow $k_{u/s}$, given by

$$\frac{\partial f}{\partial \xi} = k_\xi f + k_{u/s}\left(f_{u/s}, \xi_{u/s}\right). \tag{3.12}$$

The present work employs a three-point, second-order-accurate, upwind finite-difference scheme in the form

$$k_\xi = \frac{1}{\xi_i - \xi_{i-1}} + \frac{1}{\xi_i - \xi_{i-2}} \tag{3.13}$$

$$k_{u/s} = \left(\frac{1}{\xi_{i-1} - \xi_{i-2}} - \frac{1}{\xi_i - \xi_{i-2}}\right) f_{i-2} - \left(\frac{1}{\xi_i - \xi_{i-1}} + \frac{1}{\xi_{i-1} - \xi_{i-2}}\right) f_{i-1} \tag{3.14}$$

where the subscript i represents the local ξ position and where $i-1$ and $i-2$ are upstream positions. Equations 3.13 and 3.14 are undefined for the first two ξ stations, however f and $\partial f/\partial \xi$ are known at $i = 1$. The flow is assumed to be self-similar for the first station, therefore $\xi = 0$ there. For the second station ξ is calculated by integrating equations 3.6c while assuming that

$$u^* = u_e = k_c s^m, \tag{3.15}$$

where m is the exponent characterising the inviscid flow as given by Hess and Faulkner (1965), in which $m = 1$ for blunt leading edges and $0 < m < 1$ for sharp leading edges. k_c is a scaling constant (u_∞ in the present work). Inserting the above into equation 3.6d yields

$$\xi_s = v u^* = v k_c s^m, \tag{3.16}$$

	$\mathbf{u}_\infty = \mathbf{0}$	$\mathbf{u}_\infty \neq \mathbf{0}$
β_H	0	$\frac{2m}{m+1}$
α_H	1	$2 - \beta_H$
γ	α_H	β_H
ζ_r	0	$\left(\frac{\Omega \partial r/\partial s}{\partial u_e/\partial s}\right)^2$
L_ξ	1	$\sqrt{\frac{1}{R_\infty \partial u_e/\partial s}}$

Table 3.1: Self-similar coefficient values (equations 3.6b and 3.9a–d) at $\xi = 0$ for quiescent and axial flow cases.

while integration results in

$$\xi = \frac{k_c s^{m+1}}{m+1} \tag{3.17}$$

For the self-similar leading edge case, where $\xi = 0$, the coefficients given by equations 3.6b and 3.9a–d are tabulated in table 3.1, where derivatives of u_e and r in s are obtained by numerical differentiation.

3.3.2 Reduction to linear ordinary differential equations

The boundary layer equations (3.8a,b) can be converted into a system of coupled first-order ODEs by introducing the following variables

$$f' = u, \qquad u' = \tau \qquad \text{and} \qquad g' = w, \qquad w' = \sigma, \tag{3.18a–d}$$

and then linearising using the following expansions in f, u, τ, g, w and σ, where the subscript n refers to the n-th iteration,

$$f = f_n + \Delta f, \quad u = u_n + \Delta u, \quad \tau = \tau_n + \Delta \tau, \tag{3.19a–c}$$

$$g = g_n + \Delta g, \quad w = w_n + \Delta w, \quad \sigma = \sigma_n + \Delta \sigma. \tag{3.19d–f}$$

The resultant equations can be written in matrix form as

$$\begin{bmatrix} \Delta\tau \\ \Delta u \\ \Delta f \\ \Delta\sigma \\ \Delta w \\ \Delta g \end{bmatrix}' = \begin{bmatrix} A_{\tau\tau} & A_{\tau u} & A_{\tau f} & 0 & A_{\tau w} & 0 \\ 1 & 0 & 0 & 0 & 0 & 0 \\ 0 & 1 & 0 & 0 & 0 & 0 \\ 0 & A_{\sigma u} & A_{\sigma f} & A_{\sigma\sigma} & A_{\sigma w} & 0 \\ 0 & 0 & 0 & 1 & 0 & 0 \\ 0 & 0 & 0 & 0 & 1 & 0 \end{bmatrix} \begin{bmatrix} \Delta\tau \\ \Delta u \\ \Delta f \\ \Delta\sigma \\ \Delta w \\ \Delta g \end{bmatrix} + \begin{bmatrix} B_\tau \\ B_u \\ B_f \\ B_\sigma \\ B_w \\ B_g \end{bmatrix} \tag{3.20}$$

where the terms of the matrix are given by

$$\begin{aligned} A_{\tau\tau} &= -\alpha_H f_n - f_n - 2\xi \frac{\partial f_n}{\partial \xi} \\ A_{\tau u} &= 2\gamma u_n + 2\xi k_\xi u_n + 2\xi \frac{\partial u_n}{\partial \xi} \\ A_{\tau f} &= -\alpha_H \tau_n - \tau_n - 2\xi k_\xi \tau_n \\ A_{\tau w} &= -2\alpha_H \zeta_r w_n \\ A_{\sigma\sigma} &= -\alpha_H f_n - f_n - 2\xi \frac{\partial f_n}{\partial \xi} \\ A_{\sigma w} &= 2\alpha_H u_n + 2\xi k_\xi u_n \\ A_{\sigma u} &= 2\alpha_H w_n + 2\xi \frac{\partial w_n}{\partial \xi} \\ A_{\sigma f} &= -\alpha_H \sigma_n - \sigma_n - 2\xi k_\xi \sigma_n \end{aligned} \tag{3.21a–h}$$

and where the B vector is a residual function of the (known) previous iteration,

$$\begin{aligned} B_\tau &= -\tau_n' - \alpha_H f_n \tau_n - f_n \tau_n - 2\xi \tau_n \frac{\partial f_n}{\partial \xi} + \gamma u_n^2 + 2\xi u_n \frac{\partial u_n}{\partial \xi} - \alpha_H \zeta_r w_n^2 - \beta_H \\ B_u &= \tau_n - u_n' \\ B_f &= u_n - f_n' \\ B_\sigma &= -\sigma_n' - \alpha_H f_n \sigma_n - f_n \sigma_n - 2\xi \sigma_n \frac{\partial f_n}{\partial \xi} + 2\alpha_H u_n w_n + 2\xi u_n \frac{\partial w_n}{\partial \xi} \\ B_w &= \sigma_n - w_n' \\ B_u &= w_n - g_n'. \end{aligned} \tag{3.22a–f}$$

A more complete derivation of the 6x6 system of ODEs from the boundary layer equations can be found in appendix B.2. As the u- and w-momentum equations are only weakly coupled, they can be approximated by two partially-coupled 3x3 systems of

ODEs. This yields some computational savings with a negligible reduction in accuracy. A derivation of this partially-coupled set of equations can be found in appendix B.3.

3.3.3 Compact-difference scheme

The ODEs given by 3.20 can be written more generally as

$$\zeta' = A\zeta + B. \tag{3.23}$$

This equation can be solved using a discretisation in the η-direction, namely a stretched η mesh, with near-wall $\Delta\eta = 0.02$, a stretch factor of 1.1 and a total of 36 points for $0 < \eta < 6$. In the present work the approach taken by the QinetiQ swept-tapered boundary layer tool, `BL2D`, is adopted and the ODEs are solved using a 4^{th}-order accurate, two-point compact-difference Taylor-Maclaurin scheme (Malik, 1990) in order to obtain a solution. This can be written as

$$\left[\zeta_{j+1} - \frac{\Delta\eta_j}{2}\zeta'_{j+1} + \frac{\Delta\eta_j^2}{12}\zeta''_{j+1}\right] - \left[\zeta_j + \frac{\Delta\eta_j}{2}\zeta'_j + \frac{\Delta\eta_j^2}{12}\zeta''_j\right] = O\left(\Delta\eta_j^5\right) \tag{3.24}$$

where i and j represent the indices of adjacent points on the η-mesh and

$$\Delta\eta_j = \eta_{j+1} - \eta_j. \tag{3.25}$$

The equation for the 2^{nd} derivative of the ζ function can be written as

$$\begin{aligned} \zeta'' &= A'\zeta + B' + A(A\zeta + B) \\ &= (A' + A^2)\zeta + (B' + AB), \end{aligned} \tag{3.26}$$

where a prime denotes differentiation in the η direction. Thus, the compact-difference expression (3.24) becomes

$$\begin{aligned} \left[\zeta_{j+1}\left(1 - \frac{\Delta\eta_j}{2}A_{j+1} + \frac{\Delta\eta_j^2}{12}(A' + A^2)_{j+1}\right)\right] - \left[\zeta_j\left(1 + \frac{\Delta\eta_j}{2}A_j + \frac{\Delta\eta_j^2}{12}(A' + A^2)_j\right)\right] \\ = \frac{\Delta\eta_j}{2}(B_{j+1} + B_j) - \frac{\Delta\eta_j^2}{12}\left[(B' + AB)_{j+1} - (B' + AB)_j\right]. \end{aligned} \tag{3.27}$$

where the first and second derivatives of the solution vectors f_n, u_n, τ_n, etc. are obtained using a cubic spline fit. Equation 3.27 can be applied over an η-mesh of size N, resulting

in a rectangular matrix of size $N-1$ by N,

$$\begin{bmatrix} [A_{1,n-1}] & [A_{2,n-1}] & & & & & & \\ & [A_{1,n-2}] & [A_{2,n-2}] & & & & & \\ & & [A_{1,n-3}] & [A_{2,n-3}] & & & & \\ & & & \ddots & \ddots & & & \\ & & & & & [A_{1,2}] & [A_{2,2}] & \\ & & & & & & [A_{1,1}] & [A_{2,1}] \end{bmatrix} \begin{bmatrix} [\zeta_n] \\ [\zeta_{n-1}] \\ [\zeta_{n-2}] \\ \vdots \\ [\zeta_2] \\ [\zeta_1] \end{bmatrix} = \begin{bmatrix} [B_{n-1}] \\ [B_{n-2}] \\ \vdots \\ [B_2] \\ [B_1] \end{bmatrix} \tag{3.28}$$

The matrix equation contains redundant boundary condition relations. A column can be removed from the matrix for each of these resulting in a square matrix which can be solved using regular elimination methods.

3.3.4 Edge velocity

In an axial flow the switchable velocity scale (equation 3.5) is equal to the slip velocity, u_e for an inviscid flow. The accuracy of the calculated boundary layer flow depends largely on the accuracy of the edge velocity provided. For cases where an analytical solution is available, such as the flow over a cone for example, or where a more realistic empirical distribution is available, such as for the flow over a sphere by Fage (1936), this is not a problem. However when more generalised bodies of revolution are to be analysed an accurate inviscid solution is sought. The present work uses a vortex sheet method as described by Lewis (1991, p146-160).

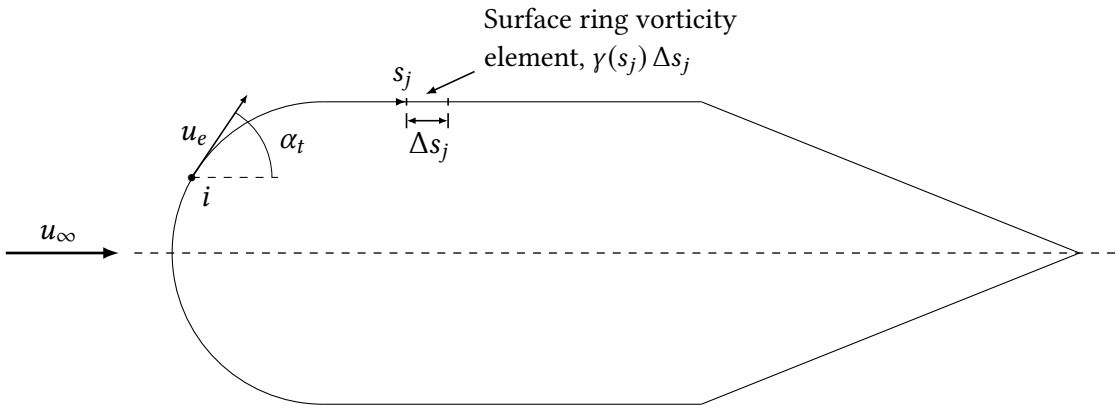

Figure 3.3: Axi-symmetric surface ring vorticity model, adapted from Lewis (1991).

The inviscid flow around a body, figure 3.3, is bounded by a sheet of surface ring vorticity of strength $\gamma(s) = u_e$. The Dirichlet boundary condition of zero velocity at

the wall and a parallel flow assumption can be described using the following Fredholm integral equation a point s_i,

$$\oint \bar{K}(s_i, s_j)\,\gamma(s_j)\,ds_j - {}^1\!/_2\,\gamma(s_i) + u_\infty \cos\alpha_t = 0 \tag{3.29}$$

where $\bar{K}(s_i, s_j)$ is a coupling coefficient which represents the induced velocity at a point s_i by a vortex at s_j. Applying the Biot-Savart law to a ring vortex ultimately reveals the following expression for the coupling coefficient

$$\bar{K}(s_i, s_j) = u_{ij}\cos\alpha_t + w_{ij}\sin\alpha_t. \tag{3.30}$$

where α_t is the local body gradient, namely

$$\alpha_t = \tan^{-1}(dr/dx), \tag{3.31}$$

and where x and r are the non-dimensionalised co-ordinates

$$x = \frac{x_i - x_j}{r_j}, \qquad r = \frac{r_i}{r_j}. \tag{3.32a,b}$$

The induced velocity components for a unit ring vortex are shown here as derived by Gibson (1972),

$$u_{ij} = -\frac{1}{2\pi r_j\sqrt{x^2 + (r+1)^2}}\left\{K(k) - \left[1 + \frac{2(r-1)}{x^2 + (r-1)^2}\right]E(k)\right\} \tag{3.33a}$$

$$w_{ij} = \frac{x/r}{2\pi r_j\sqrt{x^2 + (r+1)^2}}\left\{K(k) - \left[1 + \frac{2r}{x^2 + (r-1)^2}\right]E(k)\right\}, \tag{3.33b}$$

where $K(k)$ and $E(k)$ are complete elliptic integrals of the first and second kind wherein k is given by

$$k = \sqrt{\frac{4r}{x^2 + (r+1)^2}}. \tag{3.34}$$

By discretising the axi-symmetric body into N elements, equation 3.29 can be expressed as the sum of all ring vortex elements in the form $\gamma(s_j)\,\Delta s_j$, as

$$\sum_{j=1}^{N} \bar{K}(s_i, s_j)\,\gamma(s_j)\,\Delta s_j = -u_\infty \cos\alpha_t, \tag{3.35}$$

in which the $-1/2\gamma(s_i)$ term has been absorbed into the coupling coefficient as

$$\bar{K}(s_i, s_j)\,\Delta s_i = \bar{K}(s_i, s_j)\,\Delta s_i - 1/2 \qquad \text{for} \qquad i = j \tag{3.36}$$

Equation 3.35 may be solved in matrix form using standard techniques and the solution vector $\gamma(s_j)$ will directly yield the unit velocities near the surface at each station, u_e/u_∞.

$$\begin{bmatrix} K_{11} & K_{12} & K_{13} & \cdots & K_{1N} \\ K_{21} & K_{22} & K_{23} & \cdots & K_{2N} \\ K_{31} & K_{32} & K_{33} & \cdots & K_{3N} \\ \vdots & \vdots & \vdots & \ddots & \vdots \\ K_{N1} & K_{N2} & K_{N3} & \cdots & K_{NN} \end{bmatrix} \begin{bmatrix} \gamma_1 \\ \gamma_2 \\ \gamma_3 \\ \vdots \\ \gamma_N \end{bmatrix} = \begin{bmatrix} \text{rhs}_1 \\ \text{rhs}_2 \\ \text{rhs}_3 \\ \vdots \\ \text{rhs}_N \end{bmatrix} \tag{3.37}$$

and where the coupling coefficients are now

$$\begin{cases} K(s_i, s_j) & = (u_{ij}\cos\alpha_t + w_{ij}\sin\alpha_t)\,\Delta s_j & \text{for} \quad i \neq j \\ K(s_i, s_j) & = (u_{ij}\cos\alpha_t + w_{ij}\sin\alpha_t)\,\Delta s_i - 1/2 & \text{for} \quad i = j \end{cases} \tag{3.38}$$

The described vortex sheet method provides a good approximation to the edge velocity for a large variety of axi-symmetric bodies. Figure 3.4 shows a comparison with experimental results for an arbitrary body of revolution by Lewis (1991). The experimental results were obtained using surface pressure measurements and show good agreement with the vortex sheet method. The caveat here is that sharp discontinuities in curvature are not handled well (here noted at $x/c \approx 0.6$) and produce nonphysical accelerations, therefore care must be taken during model design and local point densities adjusted accordingly. Finally, agreement is also sub-optimal near the trailing edge as the real flow undergoes separation and inviscid theory fails to capture this. For the purposes of crossflow investigations however, only the fore-body solution is considered critical.

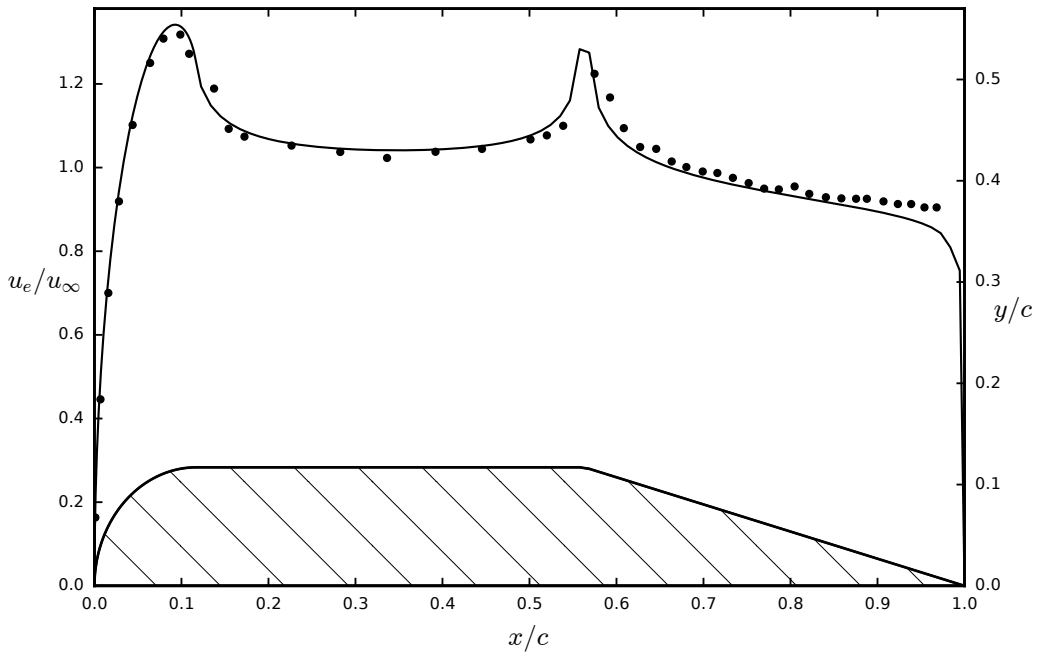

Figure 3.4: Comparison of the predicted edge velocity distribution for a hemispherically-nosed body of revolution with experimental results from Lewis (1991, p. 159) (•).

3.4 Verification of the general equations

In order to establish the validity of the proposed equations, results were compared with published velocity profiles for a variety of shapes and flow conditions. It was first necessary to confirm the correspondence between the present, general formulation and the specific formulations used to generate the results in the literature.

3.4.1 Rotating disk in still air

The equations for the mean flow of a rotating disk in still air as derived by Von Kármán (1921) are

$$f''' + 2ff'' - f'^2 + g'^2 = 0, \tag{3.39a}$$

$$g''' + 2fg'' - 2f'g' = 0, \tag{3.39b}$$

where in his formulation

$$u = r\Omega f'(\eta), \quad w = r\Omega g'(\eta), \quad v = -2\sqrt{\nu\Omega} f(\eta), \quad \eta = y\sqrt{\frac{\Omega}{\nu}}. \tag{3.40a–d}$$

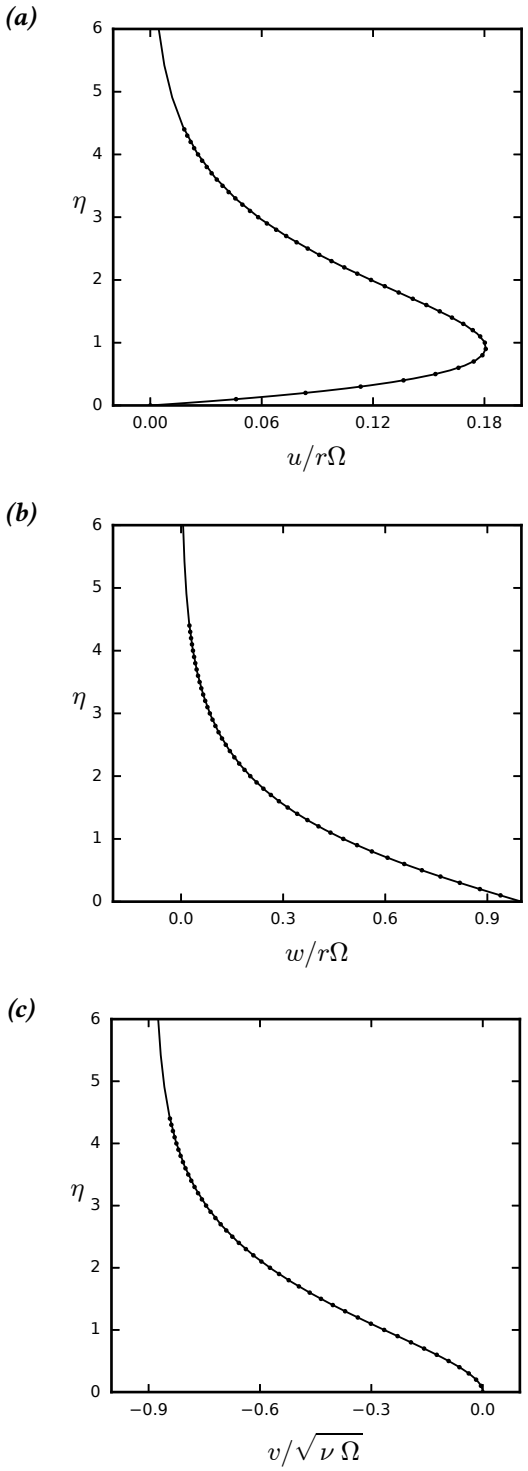

Figure 3.5: Comparison of the velocity profiles on a rotating disk, obtained using the present approach, with those reported by Benton (1966) (·); η as defined in equation 3.40d.

It was confirmed that equations 3.39a,b can be obtained by manipulating equations 3.8a,b by switching to the η defined in equation 3.40d, above, and by substituting $s = r$ in equations 3.3c and 3.6c. Comparison of the velocity profiles calculated by the present method with those generated by Benton (1966) using von Kármán's formulation, figure 3.5, also demonstrates that the present numerical scheme resolves the velocity profiles in the η direction with acceptable accuracy.

3.4.2 Rotating cone

Still air

The equations for the mean flow of a rotating cone of half-angle ψ_c in still air were derived by Wu (1959) and Tien (1960). Their formulation maintains the same form of the boundary layer equations as for a rotating disk, while including the cone half-angle ψ_c within the wall-normal co-ordinate η. This is achieved in the present method through the inclusion of the local radius r in the velocity scale u^* which is present in our transformed wall-normal co-ordinate, equations 3.5 and 3.9a–d. Garrett (2002), in an effort to match more readily experimental Reynolds numbers, includes ψ_c direction in the boundary-layer equations (3.41a,b) rather than including it in the wall-normal co-ordinate, thereby maintaining the same η scaling and as in the case of the rotating disk, equation 3.40d,

$$f''' + \left(2ff'' - f'^2 + g'^2\right)\sin\psi_c = 0, \tag{3.41a}$$

$$g''' + \left(2fg'' - 2f'g'\right)\sin\psi_c = 0. \tag{3.41b}$$

Other definitions are as in equations 3.40a,b, above, noting that the wall-normal velocity component for the cone is given by

$$v = -2\sin\psi_c\sqrt{\nu\Omega}f(\eta) \tag{3.42}$$

Equations 3.8a,b can be manipulated as for the disk case, but using $r = s\ \sin\psi_c$ to obtain equations 3.41a,b. Comparison of the velocity profiles calculated by the present method with those generated by Garrett (2002) for the rotating cone in still air, figure 3.6, validates our more general formulation of the boundary layer equations.

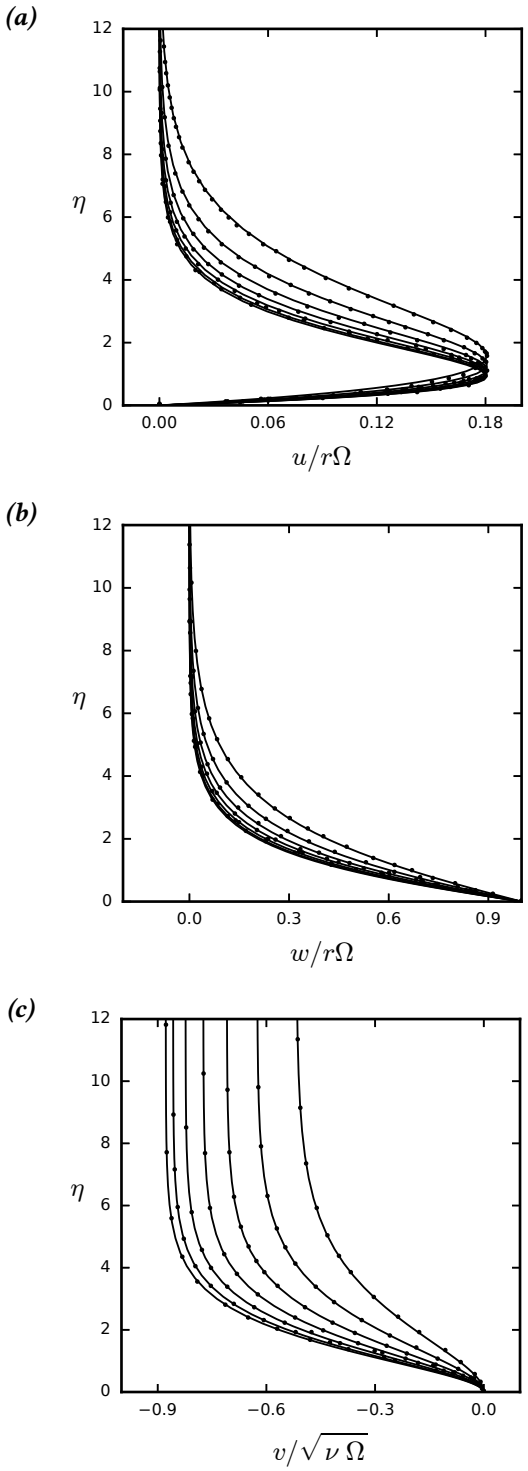

Figure 3.6: Comparison of the velocity profiles on a rotating cone (in still air) of half-angle $\psi_c = 20^\circ \rightarrow 80^\circ$ in 10° increments (right to left), obtained using the present approach, with those reported by Garrett (2002) ($\cdot$); η as defined in equation 3.40d.

Imposed axial flow

Koh and Price (1967) derived the mean flow equations for a rotating cone in an axial flow. In this case there exists no similarity transformation to reduce the mean flow equations from partial differential equations to a set of ODEs. Koh's approach assumes a power law for the boundary layer edge velocity, u_e, and incorporates this in the transformations, causing the boundary layer equations to take on a more complex form,

$$\begin{aligned} f''' \;+\; f f'' + \frac{2m}{m+3}(1-f'^2) \\ + \frac{2\xi}{m+3}\left[g'^2 + 2(1-m)\left(\frac{\partial f}{\partial \xi}f'' - \frac{\partial f'}{\partial \xi}f'\right)\right] \;=\; 0, \end{aligned} \tag{3.43a}$$

$$\begin{aligned} g''' \;+\; f g'' - \frac{4}{m+3}f'g' \\ + \frac{4(1-m)\xi}{m+3}\left(\frac{\partial f}{\partial \xi}g'' - \frac{\partial g'}{\partial \xi}f'\right) \;= 0. \end{aligned} \tag{3.43b}$$

m depends only on the angle ψ_c. The non-dimensional velocity components are given by

$$u = \bar{u}_e f'(\xi,\eta), \qquad w = \omega \bar{x}^{1/3} g'(\xi,\eta), \tag{3.44a, b}$$

$$v = -\left(\frac{6}{m+3}\nu \bar{x}\bar{u}_e\right)^{1/2}\left[\left(\frac{1}{2\bar{x}} + \frac{1}{2\bar{u}_e}\right)f(\xi,\eta) + \frac{\partial \xi}{\partial \bar{x}}\frac{\partial f}{\partial \xi} + \frac{\partial \eta}{\partial \bar{x}}f'\right], \tag{3.44c}$$

where

$$\xi \;=\; \left(\frac{\bar{w}_v}{\bar{u}_e}\right)^2 = \left(\frac{\omega}{\bar{k_c}}\bar{x}^{(1-m)/3}\right)^2, \quad \eta \;=\; \bar{y}\left(\frac{m+3}{6}\frac{\bar{u}_e}{\nu \bar{x}}\right)^{1/2}, \quad \omega \;=\; \Omega\left(3l^2 \sin\psi_c\right)^{1/3}, \tag{3.45a–c}$$

and where l is an arbitrary length scale, k_c is a flow constant and the transformed length scales and edge velocity are

$$\bar{x} \;=\; \frac{1}{l^2}\int_0^s r^2 ds, \qquad \bar{y} \;=\; \frac{r}{l}y, \qquad \bar{u}_e \;=\; k_c \bar{x}^{m/3}. \tag{3.46a–c}$$

Equations 3.8a,b can be manipulated using $r = s \sin\psi_c$, defining the velocity scale $u^* = u_e = k_c\, s^m$ and adopting η as in equation 3.45b to obtain equations 3.43a,b. Comparison of the profiles obtained from the present finite-difference method with those generated by Koh and Price (1967) for the rotating cone in an axial flow, figure 3.7, confirms that the velocity derivatives are correctly captured in our approach. Differences in w are attributed to a reduced resolution in the source image from which results were digitised.

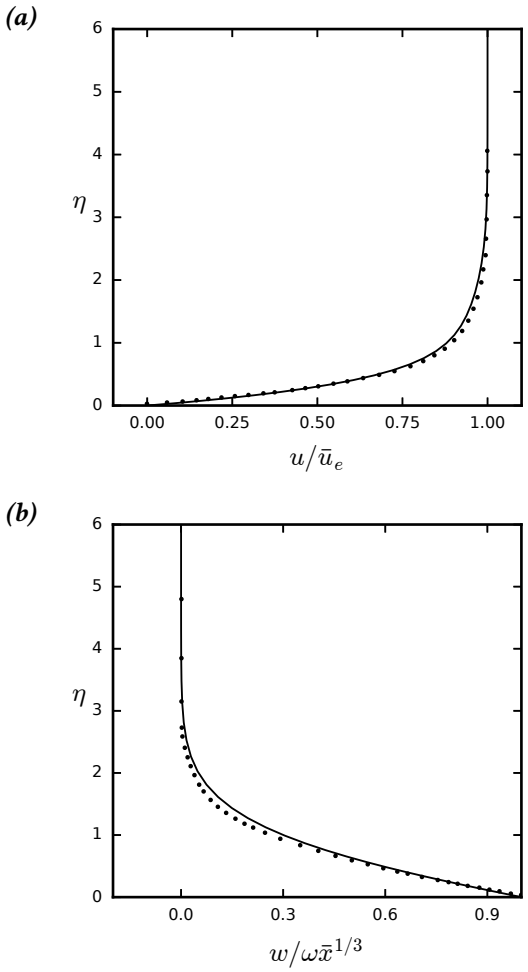

Figure 3.7: Comparison of the velocity profiles on a rotating cone (in an axial flow) of half-angle $\psi_c = 53.5°$ and $\xi = 10$, obtained using the present approach, with those reported by Koh and Price (1967) (·); η as defined in equation 3.45b.

However, the agreement with the velocity profiles published by Garrett, Hussain and Stephen (2010), figure 3.8, is not good, particularly in the u-component near $\eta = 1$. The approach adopted by Garrett, Hussain and Stephen (2010), an adaptation of the method of Koh and Price (1967), aimed to address limitations in the results presented in Garrett (2002), from which the present work also differs. A key point is the non-monotonic development of the u-velocity peak in the meridional direction, highlighted by Hussain (2010, p28) but not present in our results, nor indeed in Garrett's analysis of the rotating sphere problem, Garrett (2002).

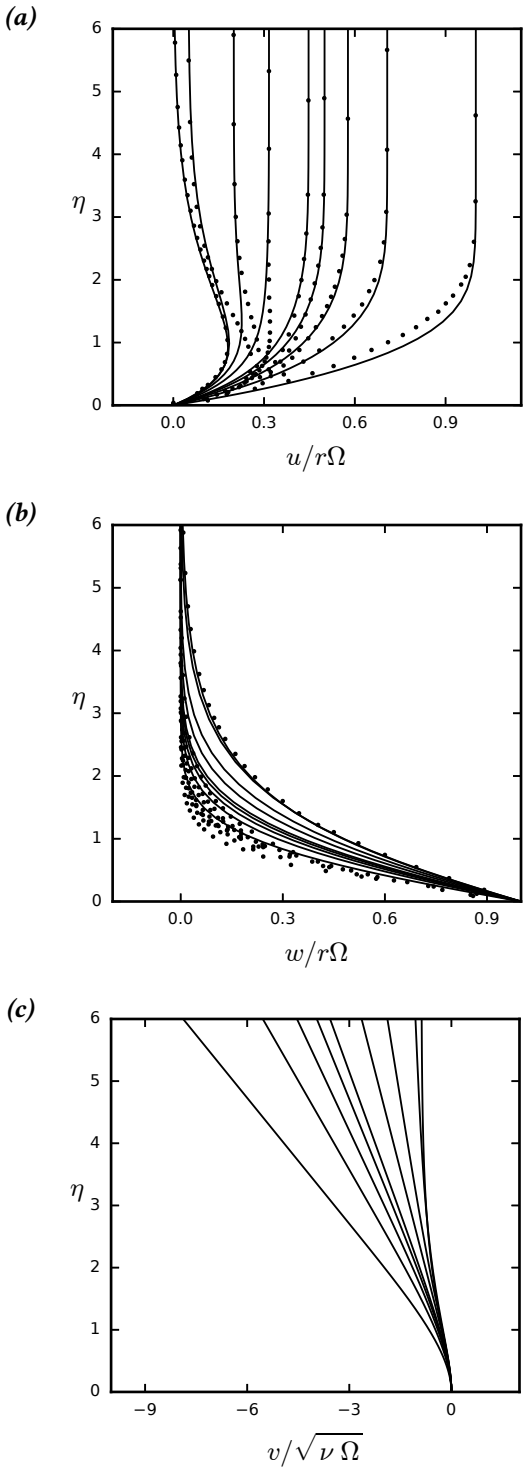

Figure 3.8: Comparison of the velocity profiles on a rotating cone (in an axial flow) of half-angle $\psi_c = 70^\circ$ and $\xi = 1, 2, 3, 4, 5, 10, 25, 400$ and ∞ (right to left), obtained using the present approach, with those reported by Garrett, Hussain and Stephen (2010) and Hussain (2010) ($\cdot$); η as defined in equation 3.40d.

3.4.3 Rotating sphere

Still air

The equations for the boundary layer of a rotating sphere in still air, first investigated by Howarth (1951), are shown here as formulated by Manohar (1967),

$$f''' + \left(ff'' + g'^2\right)\cot\theta_l = \left[f'\frac{\partial f'}{\partial \theta_l} - f''\frac{\partial f}{\partial \theta_l}\right] \tag{3.47a}$$

$$g''' + \left(fg'' + f'g'\right)\cot\theta_l = \left[f'\frac{\partial g'}{\partial \theta_l} - g''\frac{\partial f}{\partial \theta_l}\right], \tag{3.47b}$$

where θ_l is the angle of latitude measured from the axis of rotation, the wall-normal co-ordinate η is as defined in equation 3.40d and non-dimensional velocity components are given by

$$u = r_0\Omega f'(\eta, \theta_l), \quad w = r_0\Omega g'(\eta, \theta_l), \quad v = -\sqrt{\nu\Omega}\left(\cot\theta_l f(\eta, \theta_l) + \frac{\partial f}{\partial \theta_l}\right) \tag{3.48a–c}$$

where r_0 is the radius of the sphere. Equations 3.47a,b can be obtained from 3.8a,b by using $r = r_0 \sin\theta_l$, $s = r\theta_l$ and adopting η as defined in equation 3.40d. Figure 3.9 presents a comparison of the velocity profiles computed using the present approach with those generated by Garrett (2002), Garrett and Peake (2002) and Segalini and Garrett (2017), who made use of the above formulation.

Imposed axial flow

The equations for the boundary layer of a rotating sphere in an axial flow were originally derived by El-Shaarawi, El-Refaie and El-Bedeawi (1985) and are shown here as presented by Garrett (2002)

$$f''' + \left(ff'' + g'^2\right)\cot\theta_l + T_s^2 u_0\frac{\partial u_0}{\partial \theta_l} = \left[f'\frac{\partial f'}{\partial \theta_l} - f''\frac{\partial f}{\partial \theta_l}\right] \tag{3.49a}$$

$$g''' + \left(fg'' + f'g'\right)\cot\theta_l = \left[f'\frac{\partial g'}{\partial \theta_l} - g''\frac{\partial f}{\partial \theta_l}\right], \tag{3.49b}$$

where θ_l is the angle of latitude measured from the axis of rotation, T_s is the ratio of freestream axial flow velocity to rotational velocity, $T_s = u_\infty/r_0\Omega$, and u_0 is a non-dimensionalised edge velocity, $u_0 = u_e/u_\infty$. The wall-normal co-ordinate η and stream function definitions maintain the same scaling as in the case of the rotating sphere in

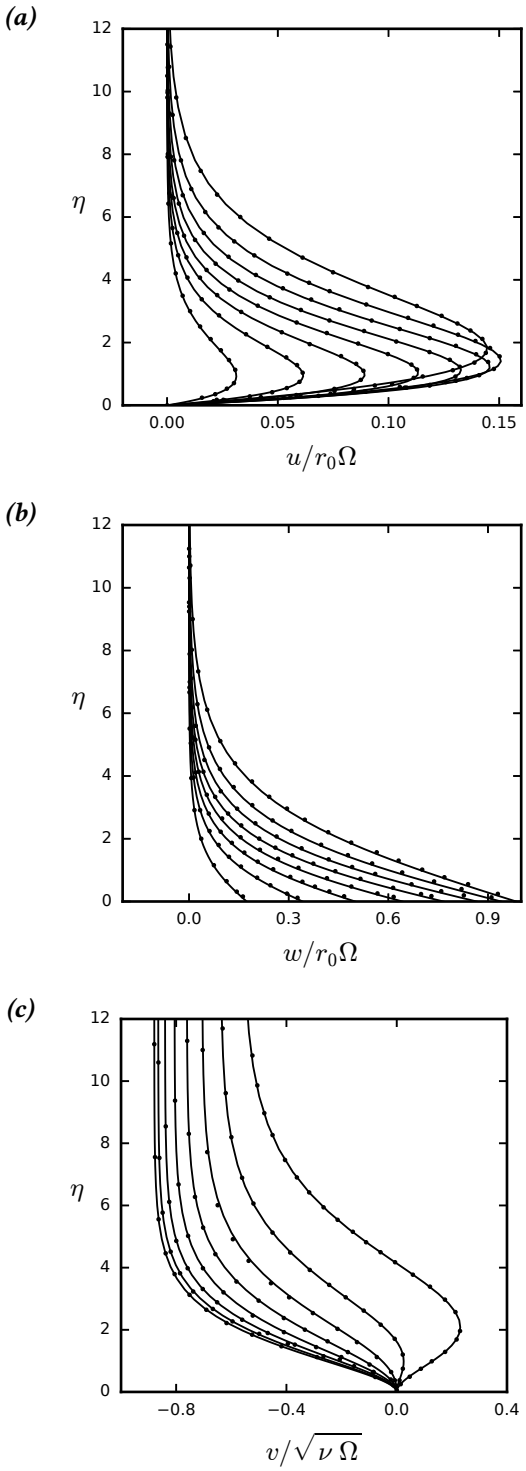

Figure 3.9: Comparison of the velocity profiles on a rotating sphere (in still air) at $\theta_l = 10^\circ \rightarrow 80^\circ$ in 10° increments (left to right), obtained using the present approach, with those reported by Garrett (2002), Garrett and Peake (2002) and Segalini and Garrett (2017) (·); η as defined in equation 3.40d.

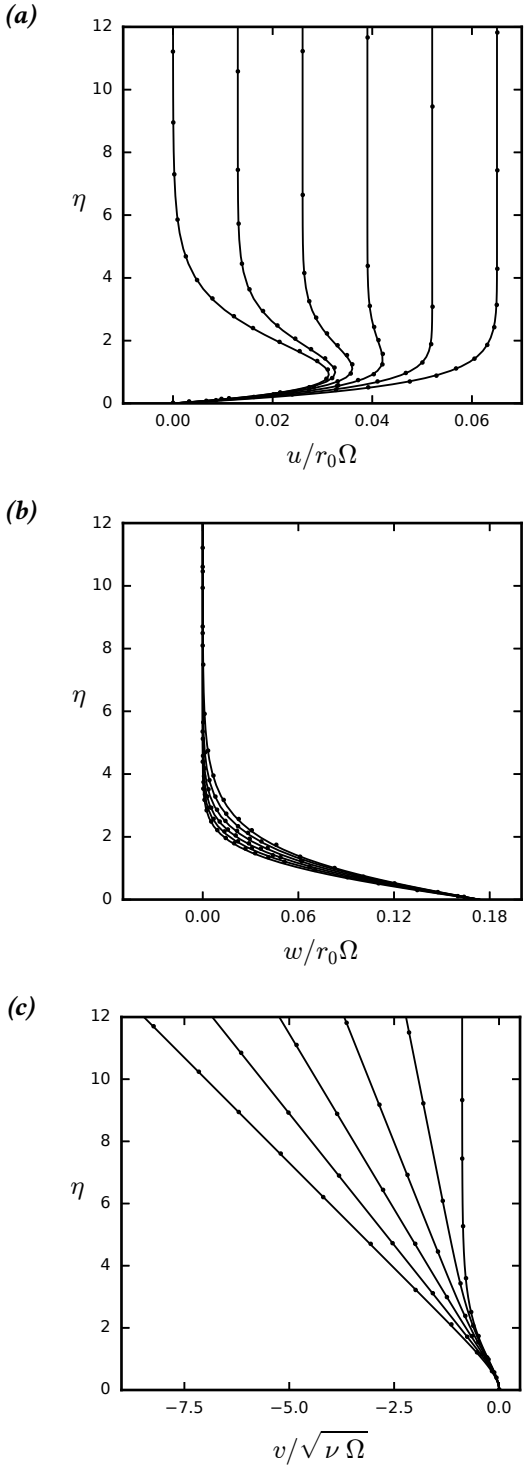

Figure 3.10: Comparison of the velocity profiles on a rotating sphere (in an axial flow) at $\theta_l = 10^\circ$ and $T_s = 0, 0.05, 0.1, 0.15, 0.2$ and 0.25 (left to right), obtained using the present approach, with those reported by Garrett (2002) ($\cdot$); η as defined in equation 3.40d.

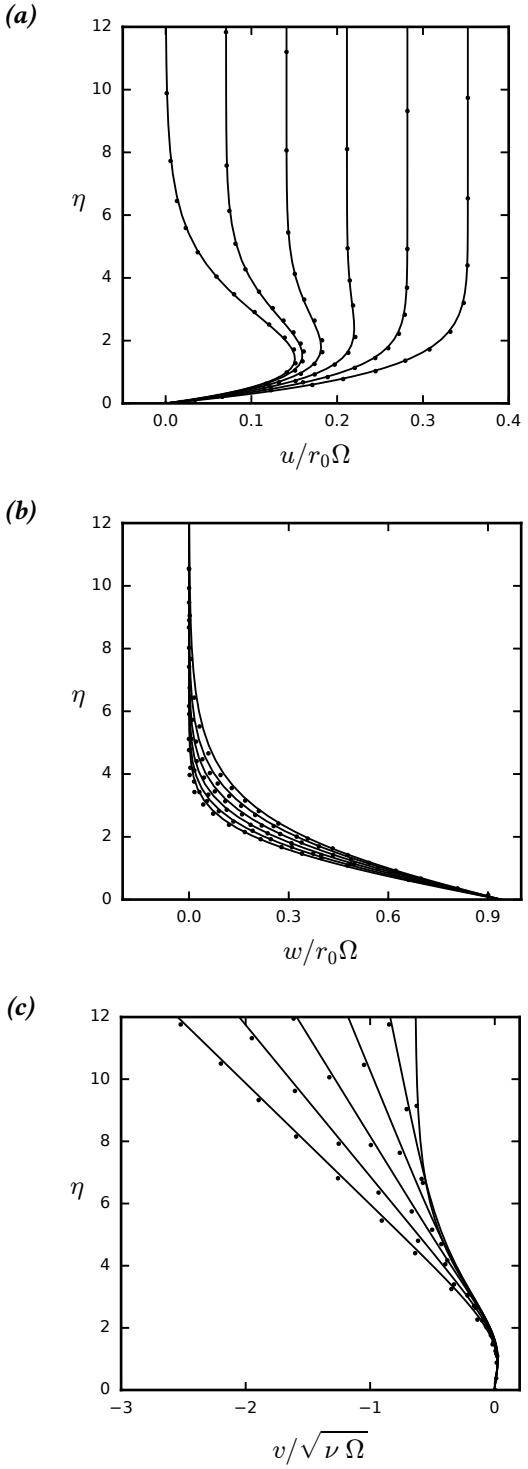

Figure 3.11: Comparison of the velocity profiles on a rotating sphere (in an axial flow) at $\theta_l = 70^\circ$ and $T_s = 0, 0.05, 0.1, 0.15, 0.2$ and 0.25 (left to right), obtained using the present approach, with those reported by Garrett (2002) (·); η as defined in equation 3.40d.

still air, equations 3.48a–c and 3.40d. The transformation of equations 3.8a,b to equations 3.49a,b follows a similar approach to that described in section 3.4.3. The comparison of the results from present method with those generated by Garrett (2002) in figure 3.10, for $\theta_l = 10^\circ$ and figure 3.11, for $\theta_l = 70^\circ$ are again very good.

3.4.4 Rotating prolate spheroid in still air

The equations for the boundary layer of a rotating prolate spheroid in still air, first investigated by Fadnis (1954), are shown here as formulated by Samad and Garrett (2010),

$$f'''\sqrt{\frac{1-e^2}{1-e^2\cos^2\theta_l}} + g'^2\cot\theta_l + \left(\frac{e^2\cos\theta_l\sin\theta_l}{1-e^2\cos^2\theta_l} + \cot\theta_l\right) ff'' = \left[f'\frac{\partial f'}{\partial\theta_l} - f''\frac{\partial f}{\partial\theta_l}\right] \tag{3.50a}$$

$$g'''\sqrt{\frac{1-e^2}{1-e^2\cos^2\theta_l}} - f'g'\cot\theta_l + \left(\frac{e^2\cos\theta_l\sin\theta_l}{1-e^2\cos^2\theta_l} + \cot\theta_l\right) fg'' = \left[f'\frac{\partial g'}{\partial\theta_l} - g''\frac{\partial f}{\partial\theta_l}\right] \tag{3.50b}$$

where θ_l is the angle of latitude measured from the axis of rotation in an elliptical co-ordinate system and e is the eccentricity of the ellipsoid. The wall-normal co-ordinate is defined as $\eta = (\Omega^*/\nu^*)^{1/2}(\eta^* - \eta_0^*)$, where * denotes dimensional quantities in his formulation and η^* and η_0^* are the total wall-normal distance from the axis of revolution and wall-normal distance from the axis of revolution to the surface of the spheroid, respectively. This should be analogous to η as defined in equation 3.40d. The non-dimensional velocity components u, w are defined as for the sphere in equations 3.48a,b but v is given by

$$v = -\sqrt{\nu\Omega}\left[\left(\frac{e^2\cos\theta_l\sin\theta_l}{1-e^2\cos^2\theta_l} + \cot\theta_l\right) f(\eta,\theta_l) + \frac{\partial f}{\partial\theta_l}\right] \tag{3.51}$$

where here for a prolate spheroid r_0 is the maximum radial thickness, the length of the semi-minor axis. Due to the complex relation between r and s for a spheroid we have not verified that equations 3.8a,b can be transformed to 3.50a,b. Nevertheless, velocity profiles calculated by the present method compare well with those generated by Samad and Garrett (2010) in figure 3.12 for $e = 0.3$; however, for the higher eccentricity case of $e = 0.7$, figure 3.13, the agreement, while good initially, is poor at increased

latitude θ_l. The discrepancy appears to be connected with the different mapping of the η co-ordinates used by Samad and Garrett (2010) and Samad and Garrett (2014) and in the present work, as the magnitudes of the peak velocities agree closely. There is some ambiguity in the definition of η_0^* between Samad and Garrett (2010) and Samad and Garrett (2014) which may explain the discrepancies at higher θ_l for large eccentricities. In former η_0^* is defined as the wall-normal distance to the surface from the axis of revolution while in the latter it is defined as the length of the semi-major axis. From this it would follow that differences would be greatest at higher eccentricities and latitudes. Unfortunately it was still not possible to obtain a better match under these assumptions.

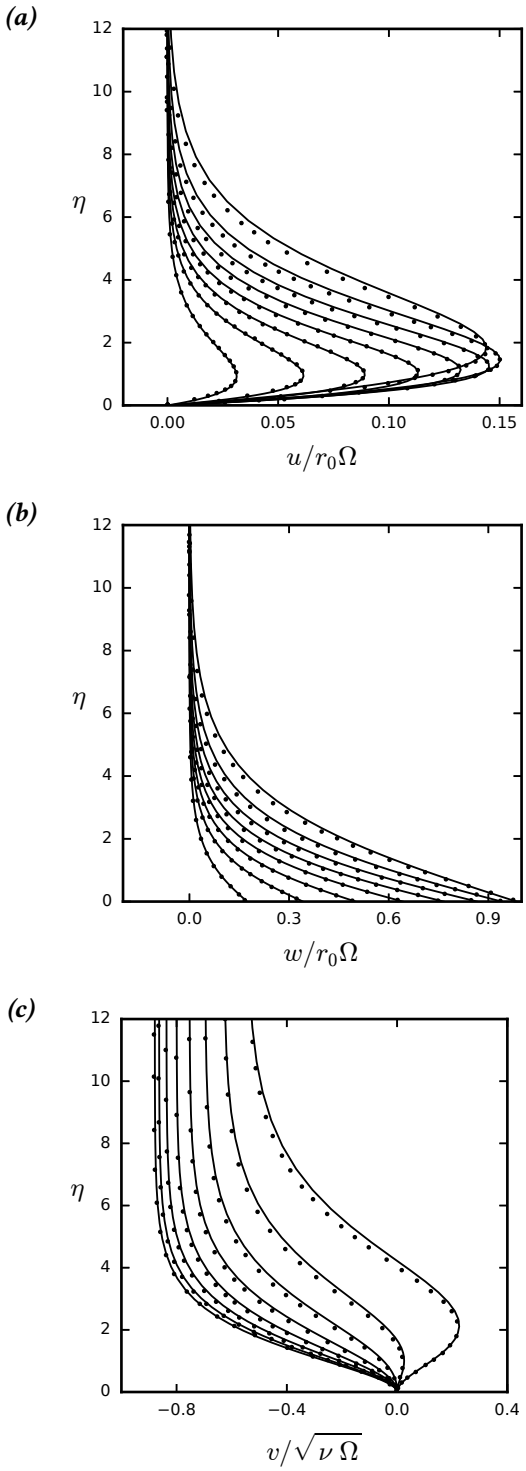

Figure 3.12: Comparison of the velocity profiles on a rotating prolate spheroid (in still air) with eccentricity 0.3 at $\theta_l = 10^\circ \longrightarrow 80^\circ$ in 10° increments (left to right), obtained using the present approach, with those reported by Samad and Garrett (2010) ($\cdot$); η as defined in equation 3.40d.

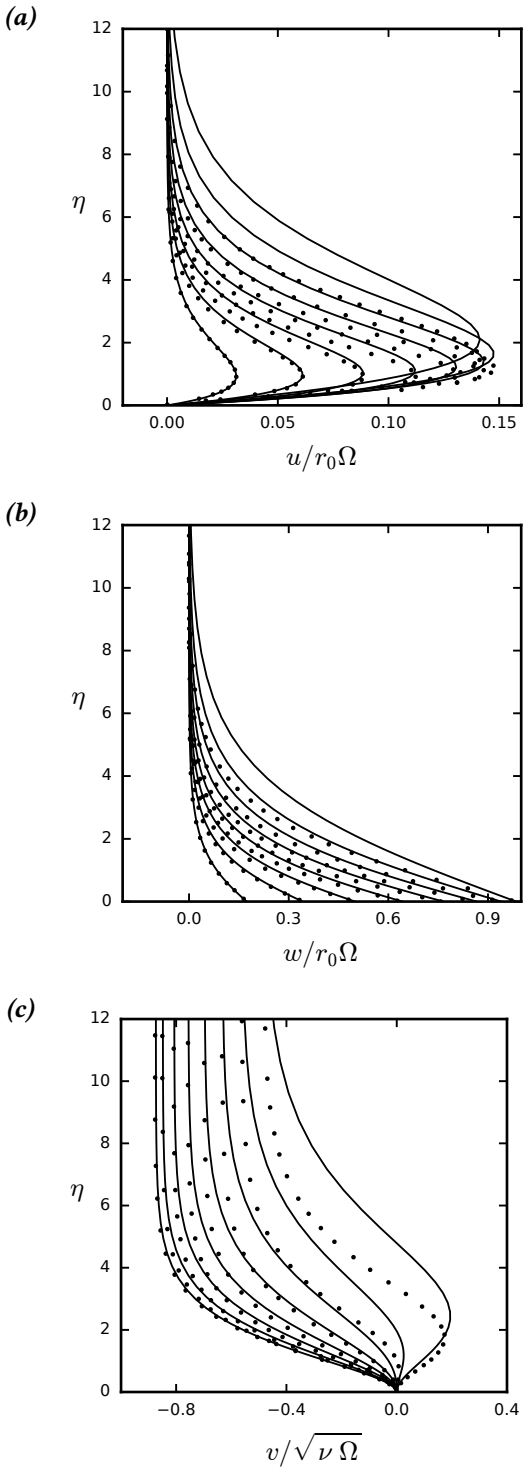

Figure 3.13: Comparison of the velocity profiles on a rotating prolate spheroid (in still air) with eccentricity 0.7 at $\theta_l = 10^\circ \longrightarrow 80^\circ$ in 10° increments (left to right), obtained using the present approach, with those reported by Samad and Garrett (2010) (·); η as defined in equation 3.40d.

4

The stability of the boundary layer on rotating axi-symmetric bodies

Contents

This chapter describes the approach taken in the present work, based on the three-dimensional linear stability analysis method outlined in Mack (1984), to analyse the linear stability of boundary layers on general rotating bodies of revolution developed within the previous chapter. The perturbation and stability equations are derived in a general orthogonal curvilinear co-ordinate system and an outline of the solution strategy is presented. The formulation is then verified by comparison with convective instability analyses for the rotating sphere in an axial flow in Garrett (2002) and Garrett and Peake (2004).

4.1 Mathematical formulation

4.1.1 Perturbation equations

The perturbation equations for a general body of revolution are derived from the 3-D, incompressible, N-S equations in orthogonal curvilinear co-ordinates, $\bar{x}$, $\bar{y}$ and $\bar{z}$. In the present work these represent the streamline, wall-normal and crossflow directions, respectively, as shown in figure 4.1. U, V and W are then the velocity components in these respective directions and ϕ_s is the angle between the meridional and external streamline and directions, $\bar{x}$ and s.

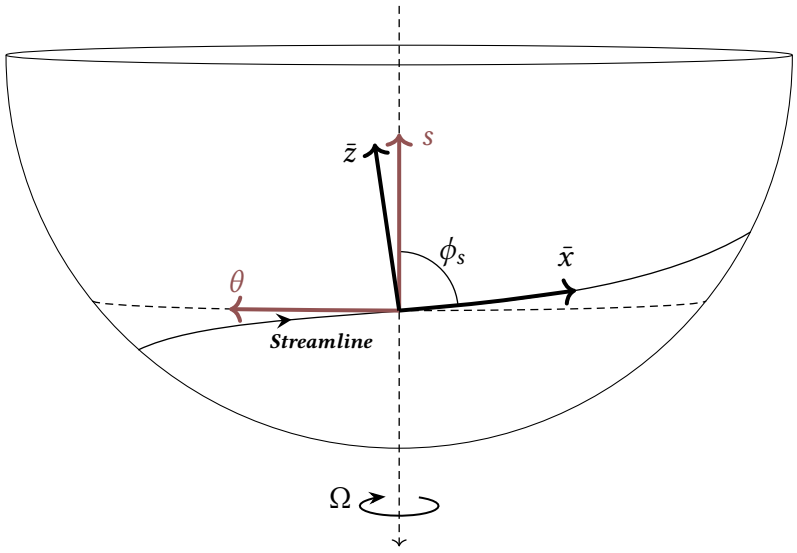

Figure 4.1: A sketch of the co-ordinate system employed for the solution of the stability equations. The angle between the meridional and streamline directions is given by ϕ_s (equation 4.30).

The element lengths in each direction are $h_x d\bar{x}$, $h_y d\bar{y}$ and $h_z d\bar{z}$, where the metrics, which provide a measure of how the transformed co-ordinate changes the position of the point, without loss of generality satisfy

$$h_x = h_x(\bar{x}, \bar{y}, \bar{z}), \qquad h_y = 1, \qquad h_z = h_z(\bar{x}, \bar{y}, \bar{z}). \tag{4.1a–c}$$

The incremental arc length is then given by the magnitude of the individual element lengths,

$$dS = \sqrt{(h_x d\bar{x})^2 + (d\bar{y})^2 + (h_z d\bar{z})^2}. \tag{4.2}$$

As the stability equations will be solved in a frame of reference rotating at a constant angular velocity $\vec{\Omega}$, which is acting in the direction along the axis of rotation with magnitude Ω, additional 'fictitious' terms will appear in the momentum equations compared to in an inertial frame of reference,

$$\left(\frac{d\vec{u}_{\text{in}}}{dt}\right)_{\text{in}} = \left(\frac{d\vec{u}_{\text{rot}}}{dt}\right)_{\text{rot}} + 2\vec{\Omega} \times \vec{u}_{\text{rot}} + \vec{\Omega} \times \left(\vec{\Omega} \times \vec{r}\right) + \frac{d\vec{\Omega}}{dt} \times \vec{r}, \tag{4.3}$$

where $\vec{r}$ is the perpendicular distance to the axis of rotation. The first of these additional terms represents the Coriolis acceleration. The second term is due to centripetal forces, acting normal to and towards the axis of rotation. Finally, the third term is known as the Euler acceleration, which acts parallel to the axis of rotation, as a reaction to angular accelerations.

Since $\vec{\Omega}$ is a constant vector the Euler acceleration term vanishes. Furthermore, the centripetal acceleration can be expressed as the gradient of a potential,

$$\vec{\Omega} \times \left(\vec{\Omega} \times \vec{r}\right) = -\frac{1}{2}\nabla\left(\vec{\Omega} \times \vec{r}\right)^2 = -\frac{\Omega^2}{2}\nabla\vec{r}^2. \tag{4.4}$$

The components of the velocity and angular velocity at a point on the surface of the body are given by

$$\vec{u}_{\text{rot}} = \begin{bmatrix} U \\ V \\ W \end{bmatrix}, \qquad \vec{\Omega} = \begin{bmatrix} \Omega_x \\ \Omega_y \\ \Omega_z \end{bmatrix}, \tag{4.5}$$

leading to a the Coriolis term

$$2\vec{\Omega} \times \vec{u}_{\text{rot}} = 2\begin{bmatrix} \Omega_y W - \Omega_z V \\ \Omega_z U - \Omega_x W \\ \Omega_x V - \Omega_y U \end{bmatrix}. \tag{4.6}$$

The continuity equation in the aforementioned co-ordinate system and in a rotating frame of reference is then

$$\frac{1}{h_x h_z}\left[\frac{\partial}{\partial\bar{x}}\left(h_z U\right) + \frac{\partial}{\partial\bar{y}}\left(h_x h_z V\right) + \frac{\partial}{\partial\bar{z}}\left(h_x W\right)\right] = 0 \tag{4.7}$$

while the complete N-S equations in this form are

$$\begin{aligned}
&\frac{\partial U}{\partial t} + \frac{U}{h_x}\frac{\partial U}{\partial \bar{x}} + V\frac{\partial U}{\partial \bar{y}} + \frac{W}{h_z}\frac{\partial U}{\partial \bar{z}} + \frac{1}{h_x}UV\frac{\partial h_x}{\partial \bar{y}} + \frac{1}{h_x h_z}\left[UW\frac{\partial h_x}{\partial \bar{z}} - W^2\frac{\partial h_z}{\partial \bar{x}}\right] \\
&\quad + 2\left(\Omega_y W - \Omega_z V\right) - \frac{\Omega^2}{2}\nabla\vec{r}^2 \\
&\quad = -\frac{1}{h_x}\frac{\partial P}{\partial \bar{x}} + \frac{1}{Re\, h_x}\frac{\partial}{\partial \bar{x}}\left(\frac{1}{h_x h_z}\left[\frac{\partial}{\partial \bar{x}}(h_z U) + \frac{\partial}{\partial \bar{y}}(h_x h_z V) + \frac{\partial}{\partial \bar{z}}(h_x W)\right]\right) \\
&\quad - \frac{1}{Re\, h_z}\left[\frac{\partial}{\partial \bar{y}}\left(\frac{h_z}{h_x}\left[\frac{\partial}{\partial \bar{x}}(V) - \frac{\partial}{\partial \bar{y}}(h_x U)\right]\right) - \frac{\partial}{\partial \bar{z}}\left(\frac{1}{h_x h_z}\left[\frac{\partial}{\partial \bar{z}}(h_x U) - \frac{\partial}{\partial \bar{x}}(h_z W)\right]\right)\right]
\end{aligned}$$

$$\begin{aligned}
&\frac{\partial V}{\partial t} + \frac{U}{h_x}\frac{\partial V}{\partial \bar{x}} + V\frac{\partial V}{\partial \bar{y}} + \frac{W}{h_z}\frac{\partial V}{\partial \bar{z}} - \frac{1}{h_x}U^2\frac{\partial h_x}{\partial \bar{x}} - \frac{1}{h_z}W^2\frac{\partial h_z}{\partial \bar{y}} + 2\left(\Omega_z U - \Omega_x W\right) - \frac{\Omega^2}{2}\nabla\vec{r}^2 \\
&\quad = -\frac{\partial P}{\partial \bar{y}} + \frac{1}{Re}\frac{\partial}{\partial \bar{y}}\left(\frac{1}{h_x h_z}\left[\frac{\partial}{\partial \bar{x}}(h_z U) + \frac{\partial}{\partial \bar{y}}(h_x h_z V) + \frac{\partial}{\partial \bar{z}}(h_x W)\right]\right) \\
&\quad - \frac{1}{Re\, h_x h_z}\left[\frac{\partial}{\partial \bar{z}}\left(\frac{h_x}{h_z}\left[\frac{\partial}{\partial \bar{y}}(h_z W) - \frac{\partial}{\partial \bar{z}}(V)\right]\right) - \frac{\partial}{\partial \bar{x}}\left(\frac{h_z}{h_x}\left[\frac{\partial}{\partial \bar{x}}(V) - \frac{\partial}{\partial \bar{y}}(h_x U)\right]\right)\right]
\end{aligned}$$

$$\begin{aligned}
&\frac{\partial W}{\partial t} + \frac{U}{h_x}\frac{\partial W}{\partial \bar{x}} + V\frac{\partial W}{\partial \bar{y}} + \frac{W}{h_z}\frac{\partial W}{\partial \bar{z}} + \frac{1}{h_x h_z}\left[UW\frac{\partial h_z}{\partial \bar{x}} - U^2\frac{\partial h_x}{\partial \bar{z}}\right] + \frac{1}{h_z}VW\frac{\partial h_z}{\partial \bar{y}} \\
&\quad + 2\left(\Omega_x V - \Omega_y U\right) - \frac{\Omega^2}{2}\nabla\vec{r}^2 \\
&\quad = -\frac{1}{h_z}\frac{\partial P}{\partial \bar{z}} + \frac{1}{Re\, h_z}\frac{\partial}{\partial \bar{z}}\left(\frac{1}{h_x h_z}\left[\frac{\partial}{\partial \bar{x}}(h_z U) + \frac{\partial}{\partial \bar{y}}(h_x h_z V) + \frac{\partial}{\partial \bar{z}}(h_x W)\right]\right) \\
&\quad - \frac{1}{Re\, h_x}\left[\frac{\partial}{\partial \bar{x}}\left(\frac{1}{h_x h_z}\left[\frac{\partial}{\partial \bar{z}}(h_x U) - \frac{\partial}{\partial \bar{x}}(h_z W)\right]\right) - \frac{\partial}{\partial \bar{y}}\left(\frac{h_x}{h_z}\left[\frac{\partial}{\partial \bar{y}}(h_z W) - \frac{\partial}{\partial \bar{z}}(V)\right]\right)\right]
\end{aligned} \tag{4.8a–c}$$

Equations 4.7 and 4.8a–c have been non-dimensionalised using the following length, velocity, time and pressure scales, respectively:

$$L = \delta^*, \quad Q_e = \sqrt{u_e^2 + (r\Omega)^2}, \quad T = \frac{L}{Q_e}, \quad P = \rho Q_e^2, \tag{4.9a–d}$$

where δ^* is the boundary layer displacement thickness, calculated by numerical integration from the volumetric flow rate in the streamline direction,

$$\delta^* = \frac{1}{Q_e}\int_0^\infty (Q_e - U)\, dx, \tag{4.10}$$

u_e and $r\Omega$ are the local slip velocities in the s and θ directions, respectively, as defined previously in section 3.2. The local Reynolds number is then given by

$$Re = \frac{L\,Q_e}{\nu} = \frac{\delta^* \sqrt{u_e^2 + (r\Omega)^2}}{\nu}. \tag{4.11}$$

The chosen velocity scale, namely the magnitude of the edge flow, will provide a consistent means of solution for cases ranging from quiescent-rotating to axial flow non-rotating cases. The next step is to define curvature coefficients,

$$\kappa_{xx} = 0, \qquad \kappa_{xy} = \frac{1}{h_x}\frac{\partial h_x}{\partial \bar{y}}, \qquad \kappa_{xz} = \frac{1}{h_x h_z}\frac{\partial h_x}{\partial \bar{z}}, \tag{4.12a,b}$$

$$\kappa_{zz} = 0, \qquad \kappa_{zx} = \frac{1}{h_z h_x}\frac{\partial h_z}{\partial \bar{x}}, \qquad \kappa_{zy} = \frac{1}{h_z}\frac{\partial h_z}{\partial \bar{y}}, \tag{4.12c,d}$$

where the absence of κ_{yx}, κ_{yy} and κ_{yz} is a result of the normal direction being straight. The perturbation equations can now be formed by applying a vanishingly small perturbation to equations 4.7 and 4.8a–c, thereby splitting the flow variables into time-averaged and fluctuating components, of the form

$$(U,\ V,\ W,\ P) \ = \ (u + \tilde{u},\ v + \tilde{v},\ w + \tilde{w},\ p + \tilde{p})\,. \tag{4.13}$$

Transition is deemed to be caused due to the growth of primary instabilities and the applied perturbations are assumed to be small enough so as to be considered as linear. After substitution and the subsequent subtraction of the the mean-flow terms, a number of terms may be discarded, assumed to be negligible, such as derivatives of curvature and quadratic curvature terms. The metric (h_i) terms can also be absorbed into the $\bar{x}$, $\bar{y}$ and $\bar{z}$ co-ordinates as follows, $\partial x = h_x \partial \bar{x}$, $\partial y = h_y \partial \bar{y}$ and $\partial z = h_z \partial \bar{z}$, yielding the final form of the perturbation equations

$$\kappa_{zx}\tilde{u} + \frac{\partial \tilde{u}}{\partial x} + \kappa_{xy}\tilde{v} + \kappa_{zy}\tilde{v} + \frac{\partial \tilde{v}}{\partial y} + \kappa_{xz}\tilde{w} + \frac{\partial \tilde{w}}{\partial z} = 0 \tag{4.14}$$

$$
\begin{aligned}
&\frac{\partial \tilde{u}}{\partial t} + u\frac{\partial \tilde{u}}{\partial x} + \tilde{u}\frac{\partial u}{\partial x} + v\frac{\partial \tilde{u}}{\partial y} + \tilde{v}\frac{\partial u}{\partial y} + w\frac{\partial \tilde{u}}{\partial z} + \tilde{w}\frac{\partial u}{\partial z} + \kappa_{xy}\left(u\tilde{v} + v\tilde{u}\right) \\
&\quad + \kappa_{xz}\left(u\tilde{w} + w\tilde{u}\right) - 2\kappa_{zx}w\tilde{w} + 2\left(\Omega_y\tilde{w} - \Omega_z\tilde{v}\right) = -\frac{\partial \tilde{p}}{\partial x} \\
&\quad + \frac{1}{Re}\left[\kappa_{zx}\frac{\partial \tilde{u}}{\partial x} + \left(\kappa_{xy} + \kappa_{zy}\right)\frac{\partial \tilde{u}}{\partial y} + \kappa_{xz}\frac{\partial \tilde{u}}{\partial z} + \frac{\partial^2 \tilde{u}}{\partial x^2} + \frac{\partial^2 \tilde{u}}{\partial y^2}\right. \\
&\quad \left. + \frac{\partial^2 \tilde{u}}{\partial z^2} + 2\kappa_{xy}\frac{\partial \tilde{v}}{\partial x} + 2\kappa_{xz}\frac{\partial \tilde{w}}{\partial x} - \kappa_{zx}\frac{\partial \tilde{w}}{\partial z}\right]
\end{aligned}
$$

$$
\begin{aligned}
&\frac{\partial \tilde{v}}{\partial t} + u\frac{\partial \tilde{v}}{\partial x} + \tilde{u}\frac{\partial v}{\partial x} + v\frac{\partial \tilde{v}}{\partial y} + \tilde{v}\frac{\partial v}{\partial y} + w\frac{\partial \tilde{v}}{\partial z} + \tilde{w}\frac{\partial v}{\partial z} - 2\kappa_{xy}u\tilde{u} - 2\kappa_{zy}w\tilde{w} \\
&\quad + 2\left(\Omega_z\tilde{u} - \Omega_x\tilde{w}\right) = -\frac{\partial \tilde{p}}{\partial y} + \frac{1}{Re}\left[\kappa_{zx}\frac{\partial \tilde{v}}{\partial x} + \left(\kappa_{xy} + \kappa_{zy}\right)\frac{\partial \tilde{v}}{\partial y} + \kappa_{xz}\frac{\partial \tilde{v}}{\partial z}\right. \qquad (4.15\text{a–c}) \\
&\quad \left. + \frac{\partial^2 \tilde{v}}{\partial x^2} + \frac{\partial^2 \tilde{v}}{\partial y^2} + \frac{\partial^2 \tilde{v}}{\partial z^2} - \kappa_{xy}\frac{\partial \tilde{u}}{\partial x} - \kappa_{zy}\frac{\partial \tilde{w}}{\partial z}\right]
\end{aligned}
$$

$$
\begin{aligned}
&\frac{\partial \tilde{w}}{\partial t} + u\frac{\partial \tilde{w}}{\partial x} + \tilde{u}\frac{\partial w}{\partial x} + v\frac{\partial \tilde{w}}{\partial y} + \tilde{v}\frac{\partial w}{\partial y} + w\frac{\partial \tilde{w}}{\partial z} + \tilde{w}\frac{\partial w}{\partial z} + \kappa_{zx}\left(u\tilde{w} + w\tilde{u}\right) \\
&\quad - 2\kappa_{xz}u\tilde{u} + \kappa_{zy}\left(v\tilde{w} + w\tilde{v}\right) + 2\left(\Omega_x\tilde{v} - \Omega_y\tilde{u}\right) = -\frac{\partial \tilde{p}}{\partial z} \\
&\quad + \frac{1}{Re}\left[\kappa_{zx}\frac{\partial \tilde{w}}{\partial x} + \left(\kappa_{zy} + \kappa_{xy}\right)\frac{\partial \tilde{w}}{\partial y} + \kappa_{xz}\frac{\partial \tilde{w}}{\partial z} + \frac{\partial^2 \tilde{w}}{\partial x^2} + \frac{\partial^2 \tilde{w}}{\partial y^2}\right. \\
&\quad \left. + \frac{\partial^2 \tilde{w}}{\partial z^2} + 2\kappa_{zx}\frac{\partial \tilde{u}}{\partial z} - \kappa_{xz}\frac{\partial \tilde{u}}{\partial x} + 2\kappa_{zy}\frac{\partial \tilde{v}}{\partial z}\right].
\end{aligned}
$$

A more complete derivation of the perturbation equations can be found in appendix C.1.

4.1.2 Stability equations

Continuing with the approach described in Mack (1984), the stability equations can be formed by assuming a wave-like perturbation of the form

$$(\tilde{u},\ \tilde{v},\ \tilde{w},\ \tilde{p}) \ = \ (\hat{u},\ \hat{v},\ \hat{w},\ \hat{p})\, e^{i\Phi}, \tag{4.16}$$

where

$$\Phi = \alpha x + \beta z - \omega t. \tag{4.17}$$

Here α is the wavenumber in the streamline (x) direction, β the wavenumber in the crossflow (z) direction, and ω is the frequency of the disturbance. Stability analysis can be performed in space, time or both. Early stability analyses employed temporal amplification theory, which assumes disturbances grow only in time and wherein α and β are real and ω is complex. The resulting stability equations are linear in ω_i and easily solved. In a steady mean flow however, the amplitudes of normal disturbances grow only in space. Gaster (1962) was able to prove that in 2-D (and 3-D using Squire's transformations), for small amplification rates, spatial amplification theory yielded equal frequencies to temporal theory and temporal and spatial growth rates were related by the group velocity. Spatial theory, wherein α and β are complex and ω is real, can more readily produce spatial amplification rates at the cost of increased computational complexity (owing to the resultant stability equations being quadratic in α_i). The present work will focus on the investigation of convective instabilities using spatial amplification theory. Crossflow modes, which predominantly cause transition in rotating boundary layers, are associated with low-frequency wavenumber vectors at angles of almost 90° to the local streamline (figure 4.2). The magnitude of the wavenumber vectors is given by

$$k_w = \sqrt{\left(\alpha_r^2 + \beta_r^2\right)}, \tag{4.18}$$

and their wave angle is given by

$$\psi_w = \tan^{-1}\left(\frac{\beta_r}{\alpha_r}\right). \tag{4.19}$$

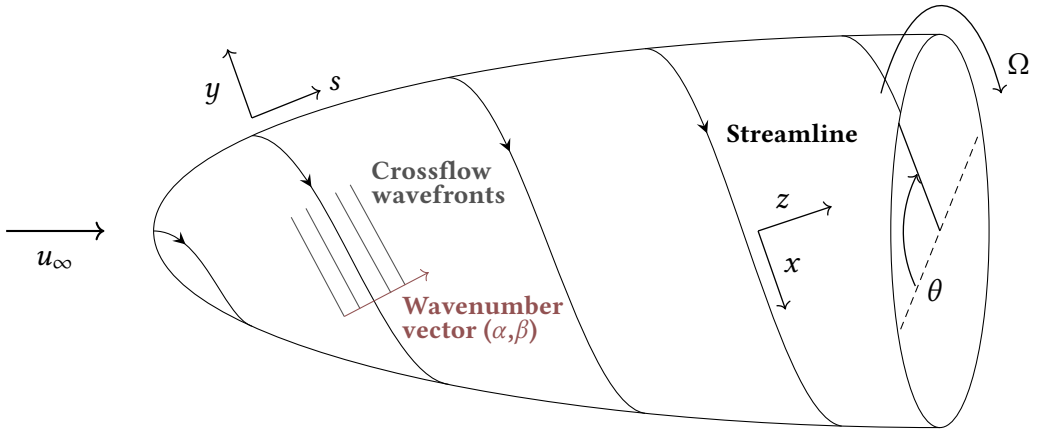

Figure 4.2: A sketch of the direction of crossflow wavefronts and wavenumber vectors on a rotating body.

Substituting equation 4.16 into the perturbation equations (4.14 and 4.15a–c) and assuming the flow to be parallel with the wall within the boundary layer, i.e. $v = 0$, $u(y)$ and $w(y)$, results in

$$\kappa_{zx}\hat{u} + i\alpha\hat{u} + \kappa_{xy}\hat{v} + \kappa_{zy}\hat{v} + \frac{\partial\hat{v}}{\partial y} + \kappa_{xz}\hat{w} + i\beta\hat{w} = 0, \tag{4.20}$$

$$\begin{aligned}
&-i\omega\hat{u} + i\alpha u\hat{u} + \hat{v}\frac{\partial u}{\partial y} + i\beta w\hat{u} + \kappa_{xy}u\hat{v} + \kappa_{xz}\left(u\hat{w} + w\hat{u}\right) - 2\kappa_{zx}w\hat{w} + 2\left(\Omega_y\hat{w} - \Omega_z\hat{v}\right) \\
&\quad = -i\alpha\hat{p} + \frac{1}{Re}\Bigg[i\alpha\kappa_{zx}\hat{u} + \left(\kappa_{xy} + \kappa_{zy}\right)\frac{\partial\hat{u}}{\partial y} + i\beta\kappa_{xz}\hat{u} - \alpha^2\hat{u} + \frac{\partial^2\hat{u}}{\partial y^2} - \beta^2\hat{u} \\
&\quad + 2i\alpha\kappa_{xy}\hat{v} + 2i\alpha\kappa_{xz}\hat{w} - i\beta\kappa_{zx}\hat{w}\Bigg],
\end{aligned}$$

$$\begin{aligned}
&-i\omega\hat{v} + i\alpha u\hat{v} + i\beta w\hat{v} - 2\kappa_{xy}u\hat{u} - 2\kappa_{zy}w\hat{w} + 2\left(\Omega_z\hat{u} - \Omega_x\hat{w}\right) = -\frac{\partial\hat{p}}{\partial y} \\
&\quad + \frac{1}{Re}\Bigg[i\alpha\kappa_{zx}\hat{v} + \left(\kappa_{xy} + \kappa_{zy}\right)\frac{\partial\hat{v}}{\partial y} + i\beta\kappa_{xz}\hat{v} - \alpha^2\hat{v} + \frac{\partial^2\hat{v}}{\partial y^2} - \beta^2\hat{v} - i\alpha\kappa_{xy}\hat{u} - i\beta\kappa_{zy}\hat{w}\Bigg],
\end{aligned}$$

$$\begin{aligned}
&-i\omega\hat{w} + i\alpha u\hat{w} + \hat{v}\frac{\partial w}{\partial y} + i\beta w\hat{w} + \kappa_{zx}\left(u\hat{w} + w\hat{u}\right) - 2\kappa_{xz}u\hat{u} + \kappa_{zy}w\hat{v} + 2\left(\Omega_x\hat{v} - \Omega_y\hat{u}\right) \\
&\quad = -i\beta\hat{p} + \frac{1}{Re}\Bigg[i\alpha\kappa_{zx}\hat{w} + \left(\kappa_{zy} + \kappa_{xy}\right)\frac{\partial\hat{w}}{\partial y} + i\beta\kappa_{xz}\hat{w} - \alpha^2\hat{w} + \frac{\partial^2\hat{w}}{\partial y^2} - \beta^2\hat{w} \\
&\quad + 2i\beta\kappa_{zx}\hat{u} - i\alpha\kappa_{xz}\hat{u} + 2i\beta\kappa_{zy}\hat{v}\Bigg],
\end{aligned} \tag{4.21a–c}$$

where the non-dimensionalising scales are the same as defined in equations 4.9a–d. Equations 4.20 and 4.21a–c have been verified against those published by Malik and Spall (1991), after compressibility terms and the appropriate curvatures are excluded. These can then be expressed as a system of 6 first order ODEs in the y direction by making the following substitutions

$$\tau_u = \frac{\partial \hat{u}}{\partial y}, \quad \tau_w = \frac{\partial \hat{w}}{\partial y}, \tag{4.22a,b}$$

which results in

$$\begin{aligned}
\hat{u}' &= \tau_{\hat{u}} \\
\tau'_{\hat{u}} &= \left[(-i\omega + i\alpha u + i\beta w + \kappa_{xz} w)\, Re + \alpha^2 + \beta^2 - i\alpha\kappa_{zx} - i\beta\kappa_{xz} \right]\hat{u} \\
&\quad - \left[\kappa_{xy} + \kappa_{zy}\right]\tau_{\hat{u}} \;+\; \left[\left(\kappa_{xz} u - 2\kappa_{zx} w + 2\Omega_y\right) Re - 2i\alpha\kappa_{xz} + i\beta\kappa_{zx} \right]\hat{w} \\
&\quad + i\alpha Re\, \hat{p} \;+\; \left[\left(u' + \kappa_{xy} u - 2\Omega_z\right) Re - 2i\alpha\kappa_{xy} \right]\hat{v} \\
\hat{p}' &= \left[2\kappa_{xy} u - \frac{1}{Re} i\alpha\kappa_{xy} - 2\Omega_z\right]\hat{u} - \frac{1}{Re}\left(i\alpha + \kappa_{zx}\right)\tau_{\hat{u}} \;+\; \left[2\kappa_{zy} w - \frac{1}{Re} i\beta\kappa_{zy} + 2\Omega_x\right]\hat{w} \\
&\quad + \left[i\omega - i\alpha u \;-\; i\beta w - \frac{1}{Re}\left(\alpha^2 + \beta^2 - i\alpha\kappa_{zx} - i\beta\kappa_{xz}\right) \right]\hat{v} \;-\; \frac{1}{Re}\left(i\beta + \kappa_{xz}\right)\tau_{\hat{w}} \\
\hat{v}' &= -\left[\kappa_{zx} + i\alpha\right]\hat{u} \;-\; \left[\kappa_{xz} + i\beta\right]\hat{w} \;-\; \left[\kappa_{xy} + \kappa_{zy}\right]\hat{v} \\
\hat{w}' &= \tau_{\hat{w}} \\
\tau'_{\hat{w}} &= \left[\left(\kappa_{zx} w - 2\kappa_{xz} u - 2\Omega_y\right) Re - 2i\alpha\kappa_{zx} + i\alpha\kappa_{xz} \right]\hat{u} \\
&\quad + \left[(-i\omega + i\alpha u + i\beta w + \kappa_{zx} u)\, Re + \alpha^2 + \beta^2 - i\alpha\kappa_{zx} - i\beta\kappa_{xz} \right]\hat{w} \\
&\quad + i\beta Re\, \hat{p} \;+\; \left[\left(w' + \kappa_{zy} w + 2\Omega_x\right) Re - 2i\beta\kappa_{zy} \right]\hat{v} \;-\; \left[\kappa_{xy} + \kappa_{zy}\right]\tau_{\hat{w}}
\end{aligned} \tag{4.23a–f}$$

4.2 Solution strategy

In the present work a modified approach taken by the QinetiQ e^N linear stability tool, `CoDS`, is adopted in order to solve the stability equations derived in the previous section. Equations 4.23a–f are a system of 6 first order ODEs and, using the shooting

method described in Mack, 1984, can be solved using the 4^{th} order compact-difference scheme of Malik, 1990, as similarly employed in chapter 3 to solve the boundary layer equations. The format used to supply the mean-flow data to the stability analysis is detailed in appendix C.3.

4.2.1 Eigenvalue search

Equations 4.23a–f are a system of ODEs in y and can be written more generally as the homogeneous equation

$$\zeta' = A\zeta. \tag{4.24}$$

This can be solved using a shooting method for a given ω, β and Re, as well as knowledge of the local curvature and velocity profile, using an initial guess for α. The wall-normal velocity boundary condition is left free in equation 4.24, and stipulated by iteration using Newton's method until $\hat{v}_w = 0$ is satisfied within a predefined tolerance. This is performed by using a 4^{th} order compact-difference scheme to solve for the derivative w.r.t. the independent parameter α. This derivative can be written as

$$\frac{\partial \zeta'}{\partial \alpha} = A\frac{\partial \zeta}{\partial \alpha} + \frac{\partial A}{\partial \alpha}\zeta \tag{4.25}$$

$$\frac{\partial \zeta''}{\partial \alpha} = \frac{\partial A'}{\partial \alpha}\zeta + A'\frac{\partial \zeta}{\partial \alpha} + A\left(2\frac{\partial A}{\partial \alpha}\zeta + A\frac{\partial \zeta}{\partial \alpha}\right) = \left(A' + A^2\right)\frac{\partial \zeta}{\partial \alpha} + \left(\frac{\partial A'}{\partial \alpha} + 2A\frac{\partial A}{\partial \alpha}\right) \tag{4.26}$$

where the corresponding compact-difference is then

$$\left[\left.\frac{\partial \zeta}{\partial \alpha}\right|_{j+1}\left(1 - \frac{\Delta\eta_j}{2}A_{j+1} + \frac{\Delta\eta_j^2}{12}(A' + A^2)_{j+1}\right)\right] - \left[\left.\frac{\partial \zeta}{\partial \alpha}\right|_{j}\left(1 + \frac{\Delta\eta_j}{2}A_j + \frac{\Delta\eta_j^2}{12}(A' + A^2)_j\right)\right]$$
$$= \frac{\Delta\eta_j^2}{12}\left[\zeta_j\left(\frac{\partial A'}{\partial \alpha} + 2A\frac{\partial A}{\partial \alpha}\right) - \zeta_{j+1}\left(\frac{\partial A'}{\partial \alpha} + 2A\frac{\partial A}{\partial \alpha}\right)\right]. \tag{4.27}$$

Once a solution is obtained, the method is then marched in the ω, x and β directions sequentially. The limits of the spanwise wavenumber search are determined from an initial analysis of the boundary layer data using the the above shooting method. The frequency and spatial ranges are marched in until a region of prolonged stability is encountered. The complete A derivative matrices, A', $\frac{\partial A}{\partial \alpha}$ and $\frac{\partial A'}{\partial \alpha}$, for the compact-difference scheme are given in appendix C.4.

4.2.2 N-factor calculation

Three-dimensional boundary layers theoretically possess spatial growth rates both in the streamline and crossflow directions. In order to capture this, their N-factors are defined as

$$N_{\omega,\beta_r}(x,z) = \int_{\alpha_i=0}^{x} -\alpha_i\left(x, z(x), \omega, \beta_r(x)\right) dx + \int_{\beta_i=0}^{z} -\beta_i\left(x(z), z, \omega, \beta_r(z)\right) dz. \quad (4.28)$$

To enable their calculation, spatial stability analysis assumes that the spanwise growth rate, β_i is zero. This stems from the prescription that the flow is invariant in the spanwise direction and therefore the instabilities are too. This results in the following simplified equation for the calculation of local N-factors

$$N_{\omega,\beta_r}(x,z) = \int_{\alpha_i=0}^{x} -\alpha_i\left(x, \omega, \beta_r\right) dx. \quad (4.29)$$

The integration path is defined by the group velocity ($\partial\beta_r/\partial\alpha_r$) direction for any given mode, which usually lies within a few degrees of the local streamline. An approximation can be made by setting the integration path as the direction of the local streamline.

4.2.3 Curvature terms

Curvature is defined as the rate of change of the direction of a curve with respect to the distance travelled along said curve. The curvature terms defined in equations 4.12a–d are in the streamline-crossflow co-ordinate system and can be split into two groups:

- κ_{xy} and κ_{zy} are associated with the geodesic curvature of the body.
- κ_{xz} and κ_{zx} are associated with accelerations of the inviscid flow on a developed plane with the surface.

The principal curvatures at a point on a surface correspond to the maximum and minimum curvatures at that point. The paths along a surface which connect all curvature maxima and minima are known as the principal directions. For an axi-symmetric body these lie in the meridional and azimuthal directions (s and θ in figure 4.2). Therefore, in order to calculate κ_{xy} and κ_{zy}, which are in the streamline direction, we can calculate the principal curvatures and rotate them by the external streamline angle, ϕ_s, where

$$\phi_s = \tan^{-1}\left(\frac{r\Omega}{u_e}\right). \quad (4.30)$$

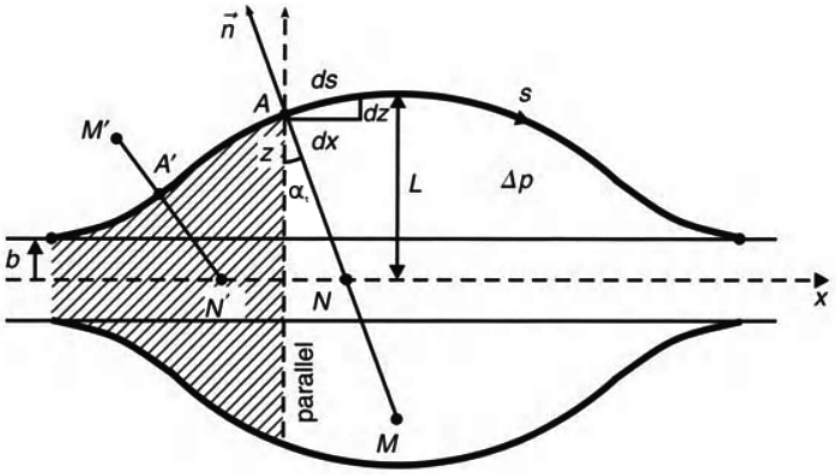

Figure 4.3: Sketch of an axi-symmetric droplet on a string of radius b and the relevant dimensions for the calculation of principal radii of curvature, from Gennes, Brochard-Wyart and Quéré (2004).

For a general body of revolution, figure 4.3, we can define

$$z = R_2 \cos\alpha_t, \qquad ds = -R_1 \, d\alpha_t, \tag{4.31}$$

where R_1 and R_2 are the principal radii of curvature in the meridional and azimuthal directions, respectively, denoted by $A - M$ and $A - N$ in figure 4.3, α_t is the angle of the local surface tangent with respect to the axis of revolution, z is the local radius from the axis of revolution and ds is the incremental meridional curvilinear length. Furthermore, in the meridional direction we can also define

$$dz = ds \sin\alpha_t, \qquad dx = ds \cos\alpha_t. \tag{4.32}$$

If we adopt the notation $\dot{z} = \partial z/\partial x$ and $\ddot{z} = \partial^2 z/\partial x^2$, we obtain

$$ds = dx\sqrt{1 + \ddot{z}^2}, \tag{4.33}$$

where it can then be shown that

$$\frac{\partial \alpha_t}{\partial s}\left(= -\frac{1}{R_1}\right) = \frac{\partial \alpha_t}{\partial x}\frac{\partial x}{\partial s} = \frac{\partial \alpha_t}{\partial x}\left(\frac{1}{\sqrt{1 + \ddot{z}^2}}\right). \tag{4.34}$$

Also, since the tangent at a point is given by $\partial z/\partial x = \tan\alpha_t$, it follows that

$$\frac{\partial^2 z}{\partial x^2} = \frac{\partial}{\partial x}(\tan\alpha_t) = \left(1 + \tan^2\alpha_t\right)\frac{\partial \alpha_t}{\partial x} = \sec^2\alpha_t \frac{\partial \alpha_t}{\partial x} \tag{4.35}$$

and therefore,

$$\ddot{z} = \frac{1}{\cos\alpha_t}\frac{\partial \alpha_t}{\partial x}, \tag{4.36}$$

or

$$\frac{\partial \alpha_t}{\partial x} = \frac{\ddot{z}}{1+\dot{z}^2}. \tag{4.37}$$

Finally, the principal radius of curvature in the meridional direction is given by

$$R_1 = -\frac{\partial s}{\partial \alpha_t} = \frac{\partial x}{\partial \alpha_t}\frac{\partial s}{\partial x} = \frac{\left(1+\dot{z}^2\right)^{3/2}}{\ddot{z}}, \tag{4.38}$$

and in the azimuthal direction

$$R_2 = \frac{z}{\cos\alpha_t} = z\sqrt{1+\dot{z}^2}. \tag{4.39}$$

As $b \longrightarrow 0$ in figure 4.3 the body of revolution develops a sharp point. In this case, it follows that at the leading edge $R_2 \longrightarrow 0$. If however we consider a simple blunt body, such as a sphere, for which it is clear that at the leading edge $R_2 = R_1$, following the above reasoning will instead result in $R_2 \longrightarrow \infty$, which is clearly incorrect. This can be resolved by employing a Taylor expansion, after which it can be shown that indeed $R_2 = R_1$ for a blunt leading edge. A full proof can be found in appendix C.5.

The principal curvatures are inversely related to the principal radii of curvature,

$$\kappa_1 = \frac{1}{R_1} \qquad \text{and} \qquad \kappa_2 = \frac{1}{R_2}. \tag{4.40}$$

Clockwise rotation of principal curvatures is achieved by employing Euler's curvature formula,

$$\kappa_{xy} = \kappa_1\cos^2\phi_s + \kappa_2\sin^2\phi_s, \tag{4.41a}$$

$$\kappa_{zy} = \kappa_1\sin^2\phi_s + \kappa_2\cos^2\phi_s. \tag{4.41b}$$

where ϕ_s is the previously defined external streamline angle.

Finally, for an axi-symmetric body the streamline curvature terms can be obtained by using numerical integration to determine the rate of change of the streamline angle with the meridional curvilinear co-ordinate, $\partial\phi_s/\partial s$, and subsequently resolving the components in the streamline and crossflow directions,

$$\kappa_{xz} = -\frac{\partial \phi_s}{\partial s}\cos\phi_s, \tag{4.42a}$$

$$\kappa_{zx} = -\frac{\partial \phi_s}{\partial s}\sin\phi_s. \tag{4.42b}$$

4.2.4 Coriolis terms

The Coriolis terms described in section 4.1.1 include angular velocity components resolved in the streamline, crossflow and wall-normal directions. In order to more easily calculate these for a rotating body of revolution it is desirable to evaluate the angular velocity components in the meridional, azimuthal and wall-normal directions and then perform a rotation. Figure 4.4 provides a sketch of the angular velocity vector which, for

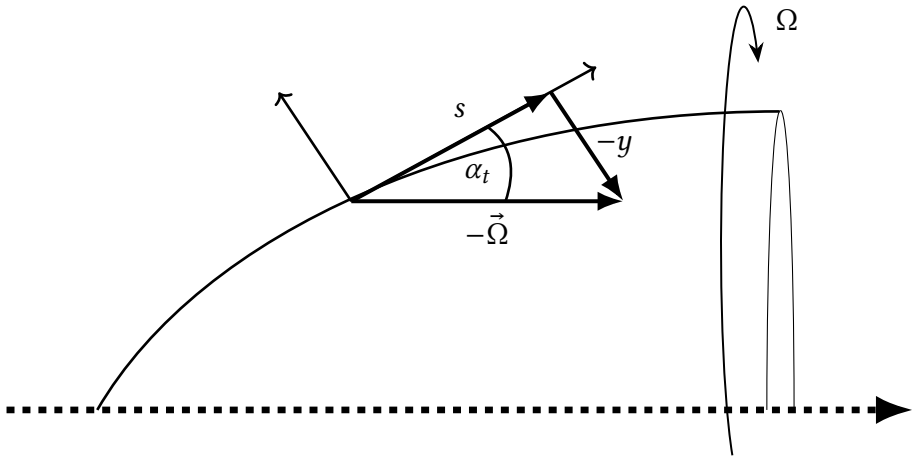

Figure 4.4: Sketch of the components of the angular velocity vector in the meridional and wall-normal directions.

an anti-clockwise rotation as seen from front, has a magnitude Ω and direction toward the leading edge, parallel to the axis of revolution. The components of this angular velocity at a point in the curvilinear meridional direction (s) are given by

$$\begin{bmatrix} \Omega_s \\ \Omega_y \\ \Omega_\theta \end{bmatrix} = -\Omega \begin{bmatrix} \cos\alpha_t \\ -\sin\alpha_t \\ 0 \end{bmatrix}, \tag{4.43}$$

where α_t is the angle of the local tangent with the axis of revolution. The clockwise rotation from the meridional and azimuthal to the streamline and crossflow directions (figure 4.1) about the wall-normal direction, y, is performed by

$$\begin{bmatrix} \Omega_x \\ \Omega_y \\ \Omega_z \end{bmatrix} = \begin{bmatrix} \cos\phi_s & 0 & \sin\phi_s \\ 0 & 1 & 0 \\ -\sin\phi_s & 0 & \cos\phi_s \end{bmatrix} \begin{bmatrix} \Omega_s \\ \Omega_y \\ \Omega_\theta \end{bmatrix}, \tag{4.44}$$

where ϕ_s is the angle between the meridional and streamline directions. The resulting components of the angular velocity are then

$$\begin{bmatrix}\Omega_x\\ \Omega_y\\ \Omega_z\end{bmatrix} = \Omega \begin{bmatrix}-\cos\alpha_t \cos\phi_s\\ \sin\alpha_t\\ \cos\alpha_t \sin\phi_s\end{bmatrix}. \tag{4.45}$$

4.2.5 Boundary layer profile manipulations

The previously derived boundary layer equations are solved in an inertial frame of reference in the meridional and azimuthal directions. Switching to a rotating frame of reference in the streamline and crossflow directions will require a series of manipulations to the resultant velocity profiles and their derivatives. Figure 4.5 depicts this progression from an inertial (a), to a rotating frame of reference (b), and finally the rotation to the streamline and crossflow directions (c). Moving from an inertial to a rotating frame of reference only necessitates the modification of the azimuthal, w, velocity. In an inertial frame of reference (as in equation 3.7b) this is initially

$$w_{\text{in}} = r\Omega g'. \tag{4.46}$$

The azimuthal velocity in a rotating frame of reference can then be obtained by inverting the wall and edge boundary conditions as follows,

$$\begin{aligned} w_{\text{rot}} &= r\Omega - w_{\text{in}} \\ &= r\Omega\,(1 - g')\,, \end{aligned} \tag{4.47}$$

where a similar transformation is carried out for the derivatives in the wall-normal co-ordinate. The velocity profiles are also re-scaled at this stage, now non-dimensionalising by the total edge velocity, Q_e (as defined in equation 4.9a–d). The final step is to rotate the velocity profiles from the meridional and azimuthal directions to the streamline and crossflow directions about the wall-normal co-ordinate. This is performed in the same manner as previously for the angular velocity components of the Coriolis terms, equation 4.44.

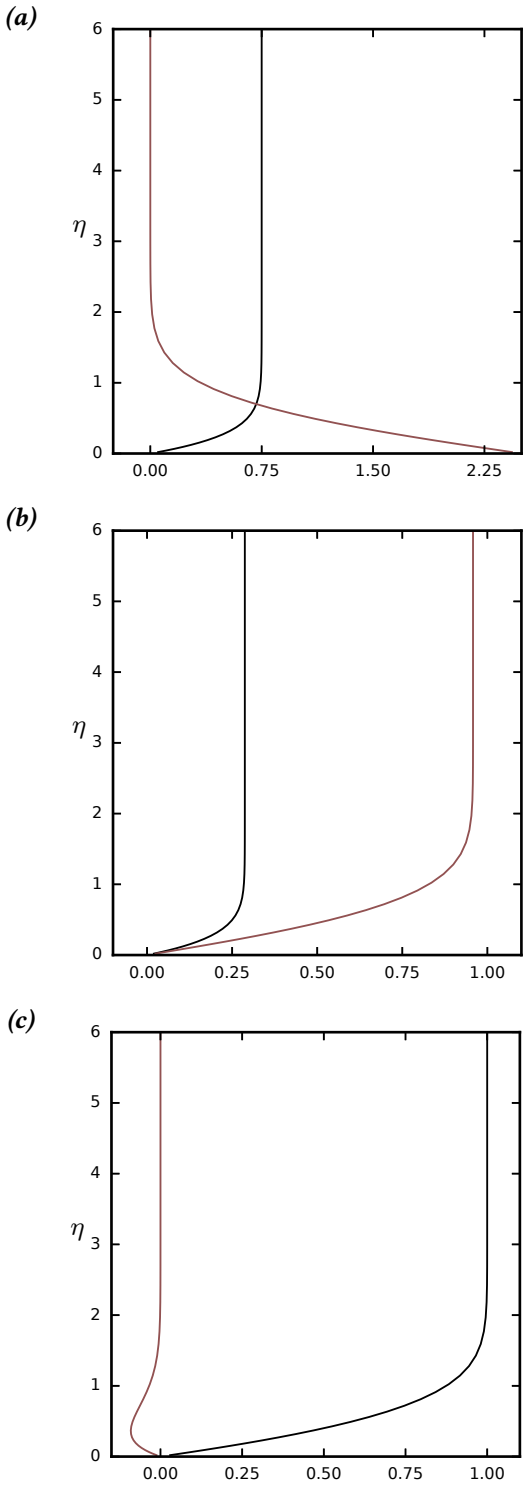

Figure 4.5: Manipulation sequence for example boundary layer profiles; *a*) u (——) and w (——) in an inertial frame of reference, *b*) u (——) and w (——) in a rotating frame of reference, *c*) rotation to streamline (——) & crossflow (——) directions.

4.3 Verification of stability equations

In order to verify the formulation of the stability equations derived in the present work, comparisons will be made with results published in the literature. As alluded to in section 1.5, there is a limited body of work on the linear stability of rotating bodies in an incompressible axial flow. Kobayashi (1981) performs a temporal analysis on a rotating cone in an axial flow, generating neutral curves and predicting vortex angles. Garrett (2002) uses a spatio-temporal method to conduct a spatial convective instability analysis on a rotating sphere and cone, both in an axial flow and in still air. Finally, Samad and Garrett (2014) investigate the convective instability on quiescent rotating spheroids. The latter is unsuitable for comparison due to the lack of agreement in boundary layer profiles with the present work, described in section 3.4.4, while the work of Kobayashi employs a temporal analysis and does not include meridional curvature, so is not ideal. The present work will therefore proceed to compare results with the work published by Garrett (2002) on the convective instability of stationary vortices on a rotating sphere in an axial flow.

The formulation of his work is set in a fixed frame of reference, removing the need for Coriolis terms, contrary to the present formulation. Due to this however, in order to investigate stationary vortices, his analysis prescribes that the vortices must rotate at a fixed multiple of the sphere surface velocity, thereby fixing the ratio ω_r/β_r, given by

$$\omega_r = c\beta_r \sin\theta_l, \tag{4.48}$$

where c is the ratio of vortex speed to the local surface velocity and θ_l is the angle of latitude measured from the equator. At lower latitudes stationary waves, using a ratio of $c = 1$, provide an accurate estimate of vortex speed, though at higher latitudes ($\theta_l > 70°$) Kobayashi and Arai (1990) found that vortices rotated at the slower speed of $c = 0.76$. As the present work is set in a rotating frame of reference, stationary waves are here obtained by dictating that $\omega = 0$. In order to more accurately predict the inviscid edge velocity of the flow around a sphere at higher latitudes, Garrett also used the following empirical relation, detailed in Fage (1936),

$$u_e(\theta_l) \approx 1.5\theta_l - 0.4371\theta_l^3 + 0.1481\theta_l^5 - 0.0423\theta_l^7, \tag{4.49}$$

where $u_e(\theta_l)$ is the edge velocity at a latitude θ_l (in radians). For this, at a single latitude of $\theta_l = 30°$, he produces a plot, figure 4.6, of stationary ($c = 1$) neutral curves for increasing T_s, the ratio between oncoming axial flow and the maximum rotational velocity,

$$T_s = \frac{u_\infty}{r_0 \Omega}, \tag{4.50}$$

where u_∞ is the axial freestream velocity, r_0 is the radius of the sphere and Ω is the angular velocity.

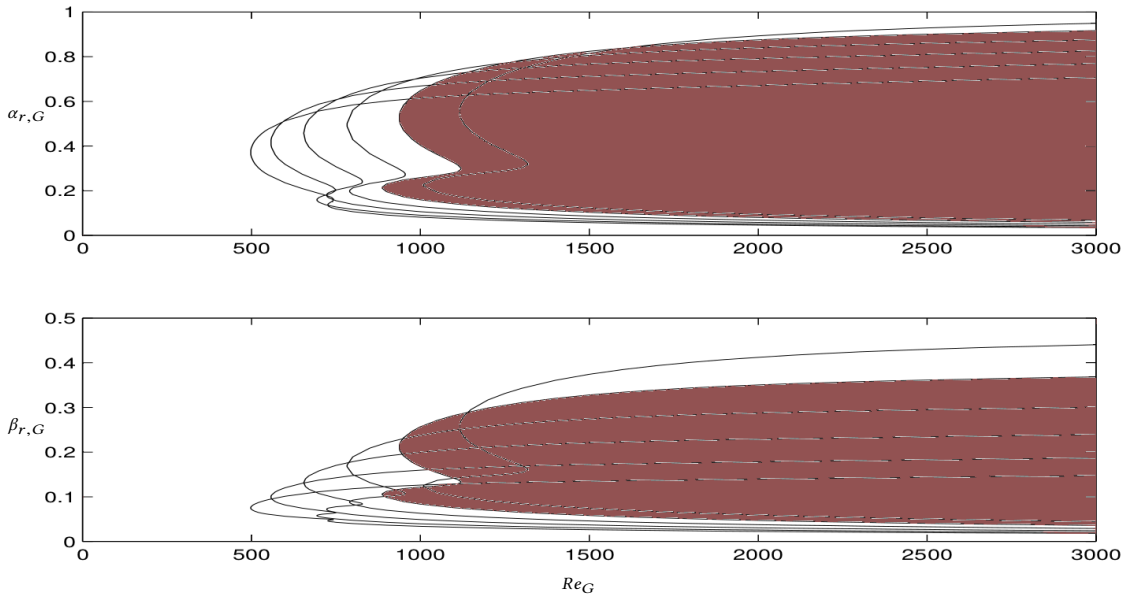

Figure 4.6: Neutral curves for the convective instability of stationary vortices on a rotating sphere in an axial flow, Garrett (2002) at $\theta_l = 30°$, $T_s = 0.0 \longrightarrow 0.25$ (left to right). Highlighted region outlines $T_s = 0.2$.

The Reynolds number used in his analysis is given by

$$Re_G = \frac{u_m \delta}{\nu} \tag{4.51}$$

where the velocity scale taken is the maximum angular velocity of the sphere and the length scale is given my the boundary layer thickness,

$$u_m = r_0 \Omega, \qquad \delta = \sqrt{\frac{\nu}{\Omega}}. \tag{4.52a,b}$$

It it worth noting that this Reynolds number does not represent a spacial progression, therefore it follows that for a fixed spherical radius and atmospheric conditions, it will depend only on the angular velocity of the sphere.

The present method is based on the engineering e^N tool CoDS, and performs its eigenvalue search by also marching in the spatial direction, described previously in section 4.2.1. Therefore, calculating a neutral curve such as in figure 4.6 requires the method to be run numerous times in order to capture the neutral points at multiple Reynolds numbers. Furthermore, the tool was designed to obtain the most amplified modes in a robust manner, with the ultimate goal of producing an N-factor distribution, and therefore will not necessarily return stationary neutral points. In order to obtain these, the method must be forced into locating them by providing initial guesses very close to neutral stability, usually within 3 significant figures for both α_r and β_r. In practice the neutral points are obtained by interpolating between both very lightly damped and amplified points.

The neutral curve for $T_s = 0.2$ (highlighted in figure 4.6) is chosen for comparison as both the upper and lower lobes, representing the inflectional crossflow and streamline-curvature instabilities respectively, are well established. In order to generate the above neutral curve using the present method the Reynolds number range must be decomposed into combinations of axial flow rate and angular velocity. Re-arranging equations 4.52a,b and 4.51 we obtain

$$\Omega = \nu \left(\frac{Re_G}{r_0} \right)^2 . \tag{4.53}$$

Assuming standard sea-level conditions (ν = 1.463E-5 $m^2 s^{-1}$) and radius $r_0 = 0.5m$, and substituting into equation 4.53, the corresponding freestream velocities and axial flow rates for the Reynolds number range given in table 4.1 can be obtained. The wavenumbers generated by the present method are in the streamline, x, and crossflow, z, directions, however the wavenumbers in figure 4.6 are in the meridional and azimuthal directions, s and θ (as in figure 4.1). To convert between the two the resultant eigenvalues are rotated in the anti-clockwise direction by the streamline angle ψ_s, given by the local external streamline direction, as in equation 4.30. This is achieved by using the standard relation for an anti-clockwise rotation

$$\beta_{r,G} = \alpha_r \sin \phi_s + \beta_r * \cos \phi_s \tag{4.54}$$

Re_G	$\Omega\ (rad\,s^{-1})$	$u_\infty\ (ms^{-1})$	Re_G	$\Omega\ (rad\,s^{-1})$	$u_\infty\ (ms^{-1})$
420	*10.33*	*1.03*	*700*	*28.69*	*2.87*
425	*10.58*	*1.06*	*715*	*29.93*	*2.99*
450	*11.86*	*1.19*	*750*	*32.93*	*3.29*
475	*13.21*	*1.32*	*800*	*37.47*	*3.75*
500	*14.64*	*1.46*	*900*	*47.42*	*4.74*
550	*17.71*	*1.77*	*1000*	*58.55*	*5.85*
600	*21.08*	*2.11*	*1200*	*84.31*	*8.43*
650	*24.74*	*2.47*	*1400*	*114.75*	*11.48*
675	*26.68*	*2.67*	*1600*	*149.88*	*14.99*
680	*27.07*	*2.71*	*1800*	*189.69*	*18.97*
688	*27.71*	*2.77*	*2000*	*234.19*	*23.42*

Table 4.1: Corresponding angular velocities and axial flow rates for a selection of Reynolds numbers assuming sea-level conditions and $r_0 = 0.5m$.

where ϕ_s is the angle between the meridional and streamline directions. The meridional wavenumber $\alpha_{r,G}$ can then be obtained by using the known constant wavenumber magnitude, k_w, between the two directions. Finally, the eigenvalues must be re-scaled by dividing by the displacement thickness, the length scale in the present method, and multiplying by δ, equations 4.52a,b.

The resulting neutral curve of interpolated, stationary eigenvalues for a sphere in an axial flow at a latitude of $\theta_l = 30°$, and velocity ratio $T_s = 0.2$, is shown in figure 4.7. Comparing this to figure 4.6 is it apparent that the results differ in magnitude, appearing more similar to the neutral curves at $\theta_l = 50°$ found in the appendix of Garrett (2002), however the general trends are preserved, with both the crossflow and streamline-curvature lobes appearing. Reasons for the discrepancies between neutral curves are attributed to some uncertainty in the conditions and boundary layer data used. Furthermore, the present method employs the parallel flow assumption within the boundary layer, where $v(s, y, \theta) = 0$. In contrast, Garrett (2002) presents a formulation in which he retains $v(y)$, arguing later that the parallel flow assumption is valid at lower latitudes, where the boundary layer is fully developed by $\eta = 5$. At higher latitudes however the effects are slightly greater with the boundary layer not being fully developed until circa $\eta = 10$.

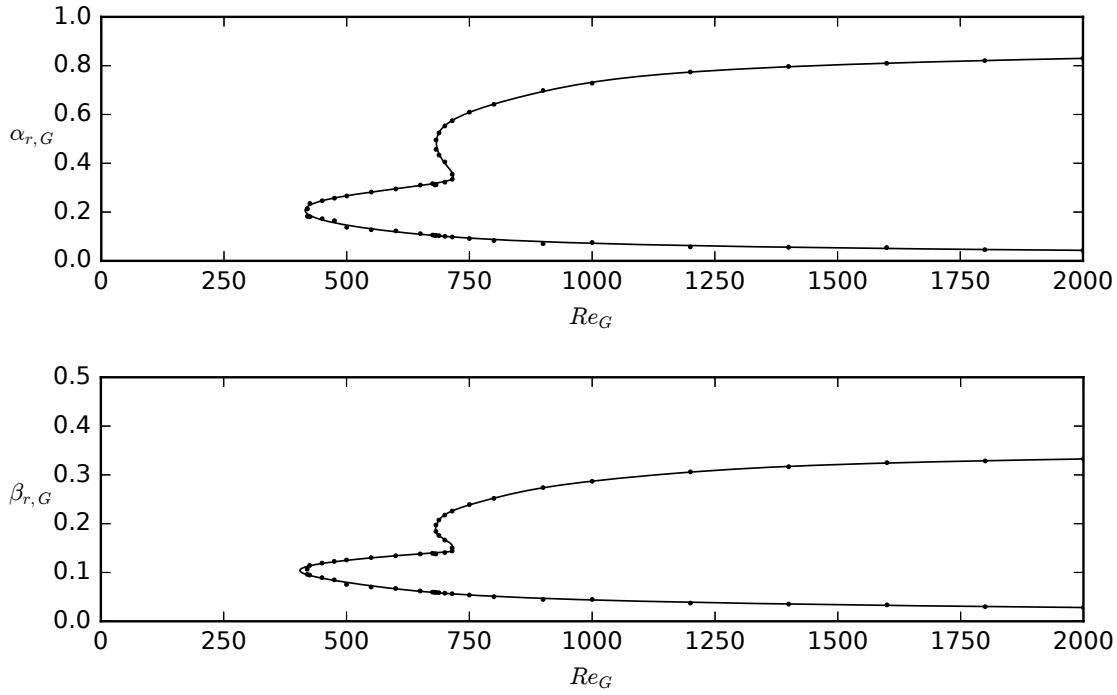

Figure 4.7: Spline-fit neutral curve for the convective instability of stationary vortices on a rotating sphere in an axial flow at $\theta_l = 30^\circ$, $T_s = 0.2$, with both geodesic and streamline curvature terms included; interpolated neutral stationary points from present work (·).

The present work includes both geodesic curvature, κ_{xy} and κ_{zy}, as well as retaining the curvature of the inviscid streamline, κ_{xz} and κ_{zx}. Figure 4.8 shows the neutral curve for the same case as presented in figure 4.7 without the inclusion of the additional inviscid streamline curvature terms. The differences are very slight, re-affirming that the flow is spanwise-invariant. Finally, the neutral curve for the case where all curvature terms are neglected is shown in figure 4.9. The resultant neutral curve tends towards the Orr-Sommerfeld solution, with the irregular features attributed to the presence of the higher-order Coriolis acceleration terms.

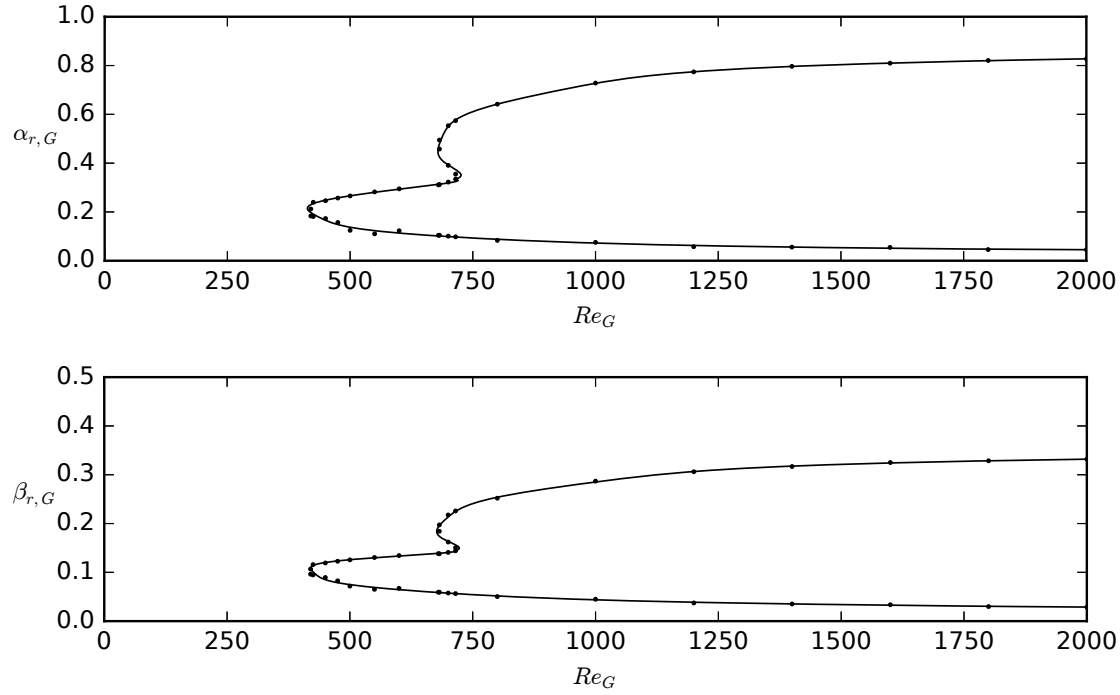

Figure 4.8: Spline-fit neutral curve for the convective instability of stationary vortices on a rotating sphere in an axial flow at $\theta_l = 30°$, $T_s = 0.2$, with only geodesic curvature terms included; interpolated neutral stationary points from present work (·).

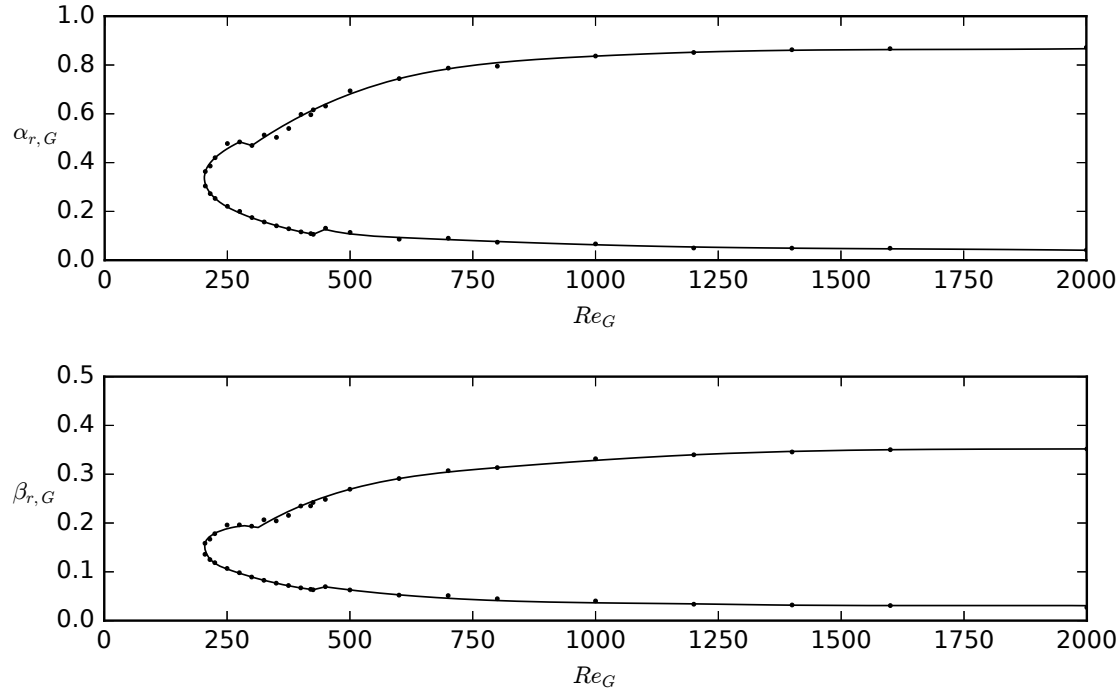

Figure 4.9: Spline-fit neutral curve for the convective instability of stationary vortices on a rotating sphere in an axial flow at $\theta_l = 30°$, $T_s = 0.2$, without curvature terms included; interpolated neutral stationary points from present work (·).

5

Growth and decay of crossflow vortices on rotating axi-symmetric bodies

Contents

In this chapter the axi-symmetric boundary layer method described in chapter 3 and the stability method described in chapter 4 are combined to investigate the stability of axi-symmetric boundary layers, in particular cases exhibiting non-monotonic growth of crossflow modes. The effects of increases in axial flow rate, angular velocity and curvature are explored. Finally, a selection of aerofoil-body shapes are analysed and non-monotonic crossflow development is discussed.

5.1 Comparison with the swept-wing boundary layer

The boundary layer due to a rotating body generates a crossflow, as detailed in section 1.5. In order to be a useful analogue to swept-wing flow there needs to be a strong similarity between the shape of the velocity profiles from a rotating body in an axial flow, and their evolution over the surface, and those on a swept-wing. Figure 5.1 compares the dimensionless velocity profiles in the streamline and crossflow directions, and their wall-normal derivatives, for a rotating prolate spheroid of eccentricity $e = 0.4$ in a $5ms^{-1}$ axial flow with a velocity ratio $T_s = 0.2$, with those on a 30°-swept NACA0012 at 0° incidence in a $10ms^{-1}$ axial flow. Both sets of velocity profiles shown here are in a region of high curvature, within 0.020 to 0.025 x/c. It can be concluded that velocity profiles on a rotating axi-symmetric body are indeed very similar to those on a swept wing, the only differences appearing in the second wall-normal derivatives.

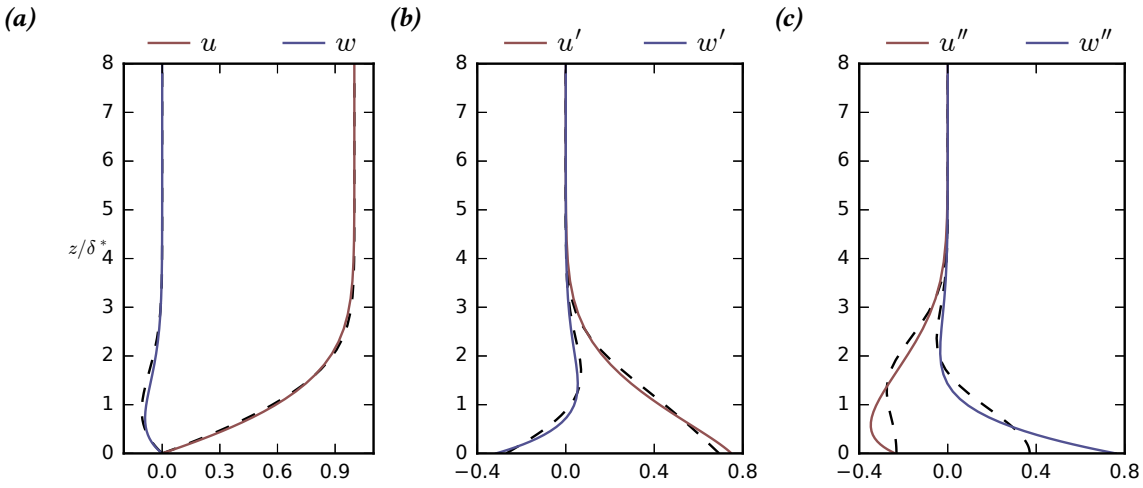

Figure 5.1: Comparisons of non-dimensional streamline and crossflow velocity profiles, and their derivatives in the wall-normal direction (denoted by a prime), for a rotating prolate spheroid, of eccentricity $e = 0.4$, in a $5ms^{-1}$ axial flow with a velocity ratio $T_s = 0.2$ (coloured lines), with those from a 30°-swept NACA0012 at 0° incidence and in a $10ms^{-1}$ axial flow (dashed lines).

5.2 Initial survey of the parameter space

To correctly identify experimental candidates capable of producing N-factor distributions similar to those shown in figure 1.7, the parameter space of the problem must first be explored and known results confirmed. Figure 5.2 presents the envelope of maximum

N-factors for a rotating sphere in an axial flow. The inviscid solution is obtained here for the sphere using the empirical relation from Fage (1936), equation 4.49, in order to better model the physical flow. The radius of the sphere is $0.5m$, while the angular velocity is $\Omega = 50s^{-1}$ and the axial flow velocity is $u_\infty = 5ms^{-1}$. The envelope, denoted by the black line, consists of the maximum N-factors at a given x/c location, for a number of individual instability modes of varying wavenumbers, wave angles and frequencies. Figure 5.3 compares the resultant envelopes of maximum N-factors for

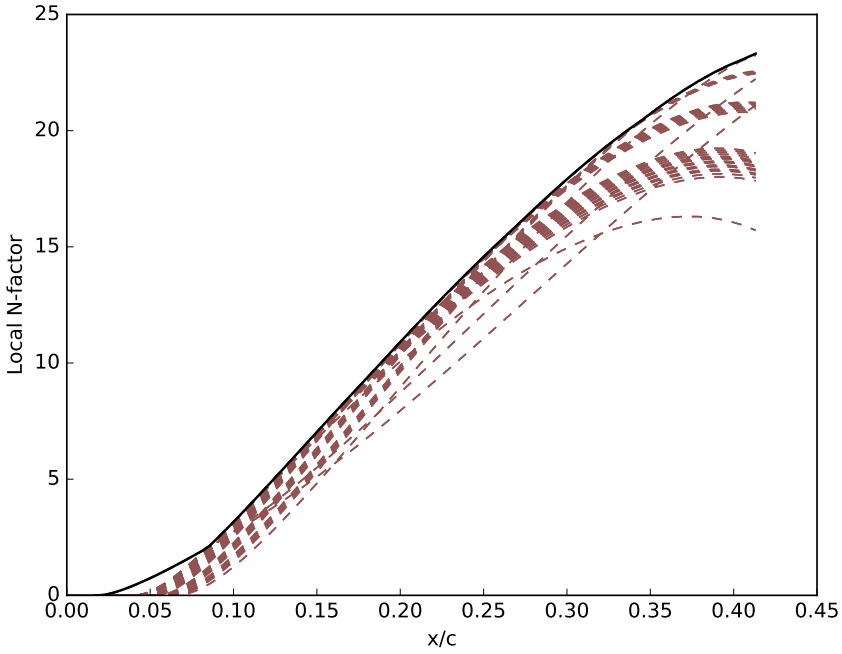

Figure 5.2: Envelope of maximum N-factors for a rotating sphere of radius $0.5m$, rotating at an angular velocity of $\Omega = 50s^{-1}$ in a $u_\infty = 5ms^{-1}$ axial flow. Constituent crossflow N-factor modes given by (——).

a rotating sphere in an increasingly large axial flow. The radius of the sphere is $0.5m$ and the angular velocity is held constant at $\Omega = 50s^{-1}$. The axial flow is increased from $u_\infty = 4 \longrightarrow 10ms^{-1}$ in steps of $1ms^{-1}$, top to bottom in figure 5.3. The result is the apparent stabilisation effect on instability growth of increased axial flow, which is in accordance with the findings of Garrett (2002) and Garrett and Peake (2004).

The effect of increased angular velocity, while maintaining a constant axial flow rate, for a sphere is shown in figure 5.4. The radius of the sphere is $0.5m$ and the axial flow velocity is held constant at $u_\infty = 5ms^{-1}$. The angular velocity is increased

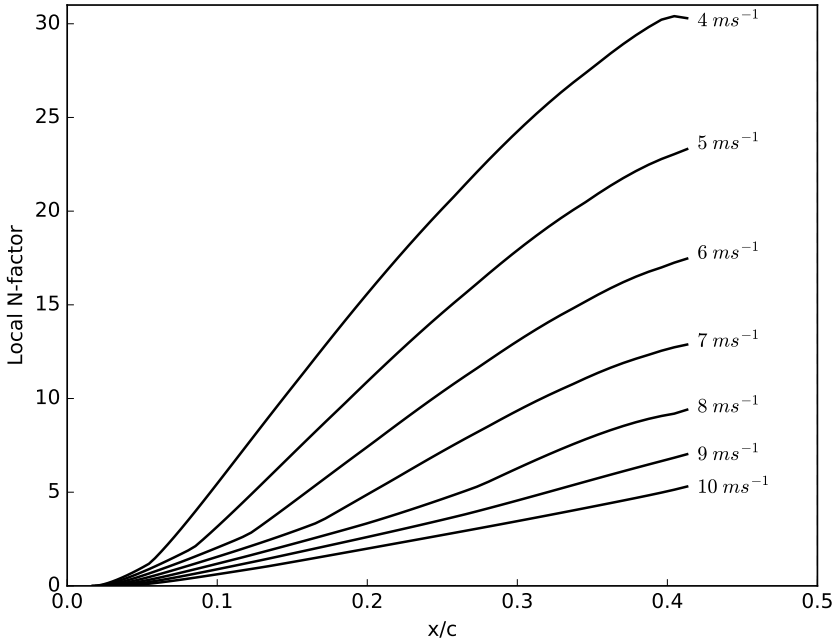

Figure 5.3: Envelopes of maximum N-factors for a rotating sphere of radius $0.5m$, rotating at an angular velocity of $\Omega = 50s^{-1}$ in an axial flow, $u_\infty = 4 \longrightarrow 10ms^{-1}$.

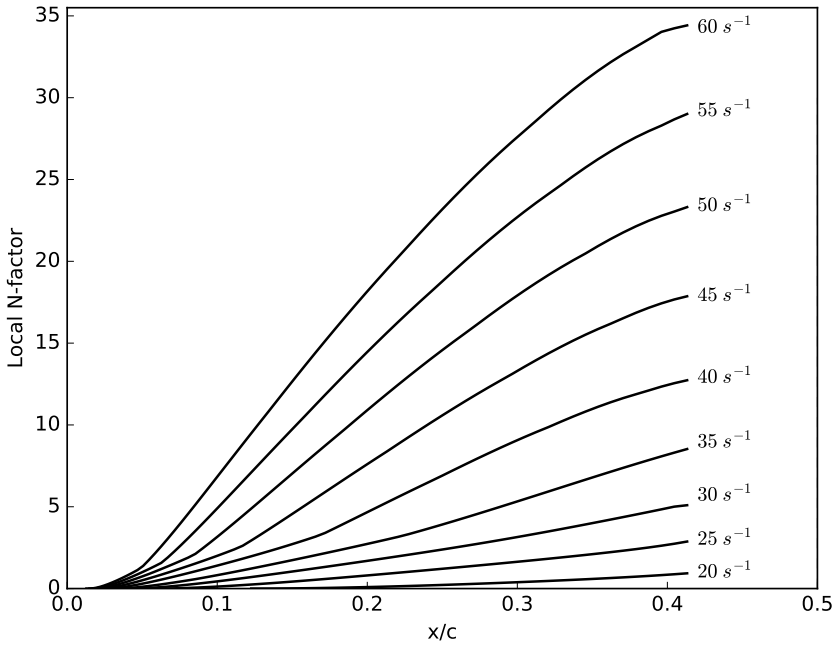

Figure 5.4: Envelopes of maximum N-factors for a rotating sphere of radius $0.5m$, in an axial flow $u_\infty = 5ms^{-1}$, rotating at an angular velocity of $\Omega = 20 \longrightarrow 60s^{-1}$.

from $\Omega = 20 \rightarrow 60s^{-1}$ in steps of $5s^{-1}$, bottom to top in figure 5.4. Again, the inviscid solution from Fage (1936) is used. Here the result is that increased angular velocity has a destabilising effect on instability growth. This follows simply from the analogy that increased rotational speed has a similar effect on crossflow velocity profiles to increased sweep angle.

Finally, the effect of increased leading edge curvature is explored by analysing the stability of prolate spheroids of increasing eccentricity in an axial flow. Figure 5.5 compares the maximum N-factor envelopes for prolate spheroids of eccentricity $e = 0.0 \rightarrow 0.8$ in steps of 0.2, in an axial flow of $u_\infty = 5ms^{-1}$ and at a constant ratio of axial flow rate to maximum circumferential velocity (where the radius is taken at the pole of the spheroid), $T_S = 0.2$. Here the inviscid solution is obtained using the axi-symmetric vortex sheet method described in section 3.3.4. The resulting trends indicate that increased leading edge curvature has a small stabilising effect on instability growth rates at low latitudes, though at higher latitudes the trends are less clear. This is

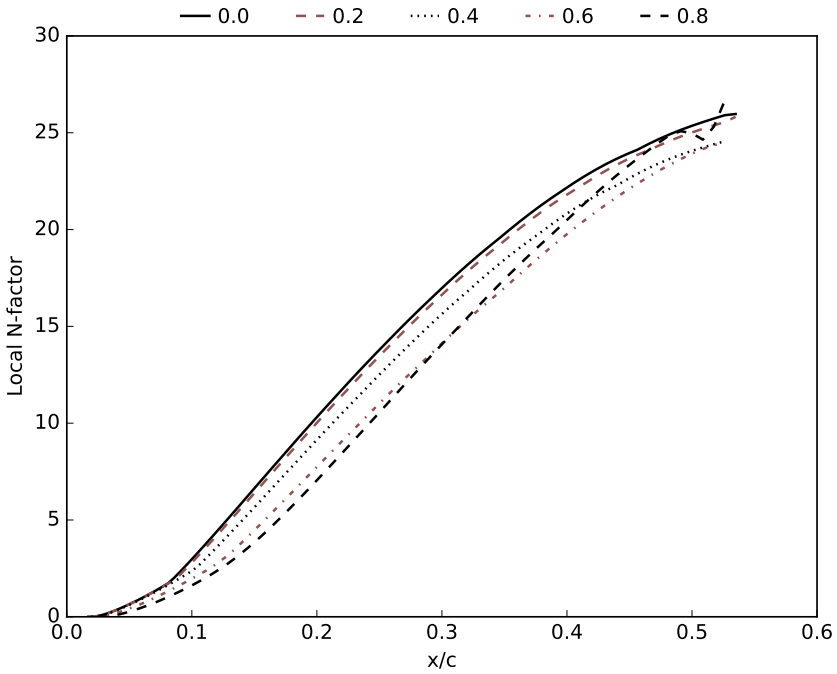

Figure 5.5: Envelopes of maximum N-factors for prolate spheroids of increasing eccentricity, $e = 0.0 \rightarrow 0.8$, in an axial flow; $T_s = 0.2, u_\infty = 5ms^{-1}$.

perhaps due to the inviscid pressure distributions, shown in figure 5.6, obtained from the

vortex sheet method. The higher eccentricity cases begin to generate higher N-factors due to the increased favourable pressures at lower latitudes.

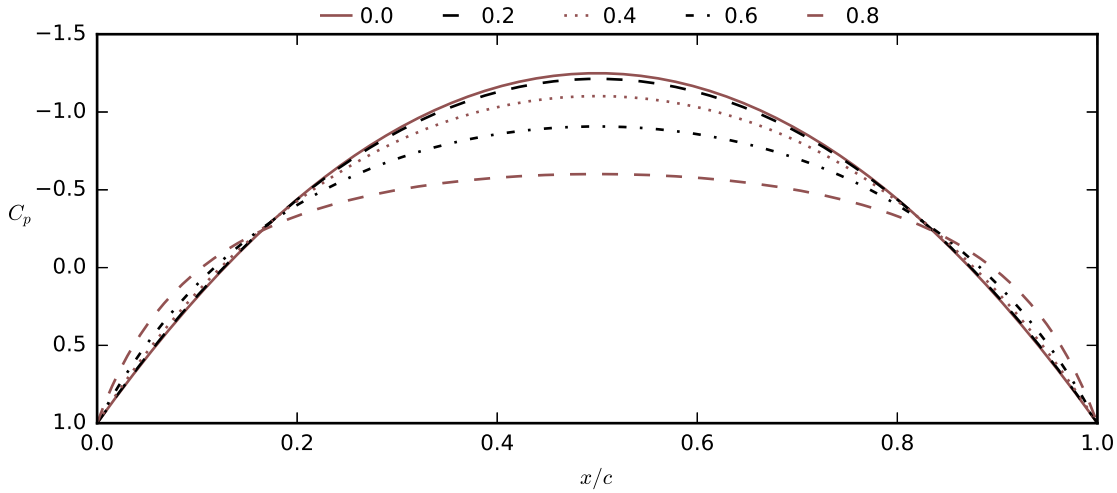

Figure 5.6: Pressure distributions generated prolate spheroids of increasing eccentricity, $e = 0.0 \longrightarrow 0.8$, in an axial flow; $T_s = 0.2, u_\infty = 5ms^{-1}$.

The N-factor envelopes for the prolate spheroids in figure 5.5 terminate shortly after the pole (at $0.5x/c$) as the boundary layer solution fails as a consequence of laminar separation due to the strong adverse pressure gradient. In order to obtain the stability characteristics shown in figure 1.7, in which crossflow growth temporarily plateaus before continuing to grow, the pressure gradients over the body must be controlled more carefully to avoid flow separation.

5.3 Axi-symmetric aerofoils

In order to avoid separation less severe pressure gradients are sought, therefore more complex shapes must be investigated. One method to rapidly analyse the characteristics of multiple shapes is by making use of 2-D aerofoils, and rotating their upper surfaces around the chord line to generate axi-symmetric bodies. Figure 5.7 shows the pressure distribution generated by an axi-symmetric body based on the NACA0010 in a $10ms^{-1}$ axial flow and rotating at $\Omega = 50s^{-1}$. Comparing this to the pressure distributions generated by the prolate spheroids in figure 5.6, it is apparent that the NACA0010 body generates its minimum pressures near the leading edge, and these are less severe than

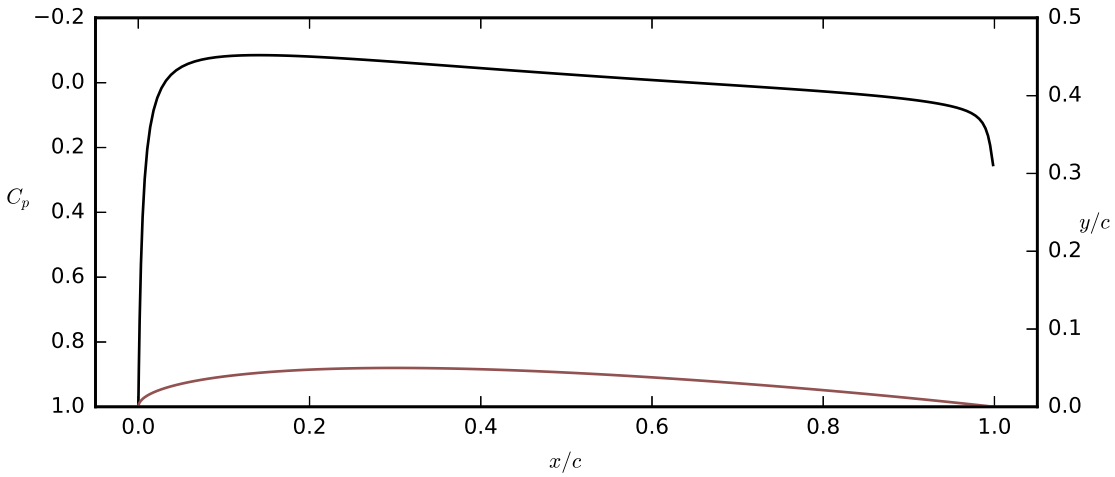

Figure 5.7: Pressure distribution generated by the axi-symmetric body based on the NACA0010 (——) in an axial flow; $u_\infty = 10ms^{-1}$, $\Omega = 50s^{-1}$.

for a prolate spheroid. The favourable pressure gradient is followed by a small roof-top, before a long constant adverse pressure gradient begins around $0.25x/c$. The result is a boundary layer that remains attached for longer after the point of maximum thickness.

Figure 5.8 compares a series of bodies, generated by rotating symmetrical NACA

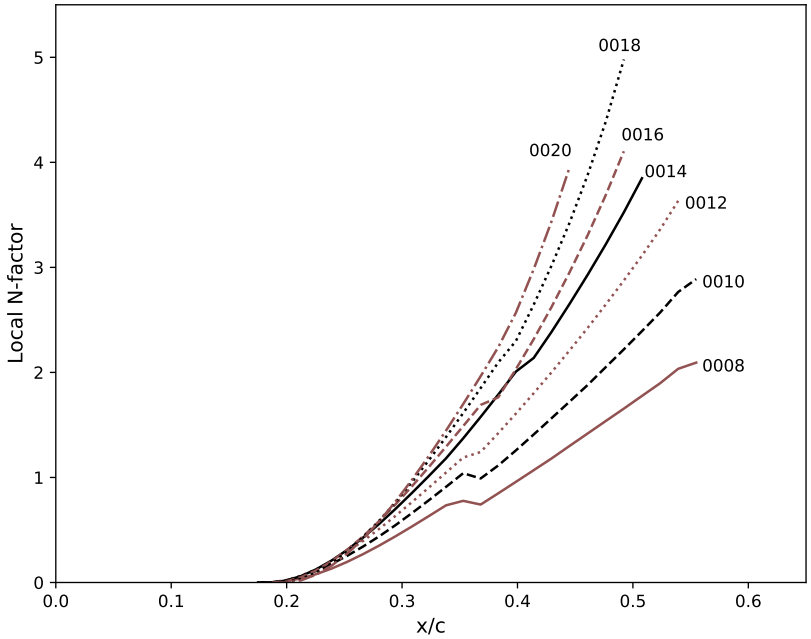

Figure 5.8: Envelopes of maximum N-factors for an axi-symmetric body generated by rotating symmetrical NACA aerofoils of increasing thickness about the chord line; $\Omega = 50s^{-1}$, $u_\infty = 10ms^{-1}$, NACA0008 → NACA0020, bottom to top.

aerofoils of increasing thickness about the chord line, ranging from NACA0008 to a NACA0020. The axial flow is kept constant at $u_\infty = 10ms^{-1}$, while the angular velocity is held at $\Omega = 50s^{-1}$. The inviscid solution is again obtained using a vortex sheet method. From this it can be observed that increasing the thickness of the NACA00XX aerofoil has a de-stabilising effect on N-factor growth, presumably due to the decreased leading edge curvature. It is interesting to note that the more slender axi-symmetric bodies, such as the one based on the NACA0008, exhibits a plateau in N-factor growth near $0.25x/c$. Figure 5.9 shows the evolution of crossflow velocity profiles in the region surrounding

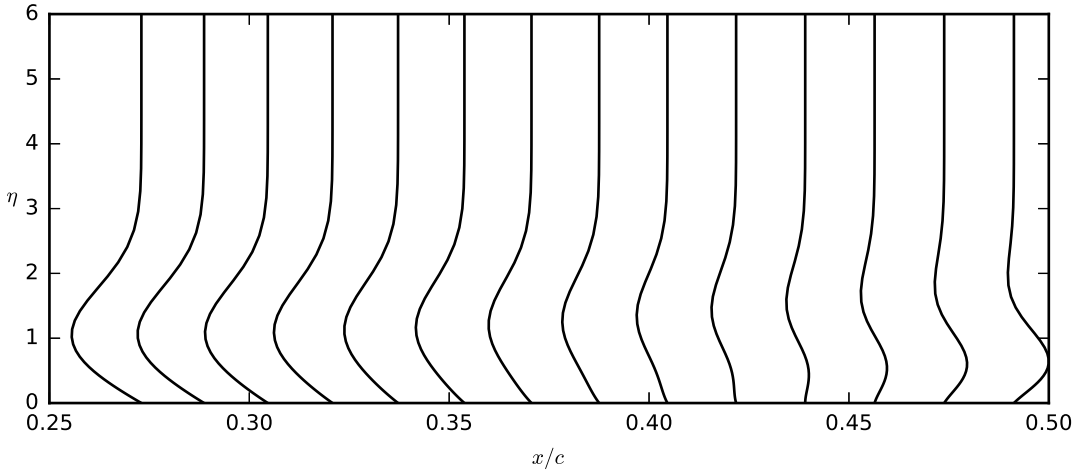

Figure 5.9: Evolution of crossflow velocity profiles in the region surrounding the plateau in maximum N-factors for the axi-symmetric body based on the NACA0010; $u_\infty = 10ms^{-1}$, $\Omega = 50s^{-1}$.

the plateau for the NACA0010. A reversal of the crossflow direction can be observed here. This reversal in crossflow direction can be attributed to the adverse change in pressure gradient, shown in figure 5.7. Furthermore, Coriolis accelerations tend towards the poles, or points of maximum thickness, so are also reversed in the aft-body region.

Transonic aerofoils, such as the RAE2822, are designed to control the position of the shock wave at transonic speeds, reducing wave drag. They generate extended regions of near-flat, favourable pressure gradients on the fore-body, before a relatively sharp recovery is allowed after the shock, shown in figure 5.10. For an incompressible axi-symmetric aerofoil, there is no shock, and the pressure gradients are significantly weaker. Figure 5.11 compares the maximum N-factor envelopes for a body generated by rotating the upper surface of an RAE2822 about the chord line, at a constant axial flow

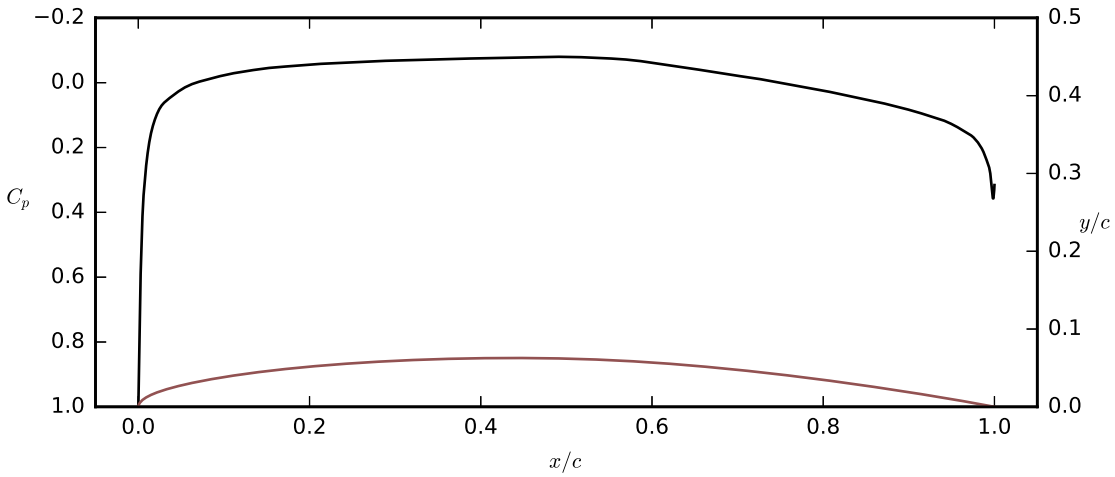

Figure 5.10: Pressure distribution generated by the axi-symmetric body based on the RAE2822 (——) in an axial flow; $u_\infty = 10ms^{-1}$, $\Omega = 45s^{-1}$.

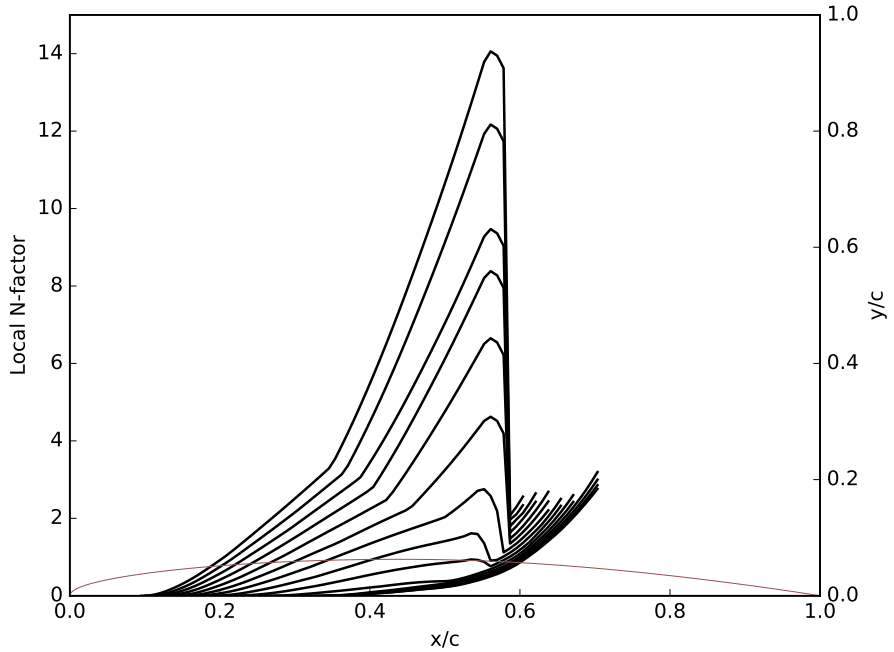

Figure 5.11: Envelopes of maximum N-factors for an axi-symmetric body generated by rotating the upper surface of an RAE2822 (——) about the chord line; $u_\infty = 10ms^{-1}$, $\Omega = 10 \longrightarrow 80s^{-1}$ in steps of $5s^{-1}$, bottom to top.

rate of $u_\infty = 10ms^{-1}$, and increasing angular velocity $\Omega = 10 \longrightarrow 80s^{-1}$ in steps of $5s^{-1}$, bottom to top. N-factor growth appears to halt rapidly in the aft-body region, greatly reducing maximum the N-factors, with growth resuming thereafter until boundary layer separation occurs.

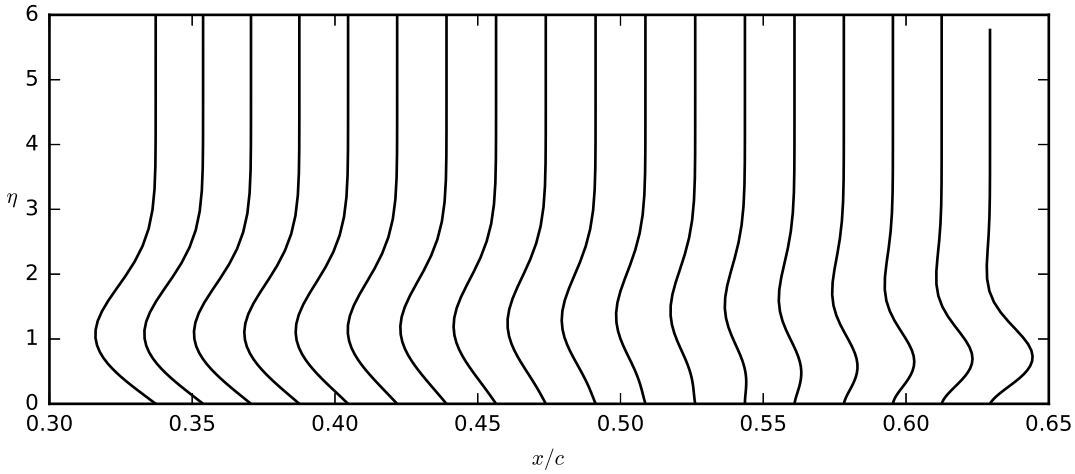

Figure 5.12: Evolution of crossflow velocity profiles in the region surrounding the sharp drop in maximum N-factors in the aft-body region of the axi-symmetric body based on the RAE2822; $u_\infty = 10ms^{-1}$, $\Omega = 45s^{-1}$.

Inspecting the crossflow velocity profiles surrounding this region for a single case, where $u_\infty = 10ms^{-1}$ and $\Omega = 45s^{-1}$, a reversal of the crossflow direction can once more be observed, with boundary layer separation occurring thereafter. Finally, examining

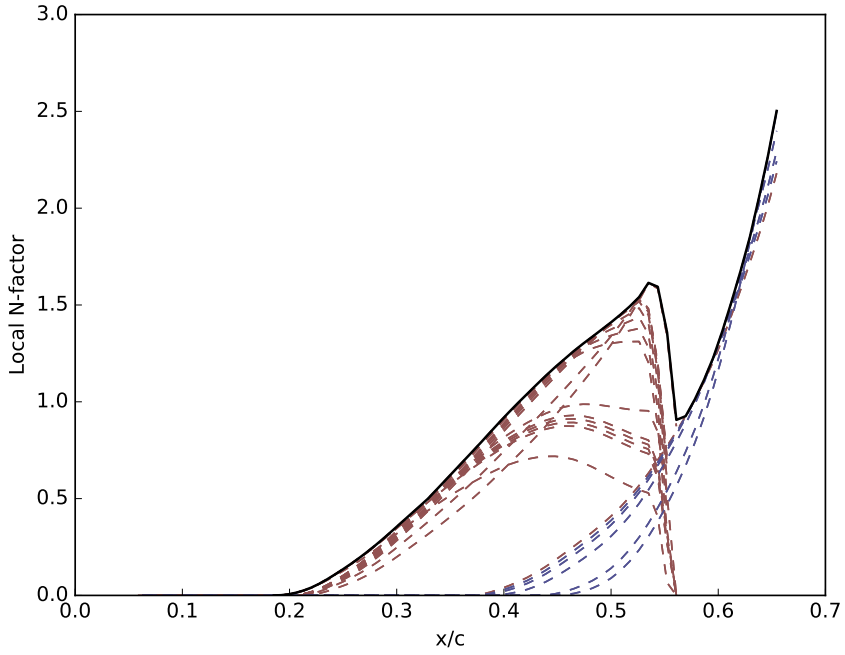

Figure 5.13: Envelope of maximum N-factors for an axi-symmetric body generated by rotating the upper surface of an RAE2822 about the chord line; $u_\infty = 10ms^{-1}$, $\Omega = 45s^{-1}$; Crossflow N-factors (——), T-S N-factors (——).

the instability modes that make up the N-factor envelope for a single case provides further insight. Figure 5.13 presents a selection of constituent modes, colour-coded red for crossflow and blue for T-S. The former, consists of low frequency ($22 \rightarrow 56Hz$) and higher spanwise wavenumbers ($595 \rightarrow 650m^{-1}$), the latter consists of higher frequency ($128 \rightarrow 136Hz$) and lower spanwise wavenumbers ($-30 \rightarrow 70m^{-1}$). The onset of the adverse pressure gradient has a strong damping effect on crossflow, while promoting the growth of T-S waves.

5.4 Experimental direction

The case presented in figure 5.11, where linear theory predicts rapid growth, followed by a sharp drop in crossflow N-factors, provides an interesting candidate for future experimentation. This case would also provide a clear analogue with the growth shown in figure 1.7, on an HLFC wing. Experimentation into the modification of local curvature could be performed in the rapid growth region, at circa $0.45x/c$, in an attempt to stem crossflow growth. Investigation in the $0.55 \rightarrow 0.60x/c$ region could also be carried out, verifying whether the prediction that amplification will simply halt is true.

The experimental assembly in section 3.1 would require modification, as the assumption previously was that the fore-body would be the focus of any investigation. An axi-symmetric RAE2822 could be mounted on a longer steel shaft, leaving the air-bearing mechanism shrouded further downstream. Localised changes in shape and curvature would still possible, albeit requiring a greater segment to be re-manufactured. Alternatively, the steel shaft could be replaced with a rigid hollow rod, allowing for a suction system to be used to control instability amplification.

6 Conclusions

Contents

6.1 Motivation

The motivation for the present work stems from studies carried out by Atkin (2004) during the EU HYLTEC project, as well as by the present author during the EU AFLoNext project, described in section 1.4. As a part of these studies, the design of laminar flow control systems to a set of N-factor thresholds were examined. The use of linear stability theory in these projects resulted in an N-factor plateau just below the chosen control N-factor. The motivation of the present work was whether the sudden damping of amplified crossflow modes predicted by linear theory was physical, and if so, whether there existed a modal amplitude beyond which the control of instability growth was no longer possible using conventional means, such as modifications to pressure gradient, curvature and using suction. An investigation into this would require precise controls on crossflow mode growth, while exploring a range of governing factors, for example

sweep and pressure gradient for an aerofoil. In order to accomplish this within the limitations of a small wind tunnel, an analogue to swept-wing flow was sought.

6.2 Summary of major findings

Using the canonical rotating disk flow as a starting point, it was postulated that the addition of a concentric annulus, rotating at a different angular velocity to the inner disk, would allow controlled changes in crossflow growth just prior to non-linear saturation. An experiment was proposed using rotating disk and annulus, and an appropriate experimental arrangement and model was devised. In conjunction to this, a novel formulation for the boundary layer a rotating disk with radially variable angular velocity was derived for application on the disk-annulus system. Ultimately, it was determined that the resultant equations were elliptical in character and therefore no longer representative of the physics of the swept-wing boundary layer. Compounding this, the experiment possessed multiple risks due to flow leakages at the disk-annulus intersection, as well as worries around balance and vibration.

In order to ensure parabolicity a configuration involving a body in an axial flow was sought. Instead of variable angular velocity, it was speculated that local variations in edge velocity, induced by the body geometry, would provide an appropriate analogue to the variable pressure gradients found in the vicinity of a swept-wing leading edge. An experiment was proposed using rotating body in an axial flow, with interchangeable nose sections to allow exploration for a range of geometries and pressure distributions.

In support of the new concept, a novel formulation for the boundary layer on a generalised rotating body of revolution, both with and without an incompressible axial flow, was derived and validated against other shape-specific formulations. The formulation employs a velocity switch, u^*, to allow for a seamless transition between quiescent and axial flow investigations. Previous work on rotating bodies required a re-formulation for shape and flow specific cases. The present formulation renders these obsolete as it encompasses every sharp- or blunt-nosed axi-symmetric body, both with and without an incompressible axial flow. The boundary layer formulation was successfully combined with an axi-symmetric vortex sheet method, providing

the inviscid edge velocity for generalised shapes in an axial flow. Modifications were also made to the QinetiQ `BL2D` boundary layer method, expanding it to enable the analysis of axi-symmetric bodies using the above formulation. Validations of the method against the literature provided close agreement for the rotating disk, cone and sphere boundary layers in both quiescent and axial flow conditions. For rotating prolate spheroids of varying eccentricity in quiescent air the agreement with published results was good at low eccentricities, though at higher eccentricities larger differences were present at higher latitudes. These were accounted for as being due to a discrepancy in the mapping of η co-ordinates.

The required stability analysis of the rotating body boundary layer necessitated the derivation of the perturbation and stability equations in a general orthogonal curvilinear co-ordinate system, to include Coriolis accelerations terms as well as retaining viscous curvature. Following this derivation, it was found that equations could be derived by performing only a limited set of modifications to the stability equations for swept-wing boundary layers. Consequently it was decided to modify an existing method, which had seen extensive verification and validation against other approaches, the QinetiQ `CoDS` e^N method. The new stability equations were then implemented within `CoDS`, expanding the capability of the code to include rotating flows. `CoDS` was primarily designed to integrate instability growth rates in order to produce N-factors, but the method was applied manually to develop neutral curves for a rotating sphere in an axial flow, which were qualitatively in good agreement with results published by Garrett (2002), although there were significant quantitative differences. These were attributed mainly to scaling, though based on prior experience of verification of stability analysis tools from the principal investigator, a sustained collaborative effort with Garrett, or other authors in the field, would be required to isolate the sources of the differences.

The methods developed above were combined in order to answer the original research question, whether the boundary layer due to a rotating body could be used as a viable analogue for swept-wing flow in the context of crossflow growth control. Velocity profiles for rotating axi-symmetric bodies were shown to provide a good match to those of swept-wing flow, with differences only in the second wall-normal derivatives.

Initial analysis of increased axial flow rate over a sphere rotating at constant angular velocity confirmed the stabilising effect described by Garrett and Peake (2004). Increased angular velocity at constant axial flow rate was found to be de-stabilising in turn. The N-factor distributions for rotating prolate spheroids of varying eccentricities in an axial flow displayed a small stabilising at lower latitudes, attributed to increased leading edge curvature. For higher eccentricities, changes in the early pressure distribution led in fact to increased instability growth.

An investigation into more complex axi-symmetric shapes, created by rotating the upper surface of an aerofoil about the chord line, was carried out. The aim was to control pressure gradients sufficiently to ensure a prolonged attached flow, allowing for the interaction of a weaker adverse pressure gradient on the aft-body. The results showed that geometries could be selected which demonstrated non-monotonic N-factor growth, of the type encountered during HYLTEC and AFLoNext. An axi-symmetric body derived from the upper surface of the RAE2822 demonstrated N-factor amplification followed by sudden stabilisation.

In summary, the main contributions to the body of knowledge of the work are

- A novel formulation for the boundary layer due to a rotating disk with radially variable angular velocity.
- A novel formulation for the boundary layer due to a rotating generalised axi-symmetric body, both in quiescent air and an incompressible axial flow.
- An initial stability analysis into the N-factor amplification of a number of rotating axi-symmetric bodies in an axial flow.
- The realisation of a research opportunity to achieve large scale variations in crossflow amplification rates at scales suitable for university wind tunnels.

Personal highlights and achievements include extensive exposure to software development using `C++`, `Fortran` and `Python`, as well as the object-oriented programming ideology. An insight into the timescales and multitude of possible problems encountered during software development, and how to debug them, was also garnered. Finally, during my year-long hiatus from my doctoral studies whilst working on the European AFLoNext project, I experienced international collaborative design efforts and the resulting design compromises arising from competing systems work-groups.

6.3 Recommendations for future work

The preliminary investigation into axi-symmetric bodies in an axial flow has clearly suggested candidate geometries for future experimentation, with only minor modifications to the originally devised experiment. Further work would be necessary to obtain an N-factor distribution exhibiting more gradual change from growth to decay. A future experiment could then determine the validity of linear amplification theory in these conditions and provide further insight into the real tolerances required for laminar flow control systems. Furthermore, the boundary layer formulation for a generalised body of revolution, presented in chapter 3, could be used to continue investigation into the absolute instability on other geometries. Employing a stability method better suited to the generation of neutral curves is however suggested.

Appendices

A

Rotating disk & annulus

Contents

A.1 Derivation of boundary layer equations

The continuity and N-S equations for an axially-symmetric, incompressible flow in a cylindrical co-ordinate system are

$$\frac{\partial}{\partial r}(ru) + \frac{\partial}{\partial y}(rv) = 0 \tag{A.1}$$

$$u\frac{\partial u}{\partial r} + v\frac{\partial u}{\partial y} - \frac{w^2}{r} = -\frac{1}{\rho}\frac{\partial P}{\partial r} + \nu\left[\frac{\partial^2 u}{\partial r^2} + \frac{\partial}{\partial r}\left(\frac{u}{r}\right) + \frac{\partial^2 u}{\partial y^2}\right] \tag{A.2a}$$

$$u\frac{\partial v}{\partial r} + v\frac{\partial v}{\partial y} = -\frac{1}{\rho}\frac{\partial P}{\partial y} + \nu\left[\frac{\partial^2 v}{\partial r^2} + \frac{1}{r}\frac{\partial v}{\partial r} + \frac{\partial^2 v}{\partial y^2}\right] \tag{A.2b}$$

$$u\frac{\partial w}{\partial r} + \frac{uw}{r} + v\frac{\partial w}{\partial y} = \nu\left[\frac{\partial^2 w}{\partial r^2} + \frac{\partial}{\partial r}\left(\frac{w}{r}\right) + \frac{\partial^2 w}{\partial y^2}\right] \tag{A.2c}$$

where u, v, w are velocity components in the directions of increasing r, y and θ. In a fixed frame of reference these are subject to the boundary conditions

$$u = v = w - r\Omega = 0 \qquad \text{at} \quad y = 0 \tag{A.3a}$$

$$u = w = 0 \qquad \text{as} \quad y \to \infty. \tag{A.3b}$$

A two-component stream function is defined

$$u = k\frac{\partial \psi}{\partial y}, \quad v = -k\frac{\partial \psi}{\partial r}, \quad w = k\frac{\partial \phi}{\partial y}, \tag{A.4a–c}$$

where k is a yet undefined common factor and ψ & ϕ are defined as functions of dimensionless stream functions f and g,

$$\psi = U_d L_\xi \, f(\xi, \eta), \qquad \phi = U_d L_\xi \, g(\xi, \eta), \tag{A.5a,b}$$

wherein L_ξ and U_d are a length and velocity scale, respectively. Using the continuity equation (A.1) we can now determine the common factor k,

$$\begin{aligned}
u + r\frac{\partial u}{\partial r} + r\frac{\partial v}{\partial y} &= 0 \\
kUL\frac{\partial f}{\partial y} + r\frac{\partial}{\partial r}\left(kUL\frac{\partial f}{\partial y}\right) + r\frac{\partial}{\partial y}\left(-k\frac{\partial}{\partial r}[ULf]\right) &= 0 \\
kUL\frac{\partial f}{\partial y} + r\frac{\partial}{\partial r}\left(kUL\frac{\partial f}{\partial y}\right) - kr\frac{\partial}{\partial r}\left(UL\frac{\partial f}{\partial y}\right) &= 0 \\
kUL\frac{\partial f}{\partial y} + r\frac{\partial k}{\partial r}UL\frac{\partial f}{\partial y} &= 0 \\
k + r\frac{\partial k}{\partial r} &= 0 \\
k = \frac{A}{r} &= \frac{r_0}{r}
\end{aligned} \tag{A.6}$$

where r_0 is an arbitrary reference length. Re-inserting into equations A.4a–c the stream functions then become

$$u = \frac{r_0}{r}\frac{\partial \psi}{\partial y}, \quad v = -\frac{r_0}{r}\frac{\partial \psi}{\partial r}, \quad w = \frac{r_0}{r}\frac{\partial \phi}{\partial y}. \tag{A.7a–c}$$

In order to match Benton (1966) we set the length and velocity scales as

$$L_\xi = \frac{r^2}{r_0}, \qquad U_d = \sqrt{\Omega \nu}, \tag{A.8a,b}$$

and define a right-handed co-ordinate system in which

$$\eta \;=\; y\sqrt{\frac{\Omega}{\nu}}, \qquad \xi \;=\; r. \tag{A.9a,b}$$

Substituting these transformations into equations A.7, ultimately yields our form of the von Kármán similarity transforms for both the velocity field and pressure for a rotating disk where Ω varies with radial position,

$$u = \xi\Omega, \qquad w = \xi\Omega g', \qquad P = -\rho\nu\Omega p, \tag{A.10a–c}$$

$$\begin{aligned} v &= -\left[\sqrt{\Omega\nu}\xi\frac{\partial f}{\partial\xi} + \sqrt{\frac{\nu}{\Omega}}\eta\frac{\xi}{2}\frac{\partial\Omega}{\partial\xi}f' + \sqrt{\frac{\nu}{\Omega}}\frac{\xi}{2}\frac{\partial\Omega}{\partial\xi}f + 2\sqrt{\Omega\nu}f\right] \\ &= -2\sqrt{\Omega\nu}f - \xi\sqrt{\Omega\nu}\left[\frac{\partial f}{\partial\xi} - \frac{1}{2\Omega}\frac{\partial\Omega}{\partial\xi}(\eta f' + f)\right] \end{aligned} \tag{A.10d}$$

where a prime denotes differentiation with respect to η. Inserting equations A.10a–d into the u-momentum equation (A.2a) results in

$$\begin{aligned} u\frac{\partial u}{\partial r} &= \xi\Omega f'\left[\Omega f' + \xi\frac{\partial\Omega}{\partial\xi}f' + \xi\Omega\frac{\partial f'}{\partial\xi} + \xi\Omega f''\frac{\eta}{2\Omega}\frac{\partial\Omega}{\partial\xi}\right] \\ v\frac{\partial u}{\partial y} &= -\left[\sqrt{\Omega\nu}\xi\frac{\partial f}{\partial\xi} + \sqrt{\frac{\nu}{\Omega}}\eta\frac{\xi}{2}\frac{\partial\Omega}{\partial\xi}f' + \sqrt{\frac{\nu}{\Omega}}\frac{\xi}{2}\frac{\partial\Omega}{\partial\xi}f + 2\sqrt{\Omega\nu}f\right]\xi\Omega f''\sqrt{\frac{\Omega}{\nu}} \\ -\frac{w^2}{r} &= -\xi\Omega^2 g'^2 \\ -\frac{1}{\rho}\frac{\partial P}{\partial r} &= -\frac{1}{\rho}\left[-\rho\nu\frac{\partial\Omega}{\partial\xi}p - \rho\nu\Omega\frac{\partial p}{\partial\xi} - \rho\nu\Omega p'\frac{\eta}{2\Omega}\frac{\partial\Omega}{\partial\xi}\right]\nu\frac{\partial^2 u}{\partial r^2} \\ &= \nu\left[\frac{\partial\Omega}{\partial\xi}f' + \Omega\frac{\partial f'}{\partial\xi} + \frac{\partial\Omega}{\partial\xi}f' + \xi\frac{\partial^2\Omega}{\partial\xi^2}f' + \xi\frac{\partial\Omega}{\partial\xi}\frac{\partial f'}{\partial\xi} + \Omega\frac{\partial f'}{\partial\xi} + \xi\frac{\partial\Omega}{\partial\xi}\frac{\partial f'}{\partial\xi}\right. \\ &\quad + \xi\Omega\frac{\partial^2 f'}{\partial\xi^2} + \left[\Omega f'' + \xi\frac{\partial\Omega}{\partial\xi}f'' + \xi\Omega\frac{\partial f''}{\partial\xi}\right]\frac{\eta}{\Omega}\frac{\partial\Omega}{\partial\xi} + \xi\Omega f''\frac{\eta}{2\Omega}\frac{\partial^2\Omega}{\partial\xi^2} \\ &\quad \left. + \xi\Omega f'''\frac{\eta^2}{4\Omega^2}\left(\frac{\partial\Omega}{\partial\xi}\right)^2 - \xi\Omega f''\frac{\eta}{4\Omega^2}\left(\frac{\partial\Omega}{\partial\xi}\right)^2\right] \\ \nu\frac{\partial}{\partial r}\left(\frac{u}{r}\right) &= \nu\left[\frac{\partial\Omega}{\partial\xi}f' + \Omega\frac{\partial f'}{\partial\xi} + \Omega f''\frac{\eta}{2\Omega}\frac{\partial\Omega}{\partial\xi}\right] \\ \nu\frac{\partial^2 u}{\partial y^2} &= \xi\Omega^2 f'''. \end{aligned} \tag{A.11a–g}$$

Combining and dividing by $\xi\Omega^2$ yields the final form of the u-momentum equation

$$\begin{aligned}
&f''' + 2ff'' - f'^2 + g'^2 - \frac{\xi}{\Omega}\frac{\partial\Omega}{\partial\xi}f'^2 - \xi\frac{\partial f'}{\partial\xi}f' + \xi f''\frac{\partial f}{\partial\xi} + \frac{\xi}{2\Omega}\frac{\partial\Omega}{\partial\xi}ff'' \\
&+ \nu\left[\frac{1}{\xi\Omega^2}\frac{\partial\Omega}{\partial\xi}p + \frac{1}{\xi\Omega}\frac{\partial p}{\partial\xi} + \eta\frac{1}{2\xi\Omega^2}\frac{\partial\Omega}{\partial\xi}p' + \frac{3}{\xi\Omega^2}\frac{\partial\Omega}{\partial\xi}f' + \frac{3}{\xi\Omega}\frac{\partial f'}{\partial\xi} + \frac{1}{\Omega^2}\frac{\partial^2\Omega}{\partial\xi^2}f'\right. \\
&+ \frac{2}{\Omega^2}\frac{\partial\Omega}{\partial\xi}\frac{\partial f'}{\partial\xi} + \frac{1}{\Omega}\frac{\partial^2 f'}{\partial\xi^2} + \eta\frac{3}{2\xi\Omega^2}\frac{\partial\Omega}{\partial\xi}f'' + \eta\frac{3}{4\Omega^3}\left(\frac{\partial\Omega}{\partial\xi}\right)^2 f'' + \eta\frac{1}{\Omega^2}\frac{\partial\Omega}{\partial\xi}\frac{\partial f''}{\partial\xi} \\
&\left.+ \eta\frac{1}{2\Omega^2}\frac{\partial^2\Omega}{\partial\xi^2}f'' + \eta^2\frac{1}{4\Omega^3}\left(\frac{\partial\Omega}{\partial\xi}\right)^2 f'''\right] = 0
\end{aligned} \tag{A.12}$$

Similarly, inserting equations A.10a–d into the w-momentum equation (A.2c) results in

$$\begin{aligned}
u\frac{\partial w}{\partial r} &= \xi\Omega f'\left[\Omega g' + \xi\frac{\partial\Omega}{\partial\xi}g' + \xi\Omega\frac{\partial g'}{\partial\xi} + \xi g''\frac{\eta}{2}\frac{\partial\Omega}{\partial\xi}\right] \\
\frac{uw}{r} &= \xi\Omega^2 f'g' \\
v\frac{\partial w}{\partial y} &= -\left[\sqrt{\Omega\nu}\xi\frac{\partial f}{\partial\xi} + \sqrt{\frac{\nu}{\Omega}}\eta\frac{\xi}{2}\frac{\partial\Omega}{\partial\xi}f' + \sqrt{\frac{\nu}{\Omega}}\frac{\xi}{2}\frac{\partial\Omega}{\partial\xi}f + 2\sqrt{\Omega\nu}f\right]\xi\Omega g''\sqrt{\frac{\Omega}{\nu}} \\
\nu\frac{\partial^2 w}{\partial r^2} &= \nu\left[\frac{\partial\Omega}{\partial\xi}g' + \Omega\frac{\partial g'}{\partial\xi} + \frac{\partial\Omega}{\partial\xi}g' + \xi\frac{\partial^2\Omega}{\partial\xi^2}g' + \xi\frac{\partial\Omega}{\partial\xi}\frac{\partial g'}{\partial\xi} + \Omega\frac{\partial g'}{\partial\xi}\right. \\
&\quad + \xi\frac{\partial\Omega}{\partial\xi}\frac{\partial g'}{\partial\xi} + \xi\Omega\frac{\partial^2 g'}{\partial\xi^2} + \left[\Omega g'' + \xi\frac{\partial\Omega}{\partial\xi}g'' + \xi\Omega\frac{\partial g''}{\partial\xi}\right]\frac{\eta}{\Omega}\frac{\partial\Omega}{\partial\xi} \\
&\quad \left. + \xi\Omega g''\frac{\eta}{2\Omega}\frac{\partial^2\Omega}{\partial\xi^2} + \xi\Omega g'''\frac{\eta^2}{4\Omega^2}\left(\frac{\partial\Omega}{\partial\xi}\right)^2 - \xi\Omega g''\frac{\eta}{4\Omega^2}\left(\frac{\partial\Omega}{\partial\xi}\right)^2\right] \\
\nu\frac{\partial}{\partial r}\left(\frac{w}{r}\right) &= \nu\left[\frac{\partial\Omega}{\partial\xi}g' + \Omega\frac{\partial g'}{\partial\xi} + \Omega g''\frac{\eta}{2\Omega}\frac{\partial\Omega}{\partial\xi}\right] \\
\nu\frac{\partial^2 w}{\partial y^2} &= \nu\left[\xi\Omega g'''\frac{\Omega}{\nu}\right].
\end{aligned} \tag{A.13a–f}$$

Combining and dividing by $\xi\Omega^2$ yields the final form of the w-momentum equation

$$\begin{aligned}
&g''' + 2fg'' - 2f'g' - \frac{\xi}{\Omega}\frac{\partial\Omega}{\partial\xi}f'g' - \xi\frac{\partial g'}{\partial\xi}f' + \xi\frac{\partial f}{\partial\xi}g'' + \frac{\xi}{2\Omega}\frac{\partial\Omega}{\partial\xi}fg'' \\
&+ \nu\left[\frac{3}{\xi\Omega^2}\frac{\partial\Omega}{\partial\xi}g' + \frac{3}{\xi\Omega}\frac{\partial g'}{\partial\xi} + \frac{1}{\Omega^2}\frac{\partial^2\Omega}{\partial\xi^2}g' + \frac{2}{\Omega^2}\frac{\partial\Omega}{\partial\xi}\frac{\partial g'}{\partial\xi} + \frac{1}{\Omega}\frac{\partial^2 g'}{\partial\xi^2} + \eta\frac{3}{2\xi\Omega^2}\frac{\partial\Omega}{\partial\xi}g''\right. \\
&\left. + \eta\frac{3}{4\Omega^3}\left(\frac{\partial\Omega}{\partial\xi}\right)^2 g'' + \eta\frac{1}{\Omega^2}\frac{\partial\Omega}{\partial\xi}\frac{\partial g''}{\partial\xi} + \eta\frac{1}{2\Omega^2}\frac{\partial^2\Omega}{\partial\xi^2}g'' + \eta^2\frac{1}{4\Omega^3}\left(\frac{\partial\Omega}{\partial\xi}\right)^2 g'''\right] = 0
\end{aligned} \tag{A.14}$$

Finally, inserting equations A.10a–d into the v-momentum equation (A.2b) results in

$$
\begin{aligned}
u\frac{\partial v}{\partial r} &= \xi\Omega f'\Bigg[-\sqrt{\frac{\nu}{\Omega}}\frac{\xi}{2}\frac{\partial f}{\partial \xi}\frac{\partial \Omega}{\partial \xi} - \sqrt{\Omega\nu}\frac{\partial f}{\partial \xi} - \sqrt{\Omega\nu}\xi\frac{\partial^2 f}{\partial \xi^2} + \sqrt{\frac{\nu}{\Omega}}\eta\frac{\xi}{4\Omega}\left(\frac{\partial \Omega}{\partial \xi}\right)^2 f' \\
&\quad - \sqrt{\frac{\nu}{\Omega}}\eta\frac{1}{2}\frac{\partial \Omega}{\partial \xi}f' - \sqrt{\frac{\nu}{\Omega}}\eta\frac{\xi}{2}\frac{\partial^2 \Omega}{\partial \xi^2}f' - \sqrt{\frac{\nu}{\Omega}}\eta\frac{\xi}{2}\frac{\partial \Omega}{\partial \xi}\frac{\partial f'}{\partial \xi} + \sqrt{\frac{\nu}{\Omega}}\frac{\xi}{4\Omega}\left(\frac{\partial \Omega}{\partial \xi}\right)^2 f \\
&\quad - \sqrt{\frac{\nu}{\Omega}}\frac{1}{2}\frac{\partial \Omega}{\partial \xi}f - \sqrt{\frac{\nu}{\Omega}}\frac{\xi}{2}\frac{\partial^2 \Omega}{\partial \xi^2}f - \sqrt{\frac{\nu}{\Omega}}\frac{\xi}{2}\frac{\partial \Omega}{\partial \xi}\frac{\partial f}{\partial \xi} - \sqrt{\frac{\nu}{\Omega}}\frac{\partial \Omega}{\partial \xi}f - 2\sqrt{\Omega\nu}\frac{\partial f}{\partial \xi} \\
&\quad - \sqrt{\Omega\nu}\xi\frac{\partial f'}{\partial \xi}\frac{\eta}{2\Omega}\frac{\partial \Omega}{\partial \xi} - \sqrt{\frac{\nu}{\Omega}}\eta\frac{\xi}{2}\frac{\partial \Omega}{\partial \xi}f''\frac{\eta}{2\Omega}\frac{\partial \Omega}{\partial \xi} - \sqrt{\frac{\nu}{\Omega}}\frac{\xi}{2}\frac{\partial \Omega}{\partial \xi}f'\frac{\eta}{2\Omega}\frac{\partial \Omega}{\partial \xi} \\
&\quad - 2\sqrt{\Omega\nu}f'\frac{\eta}{2\Omega}\frac{\partial \Omega}{\partial \xi}\Bigg] \\
v\frac{\partial v}{\partial y} &= \left[\sqrt{\Omega\nu}\xi\frac{\partial f}{\partial \xi} + \sqrt{\frac{\nu}{\Omega}}\eta\frac{\xi}{2}\frac{\partial \Omega}{\partial \xi}f' + \sqrt{\frac{\nu}{\Omega}}\frac{\xi}{2}\frac{\partial \Omega}{\partial \xi}f + 2\sqrt{\Omega\nu}f\right]\Bigg[-\sqrt{\Omega\nu}\xi\frac{\partial f'}{\partial \xi} \\
&\quad + \sqrt{\frac{\nu}{\Omega}}\eta\frac{\xi}{2}\frac{\partial \Omega}{\partial \xi}f'' + \sqrt{\frac{\nu}{\Omega}}\frac{\xi}{2}\frac{\partial \Omega}{\partial \xi}f' + 2\sqrt{\Omega\nu}f'\Bigg]\sqrt{\frac{\Omega}{\nu}} \\
-\frac{1}{\rho}\frac{\partial P}{\partial y} &= \nu\Omega p'\sqrt{\frac{\Omega}{\nu}} \\
\nu\frac{1}{r}\frac{\partial v}{\partial r} &= -\nu\Bigg[\sqrt{\frac{\nu}{\Omega}}\frac{1}{2}\frac{\partial f}{\partial \xi}\frac{\partial \Omega}{\partial \xi} + \frac{1}{\xi}\sqrt{\Omega\nu}\frac{\partial f}{\partial \xi} + \sqrt{\Omega\nu}\frac{\partial^2 f}{\partial \xi^2} - \sqrt{\frac{\nu}{\Omega}}\eta\frac{1}{4\Omega}\left(\frac{\partial \Omega}{\partial \xi}\right)^2 f' \\
&\quad + \sqrt{\frac{\nu}{\Omega}}\eta\frac{1}{2\xi}\frac{\partial \Omega}{\partial \xi}f' + \sqrt{\frac{\nu}{\Omega}}\eta\frac{1}{2}\frac{\partial^2 \Omega}{\partial \xi^2}f' + \sqrt{\frac{\nu}{\Omega}}\eta\frac{1}{2}\frac{\partial \Omega}{\partial \xi}\frac{\partial f'}{\partial \xi} - \sqrt{\frac{\nu}{\Omega}}\frac{1}{4\Omega}\left(\frac{\partial \Omega}{\partial \xi}\right)^2 f \\
&\quad + \sqrt{\frac{\nu}{\Omega}}\frac{1}{2\xi}\frac{\partial \Omega}{\partial \xi}f + \sqrt{\frac{\nu}{\Omega}}\frac{1}{2}\frac{\partial^2 \Omega}{\partial \xi^2}f + \sqrt{\frac{\nu}{\Omega}}\frac{1}{2}\frac{\partial \Omega}{\partial \xi}\frac{\partial f}{\partial \xi} + \sqrt{\frac{\nu}{\Omega}}\frac{1}{\xi}\frac{\partial \Omega}{\partial \xi}f \\
&\quad + 2\sqrt{\Omega\nu}\frac{1}{\xi}\frac{\partial f}{\partial \xi} + \sqrt{\Omega\nu}\frac{\partial f'}{\partial \xi}\frac{\eta}{2\Omega}\frac{\partial \Omega}{\partial \xi} + \sqrt{\frac{\nu}{\Omega}}\eta\frac{1}{2}\frac{\partial \Omega}{\partial \xi}f''\frac{\eta}{2\Omega}\frac{\partial \Omega}{\partial \xi} \\
&\quad + \sqrt{\frac{\nu}{\Omega}}\frac{1}{2}\frac{\partial \Omega}{\partial \xi}f'\frac{\eta}{2\Omega}\frac{\partial \Omega}{\partial \xi} + 2\sqrt{\Omega\nu}f'\frac{\eta}{2\xi\Omega}\frac{\partial \Omega}{\partial \xi} \\
&\quad + \left[\sqrt{\Omega\nu}\frac{\partial f'}{\partial \xi} + \sqrt{\frac{\nu}{\Omega}}\eta\frac{1}{2}\frac{\partial \Omega}{\partial \xi}f'' + \sqrt{\frac{\nu}{\Omega}}\frac{1}{2}\frac{\partial \Omega}{\partial \xi}f' + 2\sqrt{\Omega\nu}\frac{1}{\xi}f'\right]\frac{\eta}{2\Omega}\frac{\partial \Omega}{\partial \xi}\Bigg] \\
\nu\frac{\partial^2 v}{\partial y^2} &= -\Omega\left[\sqrt{\Omega\nu}\xi\frac{\partial f''}{\partial \xi} + \sqrt{\frac{\nu}{\Omega}}\eta\frac{\xi}{2}\frac{\partial \Omega}{\partial \xi}f''' + \sqrt{\frac{\nu}{\Omega}}\frac{\xi}{2}\frac{\partial \Omega}{\partial \xi}f'' + 2\sqrt{\Omega\nu}f''\right]
\end{aligned}
\tag{A.15a-e}
$$

$$
\begin{aligned}
\nu\frac{\partial^2 v}{\partial r^2} = \nu\Bigg[& \sqrt{\frac{\nu}{\Omega}}\frac{\xi}{4\Omega}\frac{\partial f}{\partial\xi}\left(\frac{\partial\Omega}{\partial\xi}\right)^2 - \sqrt{\frac{\nu}{\Omega}}\frac{1}{2}\frac{\partial f}{\partial\xi}\frac{\partial\Omega}{\partial\xi} - \sqrt{\frac{\nu}{\Omega}}\frac{\xi}{2}\frac{\partial^2 f}{\partial\xi^2}\frac{\partial\Omega}{\partial\xi} - \sqrt{\frac{\nu}{\Omega}}\frac{\xi}{2}\frac{\partial f}{\partial\xi}\frac{\partial^2\Omega}{\partial\xi^2} \\
& - \sqrt{\frac{\nu}{\Omega}}\frac{1}{2}\frac{\partial f}{\partial\xi}\frac{\partial\Omega}{\partial\xi} - \sqrt{\Omega\nu}\frac{\partial^2 f}{\partial\xi^2} - \sqrt{\frac{\nu}{\Omega}}\frac{1}{2}\xi\frac{\partial^2 f}{\partial\xi^2}\frac{\partial\Omega}{\partial\xi} - \sqrt{\Omega\nu}\frac{\partial^2 f}{\partial\xi^2} - \sqrt{\Omega\nu}\xi\frac{\partial^3 f}{\partial\xi^3} \\
& - \sqrt{\frac{\nu}{\Omega}}\eta\frac{\xi}{8\Omega^2}\left(\frac{\partial\Omega}{\partial\xi}\right)^3 f' + \sqrt{\frac{\nu}{\Omega}}\eta\frac{1}{4\Omega}\left(\frac{\partial\Omega}{\partial\xi}\right)^2 f' - \sqrt{\frac{\nu}{\Omega}}\eta\frac{\xi}{4\Omega^2}\left(\frac{\partial\Omega}{\partial\xi}\right)^3 f' \\
& + \sqrt{\frac{\nu}{\Omega}}\eta\frac{\xi}{2\Omega}\frac{\partial\Omega}{\partial\xi}\frac{\partial^2\Omega}{\partial\xi^2} f' + \sqrt{\frac{\nu}{\Omega}}\eta\frac{\xi}{4\Omega}\left(\frac{\partial\Omega}{\partial\xi}\right)^2\frac{\partial f'}{\partial\xi} + \sqrt{\frac{\nu}{\Omega}}\eta\frac{1}{4\Omega}\left(\frac{\partial\Omega}{\partial\xi}\right)^2 f' \\
& - \sqrt{\frac{\nu}{\Omega}}\eta\frac{1}{2}\frac{\partial^2\Omega}{\partial\xi^2} f' - \sqrt{\frac{\nu}{\Omega}}\eta\frac{1}{2}\frac{\partial\Omega}{\partial\xi}\frac{\partial f'}{\partial\xi} + \sqrt{\frac{\nu}{\Omega}}\eta\frac{\xi}{4\Omega}\frac{\partial\Omega}{\partial\xi}\frac{\partial^2\Omega}{\partial\xi^2} f' - \sqrt{\frac{\nu}{\Omega}}\eta\frac{1}{2}\frac{\partial^2\Omega}{\partial\xi^2} f' \\
& - \sqrt{\frac{\nu}{\Omega}}\eta\frac{\xi}{2}\frac{\partial^3\Omega}{\partial\xi^3} f' - \sqrt{\frac{\nu}{\Omega}}\eta\frac{\xi}{2}\frac{\partial^2\Omega}{\partial\xi^2}\frac{\partial f'}{\partial\xi} + \sqrt{\frac{\nu}{\Omega}}\eta\frac{\xi}{4\Omega}\left(\frac{\partial\Omega}{\partial\xi}\right)^2\frac{\partial f'}{\partial\xi} - \sqrt{\frac{\nu}{\Omega}}\eta\frac{1}{2}\frac{\partial\Omega}{\partial\xi}\frac{\partial f'}{\partial\xi} \\
& - \sqrt{\frac{\nu}{\Omega}}\eta\frac{\xi}{2}\frac{\partial^2\Omega}{\partial\xi^2}\frac{\partial f'}{\partial\xi} - \sqrt{\frac{\nu}{\Omega}}\eta\frac{\xi}{2}\frac{\partial\Omega}{\partial\xi}\frac{\partial^2 f'}{\partial\xi^2} - \sqrt{\frac{\nu}{\Omega}}\frac{\xi}{8\Omega^2}\left(\frac{\partial\Omega}{\partial\xi}\right)^3 f + \sqrt{\frac{\nu}{\Omega}}\frac{1}{4\Omega}\left(\frac{\partial\Omega}{\partial\xi}\right)^2 f \\
& - \sqrt{\frac{\nu}{\Omega}}\frac{\xi}{4\Omega^2}\left(\frac{\partial\Omega}{\partial\xi}\right)^3 f + \sqrt{\frac{\nu}{\Omega}}\frac{\xi}{2\Omega}\frac{\partial\Omega}{\partial\xi}\frac{\partial^2\Omega}{\partial\xi^2} f + \sqrt{\frac{\nu}{\Omega}}\frac{\xi}{4\Omega}\left(\frac{\partial\Omega}{\partial\xi}\right)^2\frac{\partial f}{\partial\xi} \\
& + \sqrt{\frac{\nu}{\Omega}}\frac{1}{4\Omega}\left(\frac{\partial\Omega}{\partial\xi}\right)^2 f - \sqrt{\frac{\nu}{\Omega}}\frac{1}{2}\frac{\partial^2\Omega}{\partial\xi^2} f - \sqrt{\frac{\nu}{\Omega}}\frac{1}{2}\frac{\partial\Omega}{\partial\xi}\frac{\partial f}{\partial\xi} + \sqrt{\frac{\nu}{\Omega}}\frac{\xi}{4\Omega}\frac{\partial\Omega}{\partial\xi}\frac{\partial^2\Omega}{\partial\xi^2} f \\
& - \sqrt{\frac{\nu}{\Omega}}\frac{1}{2}\frac{\partial^2\Omega}{\partial\xi^2} f - \sqrt{\frac{\nu}{\Omega}}\frac{\xi}{2}\frac{\partial^3\Omega}{\partial\xi^3} f - \sqrt{\frac{\nu}{\Omega}}\frac{\xi}{2}\frac{\partial^2\Omega}{\partial\xi^2}\frac{\partial f}{\partial\xi} + \sqrt{\frac{\nu}{\Omega}}\frac{\xi}{4\Omega}\left(\frac{\partial\Omega}{\partial\xi}\right)^2\frac{\partial f}{\partial\xi} \\
& - \sqrt{\frac{\nu}{\Omega}}\frac{1}{2}\frac{\partial\Omega}{\partial\xi}\frac{\partial f}{\partial\xi} - \sqrt{\frac{\nu}{\Omega}}\frac{\xi}{2}\frac{\partial^2\Omega}{\partial\xi^2}\frac{\partial f}{\partial\xi} - \sqrt{\frac{\nu}{\Omega}}\frac{\xi}{2}\frac{\partial\Omega}{\partial\xi}\frac{\partial^2 f}{\partial\xi^2} + \sqrt{\frac{\nu}{\Omega}}\frac{1}{2\Omega}\left(\frac{\partial\Omega}{\partial\xi}\right)^2 f \\
& - \sqrt{\frac{\nu}{\Omega}}\frac{\partial^2\Omega}{\partial\xi^2} f - \sqrt{\frac{\nu}{\Omega}}\frac{\partial\Omega}{\partial\xi}\frac{\partial f}{\partial\xi} - \sqrt{\frac{\nu}{\Omega}}\frac{\partial\Omega}{\partial\xi}\frac{\partial f}{\partial\xi} - 2\sqrt{\Omega\nu}\frac{\partial^2 f}{\partial\xi^2} \\
& - \Bigg[\sqrt{\frac{\nu}{\Omega}}\frac{\xi}{2}\frac{\partial f'}{\partial\xi}\frac{\partial\Omega}{\partial\xi} + \sqrt{\Omega\nu}\frac{\partial f'}{\partial\xi} + \sqrt{\Omega\nu}\xi\frac{\partial^2 f'}{\partial\xi^2} - \sqrt{\frac{\nu}{\Omega}}\eta\frac{\xi}{4\Omega}\left(\frac{\partial\Omega}{\partial\xi}\right)^2 f'' \\
& + \sqrt{\frac{\nu}{\Omega}}\eta\frac{1}{2}\frac{\partial\Omega}{\partial\xi} f'' + \sqrt{\frac{\nu}{\Omega}}\eta\frac{\xi}{2}\frac{\partial^2\Omega}{\partial\xi^2} f'' + \sqrt{\frac{\nu}{\Omega}}\eta\frac{\xi}{2}\frac{\partial\Omega}{\partial\xi}\frac{\partial f''}{\partial\xi} - \sqrt{\frac{\nu}{\Omega}}\frac{\xi}{4\Omega}\left(\frac{\partial\Omega}{\partial\xi}\right)^2 f' \\
& + \sqrt{\frac{\nu}{\Omega}}\frac{1}{2}\frac{\partial\Omega}{\partial\xi} f' + \sqrt{\frac{\nu}{\Omega}}\frac{\xi}{2}\frac{\partial^2\Omega}{\partial\xi^2} f' + \sqrt{\frac{\nu}{\Omega}}\frac{\xi}{2}\frac{\partial\Omega}{\partial\xi}\frac{\partial f'}{\partial\xi} + \sqrt{\frac{\nu}{\Omega}}\frac{\partial\Omega}{\partial\xi} f' + 2\sqrt{\Omega\nu}\frac{\partial f'}{\partial\xi}\Bigg]\frac{\eta}{\Omega}\frac{\partial\Omega}{\partial\xi} \\
& - \left[\sqrt{\Omega\nu}\xi\frac{\partial f'}{\partial\xi} + \sqrt{\frac{\nu}{\Omega}}\eta\frac{\xi}{2}\frac{\partial\Omega}{\partial\xi} f'' + \sqrt{\frac{\nu}{\Omega}}\frac{\xi}{2}\frac{\partial\Omega}{\partial\xi} f' + 2\sqrt{\Omega\nu} f'\right]\frac{\eta}{2\Omega}\frac{\partial^2\Omega}{\partial\xi^2} \\
& - \left[\sqrt{\Omega\nu}\xi\frac{\partial f''}{\partial\xi} + \sqrt{\frac{\nu}{\Omega}}\eta\frac{\xi}{2}\frac{\partial\Omega}{\partial\xi} f''' + \sqrt{\frac{\nu}{\Omega}}\frac{\xi}{2}\frac{\partial\Omega}{\partial\xi} f'' + 2\sqrt{\Omega\nu} f''\right]\frac{\eta^2}{4\Omega^2}\left(\frac{\partial\Omega}{\partial\xi}\right)^2 \\
& + \left[\sqrt{\Omega\nu}\xi\frac{\partial f'}{\partial\xi} + \sqrt{\frac{\nu}{\Omega}}\eta\frac{\xi}{2}\frac{\partial\Omega}{\partial\xi} f'' + \sqrt{\frac{\nu}{\Omega}}\frac{\xi}{2}\frac{\partial\Omega}{\partial\xi} f' + 2\sqrt{\Omega\nu} f'\right]\frac{\eta}{4\Omega^2}\left(\frac{\partial\Omega}{\partial\xi}\right)^2\Bigg].
\end{aligned}
\tag{A.15f}
$$

Combining and dividing by $\xi\Omega^2$ yields the final form of the v-momentum equation

$$
\begin{aligned}
&p' - 4ff' - 2f'' + \frac{\xi^2}{2\Omega}\frac{\partial f}{\partial \xi}\frac{\partial \Omega}{\partial \xi}f' + \xi\frac{\partial f}{\partial \xi}f' + \xi^2\frac{\partial^2 f}{\partial \xi^2}f' + \eta\frac{\xi}{2\Omega}\frac{\partial \Omega}{\partial \xi}f'f' \\
&+ \eta\frac{\xi^2}{2\Omega}\frac{\partial^2 \Omega}{\partial \xi^2}f'f' + \eta\frac{\xi^3}{2}\frac{\partial \Omega}{\partial \xi}\frac{\partial f'}{\partial \xi}f'f' - \frac{\xi^2}{2\Omega^2}\left(\frac{\partial \Omega}{\partial \xi}\right)^2 ff' - \frac{\xi}{2\Omega}\frac{\partial \Omega}{\partial \xi}ff' \\
&+ \frac{\xi^2}{2\Omega}\frac{\partial^2 \Omega}{\partial \xi^2}ff' - \xi^2\frac{\partial f}{\partial \xi}\frac{\partial f'}{\partial \xi} - \eta\frac{\xi^2}{2\Omega}\frac{\partial \Omega}{\partial \xi}\frac{\partial f}{\partial \xi}f'' - \eta\frac{\xi^2}{4\Omega^2}\left(\frac{\partial \Omega}{\partial \xi}\right)^2 f'f' \\
&- \frac{\xi^2}{2\Omega}\frac{\partial \Omega}{\partial \xi}\frac{\partial f'}{\partial \xi}f - \eta\frac{\xi^2}{4\Omega^2}\left(\frac{\partial \Omega}{\partial \xi}\right)^2 ff'' - 2\xi\frac{\partial f'}{\partial \xi}f - \eta\frac{\xi}{\Omega}\frac{\partial \Omega}{\partial \xi}ff'' \\
&+ \nu\Bigg[\frac{3\xi}{4\Omega^3}\left(\frac{\partial \Omega}{\partial \xi}\right)^2\frac{\partial f}{\partial \xi} - \frac{5}{\Omega^2}\frac{\partial \Omega}{\partial \xi}\frac{\partial f}{\partial \xi} - \frac{3\xi}{2\Omega^2}\frac{\partial \Omega}{\partial \xi}\frac{\partial^2 f}{\partial \xi^2} - \frac{3\xi}{2\Omega^2}\frac{\partial^2 \Omega}{\partial \xi^2}\frac{\partial f}{\partial \xi} \\
&- \frac{5}{\Omega}\frac{\partial^2 f}{\partial \xi^2} - \frac{\xi}{\Omega}\frac{\partial^3 f}{\partial \xi^3} + \eta\frac{1}{2\Omega^3}\left(\frac{\partial \Omega}{\partial \xi}\right)^2 f' - \eta\frac{5}{2\Omega^2}\frac{\partial^2 \Omega}{\partial \xi^2}f' - \eta\frac{9}{2\Omega^2}\frac{\partial \Omega}{\partial \xi}\frac{\partial f'}{\partial \xi} \\
&- \eta\frac{\xi}{2\Omega^2}\frac{\partial^3 \Omega}{\partial \xi^3}f' - \eta\frac{3\xi}{2\Omega^2}\frac{\partial^2 \Omega}{\partial \xi^2}\frac{\partial f'}{\partial \xi} - \eta\frac{3\xi}{2\Omega^2}\frac{\partial \Omega}{\partial \xi}\frac{\partial^2 f'}{\partial \xi^2} - \frac{3\xi}{8\Omega^4}\left(\frac{\partial \Omega}{\partial \xi}\right)^3 f \\
&+ \frac{5}{4\Omega^3}\left(\frac{\partial \Omega}{\partial \xi}\right)^2 f - \frac{1}{2\Omega^2}\frac{\partial^2 \Omega}{\partial \xi^2}f + \frac{3\xi}{4\Omega^3}\frac{\partial \Omega}{\partial \xi}\frac{\partial^2 \Omega}{\partial \xi^2}f - \frac{2}{\Omega^2}\frac{\partial^2 \Omega}{\partial \xi^2}f - \frac{\xi}{2\Omega^2}\frac{\partial^3 \Omega}{\partial \xi^3}f \\
&- \eta^2\frac{3}{2\Omega^3}\left(\frac{\partial \Omega}{\partial \xi}\right)^2 f'' - \eta^2\frac{3\xi}{4\Omega^3}\frac{\partial \Omega}{\partial \xi}\frac{\partial^2 \Omega}{\partial \xi^2}f'' - \eta^2\frac{3\xi}{4\Omega^3}\left(\frac{\partial \Omega}{\partial \xi}\right)^2\frac{\partial f''}{\partial \xi} \\
&- \eta^3\frac{\xi}{8\Omega^4}\left(\frac{\partial \Omega}{\partial \xi}\right)^3 f''' - \eta^2\frac{\xi}{2\Omega^4}\left(\frac{\partial \Omega}{\partial \xi}\right)^3 f'' - \eta\frac{\xi}{4\Omega^3}\left(\frac{\partial \Omega}{\partial \xi}\right)^2\frac{\partial f'}{\partial \xi} - \frac{3}{\xi\Omega}\frac{\partial f}{\partial \xi} \\
&- \eta\frac{5}{2\xi\Omega^2}\frac{\partial \Omega}{\partial \xi}f' - \frac{3}{2\xi\Omega^2}\frac{\partial \Omega}{\partial \xi}f - \frac{\xi}{\nu}\frac{\partial f''}{\partial \xi} - \eta\frac{\xi}{2\Omega\nu}\frac{\partial \Omega}{\partial \xi}f''' - \frac{\xi}{2\Omega\nu}\frac{\partial \Omega}{\partial \xi}f''\Bigg] = 0
\end{aligned}
\tag{A.16}
$$

A.2 Tabulated disk solution at constant omega

η	f	g	f'	g'	$P - P_0$
0.0	0.0000	1.0000	0.5102	-0.6159	0.0000
0.1	0.0462	0.9386	0.4163	-0.6112	0.0925
0.2	0.0836	0.8780	**0.3338**	-0.5987	0.1674
0.3	0.1133	0.8190	0.2620	-0.5803	0.2274
0.4	0.1364	0.7621	0.1999	-0.5577	0.2747
0.5	0.1536	0.7076	0.1467	-0.5321	0.3115
0.6	0.1660	0.6557	0.1015	-0.5047	0.3396
0.7	0.1742	0.6067	0.0635	-0.4764	0.3608
0.8	0.1789	0.5605	0.0317	-0.4476	0.3764
0.9	0.1807	0.5171	0.0056	-0.4191	0.3877
1.0	0.1802	0.4766	-0.0157	-0.3911	0.3955
1.1	0.1777	0.4389	-0.0327	-0.3641	0.4008
1.2	0.1737	0.4038	-0.0461	-0.3381	0.4041
1.3	0.1686	0.3712	-0.0564	-0.3133	0.4059
1.4	0.1625	0.3411	-0.0640	-0.2898	0.4066
1.5	0.1559	0.3132	-0.0693	-0.2677	0.4066
1.6	0.1487	0.2875	-0.0728	-0.2470	0.4061
1.7	0.1414	0.2638	-0.0747	-0.2276	0.4053
1.8	0.1338	0.2419	-0.0754	-0.2095	0.4043
1.9	0.1263	0.2218	-0.0751	-0.1927	0.4031
2.0	0.1189	0.2033	-0.0739	-0.1771	0.4020
2.1	0.1115	0.1864	-0.0721	-0.1627	0.4008
2.2	**0.1044**	0.1708	-0.0698	-0.1494	0.3998
2.3	0.0976	0.1565	-0.0671	-0.1371	0.3987
2.4	0.0910	0.1433	-0.0643	-0.1258	0.3978
2.5	0.0848	0.1313	-0.0612	-0.1153	0.3970
2.6	0.0788	0.1202	-0.0580	-0.1057	0.3962
2.7	0.0732	0.1101	-0.0548	-0.0969	0.3955
2.8	0.0678	0.1008	-0.0517	-0.0888	0.3949
2.9	0.0628	0.0923	-0.0485	-0.0814	0.3944
3.0	0.0581	0.0845	-0.0455	-0.0745	0.3939
3.1	0.0537	0.0774	-0.0425	-0.0683	0.3935
3.2	0.0496	0.0708	-0.0397	-0.0625	0.3932
3.3	0.0458	0.0649	-0.0369	-0.0573	0.3929
3.4	0.0422	0.0594	-0.0343	-0.0524	0.3926
3.5	0.0389	0.0544	-0.0319	-0.0480	0.3924
3.6	0.0358	0.0498	-0.0296	-0.0440	0.3922
3.7	0.0330	0.0456	-0.0274	-0.0403	0.3921
3.8	0.0304	0.0417	-0.0253	-0.0369	0.3919
3.9	0.0279	0.0382	-0.0234	-0.0337	0.3918
4.0	0.0257	0.0349	-0.0216	-0.0309	0.3917
4.1	0.0236	0.0320	-0.0200	-0.0283	0.3916
4.2	0.0217	0.0293	-0.0184	-0.0259	0.3915
4.3	0.0199	0.0268	-0.0170	-0.0237	0.3915
4.4	0.0183	0.0245	-0.0156	-0.0217	0.3914
∞	0.0000	0.0000	0.0000	0.0000	0.3911

η	f	g	f'	g'	$P - P_0$
0.0	0.0000	1.0000	0.5102	-0.6159	0.0000
0.1	0.0462	0.9386	0.4163	-0.6112	0.0925
0.2	0.0836	0.8780	**0.3380**	-0.5987	0.1674
0.3	0.1133	0.8190	0.2620	-0.5803	0.2274
0.4	0.1364	0.7621	0.1999	-0.5577	0.2747
0.5	0.1536	0.7076	0.1467	-0.5321	0.3115
0.6	0.1660	0.6557	0.1015	-0.5047	0.3396
0.7	0.1742	0.6067	0.0635	-0.4764	0.3608
0.8	0.1789	0.5605	0.0317	-0.4476	0.3764
0.9	0.1807	0.5171	0.0056	-0.4191	0.3877
1.0	0.1802	0.4766	-0.0157	-0.3911	0.3955
1.1	0.1777	0.4389	-0.0327	-0.3641	0.4008
1.2	0.1737	0.4038	-0.0461	-0.3381	0.4041
1.3	0.1686	0.3712	-0.0564	-0.3133	0.4059
1.4	0.1625	0.3411	-0.0640	-0.2898	0.4066
1.5	0.1559	0.3132	-0.0693	-0.2677	0.4066
1.6	0.1487	0.2875	-0.0728	-0.2470	0.4061
1.7	0.1414	0.2638	-0.0747	-0.2276	0.4053
1.8	0.1338	0.2419	-0.0754	-0.2095	0.4043
1.9	0.1263	0.2218	-0.0751	-0.1927	0.4031
2.0	0.1189	0.2033	-0.0739	-0.1771	0.4020
2.1	0.1115	0.1864	-0.0721	-0.1627	0.4008
2.2	**0.1045**	0.1708	-0.0698	-0.1494	0.3998
2.3	0.0976	0.1565	-0.0671	-0.1371	0.3987
2.4	0.0910	0.1433	-0.0643	-0.1258	0.3978
2.5	0.0848	0.1313	-0.0612	-0.1153	0.3970
2.6	0.0788	0.1202	-0.0580	-0.1057	0.3962
2.7	0.0732	0.1101	-0.0548	-0.0969	0.3955
2.8	0.0678	0.1008	-0.0517	-0.0888	0.3949
2.9	0.0628	0.0923	-0.0485	-0.0814	0.3944
3.0	0.0581	0.0845	-0.0455	-0.0745	0.3939
3.1	0.0537	0.0774	-0.0425	-0.0683	0.3935
3.2	0.0496	0.0708	-0.0397	-0.0625	0.3932
3.3	0.0458	0.0649	-0.0369	-0.0573	0.3929
3.4	0.0422	0.0594	-0.0343	-0.0524	0.3926
3.5	0.0389	0.0544	-0.0319	-0.0480	0.3924
3.6	0.0358	0.0498	-0.0296	-0.0440	0.3922
3.7	0.0330	0.0456	-0.0274	-0.0403	0.3921
3.8	0.0304	0.0417	-0.0253	-0.0369	0.3919
3.9	0.0279	0.0382	-0.0234	-0.0337	0.3918
4.0	0.0257	0.0349	-0.0216	-0.0309	0.3917
4.1	0.0236	0.0320	-0.0200	-0.0283	0.3916
4.2	0.0217	0.0293	-0.0184	-0.0259	0.3915
4.3	0.0199	0.0268	-0.0170	-0.0237	0.3915
4.4	0.0183	0.0245	-0.0156	-0.0217	0.3914
∞	0.0000	0.0000	0.0000	0.0000	0.3911

Table A.1: Comparison of dimensionless stream functions, their derivatives and dimensionless pressure differential - present work left, Benton (1966) right.

Results match Benton (1966) to four decimal places with the exception of the two emboldened points in f and f'. The discrepancy in f is likely rounding error while difference in f' can probably be attributed to typographical error.

B
Rotating body

Contents

B.1 Derivation of boundary layer equations

The governing equations (B.1a–c), derived by Mangler (1945), for a rotationally symmetric flow past a body of revolution, where u, v, w are velocity components in the directions of increasing s, y and θ are

$$\frac{\partial}{\partial s}(ru) + \frac{\partial}{\partial y}(rv) = 0, \tag{B.1a}$$

$$u\frac{\partial u}{\partial s} + v\frac{\partial u}{\partial y} - \frac{w^2}{r}\frac{\partial r}{\partial s} = u_e\frac{\partial u_e}{\partial s} + \nu\frac{\partial^2 u}{\partial y^2}, \tag{B.1b}$$

$$u\frac{\partial w}{\partial s} + v\frac{\partial w}{\partial y} + \frac{uw}{r}\frac{\partial r}{\partial s} = \nu\frac{\partial^2 w}{\partial y^2} \tag{B.1c}$$

In a fixed frame of reference these are subject to the boundary conditions

$$u = v = w - r\Omega = 0 \qquad \text{at} \quad y = 0 \tag{B.2a}$$

$$\begin{cases} u - u_e = w = 0, & u_\infty \neq 0 \\ u = w = 0, & u_\infty = 0 \end{cases} \qquad \text{as} \quad y \to \infty \tag{B.2b}$$

A two-component stream function is defined

$$u = \frac{1}{r}\frac{\partial \psi}{\partial y}, \quad v = -\frac{1}{r}\frac{\partial \psi}{\partial s}, \quad w = \frac{1}{r}\frac{\partial \phi}{\partial y}, \tag{B.3a–c}$$

which satisfies the continuity equation (B.1a) and which allows a consistent treatment of the azimuthal velocity component w. Subsequently ψ and ϕ are defined as functions of dimensionless stream functions f and g,

$$\psi = ru^* L_\xi f(\xi, \eta), \qquad \phi = r^2 \Omega L_\xi g(\xi, \eta), \tag{B.4a,b}$$

where L_ξ is a yet undefined viscous length scale and u^* is a switchable velocity scale of the form

$$u^* = \begin{cases} u_e, & u_\infty \neq 0 \\ r\Omega, & u_\infty = 0. \end{cases} \tag{B.5}$$

Using a variation of the Mangler-Levy-Lees transformation, a right-handed co-ordinate system is defined, in which

$$\eta = \frac{y}{L_\xi}, \qquad \xi = \int \xi_s ds. \tag{B.6a,b}$$

where ξ_s is the yet undefined transformed meridional co-ordinate derivative. Substituting these transformations into equations B.3a–c yields

$$u = u^* f', \qquad w = r\Omega g', \tag{B.7a, b}$$

$$\begin{aligned} v &= -\frac{1}{r}\left[\frac{\partial}{\partial \xi}\left(ru^* L_\xi f\right)\xi_s - \eta \frac{\xi_s}{L_\xi}\frac{\partial}{\partial \eta}\left(ru^* L_\xi f\right)\frac{\partial L_\xi}{\partial \xi}\right] \\ &= -\frac{1}{r}\left[\frac{\partial r}{\partial \xi}u^* L_\xi f \xi_s + r\frac{\partial u^*}{\partial \xi}L_\xi f \xi_s + ru^*\frac{\partial L_\xi}{\partial \xi} f \xi_s + ru^* L_\xi \frac{\partial f}{\partial \xi}\xi_s - \eta \xi_s r u^* f' \frac{\partial L_\xi}{\partial \xi}\right] \\ &= -\frac{1}{r}\frac{\partial r}{\partial \xi}u^* L_\xi f \xi_s - \frac{\partial u^*}{\partial \xi}L_\xi f \xi_s - u^*\frac{\partial L_\xi}{\partial \xi} f \xi_s - u^* L_\xi \frac{\partial f}{\partial \xi}\xi_s + \eta \xi_s u^* f' \frac{\partial L_\xi}{\partial \xi} \end{aligned} \tag{B.7c}$$

where a prime denotes differentiation with respect to η. Inserting B.7a–c into the u-momentum equation B.1b results in

$$
\begin{aligned}
u\frac{\partial u}{\partial s} &= u^* f' \left[\frac{\partial u^*}{\partial \xi} f' \xi_s + \frac{\partial f'}{\partial \xi} u^* \xi_s - \eta \frac{\xi_s}{L_\xi} \frac{\partial L_\xi}{\partial \xi} u^* f'' \right] \\
v\frac{\partial u}{\partial y} &= u^* f'' \frac{1}{L_\xi} \left[-\frac{1}{r}\frac{\partial r}{\partial \xi} u^* L_\xi f \xi_s - \frac{\partial u^*}{\partial \xi} L_\xi f \xi_s - u^* \frac{\partial L_\xi}{\partial \xi} f \xi_s - u^* L_\xi \frac{\partial f}{\partial \xi} \xi_s + \eta \xi_s u^* f' \frac{\partial L_\xi}{\partial \xi} \right] \\
-\frac{w^2}{r}\frac{\partial r}{\partial s} &= -r\Omega g'^2 \frac{\partial r}{\partial \xi} \xi_s \\
u_e \frac{\partial u_e}{\partial s} &= u_e \frac{\partial u_e}{\partial \xi} \xi_s \\
\nu \frac{\partial^2 u}{\partial y^2} &= \frac{\nu}{L_\xi^2} u^* f'''.
\end{aligned}
\tag{B.8a–e}
$$

Combining B.8a–e yields

$$
\begin{aligned}
& u^* \frac{\partial u^*}{\partial \xi} \xi_s f'^2 + u^{*2} \xi_s \frac{\partial f'}{\partial \xi} f' - \cancel{\eta \xi_s \frac{u^{*2}}{L_\xi} \frac{\partial L_\xi}{\partial \xi} f' f''} - \frac{1}{r}\frac{\partial r}{\partial \xi} u^{*2} \xi_s f f'' - u^* \frac{\partial u^*}{\partial \xi} \xi_s f f'' \\
& - \frac{u^{*2}}{L_\xi} \frac{\partial L_\xi}{\partial \xi} \xi_s f f'' - u^{*2} \xi_s \frac{\partial f}{\partial \xi} f'' + \cancel{\eta \xi_s \frac{u^{*2}}{L_\xi} \frac{\partial L_\xi}{\partial \xi} f' f''} - r\Omega^2 g'^2 \frac{\partial r}{\partial \xi} \xi_s - u_e \frac{\partial u_e}{\partial \xi} \xi_s \\
& - \frac{\nu}{L_\xi^2} u^* f''', = 0
\end{aligned}
\tag{B.9}
$$

then, dividing by $u^{*2}\xi_s$

$$
\begin{aligned}
& \frac{1}{u^*}\frac{\partial u^*}{\partial \xi} f'^2 + \frac{\partial f'}{\partial \xi} f' - \frac{1}{r}\frac{\partial r}{\partial \xi} f f'' - u^* \frac{\partial u^*}{\partial \xi} f f'' - \frac{1}{L_\xi}\frac{\partial L_\xi}{\partial \xi} f f'' \\
& - \frac{\partial f}{\partial \xi} f'' - \frac{r\Omega^2}{u^{*2}} \frac{\partial r}{\partial \xi} g'^2 - \frac{u_e}{u^{*2}} \frac{\partial u_e}{\partial \xi} - \frac{\nu}{L_\xi^2 u^* \xi_s} f'''' = 0.
\end{aligned}
\tag{B.10}
$$

Now, following Horton and Stock (1995) and defining the meridional co-ordinate derivative ξ_s and the wall-normal length scale L_ξ as

$$
L_\xi = \frac{\sqrt{2\xi}}{u^*}, \qquad \xi_s = \nu u^*, \tag{B.11a,b}
$$

which results in

$$\begin{aligned}&\frac{1}{u^*}\frac{\partial u^*}{\partial \xi}f'^2+\frac{\partial f'}{\partial \xi}f'-\frac{1}{r}\frac{\partial r}{\partial \xi}ff''-\cancel{u^*\frac{\partial u^*}{\partial \xi}ff''}+\cancel{u^*\frac{\partial u^*}{\partial \xi}ff''}-\frac{1}{2\xi}ff''\\&-\frac{\partial f}{\partial \xi}f''-\frac{r\Omega^2}{u^{*2}}\frac{\partial r}{\partial \xi}g'^2-\frac{u_e}{u^{*2}}\frac{\partial u_e}{\partial \xi}-\frac{1}{2\xi}f'''=0.\end{aligned} \tag{B.12}$$

Now, defining the following coefficients

$$\alpha_H = \frac{2\xi}{r}\frac{\partial r}{\partial \xi}, \qquad \beta_H = \frac{2\xi u_e}{u^{*2}}\frac{\partial u_e}{\partial \xi}, \qquad \gamma = \frac{2\xi}{u^*}\frac{\partial u^*}{\partial \xi}, \qquad \zeta_r = \left(\frac{r\Omega}{u^*}\right)^2, \quad (B.13a\text{–d})$$

which when re-inserted into B.12 and multiplied by 2ξ yields the final form of the u-momentum equation

$$f''' + (\alpha_H+1)ff'' + \alpha_H\zeta_r g'^2 - \gamma f'^2 + \beta_H = 2\xi\left[\frac{\partial f'}{\partial \xi}f' - \frac{\partial f}{\partial \xi}f''\right]. \tag{B.14}$$

Similarly, inserting B.7a–c into the w-momentum equation (B.1c) results in

$$\begin{aligned}u\frac{\partial w}{\partial s} &= u^* f'\left[\frac{\partial r}{\partial \xi}\Omega g'\xi_s + r\Omega\frac{\partial g'}{\partial \xi}\xi_s - \eta\frac{\xi_s}{L_\xi}r\Omega\frac{\partial L_\xi}{\partial \xi}g''\right]\\ v\frac{\partial w}{\partial y} &= r\Omega g''\frac{1}{L_\xi}\left[-\frac{1}{r}\frac{\partial r}{\partial \xi}u^*L_\xi f\xi_s - \frac{\partial u^*}{\partial \xi}L_\xi f\xi_s - u^*\frac{\partial L_\xi}{\partial \xi}f\xi_s - u^*L_\xi\frac{\partial f}{\partial \xi}\xi_s + \eta\xi_s u^* f'\frac{\partial L_\xi}{\partial \xi}\right]\\ \frac{uw}{r}\frac{\partial r}{\partial s} &= u^*\Omega f'g'\frac{\partial r}{\partial \xi}\xi_s\\ \nu\frac{\partial^2 w}{\partial y^2} &= \frac{\nu r\Omega}{L_\xi^2}g'''.\end{aligned} \tag{B.15a–d}$$

Combining B.15a–d gives

$$\begin{aligned}&u^*\frac{\partial r}{\partial \xi}\Omega\xi_s f'g' + u^* r\Omega\xi_s\frac{\partial g'}{\partial \xi}f' - \cancel{\eta\frac{\xi_s}{L_\xi}\frac{\partial L_\xi}{\partial \xi}u^* r\Omega f'g''} - \frac{\partial r}{\partial \xi}u^*\Omega\xi_s fg'' - r\Omega\frac{\partial u^*}{\partial \xi}\xi_s fg''\\&-\frac{r\Omega u^*}{L_\xi}\frac{\partial L_\xi}{\partial \xi}\xi_s fg'' - u^* r\Omega\xi_s\frac{\partial f}{\partial \xi}g'' + \cancel{\eta\frac{\xi_s}{L_\xi}\frac{\partial L_\xi}{\partial \xi}u^* r\Omega f'g''} + u^*\Omega f'g'\frac{\partial r}{\partial \xi}\xi_s - \frac{\nu r\Omega}{L_\xi^2}g''' = 0,\end{aligned} \tag{B.16}$$

then, dividing by $u^* r\Omega\xi_s$

$$\begin{aligned}&\frac{1}{r}\frac{\partial r}{\partial \xi}f'g' + \frac{\partial g'}{\partial \xi}f' - \frac{1}{r}\frac{\partial r}{\partial \xi}fg'' - \frac{1}{u^*}\frac{\partial u^*}{\partial \xi}fg'' - \frac{1}{L_\xi}\frac{\partial L_\xi}{\partial \xi}fg''\\&-\frac{\partial f}{\partial \xi}g'' + \frac{1}{r}\frac{\partial r}{\partial \xi}f'g' - \frac{\nu}{L_\xi^2 u^*\xi_s}g''' = 0\end{aligned} \tag{B.17}$$

Defining L_ξ and ξ_s as in B.11a,b, results in

$$\begin{aligned}&\frac{2}{r}\frac{\partial r}{\partial \xi}f'g' + \frac{\partial g'}{\partial \xi}f' - \frac{1}{r}\frac{\partial r}{\partial \xi}fg'' - \cancel{\frac{1}{u^*}\frac{\partial u^*}{\partial \xi}fg''} + \cancel{\frac{1}{u^*}\frac{\partial u^*}{\partial \xi}fg''} - \frac{1}{2\xi}fg'' \\ &-\frac{\partial f}{\partial \xi}g'' - \frac{1}{2\xi}g''' = 0\end{aligned} \tag{B.18}$$

Finally, the coefficient α_H is used as defined in B.13a, which when re-inserted into equation B.18 and multiplied by 2ξ gives

$$g''' + (\alpha_H + 1)fg'' - 2\alpha_H f'g' = 2\xi\left[\frac{\partial g'}{\partial \xi}f' - \frac{\partial f}{\partial \xi}g''\right]. \tag{B.19}$$

Equations B.14 and B.19 are subject to the following non-dimensional boundary conditions

$$f = f' = g = g' - 1 = 0 \qquad \text{at} \quad \eta = 0 \tag{B.20a}$$

$$\begin{cases} f' - 1 = g' = 0, & u_\infty \neq 0 \\ f' = g' = 0, & u_\infty = 0 \end{cases} \qquad \text{as} \quad \eta \to \infty \tag{B.20b}$$

B.2 Derivation of 6x6 coupled linear ODEs

The boundary layer equations detailed in chapter 3 can be converted into a 6x6 system of first-order ordinary differential equations by introducing the following variables

$$f' = u, \qquad u' = \tau \qquad \text{and} \qquad g' = w, \qquad w' = \sigma, \tag{B.21a–d}$$

which when inserted into the boundary layer equations, 3.8a,b, results in

$$\begin{aligned}&\tau' + (\alpha_H + 1)\, f\tau + 2\xi\frac{\partial f}{\partial \xi}\tau - \gamma u^2 - 2\xi\frac{\partial u}{\partial \xi}u + \alpha_H \zeta_r w^2 + \beta_H = 0 \\ &\tau = u' \\ &u = f' \\ &\sigma' + (\alpha_H + 1)\, f\sigma + 2\xi\frac{\partial f}{\partial \xi}\sigma - 2\alpha_H uw - 2\xi\frac{\partial w}{\partial \xi}u = 0 \\ &\sigma = w' \\ &w = g'.\end{aligned} \tag{B.22a–f}$$

These can then be linearised by expanding f, u, τ, g, w and σ into

$$f = f_n + \Delta f, \quad u = u_n + \Delta u, \quad \tau = \tau_n + \Delta\tau, \tag{B.23a–c}$$

$$g = g_n + \Delta g, \quad w = w_n + \Delta w, \quad \sigma = \sigma_n + \Delta\sigma, \tag{B.23d–f}$$

and where derivatives in ξ expand into a known and unknown portion, given by

$$\begin{aligned} \frac{\partial f}{\partial \xi} &= \frac{\partial}{\partial \xi}\left(f_n + \Delta f\right) \\ &= \underbrace{k_\xi \Delta f}_{\text{unknown}} + \underbrace{k_\xi f_n + k_{u/s}\left(f_{u/s}, \xi_{u/s}\right)}_{\text{known}} \\ &= k_\xi \Delta f + \frac{\partial f_n}{\partial \xi}. \end{aligned} \tag{B.24}$$

Inserting B.23a–f and B.24 into B.22a–f results in

$$\begin{aligned} &\tau_n' + \Delta\tau' + (\alpha_H + 1)\left(f_n + \Delta f\right)\left(\tau_n + \Delta\tau\right) + 2\left(\tau_n + \Delta\tau\right)\left[k_\xi \Delta f + \frac{\partial f_n}{\partial \xi}\right]\xi \\ &\quad - \gamma\left(u_n + \Delta u\right)^2 - 2\left(u_n + \Delta u\right)\left[k_\xi \Delta u + \frac{\partial u_n}{\partial \xi}\right]\xi \\ &\quad + \alpha_H \zeta_r \left(w_n + \Delta w\right)^2 + \beta_H = 0 \\ &\tau_n + \Delta\tau = u_n' + \Delta u' \\ &u_n + \Delta u = f_n' + \Delta f' \\ &\sigma_n' + \Delta\sigma' + (\alpha_H + 1)\left(f_n + \Delta f\right)\left(\sigma_n + \Delta\sigma\right) + 2\left(\sigma_n + \Delta\sigma\right)\left[k_\xi \Delta f + \frac{\partial f_n}{\partial \xi}\right]\xi \\ &\quad - 2\alpha_H\left(u_n + \Delta u\right)\left(w_n + \Delta w\right) - 2\left(u_n + \Delta u\right)\left[k_\xi \Delta w + \frac{\partial w_n}{\partial \xi}\right]\xi = 0 \\ &\sigma_n + \Delta\sigma = w_n' + \Delta w' \\ &w_n + \Delta w = g_n' + \Delta g', \end{aligned} \tag{B.25a–f}$$

which can be expanded to

$$\begin{aligned}
&\tau_n' + \Delta\tau' + \alpha_H f_n \tau_n + \alpha_H f_n \Delta\tau + \alpha_H \Delta f \tau_n + f_n \tau_n + f_n \Delta\tau + \tau_n \Delta f \\
&\quad + 2\xi k_\xi \tau_n \Delta f + 2\xi \tau_n \frac{\partial f_n}{\partial \xi} + 2\xi \Delta\tau \frac{\partial f_n}{\partial \xi} - \gamma u_n^2 - 2\gamma u_n \Delta u \\
&\quad - 2\xi k_\xi u_n \Delta u - 2\xi u_n \frac{\partial u_n}{\partial \xi} - 2\xi \Delta u \frac{\partial u_n}{\partial \xi} + \alpha_H \zeta_r w_n^2 + 2\alpha_H \zeta_r w_n \Delta w \\
&\quad + \beta_H = 0 \\
&\tau_n + \Delta\tau = u_n' + \Delta u' \\
&u_n + \Delta u = f_n' + \Delta f' \\
&\sigma_n' + \Delta\sigma' + \alpha_H f_n \sigma_n + \alpha_H f_n \Delta\sigma + \alpha_H \Delta f \sigma_n + f_n \sigma_n + f_n \Delta\sigma + \Delta f \sigma_n \\
&\quad + 2\xi k_\xi \sigma_n \Delta f + 2\xi \sigma_n \frac{\partial f_n}{\partial \xi} + 2\xi \Delta\sigma \frac{\partial f_n}{\partial \xi} - 2\alpha_H u_n w_n - 2\alpha_H u_n \Delta w \\
&\quad - 2\alpha_H \Delta u w_n - 2\xi k_\xi u_n \Delta w - 2\xi u_n \frac{\partial w_n}{\partial \xi} - 2\xi \Delta u \frac{\partial w_n}{\partial \xi} = 0 \\
&\sigma_n + \Delta\sigma = w_n' + \Delta w' \\
&w_n + \Delta w = g_n' + \Delta g'.
\end{aligned} \tag{B.26a–f}$$

Separating constants and re-organising produces

$$\begin{aligned}
\Delta\tau' &= -\alpha_H f_n \Delta\tau + \alpha_H \tau_n \Delta f - f_n \Delta\tau - \tau_n \Delta f - 2\xi k_\xi \tau_n \Delta f - 2\xi \frac{\partial f_n}{\partial \xi} \Delta\tau \\
&\quad + 2\gamma u_n \Delta u + 2\xi k_\xi u_n \Delta u + 2\xi \frac{\partial u_n}{\partial \xi} \Delta u - 2\alpha_H \zeta_r w_n \Delta w + [B_\tau] \\
\Delta u' &= \Delta\tau + [B_u] \\
\Delta f' &= \Delta u + [B_f] \\
\Delta\sigma' &= -\alpha_H f_n \Delta\sigma - \alpha_H \sigma_n \Delta f - f_n \Delta\sigma - \sigma_n \Delta f - 2\xi k_\xi \sigma_n \Delta f - 2\xi \frac{\partial f_n}{\partial \xi} \Delta\sigma \\
&\quad + 2\alpha_H u_n \Delta w + 2\alpha_H w_n \Delta u + 2\xi k_\xi u_n \Delta w + 2\xi \frac{\partial w_n}{\partial \xi} \Delta u + [B_\sigma] \\
\Delta w' &= \Delta\sigma + [B_w] \\
\Delta g' &= \Delta w + [B_g],
\end{aligned} \tag{B.27a–f}$$

where the constants are given by

$$
\begin{aligned}
[B_\tau] &= -\tau_n' - \alpha_H f_n \tau_n - f_n \tau_n - 2\xi \tau_n \frac{\partial f_n}{\partial \xi} + \gamma u_n^2 + 2\xi u_n \frac{\partial u_n}{\partial \xi} - \alpha_H \zeta_r w_n^2 - \beta_H \\
[B_u] &= \tau_n - u_n' \\
[B_f] &= u_n - f_n' \\
[B_\sigma] &= -\sigma_n' - \alpha_H f_n \sigma_n - f_n \sigma_n - 2\xi \sigma_n \frac{\partial f_n}{\partial \xi} + 2\alpha_H u_n w_n + 2\xi u_n \frac{\partial w_n}{\partial \xi} \\
[B_w] &= \sigma_n - w_n' \\
[B_u] &= w_n - g_n.
\end{aligned}
\tag{B.28a–f}
$$

The linearised ODEs, B.27a–f, can be written in matrix form, $\zeta' = A\zeta + B$, as

$$
\begin{bmatrix} \Delta\tau \\ \Delta u \\ \Delta f \\ \Delta\sigma \\ \Delta w \\ \Delta g \end{bmatrix}' = \begin{bmatrix} A_{\tau\tau} & A_{\tau u} & A_{\tau f} & 0 & A_{\tau w} & 0 \\ 1 & 0 & 0 & 0 & 0 & 0 \\ 0 & 1 & 0 & 0 & 0 & 0 \\ 0 & A_{\sigma u} & A_{\sigma f} & A_{\sigma\sigma} & A_{\sigma w} & 0 \\ 0 & 0 & 0 & 1 & 0 & 0 \\ 0 & 0 & 0 & 0 & 1 & 0 \end{bmatrix} \begin{bmatrix} \Delta\tau \\ \Delta u \\ \Delta f \\ \Delta\sigma \\ \Delta w \\ \Delta g \end{bmatrix} + \begin{bmatrix} B_\tau \\ B_u \\ B_f \\ B_\sigma \\ B_w \\ B_g \end{bmatrix} \tag{B.29}
$$

where the constants are as defined in B.28a–f and

$$
\begin{aligned}
A_{\tau\tau} &= -\alpha_H f_n - f_n - 2\xi \frac{\partial f_n}{\partial \xi} \\
A_{\tau u} &= 2\gamma u_n + 2\xi k_\xi u_n + 2\xi \frac{\partial u_n}{\partial \xi} \\
A_{\tau f} &= -\alpha_H \tau_n - \tau_n - 2\xi k_\xi \tau_n \\
A_{\tau w} &= -2\alpha_H \zeta_r w_n \\
A_{\sigma\sigma} &= -\alpha_H f_n - f_n - 2\xi \frac{\partial f_n}{\partial \xi} \\
A_{\sigma w} &= 2\alpha_H u_n + 2\xi k_\xi u_n \\
A_{\sigma u} &= 2\alpha_H w_n + 2\xi \frac{\partial w_n}{\partial \xi} \\
A_{\sigma f} &= -\alpha_H \sigma_n - \sigma_n - 2\xi k_\xi \sigma_n.
\end{aligned}
\tag{B.30a–h}
$$

In order to solve the compact-difference expression (equation 3.27) discussed in section

3.3.3, the first derivatives of A and B with respect to η are required. Namely,

$$A' = \begin{bmatrix} A'_{\tau\tau} & A'_{\tau u} & A'_{\tau f} & 0 & A'_{\tau w} & 0 \\ 0 & 0 & 0 & 0 & 0 & 0 \\ 0 & 0 & 0 & 0 & 0 & 0 \\ 0 & A'_{\sigma u} & A'_{\sigma f} & A'_{\sigma\sigma} & A'_{\sigma w} & 0 \\ 0 & 0 & 0 & 0 & 0 & 0 \\ 0 & 0 & 0 & 0 & 0 & 0 \end{bmatrix}, \qquad B' = \begin{bmatrix} B'_{\tau} \\ B'_{u} \\ B'_{f} \\ B'_{\sigma} \\ B'_{w} \\ B'_{g} \end{bmatrix} \tag{B.31}$$

where

$$\begin{aligned} A'_{\tau\tau} &= -\alpha_H f'_n - f'_n - 2\xi \frac{\partial f'_n}{\partial \xi} \\ A'_{\tau u} &= 2\gamma u'_n + 2\xi k_\xi u'_n + 2\xi \frac{\partial u'_n}{\partial \xi} \\ A'_{\tau f} &= -\alpha_H \tau'_n - \tau'_n - 2\xi k_\xi \tau'_n \\ A'_{\tau w} &= -2\alpha_H \gamma w'_n \\ A'_{\sigma\sigma} &= -\alpha_H f'_n - f'_n - 2\xi \frac{\partial f'_n}{\partial \xi} \\ A'_{\sigma w} &= 2\alpha_H u'_n + 2\xi k_\xi u'_n \\ A'_{\sigma u} &= 2\alpha_H w'_n + 2\xi \frac{\partial w'_n}{\partial \xi} \\ A'_{\sigma f} &= -\alpha_H \sigma'_n - \sigma'_n - 2\xi k_\xi \sigma'_n. \end{aligned} \tag{B.32a–h}$$

and

$$\begin{aligned} B'_{\tau} =& -\tau''_n - \alpha_H f'_n \tau_n - \alpha_H f_n \tau'_n - f'_n \tau_n - f_n \tau'_n - 2\xi \tau'_n \frac{\partial f_n}{\partial \xi} - 2\xi \tau_n \frac{\partial f'_n}{\partial \xi} \\ &+ 2\gamma u'_n u_n + 2\xi u'_n \frac{\partial u_n}{\partial \xi} + 2\xi u_n \frac{\partial u'_n}{\partial \xi} - 2\alpha_H \zeta w'_n w_n \\ B'_{u} =& \tau'_n - u''_n \\ B'_{f} =& u'_n - f''_n \\ B'_{\sigma} =& -\sigma''_n - \alpha_H f'_n \sigma_n - \alpha_H f_n \sigma'_n - f'_n \sigma_n - f_n \sigma'_n - 2\xi \sigma'_n \frac{\partial f_n}{\partial \xi} - 2\xi \sigma'_n \frac{\partial f_n}{\partial \xi} \\ &+ 2\alpha_H u'_n w_n + 2\alpha_H u_n w'_n + 2\xi u'_n \frac{\partial w_n}{\partial \xi} + 2\xi u_n \frac{\partial w'_n}{\partial \xi} \\ B'_{w} =& \sigma'_n - w''_n \\ B'_{g} =& w'_n - g''_n \end{aligned} \tag{B.33a–f}$$

B.3 Derivation of 3x3 partially-coupled linear ODEs

The boundary layer equations detailed in chapter 3 can be converted into two systems of partially-coupled 3x3 first-order equations in order to make computational savings. This is possible because there is only a weak coupling between the u- and w-momentum equations so the resultant effect on accuracy is small.

Linearisation follows the same path as for the 6x6 system in B.2 until B.25a–f, whereafter expansion and discarding of non-linear & coupled terms (in Δ)

$$
\begin{aligned}
&\tau_n' + \Delta\tau' + \alpha_H f_n \tau_n + \alpha_H f_n \Delta\tau + \alpha_H \Delta f \tau_n + f_n \tau_n + f_n \Delta\tau + \tau_n \Delta f \\
&\quad + 2\xi k_\xi \tau_n \Delta f + 2\xi \tau_n \frac{\partial f_n}{\partial \xi} + 2\xi \Delta\tau \frac{\partial f_n}{\partial \xi} - \gamma u_n^2 - 2\gamma u_n \Delta u \\
&\quad - 2\xi k_\xi u_n \Delta u - 2\xi u_n \frac{\partial u_n}{\partial \xi} - 2\xi \Delta u \frac{\partial u_n}{\partial \xi} + \alpha_H \zeta w_n^2 + \beta_H = 0 \\
&\tau_n + \Delta\tau = u_n' + \Delta u' \\
&u_n + \Delta u = f_n' + \Delta f' \\
&\sigma_n' + \Delta\sigma' + \alpha_H f_n \sigma_n + \alpha_H f_n \Delta\sigma + f_n \sigma_n + f_n \Delta\sigma + 2\xi \sigma_n \frac{\partial f_n}{\partial \xi} \\
&\quad + 2\xi \Delta\sigma \frac{\partial f_n}{\partial \xi} - 2\alpha_H u_n w_n - 2\alpha_H u_n \Delta w - 2\xi k_\xi u_n \Delta w - 2\xi u_n \frac{\partial w_n}{\partial \xi} = 0 \\
&\sigma_n + \Delta\sigma = w_n' + \Delta w' \\
&w_n + \Delta w = g_n' + \Delta g'.
\end{aligned}
\tag{B.34a–f}
$$

Separating constants then gives

$$\begin{aligned}
\Delta\tau' &= -\alpha_H f_n \Delta\tau + \alpha_H \tau_n \Delta f - f_n \Delta\tau - \tau_n \Delta f - 2\xi k_\xi \tau_n \Delta f - 2\xi \frac{\partial f_n}{\partial \xi}\Delta\tau \\
&\quad + 2\gamma u_n \Delta u + 2\xi k_\xi u_n \Delta u + 2\xi \frac{\partial u_n}{\partial \xi}\Delta u + [B_\tau] \\
\Delta u' &= \Delta\tau + [B_u] \\
\Delta f' &= \Delta u + [B_f] \qquad \text{(B.35a–f)} \\
\Delta\sigma' &= -\alpha_H f_n \Delta\sigma - f_n \Delta\sigma - 2\xi \frac{\partial f_n}{\partial \xi}\Delta\sigma + 2\alpha_H u_n \Delta w + 2\xi k_\xi u_n \Delta w + [B_\sigma] \\
\Delta w' &= \Delta\sigma + [B_w] \\
\Delta g' &= \Delta w + [B_g],
\end{aligned}$$

where the constants are given by

$$\begin{aligned}
[B_\tau] &= -\tau_n' - \alpha_H f_n \tau_n - f_n \tau_n - 2\xi \tau_n \frac{\partial f_n}{\partial \xi} + \gamma u_n^2 + 2\xi u_n \frac{\partial u_n}{\partial \xi} - \alpha_H \zeta w_n^2 - \beta_H \\
[B_u] &= \tau_n - u_n' \\
[B_f] &= u_n - f_n' \qquad \text{(B.36a–f)} \\
[B_\sigma] &= -\sigma_n' - \alpha_H f_n \sigma_n - f_n \sigma_n - 2\xi \sigma_n \frac{\partial f_n}{\partial \xi} + 2\alpha_H u_n w_n + 2\xi u_n \frac{\partial w_n}{\partial \xi} \\
[B_w] &= \sigma_n - w_n' \\
[B_u] &= w_n - g_n'.
\end{aligned}$$

The linearised u-momentum ODEs (A.35a–c) can be written in matrix form, $\zeta' = A\zeta + B$, as

$$\begin{bmatrix} \Delta\tau \\ \Delta u \\ \Delta f \end{bmatrix}' = \begin{bmatrix} A_{\tau\tau} & A_{\tau u} & A_{\tau f} \\ 1 & 0 & 0 \\ 0 & 1 & 0 \end{bmatrix} \begin{bmatrix} \Delta\tau \\ \Delta u \\ \Delta f \end{bmatrix} + \begin{bmatrix} B_\tau \\ B_u \\ B_f \end{bmatrix} \qquad \text{(B.37)}$$

in which

$$\begin{aligned}
A_{\tau\tau} &= -\alpha_H f_n - f_n - 2\xi \frac{\partial f_n}{\partial \xi} \\
A_{\tau u} &= 2\gamma u_n + 2\xi k_\xi u_n + 2\xi \frac{\partial u_n}{\partial \xi} \qquad \text{(B.38a–c)} \\
A_{\tau f} &= -\alpha_H \tau_n - \tau_n - 2\xi k_\xi \tau_n,
\end{aligned}$$

while the linearised w-momentum ODEs (A.35d–f) can be written as

$$\begin{bmatrix}\Delta\sigma\\ \Delta w\\ \Delta g\end{bmatrix}' = \begin{bmatrix}A_{\sigma\sigma} & A_{\sigma w} & 0\\ 1 & 0 & 0\\ 0 & 1 & 0\end{bmatrix}\begin{bmatrix}\Delta\sigma\\ \Delta w\\ \Delta g\end{bmatrix} + \begin{bmatrix}B_\sigma\\ B_w\\ B_g\end{bmatrix} \tag{B.39}$$

where

$$\begin{aligned} A_{\sigma\sigma} &= -\alpha_H f_n - f_n - 2\xi\frac{\partial f_n}{\partial \xi}\\ A_{\sigma w} &= 2\alpha_H u_n + 2\xi k_\xi u_n. \end{aligned} \tag{B.40a,b}$$

and the constants are as defined as in equations B.36a–f. In order to solve the compact-difference expression (equation 3.27) discussed in section 3.3.3, the first derivatives of A and B with respect to η are required. For the u-momentum equation the derivative matrices are

$$A'_u = \begin{bmatrix}A'_{\tau\tau} & A'_{\tau u} & A'_{\tau f}\\ 0 & 0 & 0\\ 0 & 0 & 0\end{bmatrix}, \qquad B'_w = \begin{bmatrix}B'_\tau\\ B'_u\\ B'_f\end{bmatrix} \tag{B.41}$$

where

$$\begin{aligned} A'_{\tau\tau} &= -\alpha_H f'_n - f'_n - 2\xi\frac{\partial f'_n}{\partial \xi}\\ A'_{\tau u} &= 2\gamma u'_n + 2\xi k_\xi u'_n + 2\xi\frac{\partial u'_n}{\partial \xi}\\ A'_{\tau f} &= -\alpha_H \tau'_n - \tau'_n - 2\xi k_\xi \tau'_n. \end{aligned} \tag{B.42a–c}$$

and

$$\begin{aligned} B'_\tau =& -\tau''_n - \alpha_H f'_n\tau_n - \alpha_H f_n\tau'_n - f'_n\tau_n - f_n\tau'_n - 2\xi\tau'_n\frac{\partial f_n}{\partial \xi} - 2\xi\tau_n\frac{\partial f'_n}{\partial \xi}\\ &+ 2\gamma u'_n u_n + 2\xi u'_n\frac{\partial u_n}{\partial \xi} + 2\xi u_n\frac{\partial u'_n}{\partial \xi} - 2\alpha_H\zeta w'_n w_n\\ B'_u =& \tau'_n - u''_n\\ B'_f =& u'_n - f''_n \end{aligned} \tag{B.43a–c}$$

For the w-momentum equation the derivative matrices are

$$A'_g = \begin{bmatrix}A_{\sigma\sigma} & A_{\sigma w} & 0\\ 0 & 0 & 0\\ 0 & 0 & 0\end{bmatrix}, \qquad B'_g = \begin{bmatrix}B'_\sigma\\ B'_w\\ B'_g\end{bmatrix} \tag{B.44}$$

where

$$\begin{aligned} A'_{\sigma\sigma} &= -\alpha_H f'_n - f'_n - 2\xi\frac{\partial f'_n}{\partial \xi}\\ A'_{\sigma w} &= 2\alpha_H u'_n + 2\xi k_\xi u'_n. \end{aligned} \tag{B.45a,b}$$

and

$$\begin{aligned} B'_\sigma =& -\sigma''_n - \alpha_H f'_n \sigma_n - \alpha_H f_n \sigma'_n - f'_n \sigma_n - f_n \sigma'_n - 2\xi \sigma'_n \frac{\partial f_n}{\partial \xi} - 2\xi \sigma_n \frac{\partial f'_n}{\partial \xi} \\ &+ 2\alpha_H u'_n w_n + 2\alpha_H u_n w'_n + 2\xi u'_n \frac{\partial w_n}{\partial \xi} + 2\xi u_n \frac{\partial w'_n}{\partial \xi} \\ B'_w =& \sigma'_n - w''_n \\ B'_g =& w'_n - g''_n \end{aligned} \tag{B.46a–c}$$

B.4 Proposed experimental assembly

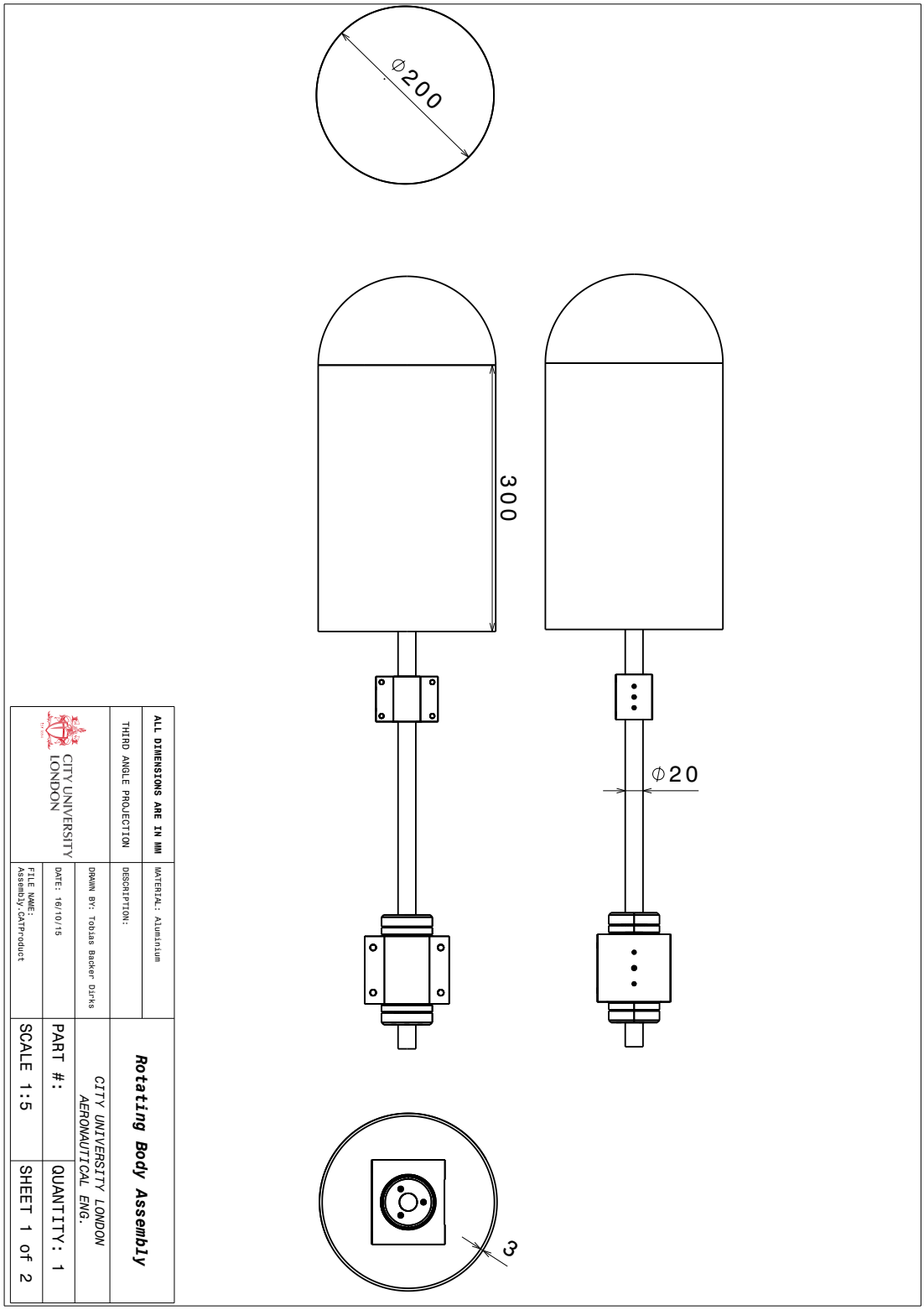

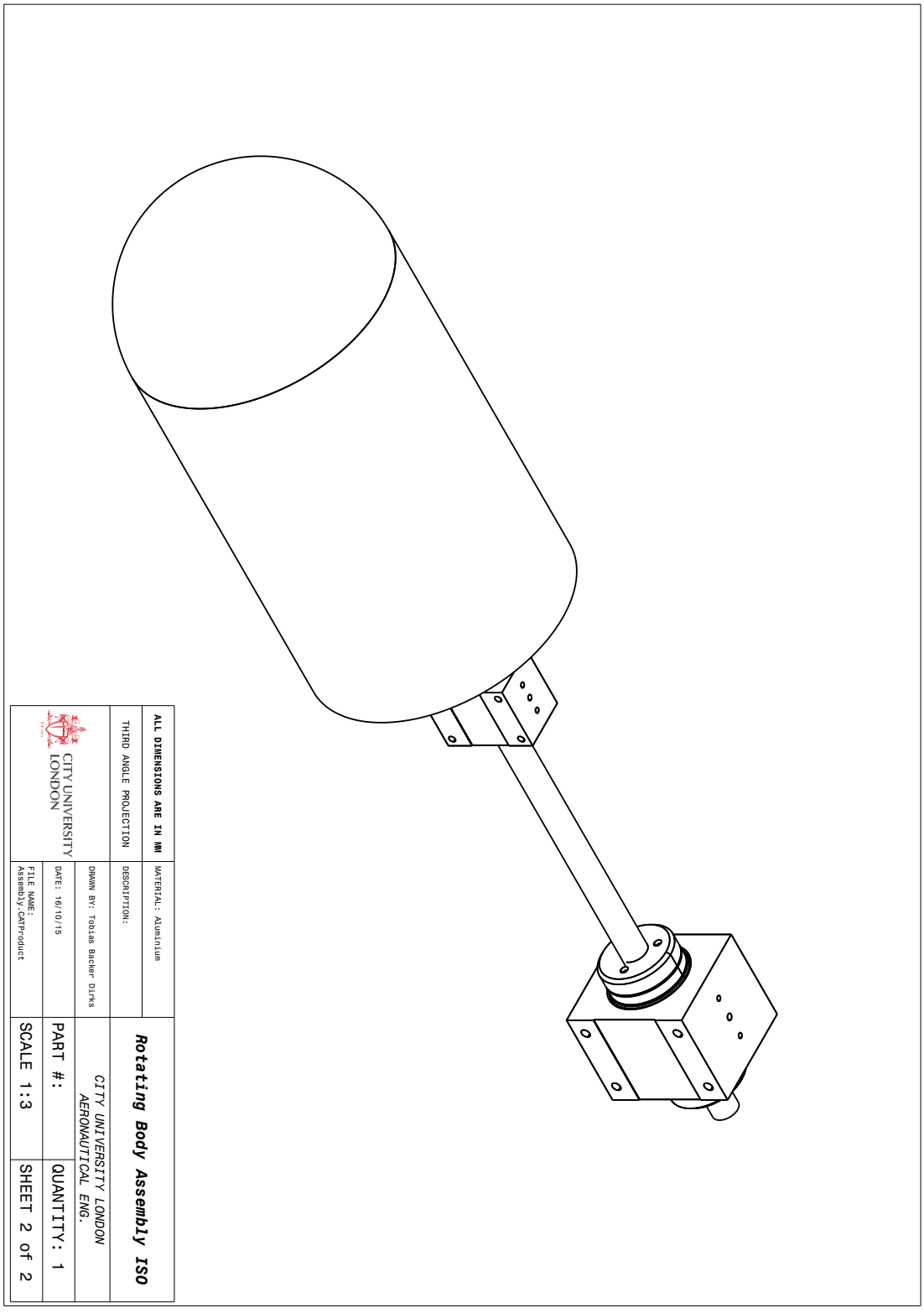
ALL DIMENSIONS ARE IN MM
MATERIAL: Aluminium
THIRD ANGLE PROJECTION
DESCRIPTION:
DRAWN BY: Tobias Backer Dirks
CITY UNIVERSITY LONDON
DATE: 16/10/15
FILE NAME: Assembly.CATProduct
Rotating Body Assembly ISO
CITY UNIVERSITY LONDON
AERONAUTICAL ENG.
PART #:
QUANTITY: 1
SCALE 1:3
SHEET 2 of 2

C
Stability equations

Contents

C.1 Derivation of the perturbation equations

The perturbation equations for a general body of revolution are derived from the 3-D, incompressible, N-S equations in orthogonal curvilinear co-ordinates, $\bar{x}$, $\bar{y}$ and $\bar{z}$. In the present work these represent the streamline, wall-normal and crossflow directions, respectively, as shown in figure 4.2, and U, V and W are the velocities in their respective directions. The scale factors, h_x, h_y and h_z, which provide a measure of how the transformed co-ordinate changes the position of the point, satisfy

$$h_x = h_x(\bar{x}, \bar{y}, \bar{z}), \qquad h_y = 1, \qquad h_z = h_z(\bar{x}, \bar{y}, \bar{z}), \tag{C.1a–c}$$

and the incremental arc length is given by the magnitude of the individual element lengths,

$$dS = \sqrt{(h_x d\bar{x})^2 + (d\bar{y})^2 + (h_z d\bar{z})^2}. \tag{C.2}$$

The governing equations therefore take on the following form

$$\frac{1}{h_x h_z}\left[\frac{\partial}{\partial \bar{x}}\left(h_z U\right)+\frac{\partial}{\partial \bar{y}}\left(h_x h_z V\right)+\frac{\partial}{\partial \bar{z}}\left(h_x W\right)\right]=0 \tag{C.3}$$

$$\begin{aligned}
&\frac{\partial U}{\partial t}+\frac{U}{h_x}\frac{\partial U}{\partial \bar{x}}+V\frac{\partial U}{\partial \bar{y}}+\frac{W}{h_z}\frac{\partial U}{\partial \bar{z}}+\frac{1}{h_x}UV\frac{\partial h_x}{\partial \bar{y}}+\frac{1}{h_x h_z}\left[UW\frac{\partial h_x}{\partial \bar{z}}-W^2\frac{\partial h_z}{\partial \bar{x}}\right]\\
&\quad+2\left(\Omega_y W-\Omega_z V\right)-\frac{\Omega^2}{2}\nabla\vec{r}^2\\
&\quad=-\frac{1}{h_x}\frac{\partial P}{\partial \bar{x}}+\frac{1}{Re\,h_x}\frac{\partial}{\partial \bar{x}}\left(\frac{1}{h_x h_z}\left[\frac{\partial}{\partial \bar{x}}\left(h_z U\right)+\frac{\partial}{\partial \bar{y}}\left(h_x h_z V\right)+\frac{\partial}{\partial \bar{z}}\left(h_x W\right)\right]\right)\\
&\quad-\frac{1}{Re\,h_z}\left[\frac{\partial}{\partial \bar{y}}\left(\frac{h_z}{h_x}\left[\frac{\partial}{\partial \bar{x}}\left(V\right)-\frac{\partial}{\partial \bar{y}}\left(h_x U\right)\right]\right)-\frac{\partial}{\partial \bar{z}}\left(\frac{1}{h_x h_z}\left[\frac{\partial}{\partial \bar{z}}\left(h_x U\right)-\frac{\partial}{\partial \bar{x}}\left(h_z W\right)\right]\right)\right]
\end{aligned}$$

$$\begin{aligned}
&\frac{\partial V}{\partial t}+\frac{U}{h_x}\frac{\partial V}{\partial \bar{x}}+V\frac{\partial V}{\partial \bar{y}}+\frac{W}{h_z}\frac{\partial V}{\partial \bar{z}}-\frac{1}{h_x}U^2\frac{\partial h_x}{\partial \bar{x}}-\frac{1}{h_z}W^2\frac{\partial h_z}{\partial \bar{y}}\\
&\quad+2\left(\Omega_z U-\Omega_x W\right)-\frac{\Omega^2}{2}\nabla\vec{r}^2\\
&\quad=-\frac{\partial P}{\partial \bar{y}}+\frac{1}{Re}\frac{\partial}{\partial \bar{y}}\left(\frac{1}{h_x h_z}\left[\frac{\partial}{\partial \bar{x}}\left(h_z U\right)+\frac{\partial}{\partial \bar{y}}\left(h_x h_z V\right)+\frac{\partial}{\partial \bar{z}}\left(h_x W\right)\right]\right)\\
&\quad-\frac{1}{Re\,h_x h_z}\left[\frac{\partial}{\partial \bar{z}}\left(\frac{h_x}{h_z}\left[\frac{\partial}{\partial \bar{y}}\left(h_z W\right)-\frac{\partial}{\partial \bar{z}}\left(V\right)\right]\right)-\frac{\partial}{\partial \bar{x}}\left(\frac{h_z}{h_x}\left[\frac{\partial}{\partial \bar{x}}\left(V\right)-\frac{\partial}{\partial \bar{y}}\left(h_x U\right)\right]\right)\right]
\end{aligned}$$

$$\begin{aligned}
&\frac{\partial W}{\partial t}+\frac{U}{h_x}\frac{\partial W}{\partial \bar{x}}+V\frac{\partial W}{\partial \bar{y}}+\frac{W}{h_z}\frac{\partial W}{\partial \bar{z}}+\frac{1}{h_x h_z}\left[UW\frac{\partial h_z}{\partial \bar{x}}-U^2\frac{\partial h_x}{\partial \bar{z}}\right]+\frac{1}{h_z}VW\frac{\partial h_z}{\partial \bar{y}}\\
&\quad+2\left(\Omega_x V-\Omega_y U\right)-\frac{\Omega^2}{2}\nabla\vec{r}^2\\
&\quad=-\frac{1}{h_z}\frac{\partial P}{\partial \bar{z}}+\frac{1}{Re\,h_z}\frac{\partial}{\partial \bar{z}}\left(\frac{1}{h_x h_z}\left[\frac{\partial}{\partial \bar{x}}\left(h_z U\right)+\frac{\partial}{\partial \bar{y}}\left(h_x h_z V\right)+\frac{\partial}{\partial \bar{z}}\left(h_x W\right)\right]\right)\\
&\quad-\frac{1}{Re\,h_x}\left[\frac{\partial}{\partial \bar{x}}\left(\frac{1}{h_x h_z}\left[\frac{\partial}{\partial \bar{z}}\left(h_x U\right)-\frac{\partial}{\partial \bar{x}}\left(h_z W\right)\right]\right)-\frac{\partial}{\partial \bar{y}}\left(\frac{h_x}{h_z}\left[\frac{\partial}{\partial \bar{y}}\left(h_z W\right)-\frac{\partial}{\partial \bar{z}}\left(V\right)\right]\right)\right]
\end{aligned} \tag{C.4a–c}$$

The stability equations are solved in a rotating frame of reference resulting in the inclusion of Coriolis terms, shown on the second line of the momentum equations. Here $\vec{\Omega}$ is the angular velocity vector with direction along the axis of revolution and magnitude Ω, while the subscripts on Ω represent its components in the $\bar{x}$, $\bar{y}$ and $\bar{z}$ directions. Equations C.3 and C.4a–c have been non-dimensionalised using the following length, velocity, time and pressure scales, respectively:

$$L = \delta^*, \quad Q_e = \sqrt{u_e^2 + (r\Omega)^2}, \quad T = \frac{L}{Q_e}, \quad \mathrm{P} = \rho Q_e^2, \tag{C.5a–d}$$

The perturbation of equations C.3 and C.4a–c is performed by splitting the flow variables into steady mean-flow and perturbation components, of the form

$$(U,\ V,\ W,\ P) \ = \ (u + \tilde{u},\ v + \tilde{v},\ w + \tilde{w},\ p + \tilde{p}), \tag{C.6}$$

which after expanding, removing $\partial r/\partial \bar{y}$ terms, and subtracting the mean-flow terms yields

$$\frac{1}{h_x h_z}\left[\frac{\partial}{\partial \bar{x}}(h_z \tilde{u}) + \frac{\partial}{\partial \bar{y}}(h_x h_z \tilde{v}) + \frac{\partial}{\partial \bar{z}}(h_x \tilde{w})\right] = 0 \tag{C.7}$$

$$\begin{aligned}
&\frac{\partial \tilde{u}}{\partial t} + \frac{1}{h_x}\left[\tilde{u}\frac{\partial u}{\partial \bar{x}} + u\frac{\partial \tilde{u}}{\partial \bar{x}}\right] + \left[\tilde{v}\frac{\partial u}{\partial \bar{y}} + v\frac{\partial \tilde{u}}{\partial \bar{y}}\right] + \frac{1}{h_z}\left[\tilde{w}\frac{\partial u}{\partial \bar{z}} + w\frac{\partial \tilde{u}}{\partial \bar{z}}\right] \\
&\quad + \frac{1}{h_x}\left[\frac{\partial h_x}{\partial \bar{y}}(u\tilde{v} + v\tilde{u})\right] + \frac{1}{h_x h_z}\left[\frac{\partial h_x}{\partial \bar{z}}(u\tilde{w} + w\tilde{u}) - \frac{\partial h_z}{\partial \bar{x}}(2w\tilde{w})\right] \\
&\quad + 2\left(\Omega_y \tilde{w} - \Omega_z \tilde{v}\right) \\
&\quad = -\frac{1}{h_x}\frac{\partial \tilde{p}}{\partial \bar{x}} + \frac{1}{Re\, h_x}\frac{\partial}{\partial \bar{x}}\left(\frac{1}{h_x h_z}\left[\frac{\partial}{\partial \bar{x}}(h_z \tilde{u}) + \frac{\partial}{\partial \bar{y}}(h_x h_z \tilde{v}) + \frac{\partial}{\partial \bar{z}}(h_x \tilde{w})\right]\right) \\
&\quad - \frac{1}{Re\, h_z}\left[\frac{\partial}{\partial \bar{y}}\left(\frac{h_z}{h_x}\left[\frac{\partial}{\partial \bar{x}}(\tilde{v}) - \frac{\partial}{\partial \bar{y}}(h_x \tilde{u})\right]\right) - \frac{\partial}{\partial \bar{z}}\left(\frac{1}{h_x h_z}\left[\frac{\partial}{\partial \bar{z}}(h_x \tilde{u}) - \frac{\partial}{\partial \bar{x}}(h_z \tilde{w})\right]\right)\right]
\end{aligned} \tag{C.8a}$$

$$\begin{aligned}
&\frac{\partial \tilde{v}}{\partial t} + \frac{1}{h_x}\left[\tilde{u}\frac{\partial v}{\partial \bar{x}} + u\frac{\partial \tilde{v}}{\partial \bar{x}}\right] + \left[\tilde{v}\frac{\partial v}{\partial \bar{y}} + v\frac{\partial \tilde{v}}{\partial \bar{y}}\right] + \frac{1}{h_z}\left[\tilde{w}\frac{\partial v}{\partial \bar{z}} + w\frac{\partial \tilde{v}}{\partial \bar{z}}\right] \\
&\quad - \frac{1}{h_x}\frac{\partial h_x}{\partial \bar{x}}(2u\tilde{u}) - \frac{1}{h_z}\left[\frac{\partial h_z}{\partial \bar{y}}(2w\tilde{w})\right] + 2\left(\Omega_z\tilde{u} - \Omega_x\tilde{w}\right) \\
&\quad = -\frac{\partial \tilde{p}}{\partial \bar{y}} + \frac{1}{Re}\frac{\partial}{\partial \bar{y}}\left(\frac{1}{h_x h_z}\left[\frac{\partial}{\partial \bar{x}}(h_z\tilde{u}) + \frac{\partial}{\partial \bar{y}}(h_x h_z\tilde{v}) + \frac{\partial}{\partial \bar{z}}(h_x\tilde{w})\right]\right) \\
&\quad - \frac{1}{Re\, h_x h_z}\left[\frac{\partial}{\partial \bar{z}}\left(\frac{h_x}{h_z}\left[\frac{\partial}{\partial \bar{y}}(h_z\tilde{w}) - \frac{\partial}{\partial \bar{z}}(\tilde{v})\right]\right) - \frac{\partial}{\partial \bar{x}}\left(\frac{h_z}{h_x}\left[\frac{\partial}{\partial \bar{x}}(\tilde{v}) - \frac{\partial}{\partial \bar{y}}(h_x\tilde{u})\right]\right)\right]
\end{aligned}$$

$$\begin{aligned}
&\frac{\partial \tilde{w}}{\partial t} + \frac{1}{h_x}\left[\tilde{u}\frac{\partial w}{\partial \bar{x}} + u\frac{\partial \tilde{w}}{\partial \bar{x}}\right] + \left[\tilde{v}\frac{\partial w}{\partial \bar{y}} + v\frac{\partial \tilde{w}}{\partial \bar{y}}\right] + \frac{1}{h_z}\left[\tilde{w}\frac{\partial w}{\partial \bar{z}} + w\frac{\partial \tilde{w}}{\partial \bar{z}}\right] \\
&\quad + \frac{1}{h_x h_z}\left[\frac{\partial h_z}{\partial \bar{x}}(u\tilde{w} + w\tilde{u}) - \frac{\partial h_x}{\partial \bar{z}}(2u\tilde{u})\right] + \frac{1}{h_z}\left[\frac{\partial h_z}{\partial \bar{y}}(v\tilde{w} + w\tilde{v})\right] \\
&\quad + 2\left(\Omega_x\tilde{v} - \Omega_y\tilde{u}\right) \\
&\quad = -\frac{1}{h_z}\frac{\partial \tilde{p}}{\partial \bar{z}} + \frac{1}{Re\, h_z}\frac{\partial}{\partial \bar{z}}\left(\frac{1}{h_x h_z}\left[\frac{\partial}{\partial \bar{x}}(h_z\tilde{u}) + \frac{\partial}{\partial \bar{y}}(h_x h_z\tilde{v}) + \frac{\partial}{\partial \bar{z}}(h_x\tilde{w})\right]\right) \\
&\quad - \frac{1}{Re\, h_x}\left[\frac{\partial}{\partial \bar{x}}\left(\frac{1}{h_x h_z}\left[\frac{\partial}{\partial \bar{z}}(h_x\tilde{u}) - \frac{\partial}{\partial \bar{x}}(h_z\tilde{w})\right]\right) - \frac{\partial}{\partial \bar{y}}\left(\frac{h_x}{h_z}\left[\frac{\partial}{\partial \bar{y}}(h_z\tilde{w}) - \frac{\partial}{\partial \bar{z}}(\tilde{v})\right]\right)\right]
\end{aligned} \tag{C.8b,c}$$

Curvature coefficients are then defined wherein

$$\kappa_{xy} = \frac{1}{h_x}\frac{\partial h_x}{\partial \bar{y}}, \qquad \kappa_{xz} = \frac{1}{h_x h_z}\frac{\partial h_x}{\partial \bar{z}}, \tag{C.9a,b}$$

$$\kappa_{zx} = \frac{1}{h_z h_x}\frac{\partial h_z}{\partial \bar{x}}, \qquad \kappa_{zy} = \frac{1}{h_z}\frac{\partial h_z}{\partial \bar{y}}. \tag{C.9c,d}$$

After substitution various small or zero terms can be discarded. These include derivatives of curvature, in-plane curvature (κ_{xx} .. etc), as well as higher order curvature terms. Resulting in the following,

$$\kappa_{zx}\tilde{u} + \frac{\partial \tilde{u}}{h_x \partial \bar{x}} + \kappa_{xy}\tilde{v} + \kappa_{zy}\tilde{v} + \frac{\partial \tilde{v}}{\partial \bar{y}} + \kappa_{xz}\tilde{w} + \frac{\partial \tilde{w}}{h_z \partial \bar{z}} = 0 \tag{C.10}$$

$$\frac{\partial \tilde{u}}{\partial t} + u\frac{\partial \tilde{u}}{h_x \partial \bar{x}} + \tilde{u}\frac{\partial u}{h_x \partial \bar{x}} + v\frac{\partial \tilde{u}}{\partial \bar{y}} + \tilde{v}\frac{\partial u}{\partial \bar{y}} + w\frac{\partial \tilde{u}}{h_z \partial \bar{z}} + \tilde{w}\frac{\partial u}{h_z \partial \bar{z}} + \kappa_{xy}\left(u\tilde{v} + v\tilde{u}\right)$$
$$+ \kappa_{xz}\left(u\tilde{w} + w\tilde{u}\right) - 2\kappa_{zx}w\tilde{w} + 2\left(\Omega_y\tilde{w} - \Omega_z\tilde{v}\right) = -\frac{\partial \tilde{p}}{h_x \partial \bar{x}}$$
$$+ \frac{1}{Re}\left[\kappa_{zx}\frac{\partial \tilde{u}}{h_x \partial \bar{x}} + \left(\kappa_{xy} + \kappa_{zy}\right)\frac{\partial \tilde{u}}{\partial \bar{y}} + \kappa_{xz}\frac{\partial \tilde{u}}{h_z \partial \bar{z}} + \frac{\partial^2 \tilde{u}}{h_x^2 \partial \bar{x}^2}\right.$$
$$\left. + \frac{\partial^2 \tilde{u}}{\partial \bar{y}^2} + \frac{\partial^2 \tilde{u}}{h_z^2 \partial \bar{z}^2} + 2\kappa_{xy}\frac{\partial \tilde{v}}{h_x \partial \bar{x}} + 2\kappa_{xz}\frac{\partial \tilde{w}}{h_x \partial \bar{x}} - \kappa_{zx}\frac{\partial \tilde{w}}{h_z \partial \bar{z}}\right]$$

$$\frac{\partial \tilde{v}}{\partial t} + u\frac{\partial \tilde{v}}{h_x \partial \bar{x}} + \tilde{u}\frac{\partial v}{h_x \partial \bar{x}} + v\frac{\partial \tilde{v}}{\partial \bar{y}} + \tilde{v}\frac{\partial v}{\partial \bar{y}} + w\frac{\partial \tilde{v}}{h_z \partial \bar{z}} + \tilde{w}\frac{\partial v}{h_z \partial \bar{z}} - 2\kappa_{xy}u\tilde{u} - 2\kappa_{zy}w\tilde{w}$$
$$+ 2\left(\Omega_z\tilde{u} - \Omega_x\tilde{w}\right) = -\frac{\partial \tilde{p}}{\partial \bar{y}} + \frac{1}{Re}\left[\kappa_{zx}\frac{\partial \tilde{v}}{h_x \partial \bar{x}} + \left(\kappa_{xy} + \kappa_{zy}\right)\frac{\partial \tilde{v}}{\partial \bar{y}}\right.$$
$$\left. + \kappa_{xz}\frac{\partial \tilde{v}}{h_z \partial \bar{z}} + \frac{\partial^2 \tilde{v}}{h_x^2 \partial \bar{x}^2} + \frac{\partial^2 \tilde{v}}{\partial \bar{y}^2} + \frac{\partial^2 \tilde{v}}{h_z^2 \partial \bar{z}^2} - \kappa_{xy}\frac{\partial \tilde{u}}{h_x \partial \bar{x}} - \kappa_{zy}\frac{\partial \tilde{w}}{h_z \partial \bar{z}}\right]$$

$$\frac{\partial \tilde{w}}{\partial t} + u\frac{\partial \tilde{w}}{h_x \partial \bar{x}} + \tilde{u}\frac{\partial w}{h_x \partial \bar{x}} + v\frac{\partial \tilde{w}}{\partial \bar{y}} + \tilde{v}\frac{\partial w}{\partial \bar{y}} + w\frac{\partial \tilde{w}}{h_z \partial \bar{z}} + \tilde{w}\frac{\partial w}{h_z \partial \bar{z}} + \kappa_{zx}\left(u\tilde{w} + w\tilde{u}\right)$$
$$- 2\kappa_{xz}u\tilde{u} + \kappa_{zy}\left(v\tilde{w} + w\tilde{v}\right) + 2\left(\Omega_x\tilde{v} - \Omega_y\tilde{u}\right) = -\frac{\partial \tilde{p}}{h_z \partial \bar{z}}$$
$$+ \frac{1}{Re}\left[\kappa_{zx}\frac{\partial \tilde{w}}{h_x \partial \bar{x}} + \left(\kappa_{zy} + \kappa_{xy}\right)\frac{\partial \tilde{w}}{\partial \bar{y}} + \kappa_{xz}\frac{\partial \tilde{w}}{h_z \partial \bar{z}} + \frac{\partial^2 \tilde{w}}{h_x^2 \partial \bar{x}^2}\right.$$
$$\left. + \frac{\partial^2 \tilde{w}}{\partial \bar{y}^2} + \frac{\partial^2 \tilde{w}}{h_z^2 \partial \bar{z}^2} + 2\kappa_{zx}\frac{\partial \tilde{u}}{h_z \partial \bar{z}} - \kappa_{xz}\frac{\partial \tilde{u}}{h_x \partial \bar{x}} + 2\kappa_{zy}\frac{\partial \tilde{v}}{h_z \partial \bar{z}}\right]. \tag{C.11a–c}$$

It is then prudent to re-dimensionalise in order to absorb the scale factor (h_i) terms into the $\bar{x}$, $\bar{y}$ and $\bar{z}$ co-ordinates as follows, $\partial x = h_x \partial \bar{x}$, $\partial y = \partial \bar{y}$ and $\partial z = h_z \partial \bar{z}$, which yields the final form of the perturbation equations,

$$\kappa_{zx}\tilde{u} + \frac{\partial \tilde{u}}{\partial x} + \kappa_{xy}\tilde{v} + \kappa_{zy}\tilde{v} + \frac{\partial \tilde{v}}{\partial y} + \kappa_{xz}\tilde{w} + \frac{\partial \tilde{w}}{\partial z} = 0 \tag{C.12}$$

$$\begin{aligned}
&\frac{\partial \tilde{u}}{\partial t} + u\frac{\partial \tilde{u}}{\partial x} + \tilde{u}\frac{\partial u}{\partial x} + v\frac{\partial \tilde{u}}{\partial y} + \tilde{v}\frac{\partial u}{\partial y} + w\frac{\partial \tilde{u}}{\partial z} + \tilde{w}\frac{\partial u}{\partial z} + \kappa_{xy}\left(u\tilde{v} + v\tilde{u}\right) \\
&\quad + \kappa_{xz}\left(u\tilde{w} + w\tilde{u}\right) - 2\kappa_{zx}w\tilde{w} + 2\left(\Omega_y\tilde{w} - \Omega_z\tilde{v}\right) = -\frac{\partial \tilde{p}}{\partial x} \\
&\quad + \frac{1}{Re}\left[\kappa_{zx}\frac{\partial \tilde{u}}{\partial x} + \left(\kappa_{xy} + \kappa_{zy}\right)\frac{\partial \tilde{u}}{\partial y} + \kappa_{xz}\frac{\partial \tilde{u}}{\partial z} + \frac{\partial^2 \tilde{u}}{\partial x^2} + \frac{\partial^2 \tilde{u}}{\partial y^2} + \frac{\partial^2 \tilde{u}}{\partial z^2}\right. \\
&\quad \left. + 2\kappa_{xy}\frac{\partial \tilde{v}}{\partial x} + 2\kappa_{xz}\frac{\partial \tilde{w}}{\partial x} - \kappa_{zx}\frac{\partial \tilde{w}}{\partial z}\right]
\end{aligned}$$

$$\begin{aligned}
&\frac{\partial \tilde{v}}{\partial t} + u\frac{\partial \tilde{v}}{\partial x} + \tilde{u}\frac{\partial v}{\partial x} + v\frac{\partial \tilde{v}}{\partial y} + \tilde{v}\frac{\partial v}{\partial y} + w\frac{\partial \tilde{v}}{\partial z} + \tilde{w}\frac{\partial v}{\partial z} - 2\kappa_{xy}u\tilde{u} - 2\kappa_{zy}w\tilde{w} \\
&\quad + 2\left(\Omega_z\tilde{u} - \Omega_x\tilde{w}\right) = -\frac{\partial \tilde{p}}{\partial y} + \frac{1}{Re}\left[\kappa_{zx}\frac{\partial \tilde{v}}{\partial x} + \left(\kappa_{xy} + \kappa_{zy}\right)\frac{\partial \tilde{v}}{\partial y}\right. \\
&\quad \left. + \kappa_{xz}\frac{\partial \tilde{v}}{\partial z} + \frac{\partial^2 \tilde{v}}{\partial x^2} + \frac{\partial^2 \tilde{v}}{\partial y^2} + \frac{\partial^2 \tilde{v}}{\partial z^2} - \kappa_{xy}\frac{\partial \tilde{u}}{\partial x} - \kappa_{zy}\frac{\partial \tilde{w}}{\partial z}\right]
\end{aligned} \tag{C.13a–c}$$

$$\begin{aligned}
&\frac{\partial \tilde{w}}{\partial t} + u\frac{\partial \tilde{w}}{\partial x} + \tilde{u}\frac{\partial w}{\partial x} + v\frac{\partial \tilde{w}}{\partial y} + \tilde{v}\frac{\partial w}{\partial y} + w\frac{\partial \tilde{w}}{\partial z} + \tilde{w}\frac{\partial w}{\partial z} + \kappa_{zx}\left(u\tilde{w} + w\tilde{u}\right) \\
&\quad - 2\kappa_{xz}u\tilde{u} + \kappa_{zy}\left(v\tilde{w} + w\tilde{v}\right) + 2\left(\Omega_x\tilde{v} - \Omega_y\tilde{u}\right) = -\frac{\partial \tilde{p}}{\partial z} \\
&\quad + \frac{1}{Re}\left[\kappa_{zx}\frac{\partial \tilde{w}}{\partial x} + \left(\kappa_{zy} + \kappa_{xy}\right)\frac{\partial \tilde{w}}{\partial y} + \kappa_{xz}\frac{\partial \tilde{w}}{\partial z} + \frac{\partial^2 \tilde{w}}{\partial x^2} + \frac{\partial^2 \tilde{w}}{\partial y^2} + \frac{\partial^2 \tilde{w}}{\partial z^2}\right. \\
&\quad \left. + 2\kappa_{zx}\frac{\partial \tilde{u}}{\partial z} - \kappa_{xz}\frac{\partial \tilde{u}}{\partial x} + 2\kappa_{zy}\frac{\partial \tilde{v}}{\partial z}\right].
\end{aligned}$$

C.2 Derivation of the stability equations

The stability equations are formed by assuming a wave-like perturbation of the form

$$\left(\tilde{u},\ \tilde{v},\ \tilde{w},\ \tilde{p}\right) = \left(\hat{u},\ \hat{v},\ \hat{w},\ \hat{p}\right)e^{i\phi} \tag{C.14}$$

where

$$\phi = \alpha x + \beta z - \omega t. \tag{C.15}$$

Here α and β are the complex wavenumbers in the x and z directions respectively, and ω is a complex frequency. These can then be substituted into the perturbation

equations (C.12 and C.13a–c), resulting in

$$\kappa_{zx}\hat{u} + i\alpha\hat{u} + \kappa_{xy}\hat{v} + \kappa_{zy}\hat{v} + \frac{\partial\hat{v}}{\partial y} + \kappa_{xz}\hat{w} + i\beta\hat{w} = 0 \tag{C.16}$$

$$\begin{aligned}
&-i\omega\hat{u} + i\alpha u\hat{u} + \hat{u}\frac{\partial u}{\partial x} + v\frac{\partial\hat{u}}{\partial y} + \hat{v}\frac{\partial u}{\partial y} + i\beta w\hat{u} + \hat{w}\frac{\partial u}{\partial z} + \kappa_{xy}\left(u\hat{v} + v\hat{u}\right) \\
&\quad + \kappa_{xz}\left(u\hat{w} + w\hat{u}\right) - 2\kappa_{zx}w\hat{w} + 2\left(\Omega_y\hat{w} - \Omega_z\hat{v}\right) = -i\alpha\hat{p} \\
&\quad + \frac{1}{Re}\Bigg[i\alpha\kappa_{zx}\hat{u} + \left(\kappa_{xy} + \kappa_{zy}\right)\frac{\partial\hat{u}}{\partial y} + i\beta\kappa_{xz}\hat{u} - \alpha^2\hat{u} + \frac{\partial^2\hat{u}}{\partial y^2} - \beta^2\hat{u} \\
&\quad + 2i\alpha\kappa_{xy}\hat{v} + 2i\alpha\kappa_{xz}\hat{w} - i\beta\kappa_{zx}\hat{w}\Bigg] \\
&-i\omega\hat{v} + i\alpha u\hat{v} + \hat{u}\frac{\partial v}{\partial x} + v\frac{\partial\hat{v}}{\partial y} + \hat{v}\frac{\partial v}{\partial y} + i\beta w\hat{v} + \hat{w}\frac{\partial v}{\partial z} - 2\kappa_{xy}u\hat{u} - 2\kappa_{zy}w\hat{w} \\
&\quad + 2\left(\Omega_z\hat{u} - \Omega_x\hat{w}\right) = -\frac{\partial\hat{p}}{\partial y} + \frac{1}{Re}\Bigg[i\alpha\kappa_{zx}\hat{v} + \left(\kappa_{xy} + \kappa_{zy}\right)\frac{\partial\hat{v}}{\partial y} \\
&\quad + i\beta\kappa_{xz}\hat{v} - \alpha^2\hat{v} + \frac{\partial^2\hat{v}}{\partial y^2} - \beta^2\hat{v} - i\alpha\kappa_{xy}\hat{u} - i\beta\kappa_{zy}\hat{w}\Bigg] \\
&-i\omega\hat{w} + i\alpha u\hat{w} + \hat{u}\frac{\partial w}{\partial x} + v\frac{\partial\hat{w}}{\partial y} + \hat{v}\frac{\partial w}{\partial y} + i\beta w\hat{w} + \hat{w}\frac{\partial w}{\partial z} + \kappa_{zx}\left(u\hat{w} + w\hat{u}\right) \\
&\quad - 2\kappa_{xz}u\hat{u} + \kappa_{zy}\left(v\hat{w} + w\hat{v}\right) + 2\left(\Omega_x\hat{v} - \Omega_y\hat{u}\right) = -i\beta\hat{p} \\
&\quad + \frac{1}{Re}\Bigg[i\alpha\kappa_{zx}\hat{w} + \left(\kappa_{zy} + \kappa_{xy}\right)\frac{\partial\hat{w}}{\partial y} + i\beta\kappa_{xz}\hat{w} - \alpha^2\hat{w} + \frac{\partial^2\hat{w}}{\partial y^2} - \beta^2\hat{w} \\
&\quad + 2i\beta\kappa_{zx}\hat{u} - i\alpha\kappa_{xz}\hat{u} + 2i\beta\kappa_{zy}\hat{v}\Bigg]
\end{aligned} \tag{C.17a–c}$$

Subsequently, the flow is assumed to be parallel with the wall within the boundary layer, wherein $v = 0$, $u(y)$ and $w(y)$, therefore

$$\kappa_{zx}\hat{u} + i\alpha\hat{u} + \kappa_{xy}\hat{v} + \kappa_{zy}\hat{v} + \frac{\partial\hat{v}}{\partial y} + \kappa_{xz}\hat{w} + i\beta\hat{w} = 0 \tag{C.18}$$

$$-i\omega\hat{u} + i\alpha u\hat{u} + \hat{v}\frac{\partial u}{\partial y} + i\beta w\hat{u} + \kappa_{xy}u\hat{v} + \kappa_{xz}\left(u\hat{w} + w\hat{u}\right) - 2\kappa_{zx}w\hat{w} + 2\left(\Omega_y\hat{w} - \Omega_z\hat{v}\right)$$
$$= -i\alpha\hat{p} + \frac{1}{Re}\left[i\alpha\kappa_{zx}\hat{u} + \left(\kappa_{xy} + \kappa_{zy}\right)\frac{\partial\hat{u}}{\partial y} + i\beta\kappa_{xz}\hat{u} - \alpha^2\hat{u} + \frac{\partial^2\hat{u}}{\partial y^2} - \beta^2\hat{u}\right.$$
$$\left. + 2i\alpha\kappa_{xy}\hat{v} + 2i\alpha\kappa_{xz}\hat{w} - i\beta\kappa_{zx}\hat{w}\right]$$

$$-i\omega\hat{v} + i\alpha u\hat{v} + i\beta w\hat{v} - 2\kappa_{xy}u\hat{u} - 2\kappa_{zy}w\hat{w} + 2\left(\Omega_z\hat{u} - \Omega_x\hat{w}\right) = -\frac{\partial\hat{p}}{\partial y}$$
$$+ \frac{1}{Re}\left[i\alpha\kappa_{zx}\hat{v} + \left(\kappa_{xy} + \kappa_{zy}\right)\frac{\partial\hat{v}}{\partial y} + i\beta\kappa_{xz}\hat{v} - \alpha^2\hat{v} + \frac{\partial^2\hat{v}}{\partial y^2} - \beta^2\hat{v} - i\alpha\kappa_{xy}\hat{u} - i\beta\kappa_{zy}\hat{w}\right]$$

$$-i\omega\hat{w} + i\alpha u\hat{w} + \hat{v}\frac{\partial w}{\partial y} + i\beta w\hat{w} + \kappa_{zx}\left(u\hat{w} + w\hat{u}\right) - 2\kappa_{xz}u\hat{u} + \kappa_{zy}w\hat{v} + 2\left(\Omega_x\hat{v} - \Omega_y\hat{u}\right)$$
$$= -i\beta\hat{p} + \frac{1}{Re}\left[i\alpha\kappa_{zx}\hat{w} + \left(\kappa_{zy} + \kappa_{xy}\right)\frac{\partial\hat{w}}{\partial y} + i\beta\kappa_{xz}\hat{w} - \alpha^2\hat{w} + \frac{\partial^2\hat{w}}{\partial y^2} - \beta^2\hat{w}\right.$$
$$\left. + 2i\beta\kappa_{zx}\hat{u} - i\alpha\kappa_{xz}\hat{u} + 2i\beta\kappa_{zy}\hat{v}\right] \qquad \text{(C.19a–c)}$$

C.3 Input file descriptors and non-dimensionalisations

Boundary layer data file layout											
Record number	**Item 1**	**Item 2**	**Item 3**	**Item 4**	**Item 5**	**Item 6**	**Item 7**	**Item 8**	**Item 9**	**Item 10**	**Item 11**
1	TITLE1										
2	TITLE2										
	$** A variable number of comment lines introduced by the **$ character.										
	$ LSCALE	**OMEGA**	**UINF**								
3	LSCALE	OMEGA	UINF								
	$ NSTN	**NP**	**XC**	**DSC**	**MCURV**	**ACURV**	**TANGLE**				
4.1	NSTN	NP	XC	DSC	MCURV	ACURV	TANGLE				
	$ RLOC	**MACH**	**PHI**	**QE**							
4.2	RLOC	MACH	PHI	QE							
	$ DELTAS	**RHOE**	**TE**	**VISCE**							
4.3	DELTAS	RHOE	TE	VISCE							
	$ N	**Z**	**U**	**DU**	**DDU**	**W**	**DW**	**DDW**	**T**	**DT**	**DDT**
4.4.1	N	Z	U	DU	DDU	W	DW	DDW	T	DT	DDT
4.4.2	Structure and detail as record 4.4.1										
5, etc.	Structure as record 4. Detail as records 4.1, 4.2, 4.3, 4.4.1 etc.										

Figure C.1: Layout of boundary layer input data file for stability method described in chapter 4.

Boundary layer data file description				
Record	**Item**	**Name**	**Type**	**Description**
1	1	**TITLE1**	C*80	80 character comment line.
2	1	TITLE2	C*80	80 character comment line.
3	1	**LSCALE**	DP	Non-dimensionalising length scale in m.
	2	**OMEGA**	DP	Rotational speed in rad/s.
	3	UINF	DP	Axial free stream velocity in m/s.
4.1	1	**NSTN**	I	Station identification number.
	2	**NP**	I	Number of boundary layer points in profile (minus one).
	3	**XC**	DP	X position normalised by LSCALE.
	4	**DSC**	DP	Curvilinear S section increment normalised by LSCALE.
	5	**MCURV**	DP	Meridional curvature in m^-1.
	6	**ACURV**	DP	Azimuthal curvature in m^-1.
	7	**TANGLE**	DP	Angle, in degrees, between surface tangent and axis of revolution.
4.2	1	**RLOC**	DP	Local Reynolds number based on RHOE, QE, DELTAS and VISCE.
	2	MACH	DP	Local Mach number based on QE and TE.
	3	**PHI**	DP	Angle, in degrees, between streamline and the DS vector.
	4	**QE**	DP	Local edge flow velocity in m/s.
4.3	1	**DELTAS**	DP	Local boundary layer displacement thickness in m.
	2	**RHOE**	DP	Local edge flow density in kg/m^3.
	3	TE	DP	Local edge flow temperature in K.
	4	**VISCE**	DP	Local edge flow dynamic viscosity in kg/ms.
4.4.1	1	N	I	Wall-normal index, counting from 0 to NP.
	2	**Y**	DP	Wall-normal co-ordinate normalised by DSTAR.
	3	**U**	DP	Velocity in edge streamline direction normalised by QE.
	4	**DU**	DP	Derivative of U with respect to wall-normal direction Y.
	5	**DDU**	DP	2nd derivative of U with respect to wall-normal direction Y.
	6	**W**	DP	Velocity in crossflow direction, normalised by QE.
	7	**DW**	DP	Derivative of W with respect to wall-normal direction Y.
	8	**DDW**	DP	2nd derivative of W with respect to wall-normal direction Y.
	9	T	DP	Static temperature normalised by TE.
	10	DT	DP	Derivative of T with respect to wall-normal direction Y.
	11	DDT	DP	2nd derivative of Y with respect to wall-normal direction Y.

Figure C.2: Description of boundary layer input data file for stability method described in chapter 4.

C.4 Compact-difference derivative matrices

The stability equations may be expressed in matrix form by substituting equation C.18 into C.19a–c and linearising using the following substitutions

$$\tau_u = \frac{\partial \hat{u}}{\partial y}, \quad \tau_w = \frac{\partial \hat{w}}{\partial y}, \tag{C.20a,b}$$

and where prime denotes a derivative in the y direction. Resulting in

$$A = \begin{bmatrix} \hat{u} \\ \tau_{\hat{u}} \\ \hat{w} \\ \hat{p} \\ \hat{v} \\ \tau_{\hat{w}} \end{bmatrix}' = \begin{bmatrix} 0 & 1 & 0 & 0 & 0 & 0 \\ A_{\tau_{\hat{u}}\hat{u}} & A_{\tau_{\hat{u}}\tau_{\hat{u}}} & A_{\tau_{\hat{u}}\hat{w}} & A_{\tau_{\hat{u}}\hat{p}} & A_{\tau_{\hat{u}}\hat{v}} & 0 \\ 0 & 0 & 0 & 0 & 0 & 1 \\ A_{\hat{p}\hat{u}} & A_{\hat{p}\tau_{\hat{u}}} & A_{\hat{p}\hat{w}} & 0 & A_{\hat{p}\hat{v}} & A_{\hat{p}\tau_{\hat{w}}} \\ A_{\hat{v}\hat{u}} & 0 & A_{\hat{v}\hat{w}} & 0 & A_{\hat{v}\hat{v}} & 0 \\ A_{\tau_{\hat{w}}\hat{u}} & 0 & A_{\tau_{\hat{w}}\hat{w}} & A_{\tau_{\hat{w}}\hat{p}} & A_{\tau_{\hat{w}}\hat{v}} & A_{\tau_{\hat{w}}\tau_{\hat{w}}} \end{bmatrix} \begin{bmatrix} \hat{u} \\ \tau_{\hat{u}} \\ \hat{w} \\ \hat{p} \\ \hat{v} \\ \tau_{\hat{w}} \end{bmatrix} \tag{C.21}$$

where

$$A_{\tau_{\hat{u}}\hat{u}} = (-i\omega + i\alpha u + i\beta w + \kappa_{xz} w)\, Re + \alpha^2 + \beta^2 - i\alpha\kappa_{zx} - i\beta\kappa_{xz}$$

$$A_{\tau_{\hat{u}}\tau_{\hat{u}}} = -\kappa_{xy} - \kappa_{zy}$$

$$A_{\tau_{\hat{u}}\hat{w}} = \left(\kappa_{xz} u - 2\kappa_{zx} w + 2\Omega_y\right) Re - 2i\alpha\kappa_{xz} + i\beta\kappa_{zx}$$

$$A_{\tau_{\hat{u}}\hat{p}} = i\alpha Re$$

$$A_{\tau_{\hat{u}}\hat{v}} = \left(u' + \kappa_{xy} u - 2\Omega_z\right) Re - 2i\alpha\kappa_{xy}$$

$$A_{\hat{p}\hat{u}} = 2\kappa_{xy} u - \frac{1}{Re} i\alpha\kappa_{xy} - 2\Omega_z$$

$$A_{\hat{p}\tau_{\hat{u}}} = -\frac{1}{Re}\left(i\alpha + \kappa_{zx}\right)$$

$$A_{\hat{p}\hat{w}} = 2\kappa_{zy} w - \frac{1}{Re} i\beta\kappa_{zy} + 2\Omega_x$$

$$A_{\hat{p}\hat{v}} = i\omega - i\alpha u - i\beta w - \frac{1}{Re}\left(\alpha^2 + \beta^2 - i\alpha\kappa_{zx} - i\beta\kappa_{xz}\right)$$

$$A_{\hat{p}\tau_{\hat{w}}} = -\frac{1}{Re}\left(i\beta + \kappa_{xz}\right) \tag{C.22a–r}$$

$$A_{\hat{v}\hat{u}} = -\kappa_{zx} - i\alpha$$

$$A_{\hat{v}\hat{w}} = -\kappa_{xz} - i\beta$$

$$A_{\hat{v}\hat{v}} = -\kappa_{xy} - \kappa_{zy}$$

$$A_{\tau_{\hat{w}}\hat{u}} = \left(\kappa_{zx} w - 2\kappa_{xz} u - 2\Omega_y\right) Re - 2i\alpha\kappa_{zx} + i\alpha\kappa_{xz}$$

$$A_{\tau_{\hat{w}}\hat{w}} = (-i\omega + i\alpha u + i\beta w + \kappa_{zx} u)\, Re + \alpha^2 + \beta^2 - i\alpha\kappa_{zx} - i\beta\kappa_{xz}$$

$$A_{\tau_{\hat{w}}\hat{p}} = i\beta Re$$

$$A_{\tau_{\hat{w}}\hat{v}} = \left(w' + \kappa_{zy} w + 2\Omega_x\right) Re - 2i\beta\kappa_{zy}$$

$$A_{\tau_{\hat{w}}\tau_{\hat{w}}} = -\kappa_{xy} - \kappa_{zy}$$

The derivative of A in the y direction is then

$$B = \frac{\partial A}{\partial y} = A' = \begin{bmatrix} 0 & 0 & 0 & 0 & 0 & 0 \\ B_{\tau_{\hat{u}}\hat{u}} & 0 & B_{\tau_{\hat{u}}\hat{w}} & 0 & B_{\tau_{\hat{u}}\hat{v}} & 0 \\ 0 & 0 & 0 & 0 & 0 & 0 \\ B_{\hat{p}\hat{u}} & 0 & B_{\hat{p}\hat{w}} & 0 & B_{\hat{p}\hat{v}} & 0 \\ 0 & 0 & 0 & 0 & 0 & 0 \\ B_{\tau_{\hat{w}}\hat{u}} & 0 & B_{\tau_{\hat{w}}\hat{w}} & 0 & B_{\tau_{\hat{w}}\hat{v}} & 0 \end{bmatrix} \tag{C.23}$$

where

$$\begin{aligned} B_{\tau_{\hat{u}}\hat{u}} &= (i\alpha u' + i\beta w' + \kappa_{xz} w')\, Re \\ B_{\tau_{\hat{u}}\hat{w}} &= (\kappa_{xz} u' - 2\kappa_{zx} w')\, Re \\ B_{\tau_{\hat{u}}\hat{v}} &= \left(u'' + \kappa_{xy} u'\right) Re \\ \\ B_{\hat{p}\hat{u}} &= 2\kappa_{xy} u' \\ B_{\hat{p}\hat{w}} &= 2\kappa_{zy} w' \\ B_{\hat{p}\hat{v}} &= -i\alpha u' - i\beta w' \\ \\ B_{\tau_{\hat{w}}\hat{u}} &= (\kappa_{zx} w' - 2\kappa_{xz} u')\, Re \\ B_{\tau_{\hat{w}}\hat{w}} &= (i\alpha u' + i\beta w' + \kappa_{zx} u')\, Re \\ B_{\tau_{\hat{w}}\hat{v}} &= \left(w'' + \kappa_{zy} w'\right) Re. \end{aligned} \tag{C.24a–i}$$

The derivative of A in the streamline, α, direction is then

$$C = \frac{\partial A}{\partial \alpha} = \begin{bmatrix} 0 & 0 & 0 & 0 & 0 & 0 \\ C_{\tau_{\hat{u}}\hat{u}} & 0 & C_{\tau_{\hat{u}}\hat{w}} & C_{\tau_{\hat{u}}\hat{p}} & C_{\tau_{\hat{u}}\hat{v}} & 0 \\ 0 & 0 & 0 & 0 & 0 & 0 \\ C_{\hat{p}\hat{u}} & C_{\hat{p}\tau_{\hat{u}}} & C_{\hat{p}\hat{w}} & 0 & C_{\hat{p}\hat{v}} & C_{\hat{p}\tau_{\hat{w}}} \\ C_{\hat{v}\hat{u}} & 0 & C_{\hat{v}\hat{w}} & 0 & 0 & 0 \\ C_{\tau_{\hat{w}}\hat{u}} & 0 & C_{\tau_{\hat{w}}\hat{w}} & C_{\tau_{\hat{w}}\hat{p}} & C_{\tau_{\hat{w}}\hat{v}} & 0 \end{bmatrix} \tag{C.25}$$

where

$$\begin{aligned}
C_{\tau_{\hat{u}}\hat{u}} &= i\frac{\partial \alpha}{\partial \alpha} uRe + i\frac{\partial \beta}{\partial \alpha} wRe + 2\left(\frac{\partial \alpha}{\partial \alpha}\alpha + \frac{\partial \beta}{\partial \alpha}\beta\right) - i\frac{\partial \alpha}{\partial \alpha}\kappa_{zx} - i\frac{\partial \beta}{\partial \alpha}\kappa_{xz} \\
C_{\tau_{\hat{u}}\hat{w}} &= -2i\frac{\partial \alpha}{\partial \alpha}\kappa_{xz} + i\frac{\partial \beta}{\partial \alpha}\kappa_{zx} \\
C_{\tau_{\hat{u}}\hat{p}} &= i\frac{\partial \alpha}{\partial \alpha} Re \\
C_{\tau_{\hat{u}}\hat{v}} &= -2i\frac{\partial \alpha}{\partial \alpha}\kappa_{xy} \\
C_{\hat{p}\hat{u}} &= -\frac{i}{Re}\frac{\partial \alpha}{\partial \alpha}\kappa_{xy} \\
C_{\hat{p}\tau_{\hat{u}}} &= -\frac{i}{Re}\frac{\partial \alpha}{\partial \alpha} \\
C_{\hat{p}\hat{w}} &= -\frac{i}{Re}\frac{\partial \beta}{\partial \alpha}\kappa_{zy} \\
C_{\hat{p}\hat{v}} &= -i\frac{\partial \alpha}{\partial \alpha} u - i\frac{\partial \beta}{\partial \alpha} w - \frac{1}{Re}\left(2\left(\frac{\partial \alpha}{\partial \alpha}\alpha + \frac{\partial \beta}{\partial \alpha}\beta\right) - i\frac{\partial \alpha}{\partial \alpha}\kappa_{zx} - i\frac{\partial \beta}{\partial \alpha}\kappa_{xz}\right) \\
C_{\hat{p}\tau_{\hat{w}}} &= -\frac{i}{Re}\frac{\partial \beta}{\partial \alpha} \\
C_{\hat{v}\hat{u}} &= -i\frac{\partial \alpha}{\partial \alpha} \\
C_{\hat{v}\hat{w}} &= -i\frac{\partial \beta}{\partial \alpha} \\
C_{\tau_{\hat{w}}\hat{u}} &= -2i\frac{\partial \alpha}{\partial \alpha}\kappa_{zx} + i\frac{\partial \alpha}{\partial \alpha}\kappa_{xz} \\
C_{\tau_{\hat{w}}\hat{w}} &= i\frac{\partial \alpha}{\partial \alpha} uRe + i\frac{\partial \beta}{\partial \alpha} wRe + 2\left(\frac{\partial \alpha}{\partial \alpha}\alpha + \frac{\partial \beta}{\partial \alpha}\beta\right) - i\frac{\partial \alpha}{\partial \alpha}\kappa_{zx} - i\frac{\partial \beta}{\partial \alpha}\kappa_{xz} \\
C_{\tau_{\hat{w}}\hat{p}} &= i\frac{\partial \beta}{\partial \alpha} Re \\
C_{\tau_{\hat{w}}\hat{v}} &= -2i\frac{\partial \beta}{\partial \alpha}\kappa_{zy}
\end{aligned} \tag{C.26a–o}$$

Finally, the derivative of A in both the y and α directions is given by

$$D = \frac{\partial B}{\partial \alpha} = \frac{\partial^2 A}{\partial \alpha \partial y} = \begin{bmatrix} 0 & 0 & 0 & 0 & 0 & 0 \\ D_{\tau_{\hat{u}}\hat{u}} & 0 & 0 & 0 & 0 & 0 \\ 0 & 0 & 0 & 0 & 0 & 0 \\ 0 & 0 & 0 & 0 & D_{\hat{p}\hat{v}} & 0 \\ 0 & 0 & 0 & 0 & 0 & 0 \\ 0 & 0 & D_{\tau_{\hat{w}}\hat{w}} & 0 & 0 & 0 \end{bmatrix} \tag{C.27}$$

where

$$D_{\tau_{\hat{u}}\hat{u}} = i\frac{\partial \alpha}{\partial \alpha}u' Re + i\frac{\partial \beta}{\partial \alpha}w' Re$$

$$D_{\hat{p}\hat{v}} = -i\frac{\partial \alpha}{\partial \alpha}u' - i\frac{\partial \beta}{\partial \alpha}w' \tag{C.28a–c}$$

$$D_{\tau_{\hat{w}}\hat{w}} = i\frac{\partial \alpha}{\partial \alpha}u' Re + i\frac{\partial \beta}{\partial \alpha}w' Re$$

C.5 Leading edge curvature proof

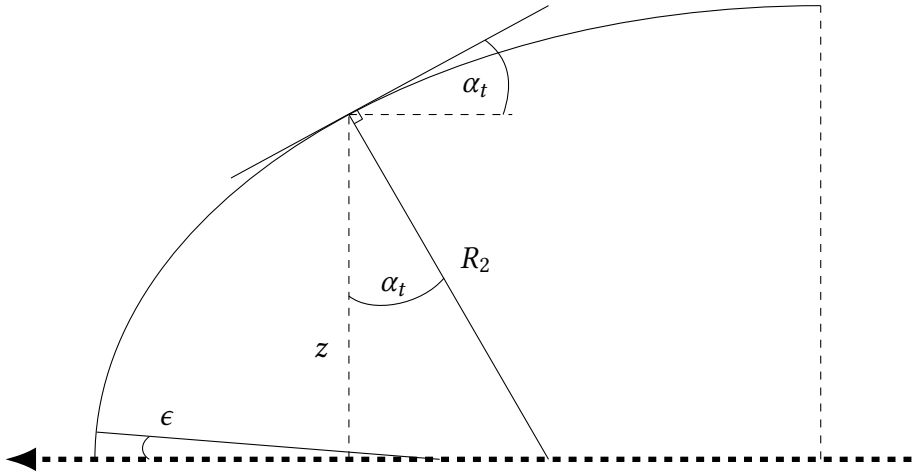

Figure C.3: Sketch of leading edge curvature for an axi-symmetric body.

For the case in which there is a blunt leading edge, let

$$\kappa_1 = \frac{1}{R_1} \qquad \text{and} \qquad \kappa_2 = \frac{1}{R_2}. \tag{C.29}$$

therefore,

$$z = \frac{cos\alpha_t}{\kappa_2}. \tag{C.30}$$

Near the leading edge,

$$\alpha_t \to \frac{\pi}{2}, \quad \text{so} \quad \frac{\pi}{2} - \alpha_t \to \epsilon \,(\text{small}) \tag{C.31}$$

therefore,

$$\cos \alpha_t \to \sin \epsilon \to \epsilon. \tag{C.32}$$

Expressing ϵ as an expansion in s:

$$\epsilon = \frac{\partial \epsilon}{\partial s} s + \frac{1}{2!} \frac{\partial^2 \epsilon}{\partial s^2} s^2 + \frac{1}{3!} \frac{\partial^3 \epsilon}{\partial s^3} s^3 + \dots \tag{C.33}$$

and as $s \to 0$ it follows that,

$$\epsilon \approx \frac{\partial \epsilon}{\partial s} s \tag{C.34}$$

so

$$z \to s \tag{C.35}$$

hence

$$\frac{\partial \epsilon}{\partial s} = -\frac{\partial \theta}{\partial s} = \kappa_1. \tag{C.36}$$

Finally, substituting C.32, C.34, C.35 and C.36 into C.30 results in

$$s \approx \frac{\kappa_1 s}{\kappa_2} \tag{C.37}$$

or more specifically,

$$\kappa_1 \approx \kappa_2 \tag{C.38}$$

Q.E.D.

References

[1] Atkin, C. 'Performance trade-off studies for a retrofit Hybrid Laminar Flow Control system'. In: *2nd AIAA Flow Control Conference*. 2004.

[2] Atkin, C. 'Laminar Flow Control: Leap or Creep?' In: *American Institute of Aeronautics and Astronautics* (2008).

[3] Atkin, C. 'e^N - Why it works; when it doesn't; what's next?' In: *ERCOFTAC Bulletin* 80 (Sept. 2009), p. 77.

[4] Backer Dirks, T. and Atkin, C. 'Systems driven HLFC design'. In: *50th 3AF Conference, Toulouse*. 2015.

[5] Backer Dirks, T. and Atkin, C. 'A consolidated method for predicting laminar boundary layers on rotating axi-symmetric bodies.' In: *European Journal of Mechanics - B/Fluids* (2018).

[6] Banks, W. H. H. 'The boundary layer on a rotating sphere'. In: *The Quarterly Journal of Mechanics and Applied Mathematics* 18.4 (1965), pp. 443–454.

[7] Banks, W. H. H. 'The laminar boundary layer on a rotating sphere'. In: *Acta Mechanica* 24.3-4 (1976), pp. 273–287.

[8] Barrow, A., Garrett, S. J. and Peake, N. 'Global linear stability of the boundary-layer flow over a rotating sphere'. In: *European Journal of Mechanics-B/Fluids* 49 (2015), pp. 301–307.

[9] Benton, E. R. 'Laminar boundary layer on an impulsively started rotating sphere'. In: *Journal of Fluid Mechanics* 23.3 (1965), pp. 611–623.

[10] Benton, E. R. 'On the flow due to a rotating disk'. In: *Journal of Fluid Mechanics* 24.04 (Mar. 1966), pp. 781–800.

[11] Cochran, W. G. 'The flow due to a rotating disc'. In: *Mathematical Proceedings of the Cambridge Philosophical Society*. Vol. 30(03). Cambridge Univ Press. 1934, pp. 365–375.

[12] Deyhle, H. and Bippes, H. 'Disturbance growth in an unstable three-dimensional boundary layer and its dependence on environmental conditions'. In: *Journal of Fluid Mechanics* 316 (1996), pp. 73–113.

[13] Eaton, J. K. *Experimental investigation of the three-dimensional boundary layer on a rotating disk*. Tech. rep. January. 1989.

[14] Eviation Aircraft. URL: https://www.eviation.co/ (visited on 01/11/2018).

[15] Fadnis, B. S. 'Boundary layer on rotating spheroids'. In: *Zeitschrift für Angewandte Mathematik und Physik (ZAMP)* 5.2 (1954), pp. 156–163.

[16] Fage, A. 'Experiments on a sphere at critical Reynolds numbers'. In: *Aero. Res. Council Gt. Brit.* (1936).

[17] Fjørtoft, R. *Application of integral theorems in deriving criteria of stability for laminar flows and for the baroclinic circular vortex*. Grøndahl & søns boktr., I kommisjon hos Cammermeyers boghandel, 1950.

[18] Floryan, J. M. and Saric, W. S. 'Stability of Gortler vortices in boundary layers'. In: *AIAA Journal* 20.3 (1982), pp. 316–324.

[19] Garrett, S. J. 'The stability and transition of the boundary layer on rotating bodies'. PhD thesis. University of Cambridge, 2002.

[20] Garrett, S. J., Hussain, Z. and Stephen, S. O. 'The cross-flow instability of the boundary layer on a rotating cone'. In: *Journal of Fluid Mechanics* 622 (Feb. 2009), p. 209.

[21] Garrett, S. J., Hussain, Z. and Stephen, S. O. 'Boundary-layer transition on broad cones rotating in an imposed axial flow'. In: *American Institute of Aeronautics and Astronautics* (2010).

[22] Garrett, S. J. and Peake, N. 'The stability and transition of the boundary layer on a rotating sphere'. In: *Journal of Fluid Mechanics* 456 (Apr. 2002), pp. 199–218.

[23] Garrett, S. J. and Peake, N. 'The stability of the boundary layer on a sphere rotating in a uniform axial flow'. In: *European Journal of Mechanics - B/Fluids* 23.2 (Mar. 2004), pp. 241–253.

[24] Garrett, S. J. and Peake, N. 'The absolute instability of the boundary layer on a rotating cone'. In: *European Journal of Mechanics - B/Fluids* 26.3 (May 2007), pp. 344–353.

[25] Gasperas, G. 'The stability of the compressible boundary layer on a sharp cone at zero angle of attack'. In: *25th AIAA Aerospace Sciences Meeting*. 1987, p. 494.

[26] Gaster, M. 'A note on the relation between temporally-increasing and spatially-increasing disturbances in hydrodynamic stability'. In: *Journal of Fluid Mechanics* 14.2 (1962), pp. 222–224.

[27] Gaster, M. Personal communication. 1992.

[28] Gennes, P.-G. de, Brochard-Wyart, F. and Quéré, D. 'Capillarity: deformable interfaces'. In: *Capillarity and Wetting Phenomena*. Springer, 2004, pp. 1–31.

[29] Gibson, I. S. 'Application of Vortex singularities to ducted propellers'. PhD thesis. University of Newcastle upon Tyne, 1972.

[30] Green, J. E. 'Laminar Flow Control - Back to the Future?' In: *38th Fluid Dynamics Conference and Exhibit*. Fluid Dynamics and Co-located Conferences. American Institute of Aeronautics and Astronautics, June 2008.

[31] Gregory, N., Stuart, J. T. and Walker, W. S. 'On the stability of three-dimensional boundary layers with application to the flow due to a rotating disk'. In: *Philosophical Transactions of the Royal Society of London. Series A, Mathematical and Physical Sciences* (1955), pp. 155–199.

[32] Hall, P. 'The linear development of Görtler vortices in growing boundary layers'. In: *Journal of Fluid Mechanics* 130 (1983), pp. 41–58.

[33] Hall, P. 'The Gortler vortex instability mechanism in three-dimensional boundary layers'. In: *Proceedings of the Royal Society of London. A. Mathematical and Physical Sciences* 399.1816 (1985), pp. 135–152.

[34] Hall, P. 'An asymptotic investigation of the stationary modes of instability of the boundary layer on a rotating disc'. In: *Proc. R. Soc. Lond. A* 406.1830 (1986), pp. 93–106.

[35] Hess, J. L. and Faulkner, S. 'Accurate values of the exponent governing potential flow about semi-infinite cones'. In: *AIAA Journal* 3.4 (1965), pp. 767–767.

[36] Horton, H. P. and Stock, H.-W. 'Computation of compressible, laminar boundary layers on swept, tapered wings'. In: *Journal of Aircraft* 32.6 (1995), pp. 1402–1405.

[37] Howarth, L. 'CXXIX. Note on the boundary layer on a rotating sphere'. In: *London, Edinburgh, and Dublin Philosophical Magazine and Journal of Science* 42.334 (1951), pp. 1308–1315.

[38] Huerre, P. and Monkewitz, P. A. 'Local and global instabilities in spatially developing flows'. In: *Annual review of fluid mechanics* 22.1 (1990), pp. 473–537.

[39] Hussain, Z. 'Stability and transition of three-dimensional rotating boundary layers'. PhD thesis. University of Birmingham, 2010.

[40] Imayama, S. *Experimental study of the rotating-disk boundary-layer flow*. Tech. rep. May. 2012.

[41] Kegelman, J. T., Nelson, R. C. and Mueller, T. J. 'The boundary layer on an axisymmetric body with and without spin'. In: *AIAA journal* 21.11 (1983), pp. 1485–1491.

[42] Kobayashi, R. 'Linear stability theory of boundary layer along a cone rotating in axial flow'. In: *Bulletin of JSME* 24.192 (1981), pp. 934–940.

[43] Kobayashi, R. and Arai, T. 'Spiral vortex behavior in transition region and separation of three-dimensional boundary layers on spheres rotating in axial flow'. In: *Laminar-Turbulent Transition*. Springer, 1990, pp. 551–557.

[44] Kobayashi, R. and Izumi, H. 'Boundary-layer transition on a rotating cone in still fluid'. In: *Journal of Fluid Mechanics* 127 (1983), pp. 353–364.

[45] Kobayashi, R., Kohama, Y. and Kurosawa, M. 'Boundary-layer transition on a rotating cone in axial flow'. In: *Journal of Fluid Mechanics* 127 (Apr. 1983), pp. 341–352.

[46] Koh, J. C. Y. and Price, J. F. 'Non-similar boundary layer heat transfer of a rotating cone in a forced flow.' In: *Journal of Heat Transfer* 89.2 (1967), pp. 139–145.

[47] Kohama, Y. 'Flow structures formed by axisymmetric spinning bodies'. In: *AIAA journal* 23.9 (1985), pp. 1445–1447.

[48] Kohama, Y. and Kobayashi, R. 'Boundary-layer transition and the behaviour of spiral vortices on rotating spheres'. In: *Journal of Fluid Mechanics* 137 (1983), pp. 153–164.

[49] Lewis, R. I. *Vortex element methods for fluid dynamic analysis of engineering systems*. Vol. 1. Cambridge University Press, 1991.

[50] Lingwood, R. J. 'Absolute instability of the boundary layer on a rotating disk'. In: *Journal of Fluid Mechanics* 299 (Apr. 1995), pp. 17–33.

[51] Lingwood, R. J. 'An experimental study of absolute instability of the rotating-disk boundary-layer flow'. In: *Journal of Fluid Mechanics* 314 (Apr. 1996), p. 373.

[52] Mack, L. M. 'Boundary layer linear stability theory'. In: *AGARD* 709.3 (1984).

[53] Malik, M. R. *Instability and transition in rotating disk flow*. Tech. rep. 1981.

[54] Malik, M. R. 'The neutral curve for stationary disturbances in rotating-disk flow'. In: *Journal of Fluid Mechanics* 164 (1986), pp. 275–287.

[55] Malik, M. R. 'Numerical methods for hypersonic boundary layer stability'. In: *Journal of computational physics* 86.2 (1990), pp. 376–413.

[56] Malik, M. R. and Poll, D. I. A. 'Effect of curvature on three-dimensional boundary-layer stability'. In: *AIAA journal* 23.9 (1985), pp. 1362–1369.

[57] Malik, M. R. and Spall, R. E. 'On the stability of compressible flow past axisymmetric bodies'. In: *Journal of fluid mechanics* 228 (1991), pp. 443–463.

[58] Mangler, W. *Grenzschichten an Rotationskörpern bei symmetrischer Anblasung*. Bericht / A: Bericht. Aerodynamische Versuchsanstalt, 1945.

[59] Manohar, R. 'The boundary layer on a rotating sphere'. In: *Zeitschrift für Angewandte Mathematik und Physik (ZAMP)* 18.3 (1967), pp. 320–330.

[60] McLeod, J. B. 'Von Karman's swirling flow problem'. In: *Archive for Rational Mechanics and Analysis* 33.2 (1969), pp. 91–102.

[61] Merksyn, D. 'The laminar boundary-layer equations of bodies of revolution. Motion of a sphere'. In: *Proceedings of the Royal Society of London. Series A, Mathematical and Physical*. Vol. 194. 1037. 1947, pp. 218–228.

[62] Morkovin, M. V. 'On the Many Faces of Transition'. English. In: *Viscous Drag Reduction SE - 1*. Ed. by Wells, C. Springer US, 1969, pp. 1–31.

[63] Morkovin, M. V., Reshotko, E. and Herbert, T. 'Transition in open flow systems - a reassessment'. In: *Bulletin of the American Physical Society* 39.9 (1994), pp. 1882–1994.

[64] Mueller, T. J., Nelson, R. C., Kegelman, J. T. and Morkovin, M. V. 'Smoke visualization of boundary-layer transition on a spinning axisymmetric body'. In: *AIAA Journal* 19.12 (1981), pp. 1607–1608.

[65] Mueller, T. J., Nelson, R. C., Kegelman, J. T. and Zehentner, R. J. *Boundary Layer and Side Force Characteristics of Non-Spinning and Spinning Axisymmetric Bodies*. Tech. rep. Notre Dame University, Deptartment Of Aerospace and Mechanical Engineering, 1981.

[66] Obremski, H. J. et al. *A portfolio of stability characteristics of incompressible boundary layers*. Tech. rep. Advisory Group For Aerospace Research and Development Neuilly-Sur-Seine (France), 1969.

[67] Poll, D. I. A. 'Transition in the infinite swept attachment line boundary layer'. In: *Aeronaut Q* 30 (1979), pp. 607–629.

[68] Poll, D. I. A. 'Some observations of the transition process on the windward face of a long yawed cylinder'. In: *Journal of Fluid Mechanics* 150 (1985), pp. 329–356.

[69] Rayleigh, L. 'On the stability, or instability, of certain fluid motions'. In: *Proc. London Math. Soc.* 9 (1880), pp. 57–70.

[70] Reed, H. L. and Saric, W. S. 'Stability of three-dimensional boundary layers'. In: *Annual Review of Fluid Mechanics* 21 (1989), pp. 235–84.

[71] Samad, A. and Garrett, S. J. 'On the laminar boundary-layer flow over rotating spheroids'. In: *International Journal of Engineering Science* 48.12 (2010), pp. 2015–2027.

[72] Samad, A. and Garrett, S. J. 'On the stability of boundary-layer flows over rotating spheroids'. In: *International Journal of Engineering Science* 82 (2014), pp. 28–45.

[73] Saric, W. S., Reed, H. L. and White, E. B. 'Stability and Transition of Three-Dimensional Boundary Layers'. In: *Annual Review of Fluid Mechanics* 35.1 (Jan. 2003), pp. 413–440.

[74] Sawatzki, O. 'Das Strömungsfeld um eine rotierende Kugel'. In: *Acta Mechanica* 9.3-4 (1970), pp. 159–214.

[75] Schlichting, H. 'Die laminare Strömung um einen axial angeströmten rotierenden Drehkörper'. In: *Ingenieur-Archiv* 21.4 (1953), pp. 227–244.

[76] Schubauer, G. B. and Skramstad, H. K. *Laminar-boundary-layer oscillations and transition on a flat plate*. Tech. rep. National Aeronautics and Space Administration Washington DC, 1948.

[77] Segalini, A. and Garrett, S. J. 'On the non-parallel instability of the rotating-sphere boundary layer'. In: *Journal of Fluid Mechanics* 818 (2017), pp. 288–318.

[78] El-Shaarawi, M. A. I., El-Refaie, M. F. and El-Bedeawi, S. A. 'Numerical solution of laminar boundary layer flow about a rotating sphere in an axial stream'. In: *Journal of Fluids Engineering* 107 (1985), p. 97.

[79] Sheridan, R. E. *Laminar boundary layers on bodies of revolution: computer programs and vorticity budgets*. Tech. rep. Pennsylvania State University Park Ordnance Research Lab, 1968.

[80] Siemens. URL: https://www.siemens.com/press/pool/de/events/2016/corporate/2016-12-innovation/inno2016-aerobatic-airplane-e.pdf (visited on 01/11/2018).

[81] Smith, A. M. O. and Gamberoni, N. *Transition, pressure gradient and stability theory*. Douglas Aircraft Company, El Segundo Division, 1956.

[82] Taniguchi, H., Kobayashi, R. and Fukunishi, Y. 'Stability of the boundary layer on a sphere rotating in still fluid'. In: *Acta mechanica* 129.3-4 (1998), pp. 243–253.

[83] Tien, C. L. 'Heat transfer by laminar flow from a rotating cone'. In: *Journal of Heat Transfer* 82.3 (1960), pp. 252–253.

[84] U.S. Bureau of Labor Statistics. *Historical Consumer Price Index for All Urban Consumers (CPI-U)*. URL: https://www.bls.gov/cpi/tables/supplemental-files/historical-cpi-u-201806.pdf (visited on 19/07/2018).

[85] U.S. Energy Information Administration. *Europe Brent Spot Price FOB*. URL: https://www.eia.gov/dnav/pet/hist/rbrteD.htm (visited on 19/07/2018).

[86] Van Ingen, J. L. 'A suggested semi-empirical method for the calculation of the boundary layer transition region'. In: *Technische Hogeschool Delft, Vliegtuigbouwkunde, Rapport VTH-74* (1956).

[87] Van Ingen, J. L. 'The e^N method for transition prediction. Historical review of work at TU Delft'. In: *38th Fluid Dynamics Conference and Exhibit*. 2008, pp. 23–26.

[88] Von Kármán, T. 'Über laminare und turbulente Reibung'. In: *Zeitschrift fur Angewandte Mathematik und Mechanik (ZAMM)* 1.4 (1921).

[89] White, E. B. and Saric, W. S. 'Secondary instability of crossflow vortices'. In: *Journal of Fluid Mechanics* 525 (Feb. 2005), pp. 275–308.

[90] Wright Electric. URL: https://weflywright.com/ (visited on 01/11/2018).

[91] Wu, C. S. 'The three dimensional incompressible laminar boundary layer on a spinning cone'. In: *Applied Scientific Research, Section A* 8.1 (1959), pp. 140–146.

[92] Y-Combinator. URL: https://www.ycombinator.com/ (visited on 01/11/2018).